

AD-752 557

V/STOL AIRCRAFT AERODYNAMIC PREDICTION  
METHODS INVESTIGATION. VOLUME I. THEO-  
RETICAL DEVELOPMENT OF PREDICTION  
METHODS

Peter T. Wooler, et al

Northrop Corporation

Prepared for:

Air Force Flight Dynamics Laboratory

January 1972

DISTRIBUTED BY:

**NTIS**

National Technical Information Service  
U. S. DEPARTMENT OF COMMERCE  
5285 Port Royal Road, Springfield Va. 22151

**AFFDL-TR-72-26**  
**Volume I**

AD 752557

# **V/STOL AIRCRAFT AERODYNAMIC PREDICTION METHODS INVESTIGATION**

**Volume I. Theoretical Development of Prediction Methods**

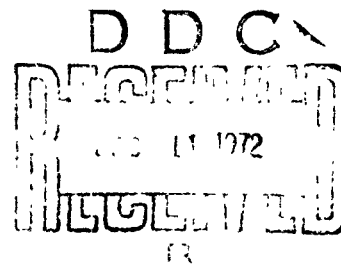
**P.T. Wooler  
H.C. Kao  
M.F. Schwendemann  
H.R. Wasson  
H. Ziegler**

**Northrop Corporation  
Aircraft Division**

**TECHNICAL REPORT AFFDL-TR-72-26, Volume I  
January 1972**

**Approved for public release; distribution unlimited.**

**NATIONAL TECHNICAL  
INFORMATION SERVICE**



**AIR FORCE FLIGHT DYNAMICS LABORATORY  
AIR FORCE SYSTEMS COMMAND  
WRIGHT-PATTERSON AIR FORCE BASE, OHIO 45433**

57

# NOTICE

When Government drawings, specifications, or other data are used for any purpose other than in connection with a definitely related Government procurement operation, the United States Government thereby incurs no responsibility nor any obligation whatsoever; and the fact that the Government may have formulated, furnished, or in any way supplied the said drawings, specifications, or other data, is not to be regarded by implication or otherwise as in any manner licensing the holder or any other person or corporation, or conveying any rights or permission to manufacture, use, or sell any patented invention that may in any way be related thereto.

ACCESSION for		
NTIS	White Section	<input checked="" type="checkbox"/>
DCC	Ext. Section	<input type="checkbox"/>
UNAN. OFFICE		<input type="checkbox"/>
JUSTIFICATION		
BY		
DISTRIBUTION/AVAILABILITY CODES		
Dist.	AVAIL. and/or SPECIAL	
A		

Copies of this report should not be returned unless return is required by security considerations, contractual obligations, or notice on a specific document.

Unclassified

Security Classification

DOCUMENT CONTROL DATA - R & D		
(Security classification of title, body of abstract and indexing or notation must be entered when the overall report is classified)		
1. ORIGINATING ACTIVITY (Corporate author) Northrop Corporation Aircraft Division Hawthorne, California		2a. REPORT SECURITY CLASSIFICATION Unclassified
		2b. GROUP
3. REPORT TITLE V/STOL AIRCRAFT AERODYNAMIC PREDICTION METHODS INVESTIGATION - Volume I		
4. DESCRIPTIVE NOTES (Type of report and inclusive dates) Final Report - 1 May 1969 to 31 January 1972		
5. AUTHOR(S) (First name, middle initial, last name) Peter T. Wooler Hsiao C. Kao Myles F. Schwendemann Howard R. Wasson Henry Ziegler		
6. REPORT DATE January 1972	7a. TOTAL NO. OF PAGES 210 237	7b. NO. OF REFS 50
8a. CONTRACT OR GRANT NO. F33615-69-C-1602	8b. ORIGINATOR'S REPORT NUMBER(S) NOR 72-9, Volume I	
8c. PROJECT NO. 698 BT		
8d. Task No. 698 BT 01	8e. OTHER REPORT NO(S) (Any other numbers that may be assigned this report) AFFDL-TR-72-26, Volume I	
9. DISTRIBUTION STATEMENT Approved for public release; distribution unlimited.		
11. SUPPLEMENTARY NOTES		12. SPONSORING MILITARY ACTIVITY Air Force Flight Dynamics Laboratory Wright-Patterson Air Force Base Ohio 45433
13. ABSTRACT Analytical engineering methods are developed for use in predicting the static and dynamic stability and control derivatives and force and moment coefficients of lift-jet, lift-fan, and vectored thrust V/STOL aircraft in the hover and transition flight regimes. The methods take into account the strong power effects, large variations in angle of attack and sideslip, and changes in aircraft geometry that are associated with high disk loaded V/STOL aircraft operating in the aforementioned flight regimes. The aircraft configurations studied have a conventional wing, fuselage and empennage. The prediction methods are suitable for use by design personnel during the preliminary design and evaluation of V/STOL aircraft of the type previously mentioned.  This report consists of four volumes. The theoretical development of the prediction methods is presented in this volume. The methods are applied to a number of V/STOL configurations in Volume II. Details of the computer programs associated with the prediction methods are given in Volume III. The results of a literature survey are presented in Volume IV.  Details of illustrations in this document may be better studied on microfiche		

DD FORM 1473  
1 NOV 66

Unclassified

Security Classification

**Unclassified**  
Security Classification

14 KEY WORDS	LINK A		LINK B		LINK C	
	ROLE	WT	ROLE	WT	ROLE	WT
V/STOL Aircraft						
XV-5A						
V/STOL Stability and Control						
Aerodynamic Characteristics (Subsonic)						
Forces (Normal Force, Lift, Side Force)						
Moments (Pitching, Rolling, Yawing)						
Rotary Derivatives						
V/STOL Aerodynamics						
Nonlinear Aerodynamics						
Wing Stall						
Separated Flows						
V/STOL Transitional Flight						
Engine Wake Effects						
Jet Exhaust Fields						
Jet Interference Effects						
Jet in Cross Flow						
Jet Path						
Multiple Jets						
Jet Interaction						
Power Effects						
Engine Inlet Effects						
Vortices						
Computer Programs						

**V/STOL AIRCRAFT AERODYNAMIC  
PREDICTION METHODS INVESTIGATION**

**Volume I  
Theoretical Development of Prediction Methods**

**P.T. Wooler  
H.C. Kao  
M.F. Schwendemann  
H.R. Wasson  
H. Ziegler**

Approved for public release; distribution unlimited.

## FOREWORD

This report summarizes the work accomplished by the Aircraft Division of Northrop Corporation, Hawthorne, California for the Air Force Flight Dynamics Laboratory, AFSC, Wright Patterson Air Force Base, Ohio, and USAF Contract No. F33615-69-C-1602 (Project 698 BT). This document constitutes the Final Report under the contract.

This work was accomplished during the period 1 May 1969 to 31 January 1972, and this report was released by the authors in January 1972. The Air Force Project Engineers were Mr. Robert Nicholson and Mr. Henry W. Woolard of the Control Criteria Branch, Flight Control Division, AFFDL. Their assistance in monitoring the work and providing data is greatly appreciated.

The authors gratefully acknowledge the assistance and cooperation of NASA Langley Research Center personnel during the wind tunnel model testing in the NASA Langley V/STOL tunnel.

Special recognition is due Mr. Richard J. Margason of NASA Langley Research Center who, besides being actively involved in the testing at Langley, has made valuable contributions to other areas of the investigation.

Various people at Northrop's Aircraft Division contributed to the investigation, particularly the following persons in the areas designated:


Lynn B. Fricke	Developed empirical methods for the wing. Was Test Engineer for the wind tunnel testing of the component model.
Hsiao C. Kao	Developed the transformation method for estimating power effects on wings and fuselages. Developed the empirical method for the body.
Myles F. Schwendemann	Developed the method for estimating engine inlet effects. Provided prediction method wind tunnel testing interface for the configuration model. Participated in the hover analysis.

Martin F. Silady	Assembled the V/STOL bibliography and was responsible for the literature survey.
Howard R. Wasson	Developed the method for mapping general sections. Developed the nonlinear body prediction method. Assisted with the development of the perturbation method.
Peter T. Wooler	Directed the technical effort and developed the nonlinear wing prediction method.
Henry Ziegler	Developed the jet flow field prediction method. Performed the analysis of wing power effects employing lifting surface theory.

Contributions have also been made by U. A. G. Brynjestad to this study in a number of areas, particularly the literature search and perturbation method development; by M. S. Cahn in the development of the method for mapping general sections and perturbation method development; by members of the Northrop Aerospace Laboratories in respect to model design, fabrication, testing and data reduction — especially T. Comerinsky, F. W. Peitzman, E. G. Kontos and W. S. Ramos.

This report contains no classified information.

This technical report has been reviewed and is approved.

  
 C. B. Westbrook  
 Chief, Control Criteria Branch  
 Flight Control Division  
 Air Force Flight Dynamics Laboratory



## ABSTRACT

Analytical engineering methods are developed for use in predicting the static and dynamic stability and control derivatives and force and moment coefficients of lift-jet, lift-fan, and vectored thrust V/STOL aircraft in the hover and transition flight regimes. The methods take into account the strong power effects, large variations in angle of attack and sideslip, and changes in aircraft geometry that are associated with high disk loaded V/STOL aircraft operating in the aforementioned flight regimes. The aircraft configurations studied have a conventional wing, fuselage and empennage. The prediction methods are suitable for use by design personnel during the preliminary design and evaluation of V/STOL aircraft of the type previously mentioned.

This report consists of four volumes. The theoretical development of the prediction methods is presented in this volume. The methods are applied to a number of V/STOL configurations in Volume II. Details of the computer programs associated with the prediction methods are given in Volume III. The results of a literature survey are presented in Volume IV.

Preceding page blank

## TABLE OF CONTENTS

Section	Page
I INTRODUCTION .....	1
1. PURPOSE .....	2
2. TECHNICAL APPROACH .....	2
3. REPORT ORGANIZATION .....	3
II JET FLOW FIELD THEORY .....	5
1. SINGLE JET ANALYTICAL MODEL .....	7
a. Normally Exhausting Jet .....	7
(1) Equations of Motion .....	9
(2) Integration of the Equations of Motion .....	11
(3) Determination of Empirical Parameters .....	14
(4) Calculation of the Induced Velocity Field .....	16
b. Arbitrary Jet Direction .....	23
2. COMPARISONS OF SINGLE JET-COMPUTATIONS WITH TEST DATA .....	26
a. Jet Centerlines .....	26
b. Induced Pressures .....	31
3. MULTIPLE JET ANALYTICAL MODEL .....	42
a. Two-Jet Computations .....	42
b. Determination of Empirical Parameters .....	45
(1) Effective Dynamic Pressure for Downstream Jets .....	45
(2) Jet Decay Characteristics .....	49
(3) Geometry of Merged Jet .....	56
4. COMPARISON OF TWO-JET CALCULATIONS WITH TEST DATA .....	57
5. APPLICATIONS TO MORE COMPLEX CONFIGURATIONS .....	72
III MAPPING METHOD FOR ARBITRARY CROSS SECTION .....	77
1. COMPUTATION OF COMPLEX POTENTIAL FOR VORTEX FLOW .....	78
2. COMPUTATION OF DERIVATIVE OF MAPPING FUNCTION WITH CORNERS .....	82
3. COMPUTATION OF MAPPING FUNCTION .....	83
4. SAMPLE CALCULATIONS OF MAPPINGS .....	84

## TABLE OF CONTENTS (Continued)

Section	Page
IV TRANSFORMATION METHOD . . . . .	88
1. INTRODUCTORY REMARKS. . . . .	88
2. COMPUTATION OF FUSELAGE PRESSURE DISTRIBUTION . . .	91
a. Segment Method . . . . .	91
(1) The Boundary Function . . . . .	91
(2) Application of Boundary Function to the Segment Method .	94
b. Three-Dimensional Modification . . . . .	98
3. COMPUTATION OF WING PRESSURE DISTRIBUTION . . . . .	101
4. COMPUTATIONS AND RESULTS . . . . .	103
V INLET FLOW FIELD . . . . .	105
1. ANALYSIS . . . . .	105
a. Lip Forces . . . . .	105
b. Surface Forces . . . . .	109
2. LIFT-FAN PROPULSION MODEL . . . . .	110
3. COMPARISON WITH PREVIOUS RESULTS . . . . .	112
4. DEVELOPMENT OF HANDBOOK METHOD . . . . .	113
VI NONLINEAR BODY AERODYNAMICS . . . . .	115
1. SLENDER BODY THEORY. . . . .	115
a. Simplified Method for Obtaining Major Mapping Coefficients .	119
2. VORTEX TRACKING METHOD . . . . .	124
3. VISCOUS CROSS FLOW METHOD . . . . .	127
VII NONLINEAR WING AERODYNAMICS . . . . .	130
1. NONLINEAR SECTION MODEL . . . . .	131
2. APPLICATION OF SECTION MODEL TO WING CALCULATIONS	137
a. Downwash Due to the Bound Vorticity . . . . .	137
b. Downwash Due to the Trailing Vorticity . . . . .	139
3. METHOD FOR CALCULATION OF WING CHARACTERISTICS . .	142
VIII EMPIRICAL METHODS USING JET FLOW FIELD THEORY . . . . .	145
1. EMPIRICAL METHODS FOR THE WING . . . . .	145
a. Equivalent Area Circle . . . . .	145
b. $\Delta\theta$ Method . . . . .	150

## TABLE OF CONTENTS (Continued)

Section	Page
c. Equivalent Plain Wing . . . . .	154
d. Application to Calculations of Downwash at Tail Surface . .	158
2. BODY METHOD . . . . .	159
a. Application of Lagally's Theorem in Relation to the Present Problem . . . . .	159
b. Lagally's Theorem and Computation for a Sphere as a Test Case . . . . .	160
c. Application of Method to Fuselage . . . . .	163
IX HOVER AERODYNAMICS . . . . .	166
1. POWER EFFECTS IN HOVER . . . . .	167
2. PERTURBATION METHOD . . . . .	174
APPENDIX I — EFFECT OF ROTARY VARIABLES . . . . .	185
APPENDIX II — DETERMINATION OF TRAILING VORTEX INTEGRAL . . . .	192
APPENDIX III — AUXILIARY CURVES USED IN EMPIRICAL METHODS FOR THE WING . . . . .	195
REFERENCES . . . . .	207

## LIST OF ILLUSTRATIONS

Figure		Page
1	Jet Exhausting Normally into the Freestream . . . . .	8
2	Entrainment Characteristics for the Jet of Reference 3 . . . . .	15
3	Sink and Doublet Distributions. . . . .	17
4	Jet-Induced Downwash Variation . . . . .	17
5	General Coordinate System . . . . .	24
6	Jet-Centered Coordinate System . . . . .	24
7	Centerlines of Jets Exhausting Normally into the Freestream. . . .	27
8	Centerlines of Jets Exhausting into the Freestream at Various Angles . . . . .	28
9	Centerlines of a Jet Exhausting into the Freestream at Various Angles . . . . .	29
10	Centerlines of Jets Exhausting into the Freestream at an Angle $\delta_j = 60^\circ$ . . . . .	30
11	Single Jet Configuration . . . . .	32
12	Induced Pressure Variation Due to a Single Jet of Velocity Ratio $U_\infty/U_{jo} = .125$ . . . . .	32
13	Induced Pressure Variation Due to a Single Jet of Velocity Ratio $U_\infty/U_{jo} = .250$ . . . . .	34
14	Pressure Distribution Around a Single Jet Exhausting at an Angle $\delta_j = 120^\circ$ into the Freestream ( $U_\infty/U_{jo} = .125$ ) . . . . .	37
15	Pressure Distribution Around a Single Jet Exhausting at an Angle $\delta_j = 90^\circ$ into the Freestream ( $U_\infty/U_{jo} = .125$ ) . . . . .	38
16	Pressure Distribution Around a Single Jet Exhausting at an Angle $\delta_j = 60^\circ$ into the Freestream ( $U_\infty/U_{jo} = .125$ ) . . . . .	39
17	Pressure Distribution Around a Single Jet Exhausting at an Angle $\delta_j = 90^\circ$ into the Freestream ( $U_\infty/U_{jo} = .125$ ) . . . . .	40
18	Pressure Distribution Around a Single Jet Exhausting at an Angle $\delta_j = 90^\circ$ into the Freestream ( $U_\infty/U_{jo} = .089$ ) . . . . .	41
19	Jet Exit Configurations . . . . .	43
20	Schematic of Jet Influence . . . . .	43
21	Centerline for a Single Jet ( $U_\infty/U_{jo} = .125$ ) . . . . .	46
22	Centerlines for Two Jets at a Spacing of 2.5 Diameters ( $U_\infty/U_{jo} = .125$ ) . . . . .	46

# LIST OF ILLUSTRATIONS (Cont'd)

Figure		Page
23	Centerlines for Two Jets at a Spacing of 5 Diameters ( $U_{\infty}/U_{jo} = .125$ ) . . . . .	47
24	Centerlines for Two Jets at a Spacing of 7.5 Diameters ( $U_{\infty}/U_{jo} = .125$ ) . . . . .	47
25	Effective Velocity Ratios of Downstream Jets in Two-Jet Configurations ( $U_{\infty}/U_{jo} = .125$ ) . . . . .	50
26	Jet Dynamic Pressure Decay for a Single Jet . . . . .	50
27	Jet Dynamic Pressure Decay for Two Jets at a Spacing of 2.5 Diameters ( $U_{\infty}/U_{jo} = .125$ ) . . . . .	51
28	Jet Dynamic Pressure Decay for Two Jets at a Spacing of 5 Diameters ( $U_{\infty}/U_{jo} = .125$ ) . . . . .	52
29	Jet Dynamic Pressure Decay for Two Jets at a Spacing of 7.5 Diameters ( $U_{\infty}/U_{jo} = .125$ ) . . . . .	53
30	Decay Characteristics of Leading Jets in Two-Jet Configurations ( $U_{\infty}/U_{jo} = .125$ ) . . . . .	54
31	Water Vapor Visualization for Two Jets at a Spacing of 2.5 Diameters ( $U_{\infty}/U_{jo} = .125$ ) . . . . .	55
32	Pressure Distribution Around Two Jets at a Spacing of 2.5 Diameters ( $U_{\infty}/U_{jo} = .125$ ) . . . . .	59
33	Pressure Distribution Around Two Jets at a Spacing of 5 Diameters ( $U_{\infty}/U_{jo} = .125$ ) . . . . .	60
34	Pressure Distribution Around Two Jets at a Spacing of 7.5 Diameters ( $U_{\infty}/U_{jo} = .125$ ) . . . . .	61
35	Two-Jet Configuration with Sideslip . . . . .	62
36	Spanwise Two-Jet Configuration . . . . .	62
37	Induced Pressure Variation for a Two-Jet Configuration at Zero Sideslip (Spacing = $5 d_o$ , $U_{\infty}/U_{jo} = .125$ ) . . . . .	63
38	Induced Pressure Variation for a Two-Jet Configuration at Sideslip $\beta = 20^\circ$ (Spacing = $5 d_o$ , $U_{\infty}/U_{jo} = .125$ ) . . . . .	64
39	Induced Pressure Variation for a Two-Jet Configuration at Sideslip $\beta = -20^\circ$ (Spacing = $5 d_o$ , $U_{\infty}/U_{jo} = .125$ ) . . . . .	65
40	Induced Pressure Variation for a Two-Jet Configuration at Zero Sideslip (Spacing = $2.5 d_o$ , $U_{\infty}/U_{jo} = .125$ ) . . . . .	66
41	Induced Pressure Variation for a Two-Jet Configuration at Sideslip $\beta = 20^\circ$ (Spacing = $2.5 d_o$ , $U_{\infty}/U_{jo} = .125$ ) . . . . .	67

## LIST OF ILLUSTRATIONS (Cont'd)

Figure		Page
42	Induced Pressure Variation for a Spanwise Two-Jet Configuration (Spacing = $7.5 d_o$ , $U_\infty/U_{jo} = .125$ ) . . . . .	69
43	Pressure Distribution Around Two Jets of Different Thrust Levels (Upstream Jet, $U_\infty/U_{jo} = .215$ ) (Downstream Jet, $U_\infty/U_{jo} = .150$ ) . . . . .	73
44	Three-Jet Configuration . . . . .	74
45	Centerlines for Three-Jet Configurations ( $U_\infty/U_{jo} = .125$ ) . . . . .	74
46	Induced Pressure Variation for Three-Jet Configuration ( $U_\infty/U_{jo} = .125$ ) . . . . .	75
47	Terminology for Cross Section and Circle Planes . . . . .	79
48	Mapping of Joukowski Airfoil . . . . .	85
49	Mapping of 65-010 Mod. Airfoil . . . . .	86
50	Mapping of T-38 Section at Sta. 291.5 . . . . .	87
51	Representative Configurations for Wing and Fuselage . . . . .	95
52	Parallelepiped Network . . . . .	100
53	Coordinate System for Inlet Model . . . . .	106
54	Exact and Approximate Calculation of Mapping Circle Radius . . . . .	121
55	Exact and Approximate Calculation of Mapping Coefficient $a_1$ . . . . .	121
56	Exact and Approximate Calculation of Mapping Coefficient $a_0$ . . . . .	122
57	Comparison of Coefficients Using Exact and Approximate Mapping Coefficients . . . . .	123
58	Comparison of Computed and Test Normal Force and Moment Coefficients for F-5B Body . . . . .	126
59	Comparison of Test and Theoretical Coefficients for T-38 Fuselage . . . . .	129
60	Section Moment Coefficient Test and Calculation Data . . . . .	133
61	Section Normal Force Coefficient for NACA 0012 Airfoil . . . . .	135
62	Circulation Strengths of Two Lifting Lines for NACA 0012 Airfoil . . . . .	136
63	Geometry for Bound Vorticity . . . . .	137
64	Geometry of Trailing Vorticity . . . . .	139
65	Weighting of Circulation Between the Lifting Lines . . . . .	143

# LIST OF ILLUSTRATIONS (Cont'd)

Figure		Page
66	Spanwise Loading for Aspect Ratio 5 Rectangular Wing . . . . .	144
67	Induced Forces on Flat Plate and Delta Wing . . . . .	146
68	Induced Forces on Flat Plate and Rectangular Wing, $x_j/c = 0.5$ , Equivalent Area Circle . . . . .	147
69	Induced Moments about Axis of Jet . . . . .	148
70	Equivalent Circular Areas for Rectangular and Delta Wings . . . . .	149
71	Schematic for $\Delta\theta$ Method . . . . .	150
72	Segmentation of Sample Wing . . . . .	151
73	Distribution of Surface Force Around the Jet . . . . .	152
74	Induced Forces on a Delta Wing, $\Delta\theta$ Method . . . . .	153
75	Curves for Effective Angle of Attack and Camber Calculation ( $U_{jo}/U_\infty = 5$ ) . . . . .	155
76	Curves for Effective Angle of Attack and Camber Calculation ( $U_{jo}/U_\infty = 10$ ) . . . . .	156
77	Curves for Effective Angle of Attack and Camber Calculation ( $U_{jo}/U_\infty = 15$ ) . . . . .	157
78	Jet Exhaust Effects on Tailplane . . . . .	158
79	Prolate Spheroid and Elliptic Coordinates . . . . .	164
80	Power-Effect Lift for Lift Jet with Fuselage Calculated by Lagally's Theorem and its Comparison with Transformation Method and Test Data . . . . .	165
81	Lift Loss for Circular Flat Plates, Rectangular Plenum (Reference 33) . . . . .	170
82	Lift Loss for Circular Flat Plates, Circular Plenum (Reference 33) . . . . .	171
83	Out of Ground Effect Lift Losses, Circular Plenum (Reference 33) . . . . .	173
84	Preliminary Hydrodynamic Testbed . . . . .	175
85	Typical Time Histories . . . . .	176
86	Viscous Drag Coefficient for Trapezoid Plate . . . . .	177
87	Transformed Expression for Drag Force Due to Impulsive Velocity Squared . . . . .	180



## LIST OF ILLUSTRATIONS (Cont'd)

Figure		Page
88	Transformed Data for Drag Due to Impulsive Velocity Squared . . . . .	181
89	Transformed Data Over Larger Range of s . . . . .	183
90	Drag Due to Impulsive Change in Velocity . . . . .	184

## APPENDIX ILLUSTRATIONS

I-1	Definition of Rotary Variables . . . . .	186
I-2	Computational Scheme for Rotary Variables . . . . .	186
I-3	Effect of Rotary Variable on a Jet Centerline . . . . .	189
III-1	Surface Force Distribution Around a Jet ( $U_{jo}/U_x = 5$ ) . . . . .	195
III-2	Surface Force Distribution Around a Jet ( $U_{jo}/U_x = 10$ ) . . . . .	197
III-3	Surface Force Distribution Around a Jet ( $U_{jo}/U_x = 15$ ) . . . . .	199
III-4	Surface Force Distribution Around a Jet ( $U_{jo}/U_x = 5$ ) . . . . .	201
III-5	Surface Force Distribution Around a Jet ( $U_{jo}/U_x = 10$ ) . . . . .	203
III-6	Surface Force Distribution Around a Jet ( $U_{jo}/U_x = 15$ ) . . . . .	205

# LIST OF SYMBOLS

## SECTION II

$C$	circumference of jet cross section
$C_D$	crossflow drag coefficient of jet cross section
$C_p$	pressure coefficient, $(p - p_\infty)/q_\infty$
$d$	length of major axis in elliptical representation of jet cross section
$d_o$	jet exit diameter
$\mathcal{D}$	ratio of minor to major axis
$E$	entrainment of crossflow fluid per unit length of jet
$E_1, E_2, E_3$	entrainment parameters
$F_p$	pressure force on jet boundary
$H$	development region for jet exhaust angle of $90^\circ$ , $H = .3 U_{jo}/U_\infty$
$H'$	development region for jet exhaust angles other than $90^\circ$
$p$	static pressure
$q_\infty$	crossflow dynamic pressure, $q_\infty = 1/2 \rho U_\infty^2$
$q_e$	effective crossflow dynamic pressure for downstream jet when jets are aligned in the crossflow direction
$q_j, q_{jo}$	jet dynamic pressure, jet dynamic pressure at exit
$q_\beta$	effective crossflow dynamic pressure for downstream jet when jets are not aligned in the crossflow direction
$R$	radius of curvature of jet centerline
$s$	distance along jet centerline
$s, s_1, s_2$	spacing between jets
$U_\infty$	crossflow speed
$U_j, U_{jo}$	jet speed, jet speed at exit
$U_\infty/U_{jo}$	velocity ratio, $U_\infty/U_{jo} = [q_\infty/q_{jo}]^{1/2}$

$X, Y, Z$	Cartesian coordinate system defined in Figure 5
$\beta$	sideslip angle
$\delta_j$	jet exhaust angle defined in Figure 6
$\rho$	density
$\theta$	angle between local jet velocity vector and the normal to cross-flow vector
$\theta_0$	value of $\theta$ at jet exit
$\phi, \psi$	jet exhaust angles defined in Figure 5

### SECTION III

$a_n$	real part of coefficient in expansion for $g(Z)$
$A_n$	complex coefficient of mapping function with corners contained explicitly
$b_n$	imaginary part of coefficient in expansion for $g(Z)$
$d_n$	complex coefficient of mapping function written without corners
$E$	least square error
$f(Z)$	arbitrary function of $Z$
$g(Z)$	Laurent's series in $Z$ to be evaluated
$k_m$	exponent of singularity at $m$ 'th corner
$M$	number of corners
$r_c$	radius of mapping circle
$R_b$	radial distance to point on cross section from origin of $Z$ -plane
$s$	distance around cross section
$u_b$	real component of velocity at point in cross section plane
$u_c$	real component of velocity at point in circle plane
$v_b$	imaginary component of velocity at point in cross section plane
$v_c$	imaginary component of velocity at point in circle plane
$V_b$	absolute magnitude of velocity at point in cross section plane
$W$	complex potential $\phi + i\psi$
$Z$	complex coordinate of point in cross section plane
$Z_m$	complex coordinate of $m$ 'th corner point in cross section plane

$\alpha$	local flow direction in cross section plane
$\alpha_-$	slope of cross section just before corner
$\alpha_+$	slope of cross section just after corner
$\Delta\alpha_m$	$(\alpha_+ - \alpha_-)_m$
$\beta_m$	argument of singularity at m'th corner
$\epsilon$	local error in mathematical representation of cross section slope
$\zeta$	complex coordinate of point in circle plane
$\zeta_m$	complex coordinate of m'th corner expressed in circle plane
$\theta$	angular distance around mapping circle
$\mu_m$	amplitude of singularity at m'th corner
$\phi$	potential function
$\psi$	stream function
$\omega$	angular distance around cross section

#### SECTION IV

$a_0, a_1 \dots a_n$	complex coefficients in complex potential
$a'_0, a'_1 \dots a'_n$	real parts of $a_0, a_1 \dots a_n$
$a''_0, a''_1 \dots a''_n$	imaginary parts of $a_0, a_1 \dots a_n$
$A_n, B_n$	Fourier coefficients
$b_0, b_1 \dots b_n$	complex coefficients in mapping function
$\vec{q}$	total velocity vector $\vec{q} = u \vec{i} + v \vec{j} + w \vec{k}$
$\vec{q}_j$	jet induced velocity vector $\vec{q}_j = u_j \vec{i} + v_j \vec{j} + w_j \vec{k}$
$\vec{q}_s$	velocity vector induced by network residual sources and sinks
$\vec{q}_1$	perturbation velocity vector due to body presence in freestream
$\vec{q}_2$	perturbation velocity vector due to body presence in jet induced velocity field
$Q_1, -m_1$	net flux through a parallelepiped

$r$	radial distance in mapped plane
$r_b$	radius of mapped circle
$U_j$	jet exit velocity
$U_\infty$	freestream velocity
$w'$	downwash component
$W$	complex potential
$x, y, z$	cartesian coordinates in physical plane
$Z$	complex variable in y-z plane
$\alpha$	angle of attack
$\Gamma$	circulation
$\Delta C_p$	pressure coefficient of power on minus pressure coefficient of power off
$\zeta$	complex variable in mapped plane
$\theta$	angle in mapped plane
$\theta'$	inclination angle of a tangent line in Z-plane to x-axis
$\phi$	perturbation velocity potential
$\psi$	perturbation stream function

## SECTION V

$A_f$	fan flow area
$C_D^{SCB}$	drag area of fan centerbody
$C_p$	pressure coefficient, $(P - P_\infty)/1/2 \rho U_\infty^2$
$C_t$	fan pressure rise coefficient, $\Delta P/1/2 \rho U_t^2$
$D$	drag force
$D_L$	inlet lip drag
$K$	ratio of velocity at fan entrance to freestream velocity
$L$	lift force
$L_L$	inlet lip lift force
$L_s$	surface lift force
$m$	inlet sink strength
$M$	moment
$M_{/L}$	inlet lip rolling moment

$M_{IS}$	surface rolling moment
$M_L$	inlet lip moment, normal to freestream velocity and in plane of surface containing inlet
$M_{mL}$	inlet lip pitching moment
$M_{mS}$	surface pitching moment
$P$	pressure
$P_\infty$	ambient static pressure
$P_{R1}$	pressure at control point on hemispherical control surface of radius $R_1$
$r$	radius
$R_1$	inlet lip outer radius; radius of hemispherical control surface
$T_f$	thrust carried on fan blades, net fan thrust
$u_n$	velocity normal to control surface, positive inward
$u_s$	centripetal velocity due to sink
$u_t$	fan tip speed
$u_x$	freestream velocity component at control surface
$u_z$	velocity at control surface, normal to surface containing inlet, positive downward
$\bar{U}$	velocity
$U_\infty$	freestream velocity
$\beta$	angle of sideslip
$\Delta z$	distance of lower control surface below surface containing inlet
$\phi$	angle between radius from inlet centroid to control point on the hemispherical control surface and the plane containing the inlet
$\eta$	inlet dynamic head recovery factor
$\rho$	density
$\theta$	angle between radius from inlet centroid to control point on hemispherical control surface and freestream velocity as measured in the infinite plane containing the inlet

## SECTION VI

$a_e$	ellipse semi-axis in direction of cross flow velocity
-------	---

$a_n$	n'th coefficient of mapping function
$A_n$	coefficient of complex potential written in body plane coordinate, $Z$
$A_{in}$	coefficient of complex potential written in circle plane coordinate, $\zeta$
$b_e$	ellipse semi-axis normal to cross flow velocity
$B$	coefficient of log term in complex potential written in body plane coordinate $Z$
$c_y$	characteristic body dimension upon which $C_{D_y}$ is based
$c_z$	characteristic body dimension upon which $C_{D_z}$ is based
$C_{D_o}$	drag coefficient of elliptical cylinder
$C_{D_y}$	cross flow drag coefficient of body cross section in y direction
$C_{D_z}$	cross flow drag coefficient of body cross section in z direction
$C_f$	laminar skin friction drag coefficient
$D$	coefficient of term in complex potential independent of $Z$
$F$	complex potential of body cross section
$H$	coefficient of log term in complex potential as obtained from boundary function
$l$	body length
$L$	normal force in $z$ direction
$L'$	rolling moment about x-axis
$M$	pitching moment about y-axis
$N$	yawing moment about z-axis
$p$	rolling velocity
$q$	pitching velocity
$r$	yawing velocity
$r_c$	radius of the mapping circle
$R$	complex velocity in the cross flow plane
$S$	body cross sectional area
$t$	time
$T_N$	complex potential induced by changing body cross section
$U_0$	component of freestream velocity in x direction
$U_\infty$	freestream velocity

$U_P$	potential part of cross flow velocity at separation line
$U_f$	vortex induced cross flow velocity at separation line
$V$	magnitude of local cross flow velocity at point on the body
$V_0$	component of freestream velocity in y direction
$W_0$	component of freestream velocity in z direction
$W_1$	complex velocity at vortex center
$x$	axial distance along body
$x_{cg}$	body center of gravity location
$y$	real axis in cross flow plane
$Y$	normal force in y direction
$z$	imaginary axis in cross flow plane
$Z$	complex coordinate in body cross flow plane $Z = y + iz$
$Z_B$	complex coordinate of point on body cross section
$Z_C$	centroid of body cross section
$\alpha$	resultant angle of attack
$\Gamma$	vortex strength
$\zeta$	complex coordinate in circle plane $\zeta = re^{i\theta}$
$\zeta_c$	point on the mapping circle
$\zeta_0$	separation point on cylindrical body
$\zeta_1$	location of vortex center
$\theta$	angular distance in mapping circle plane
$\rho$	freestream density
$\phi$	roll angle
$(\bar{\phantom{x}})$	complex conjugate
$(\phantom{x})'$	derivative with respect to x
$(\dot{\phantom{x}})$	derivative with respect to time
$\Re$	real part
$\Im$	imaginary part

## SECTION VII

$a, b, c$	parameters defined in Equation (123)
$A, B, \dots, I$	parameters in Equation (124) derived in Appendix II



A, B, D, I, W, $\Gamma$	matrices in downwash Equation (126)
c	airfoil chord
$C_{m_{1/4}}$	section pitching moment about 1/4 chord
$C_N$	section normal force coefficient
$C_{N_{IND}}$	circulation normal force coefficient
$(C_N)_{\alpha = 90^\circ}$	normal force at $\alpha = 90^\circ$
$d\bar{\Gamma}$	increment of vorticity
$h_1, h_2$	positions of lifting lines relative to 3/4 chord position (see p. 131)
p	rolling velocity
$P(x, y, z)$	downwash control point
q	pitching velocity
r	yawing velocity
R	distance from vortex element to downwash control point
U	mainstream velocity
$\bar{V}_L, \bar{V}_t$	velocity vectors due to lifting line and trailing vorticity respectively
$w_L, w_t$	downwash due to lifting line and trailing vorticity respectively
$W_t$	circulation weighting function $\left[ = \Gamma_1 / (\Gamma_1 + \Gamma_2) \right]$
$\bar{x}$	chordwise position of center of pressure for viscous crossflow force
$x_{c.g.}$	X - coordinate of wing rotational center
$z_{c.g.}$	Z - coordinate of wing rotational center
x, y, z	coordinates defined in Figure 63
$x_1, y_1$	coordinates defined in Figure 64
$\alpha$	angle of attack
$\alpha_o$	effective angle of attack
$\beta_o$	effective angle of sideslip
$\Gamma$	circulation strength
$\Gamma_1, \Gamma_2$	circulation strength of two lifting lines
$\phi_i$	sweepback angle of lifting line
$\xi, \eta, \zeta$	coordinates defined in Figure 63
$\eta_o, \eta_1, \dots, \eta_n$	circulation control points

## SECTION VIII.1

$C_L$	lift coefficient
$C_p$	pressure coefficient
$d_o$	jet exit diameter
$F$	jet induced force
$r$	radial coordinate in plane of jet exit
$R$	constant value of radial coordinate in plane of jet exit
$S_j$	jet exit area
$S$	planform area
$T$	jet thrust
$U_j$	jet exit velocity
$U_\infty$	freestream velocity
$w$	downwash velocity component
$x$	chordwise coordinate
$y$	spanwise coordinate
$\delta_j$	jet deflection angle (from horizontal, degrees)
$\Delta L$	lift increment due to jet operation
$\epsilon$	downwash angle (degrees)
$\theta$	angular coordinate in plane of jet exit (degrees)

## SECTION VIII.2

$F_i$	component of force vector in i-direction
$m$	source strength
$M_i$	component of moment vector in i-direction
$n_i$	component of a unit vector in i-direction
$p$	pressure
$q_{ia}$	velocity component at $\vec{r}_a$ induced by all causes except the singularity there
$\vec{r}_a$	position vector of point a
$S, dS$	surface and surface element of an infinitesimal sphere
$u_i, u_j$	velocity components in i- and j-directions

$U_{\infty}$	freestream velocity
$x_i, x_j$	cartesian coordinates in i- and j-directions
$\alpha$	angle of attack
$\vec{\mu}, \mu_i$	doublet vector and i-component of doublet vector $\vec{\mu}$
$\nu, \xi, \omega$	elliptic coordinates
$\rho$	density
$\phi$	velocity potential
Subscripts	
a	conditions at point a
o	conditions at body surface

## SECTION IX

$A_j$	jet exit area
D	drag
$D_v$	drag due to unit impulse of v
$D_v^2$	drag due to unit impulse of $v^2$
$\bar{D}$	angular mean diameter of plate
d	diameter of jet exit
G	load induced on plate
h	height of jet exit over ground plane
$\mathcal{L}\{\}$	Laplace transform
p	ambient static pressure
$P_t, p$	plenum total pressure
$q_x$	maximum jet impact pressure at x
S	planform area of plate, includes jet
s	variable of Laplace transform
T	jet thrust
t	time
V	velocity
X	distance normal to jet exit
$X_i$	point of maximum rate of impact pressure decay
$\tau$	dummy variable

**Subscript**

$\infty$

out of ground effect or steady state

f

value at end of test

## SECTION I

### INTRODUCTION

The problem of specifying the in-flight behavior of an aircraft can be considered as one of determining the effect the dynamic motion of the craft has on the fluid through which it is moving and, hence, on what forces and moments are impressed on the vehicle due to this motion. The forces and moments thus impressed on the vehicle together with thrust and inertial response completely determine the aircraft behavior. The determination of the forces and moments experienced by an aircraft is, therefore, of importance for determining aircraft performance and stability and control requirements. Methods for predicting the aerodynamic behavior of conventional aircraft have been established and are documented in a form suitable for use by the preliminary designer in Reference 1. V/STOL aircraft of the lift jet, lift fan, and vectored thrust type pose aerodynamic problems which are significantly different from the aerodynamics of conventional aircraft. New problem areas arise mainly through the interference of the lifting jet or fan efflux on the relative mainstream flow due to aircraft forward speed or natural wind. Also, due to its particular form of propulsion, a V/STOL vehicle is likely to fly at large angle of attack and/or sideslip during some part of its flight path so that nonlinear aerodynamics become an important factor in determining the aerodynamic forces and moments on these vehicles.

To date no satisfactory methods for estimating the power induced aerodynamics of the lift jet, lift fan or vectored thrust V/STOL aircraft have been established. The subject of nonlinear aerodynamics has received little attention and no generally accepted prediction methods exist at this time. This study has been concerned with obtaining the air induced forces and moments on V/STOL aircraft of the lift jet, lift fan and vectored thrust type in a convenient form to allow motion studies to be made. This requires that the magnitude of the force and moment components be determined as functions of a consistent set of flight variables.

These force and moment components are treated as being functions of the flight variables, a consistent set of which are  $\alpha$ ,  $\beta$ ,  $U$ ,  $\dot{\alpha}$ ,  $\dot{\beta}$ ,  $p$ ,  $q$ ,  $r$  and any higher order of terms such as  $\eta$  which may be considered pertinent. The basic problem of any aerodynamic stability study thus reduces to obtaining accurate functional

relationships between the forces and moments and the flight condition, for example,

$$L = L\{\alpha, \beta, U, \dot{\alpha}, \dot{\beta}, p, q, r, \dots\}$$

These functional relationships then permit all the necessary aircraft motions to be obtained assuming the thrust and inertial characteristics of the vehicle are known.

A complete functional relationship such as the above equation is seldom obtainable in practice. However, the effect of the most significant parameters on given components or parts of the aircraft is usually obtainable. These effects are added together and assumed to hold for the complete airplane.

## 1. PURPOSE

The purpose of this investigation was to develop analytical engineering methods for predicting the static and dynamic stability and control derivatives and force and moment coefficients of lift jet, lift fan, and vectored thrust V/STOL aircraft in the hover and transition flight regimes. These methods were to take into account the strong power effects, large variations in angle of attack and sideslip, and changes in aircraft geometry that are associated with high disk loaded V/STOL aircraft operating in the aforementioned flight regimes. Where appropriate, use was to be made of high speed computers to obtain solutions having reasonable time periods for implementation. The aircraft configurations studied were to have a conventional wing, fuselage and empennage. The methods developed were to be suitable for use by design personnel during the preliminary design and evaluation of V/STOL aircraft of the type previously mentioned.

## 2. TECHNICAL APPROACH

This investigation has been concerned with the development of theories for predicting the forces and moments on lift jet, lift fan and vectored thrust V/STOL aircraft. In general, due to the complexity of the interaction between the propulsive system and the airframe, it has been found necessary to use computer programs to enable the forces and moments to be calculated. Some of the methods developed are simple enough to be reduced into a handbook procedure. Examples of such methods are those based on slender body theory and the viscous cross flow hypothesis.

This investigation has followed the conventional procedure in a manner most suitable for the treatment of V/STOL aircraft.

A basic assumption, for the methods developed in this investigation, is that the power induced effects can be treated separately from the unpowered aerodynamic effects and the two sets of solutions added together to produce the total aerodynamic effect.

A second assumption is that the aerodynamics can be treated component by component and the results added together for the total aircraft. This assumption holds for both the power-induced and unpowered effects. Whenever possible, mutual interference between components has been taken into account to obtain a more accurate solution. This approach is essentially the procedure used in Reference 1 and is considered to be most suitable for use as a design tool.

The technical approach used in developing the prediction methods was based on theoretical and semi-empirical analyses. It was thought that correlation of wind tunnel test data, in terms of geometric and flow variables, would be an impossible task without theoretical and semi-empirical methods to indicate correlation variables.

An extensive literature search was conducted to identify available test data and areas for which further data was required to develop and validate the prediction methods. As a result of this literature search, two wind tunnel test programs were conducted.

In the first of these test programs, a flat plate model containing up to three nozzles was tested to assist in the development and validation of the jet flow field theory. The results of these tests have been documented in Reference 3. In the second test program, a complete configuration model was tested in the NASA Langley Research Center V/STOL tunnel. This model consisted of two wing-mounted vectored thrust engines and a lift-jet engine embedded in the fuselage. The vectored thrust nozzles were designed for exit positions at two longitudinal locations. For the aft location, two nozzle exit diameters were available. Data from this test has been used to verify the prediction methods. A data report for this test will be published by NASA at a later date.

### 3. REPORT ORGANIZATION

The report consists of four volumes, entitled:

Volume I - Theoretical Development of Prediction Methods

Volume II - Application of Prediction Methods

**Volume III - Manual for Computer Programs**  
**Volume IV - Literature Survey**

In Volume I, the aerodynamic prediction methods are developed in a form suitable for application to each aircraft component. The applicable theoretical analyses or semi-empirical bases are presented. Empirical coefficients are determined, where necessary, and then extensive comparisons of calculations with test data are made.

Volume II gives detailed examples of the application of the prediction methods to the determination of the aerodynamic forces, moments, and in some cases, surface pressure distributions, on the aircraft wing, fuselage and empennage. In each case, a sample problem is given to illustrate the application of the methods and method limitations are also discussed. Also discussed in Volume II is the wind tunnel test program conducted in the NASA Langley V/STOL tunnel and the use of the resulting data to validate the applicable prediction methods.

Volume III contains a detailed description of the computer programs developed in this investigation.

Volume IV documents the results of the literature survey conducted to identify existing test data and theoretical methods relating to this investigation.



## SECTION II

### JET FLOW FIELD THEORY

A fundamental problem in the development of methods for predicting aerodynamic characteristics of lift-jet, vectored thrust and lift-fan V/STOL aircraft is that of formulating a mathematical model to estimate the effects of the propulsion system efflux interaction with a crossflow. During the transition flight phase, this efflux is directed at large angles to the freestream and has a significant influence on the aircraft aerodynamic performance as well as on its stability and control characteristics.

A number of analytical formulations of the problem of a single jet exhausting into a crossflow exist, and details of the different approaches may be found in Reference 2. An approach to the problem of a single, normally exhausting jet, which appeared to offer possibilities of treating more complex configurations, is given in Reference 4. In this reference, an entrainment model was developed from dimensional analysis and physical considerations. The force on the jet boundary as a result of the pressure differential around the jet was accounted for by a crossflow drag. The geometry of the jet cross section was represented by an ellipse. Assuming constant and equal density for the jet and the crossflow, the continuity and momentum equations were solved for the jet path. The jet-induced velocity field was then determined by replacing the jet by a distribution of sinks and doublets.

The analytical model described above has been further extended to treat jets exhausting into arbitrarily directed freestreams as well as multiple-jet configurations. Multiple-jet configurations are treated as combinations of discrete jets, with leading jets assumed to develop independently and downstream jets assumed to exhaust into a freestream of reduced dynamic pressure.

To generate data which would substantiate these assumptions and also provide information for further refinements to the analytical model, a wind tunnel investigation of jets exhausting into a crossflow was conducted. The test configuration consisted of a four-foot diameter circular plate, containing up to three circular jets, which was elevated 12 inches from the tunnel floor and aligned with the air flow. The plate contained pressure taps to determine the surface static pressures. Jet centerlines and decay characteristics were obtained with a total head rake. Data from this investigation have been presented in Reference 3.

Data from the wind tunnel investigation have been analyzed and used to verify some of the assumptions made in the development of the analytical approach. The mathematical model has been refined using data from the wind tunnel investigation.

The single jet is considered in Sections II. 1 and II. 2. The details of the analytical model are presented. Refinements of the empirical parameters, based on analysis of the experimental data, are discussed. Extensive comparisons between theory and experimental data are presented.

Two-jet configurations are treated in Sections II. 3 and II. 4. An expression for the effective dynamic pressure which the downstream jet "sees" as a result of the blockage of the crossflow by the upstream jet is derived. The test data are used to verify that the upstream jet develops independently of the downstream jet. Calculations of jet centerlines and induced surface static pressures are compared with test data for a number of two-jet configurations.

Applications of the analytical model to more complex configurations are presented in Section II.5. Computations of the induced pressure distribution around a two-jet configuration, with the jets at different thrust levels, are compared with test data. The extension of the computational procedure to the treatment of more complex jet arrangements is carried out for a three-jet configuration. An empirical relationship for the reduction in crossflow dynamic pressure for the third jet, as a result of blockage by the two upstream jets, is given. Comparison between theory and data for the variation of surface static pressure induced by a three-jet configuration is shown.

## 1. SINGLE JET ANALYTICAL MODEL

### a. Normally Exhausting Jet

Consider a circular jet exhausting at a right angle into a uniform mainstream as shown in Figure 1. When a jet exhausts at an angle into a mainstream it is deflected partly by viscous entrainment and partly by the force on the jet boundary resulting from the pressure differential around the jet. It is assumed that the flow is incompressible and viscous effects other than entrainment are neglected. Dimensional considerations then suggest that the entrainment of mainstream fluid per unit length of jet may be written as

$$E = \rho E_1 U_\infty d \cos \theta + \frac{\rho E_2 (U_j - U_\infty \sin \theta) C}{1 + E_3 U_\infty \cos \theta / U_j} \quad (1)$$

A fluid particle approaching the jet near the plane of symmetry will be more easily entrained by the jet than a particle that is moving away from the jet. The susceptibility of the approaching particle to jet entrainment is accounted for by the term  $\rho E_1 U_\infty d \cos \theta$  in Equation (1). Particles moving away from the jet or to its side, with momentum not directed toward the jet, are less tolerant to jet entrainment. The term

$$\frac{\rho E_2 (U_j - U_\infty \sin \theta) C}{1 + E_3 \cos \theta / U_j}$$

takes this into consideration while satisfying the Ricou-Spalding solution for the freejet case when  $U_\infty = 0$ . The net force acting on the jet boundary, as a result of the pressure differential around the jet, is accounted for by a crossflow drag. The force on a jet element of unit length is

$$F_p = C_D \cdot \frac{1}{2} \rho U_\infty^2 \cos^2 \theta d \quad (2)$$

where  $C_D$  is the cross flow drag coefficient of the jet.

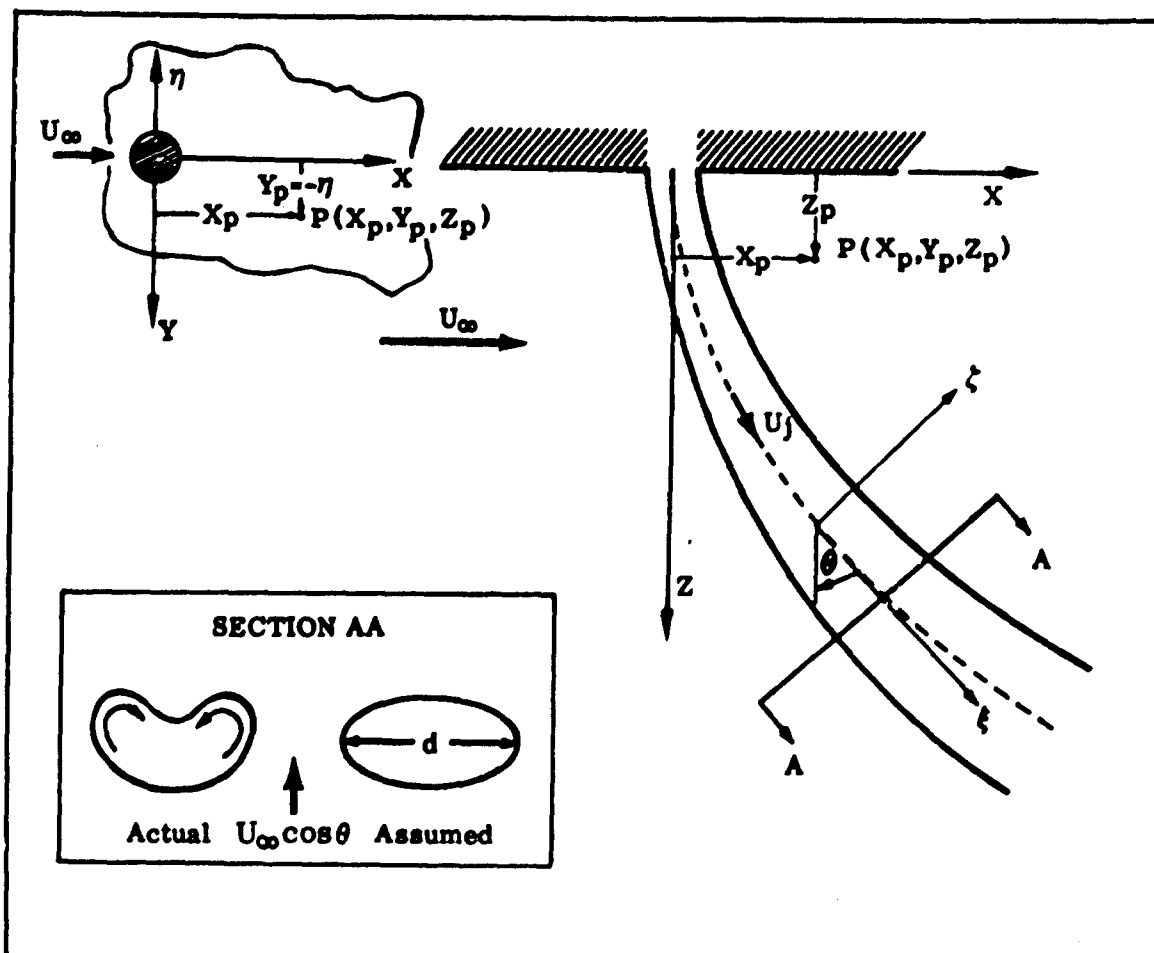


FIGURE 1. JET EXHAUSTING NORMALLY INTO THE FREESTREAM

### (1) Equations of Motion

The entrainment of mainstream fluid into the jet and the pressure forces on the boundary of the jet govern the equations of motion which can now be written, using the coordinate system defined in Figure 1.

The continuity equation may be written as

$$\rho \, d/ds (A_j U_j) = E \quad (3)$$

The only tangential forces acting on the jet are the viscous forces resulting in entrainment, so that the momentum equation for the jet flow in the tangential direction is

$$\rho \, d/ds (A_j U_j^2) = E U_\infty \sin \theta \quad (4)$$

The deflection of the jet is due to the centripetal action of the pressure force on the jet boundary and the entrainment of mainstream fluid with momentum in that direction. The force equation governing the curvature of the jet may now be written as

$$\begin{aligned} \rho A_j U_j^2 / R &= E U_\infty \cos \theta + C_D \cdot \frac{1}{2} \rho U_\infty^2 \cos^2 \theta d \\ &= \rho A_j U_j^2 X' / [1 + (X')^2]^{3/2} \end{aligned} \quad (5)$$

where  $R$  is the radius of curvature of the jet centerline and the primes denote differentiation with respect to  $Z$ . Replacing  $d/ds$  by  $\cos \theta (d/dz)$  in Equations (3) and (4) reduces the problem to one of finding  $d$ ,  $U_j$  and  $X$  as functions of  $Z$ , the entrainment parameters  $E_1$ ,  $E_2$ ,  $E_3$  and the cross flow drag coefficient  $C_D$ . However, a functional relationship between the cross sectional area  $A_j$ , the circumference  $C$  of the jet and the jet growth must be established.

Experimental observations show that there is a region in which the jet deforms from its initial circular cross section into a kidney-shaped one (Reference 8). Once this shape is attained, the jet cross section remains relatively similar (Reference 7). Since it did not appear possible to treat the exact jet shape, a simplified jet shape, an ellipse, was chosen. Correlation of data for a normally exhausting jet indicates that the extent of this region, in which the cross-sectional deformation occurs, is a function of the jet exit to mainstream velocity ratio  $U_{j0}/U_\infty$ . The extent of this region may

be expressed by  $0 \leq Z/d_0 \leq .3 U_{j0}/U_\infty$ . When  $Z/d_0 \geq .3 U_{j0}/U_\infty$ , observations show that the best fit of the jet cross section with an ellipse is one with a ratio of minor to major axis of  $1/4$ . Experimental data further indicate that, in the development region, the ratio of minor to major axis decreases linearly with distance from the jet orifice (Reference 5). Therefore, the geometry of the jet may be treated in two regions:

- A region in which the jet deforms to an elliptical cross section and the ratio of minor to major axis decreases linearly with  $Z$  from 1 at  $Z/d_0 = 0$  to  $1/4$  at  $Z/d_0 = H = .3 U_{j0}/U_\infty$

$\mathcal{D}$  = ratio of minor to major axis

$$= A(Z/d_0) + B$$

Substituting boundary conditions above, yields

$$\begin{aligned}\mathcal{D} &= 1 - \frac{.75}{H} (Z/d_0) \\ &= 1 - [5/2 (Z/d_0)(U_\infty/U_{j0})]\end{aligned}$$

then

$$\left. \begin{aligned}C &= \pi d \left[ \frac{1 + \left[1 - \frac{.75}{H} (Z/d_0)\right]^2}{2} \right]^{1/2} \\ &= \pi d \left[ \frac{1 + \left[1 - 5/2 (Z/d_0)(U_\infty/U_{j0})\right]^2}{2} \right]^{1/2} \\ A_j &= \pi \left[ 1 - \frac{.75}{H} (Z/d_0) \right] \frac{d^2}{4} \\ &= \pi \left[ 1 - 5/2 (Z/d_0)(U_\infty/U_{j0}) \right] \frac{d^2}{4}\end{aligned} \right\} 0 \leq Z/d_0 \leq H \quad (6)$$

From the preceding expressions it can be seen that if  $U_{j0} \neq 0$ , as  $U_\infty \rightarrow 0$ , the development region becomes  $0 \leq Z/d_0 \leq \infty$  and the jet retains its circular cross section, which is to be expected since the jet is now exhausting into quiescent surroundings.

- A region in which the jet retains a similar cross section

$$\left. \begin{aligned}\mathcal{D} &= 1/4 \\ C &= 2.24 d \\ A_j &= \pi d^2/16\end{aligned} \right\} Z/d_0 > H \quad (7)$$

(2) Integration of the Equations of Motion

The left hand side of Equation (3) may be rewritten as

$$\rho \, d/ds (A_j U_j) = \rho \, d/ds \left( \frac{A_j U_j^2}{U_j} \right) \quad (8)$$

now

$$\rho \, d/ds \left( \frac{A_j U_j^2}{U_j} \right) = \frac{\rho}{U_j} \, d/ds (A_j U_j^2) + \rho (A_j U_j^2) \, d/ds \left( \frac{1}{U_j} \right) \quad (9)$$

where from Equation (4)

$$\rho \, d/ds (A_j U_j^2) = E U_\infty \sin \theta \quad (10)$$

then

$$\rho \, d/ds \left( \frac{A_j U_j^2}{U_j} \right) = \frac{1}{U_j} E U_\infty \sin \theta - \left( \frac{\rho A_j U_j^2}{U_j^2} \right) \, d/ds (U_j) \quad (11)$$

substituting into (8)

$$\frac{1}{U_j} E U_\infty \sin \theta - \rho A_j \, d/ds (U_j) = E \quad (12)$$

Substituting for  $A_j$ ,  $C$  and letting  $d/ds = \cos \theta (d/dZ)$

$$\rho \pi \left( 1 - \frac{5}{2} \frac{Z}{d_0} \frac{U_\infty}{U_{j0}} \right) \frac{d^2}{4} \cos \theta \, d/dZ (U_j) = \quad (13)$$

$$\left\{ \rho E, U_\infty d \cos \theta + E_2 (U_j \cdot U_\infty \sin \theta) \pi d \left[ \frac{1 + \left| 1 - \frac{5}{2} \left( \frac{Z}{d_0} \right) \left( \frac{U_\infty}{U_{j0}} \right) \right|^2}{2} \right]^{1/2} \right\} \\ \times \left\{ \frac{U_\infty}{U_j} \sin \theta - 1 \right\}$$

Dividing by  $\rho d U_\infty$  and letting  $Z^* = Z/d_0$ ,  $U_j^* = U_j/U_{j0}$ , and  $m = U_{j0}/U_\infty$

$$\pi/4 \left(1 - \frac{5}{2} \frac{Z^*}{m}\right) d \cos \theta \frac{d}{dZ} (U_j) = \left\{ \frac{E_1 \cos \theta + \frac{E_2 (m U_j^* - \sin \theta) \pi}{1 + E_3 \cos \theta / U_j^* m} \left[ \frac{1 + (1 - \frac{5}{2} \frac{Z^*}{m})^2}{2} \right]^{1/2}}{m U_j^*} \right\} \left\{ \frac{\sin \theta - m U_j^*}{m U_j^*} \right\} \quad (14)$$

if  $d/dZ = (1/d_0) d/dZ^*$  and  $d^* = d/d_0$  then the left-hand side of (14) becomes

$$\pi/4 \left(1 - \frac{5}{2} \frac{Z^*}{m}\right) d^* \cos \theta \frac{d}{dZ^*} (U_j/U_\infty)$$

or

$$\pi/4 \left(1 - \frac{5}{2} \frac{Z^*}{m}\right) d^* \cos \theta m \frac{d}{dZ^*} (U_j^*)$$

Equating and solving

$$\frac{dU_j^*}{dZ^*} = \left\{ \frac{E_1 \cos \theta + \frac{E_2 (m U_j^* - \sin \theta) \pi}{1 + E_3 \cos \theta / U_j^* m} \left[ \frac{1 + (1 - \frac{5}{2} \frac{Z^*}{m})^2}{2} \right]^{1/2}}{m U_j^*} \right\} \times \left\{ \frac{\sin \theta - m U_j^*}{\pi/4 \left(1 - \frac{5}{2} \frac{Z^*}{m}\right) d^* m^2 U_j^* \cos \theta} \right\} \quad (15)$$

The equation for  $dU_j^*/dZ^*$  applicable for the developed region is obtained by substituting Equation (7) for  $A_j$  and  $C$  in (12)

$$\frac{dU_j^*}{dZ^*} = \frac{16}{\pi d^2 m^2 U_j^* \cos \theta} \times \left\{ E_1 \cos \theta + \frac{E_2 (m U_j^* - \sin \theta) 2.24}{1 + E_3 \cos \theta / U_j^* m} \right\} [\sin \theta - m U_j^*] \quad (16)$$



Substituting Equations (6) and (7) into Equation (3) and again letting  $Z^* = Z/d_0$ ,  $d^* = d/d_0$ ,  $U_j^* = U_j/U_{j0}$  and  $m = U_{j0}/U_\infty$  yields

$$\frac{dd^*}{dZ^*} = \left\{ E_1 \cos \theta + E_2 (m U_j^* - \sin \theta) \pi \left[ \frac{1 + (1 - 5/2 \frac{Z^*}{m})^2}{2} \right]^{1/2} \right\} \frac{d^*}{m \cos \theta} + \left[ \frac{5/8 \pi d^* \frac{U_j^*}{m} - \pi/4 d^{*2} (1 - 5/2 \frac{Z^*}{m}) \frac{dU_j^*}{dZ^*}}{\frac{\pi d^* U_j^*}{2} (1 - 5/2 \frac{Z^*}{m})} \right] \quad (17)$$

and

$$\frac{dd^*}{dZ^*} = \frac{E_1 \cos \theta + \frac{E_2 (m U_j^* - \sin \theta) 2.24}{1 + E_3 \cos \theta / U_j^* m} - \frac{E_4 m \cos \theta d^* \frac{dU_j^*}{dZ^*}}{(\pi/8) m \cos \theta U_j^*}}{(\pi/8) m \cos \theta U_j^*} \quad (18)$$

Substituting Equations (6) and (7) into Equation (5) leads to

$$\frac{d^2 X^*}{dZ^{*2}} = \left[ 1 + \left( \frac{dX^*}{dZ^*} \right)^2 \right]^{3/2} \times \left\{ \frac{(E_1 + 5C_D) \cos \theta + \frac{E_2 (m U_j^* - \sin \theta) \pi \left[ \frac{1 + (1 - 5/2 \frac{Z^*}{m})^2}{2} \right]}{1 + E_3 \cos \theta / U_j^* m}}{m^2 (\pi/4) d^* U_j^{*2} (1 - 5/2 \frac{Z^*}{m})} \right\} \cos \theta \quad (19)$$

and

$$\frac{d^2 X^*}{dZ^{*2}} = \left[ 1 + \left( \frac{dX^*}{dZ^*} \right)^2 \right]^{3/2} \times \frac{16 \cos \theta}{\pi m^2 d^* U_j^{*2}} \left\{ (E_1 + 5C_D) \cos \theta + \frac{E_2 (m U_j^* - \sin \theta) 2.24}{1 + E_3 \cos \theta / U_j^* m} \right\} \quad (20)$$

Equations (15), (17) and (19) are applicable to the development region of the jet and Equations (16), (18) and (20) are applicable for the developed region, that is, when  $Z^*/m > .3$ .

With the additional substitution

$$\cos \theta = \frac{1}{[1 + (dX^*/dZ^*)^2]^{1/2}}$$

$$\sin \theta = \frac{dX^*/dZ^*}{[1 + (dX^*/dZ^*)^2]^{1/2}}$$

the preceding equations are seen to constitute a set of differential equations to be solved for  $U_j^*$ ,  $d^*$ , and  $X^*$  as functions of  $Z^*$  and the parameters  $E_1$ ,  $E_2$ ,  $E_3$ , and  $C_D$ .

Initial conditions at the jet exit are

$$Z^* = 0., \quad X^* = 0., \quad U_j^* = 1., \quad \text{and} \quad dX^*/dZ^* = 0.$$

It has not been possible to integrate these equations in closed form, but they have been integrated numerically with the aid of a digital computer. The system of first order differential equations is solved by means of a fourth order Adams predictor/corrector method using a Runge-Kutta starting solution.

### (3) Determination of Empirical Parameters

The parameter  $E_2$  is determined by considering the results for a freejet, since  $E_2$  is the only parameter remaining in Equation (1) when  $U_\infty = 0$ . From the data of Reference 6,  $E_2$  was originally determined to be .08, on the basis of measured entrainment rates in the fully developed region of a jet exhausting into a quiescent environment.

The entrainment of ambient fluid into a jet in the development region will generally be a function of the exit characteristics of the jet and therefore will usually vary from test to test. The entrainment characteristics of the jet of Reference 3 are shown in Figure 2. It is observed that entrainment of fluid by the jet increases in the development region and approaches the asymptotic value of Reference 6.

The variation of entrainment with distance from the jet exit has been incorporated into the jet model by allowing  $E_2$  to vary in the development region. Knowledge of the entrainment characteristics for the static case is, therefore, used in determining crossflow effects. For the calculations presented in this report, the variation of  $E_2$

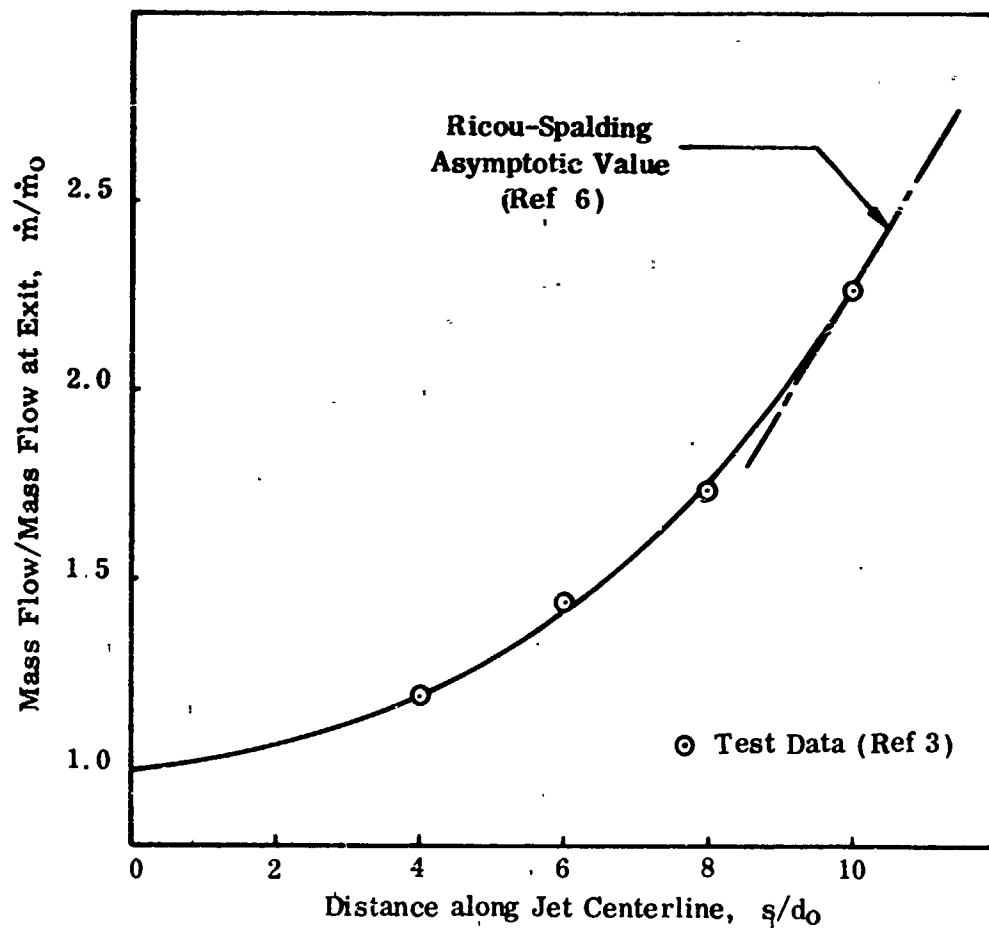


FIGURE 2. ENTRAINMENT CHARACTERISTICS  
FOR THE JET OF REFERENCE 3

in the development region to its asymptotic value of .08 is based on the information of Figure 2.

$C_D$  is also varied in the development region to take into account the change in the cross-sectional profile of the jet in this region. The relationship between  $C_D$  and the cross section of the jet which is employed in the computations has been obtained from an investigation of the data presented in Reference 25 and is given by

$$C_D = \left[ -\frac{1}{D^2} + \frac{6.6}{D} + .4 \right] / 6$$

where  $D$  is the ratio of minor to major axis of the ellipse representing the cross section of the jet in the development region. This expression for  $C_D$  was derived from subcritical test data and thus the range of Reynolds numbers for which it can be considered valid is approximately  $10^2 \leq Re \leq 10^5$ . Variations in  $C_D$  do not appear to have a great effect on the predicted values of jet-induced velocities, so that use of the expression outside the Reynolds number range defined above is not expected to lead to significant errors.

The parameters  $E_1$  and  $E_3$  were chosen at values giving good correlation between experimentally and theoretically determined jet centerlines and jet-induced surface pressures. The details on the test data utilized are presented in Section II. 2. This approach led to a final set of values of  $E_1 = .45$  and  $E_3 = 30$ .

#### (4) Calculation of the Induced Velocity Field

To obtain the velocity field due to the jet interference, the entrained fluid is represented by a uniform sink distribution along an axis normal to the mainstream and the jet blockage effect by a doublet distribution along the jet centerline as shown in Figure 3. The strength of the doublet distribution is obtained from the  $1/Z$  term in the complex velocity potential expansion  $W(Z)$  for the two-dimensional flow past an ellipse. In effect, by replacing the jet with a doublet distribution, the flow past an equivalent circular cylinder is being considered.

Consider an element of the jet, length  $\delta s$ , centered at  $(X, 0, Z)$ . The sink strength per unit distance in the  $\eta$  direction will then be given by

$$\bar{m} = \left[ E_1 U_\infty d \cos \theta + \frac{E_2 (U_j - U_\infty \sin \theta) C}{1 + E_3 \cos \theta / U_j} \right] \frac{\delta s}{d} \quad (21)$$

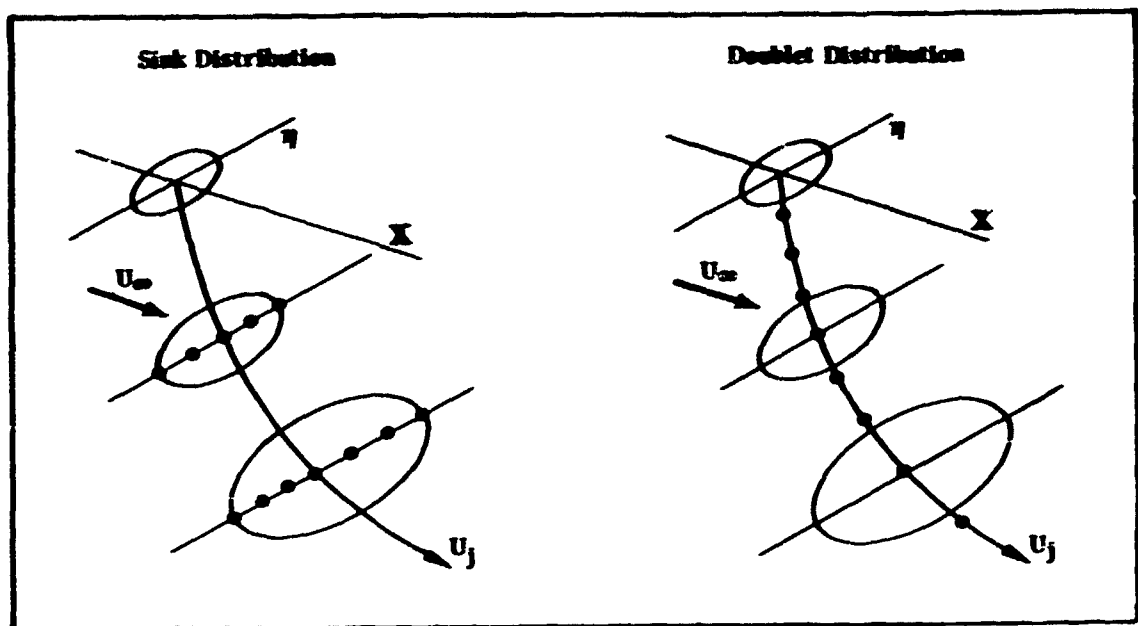


FIGURE 3. SINK AND DOUBLET DISTRIBUTIONS

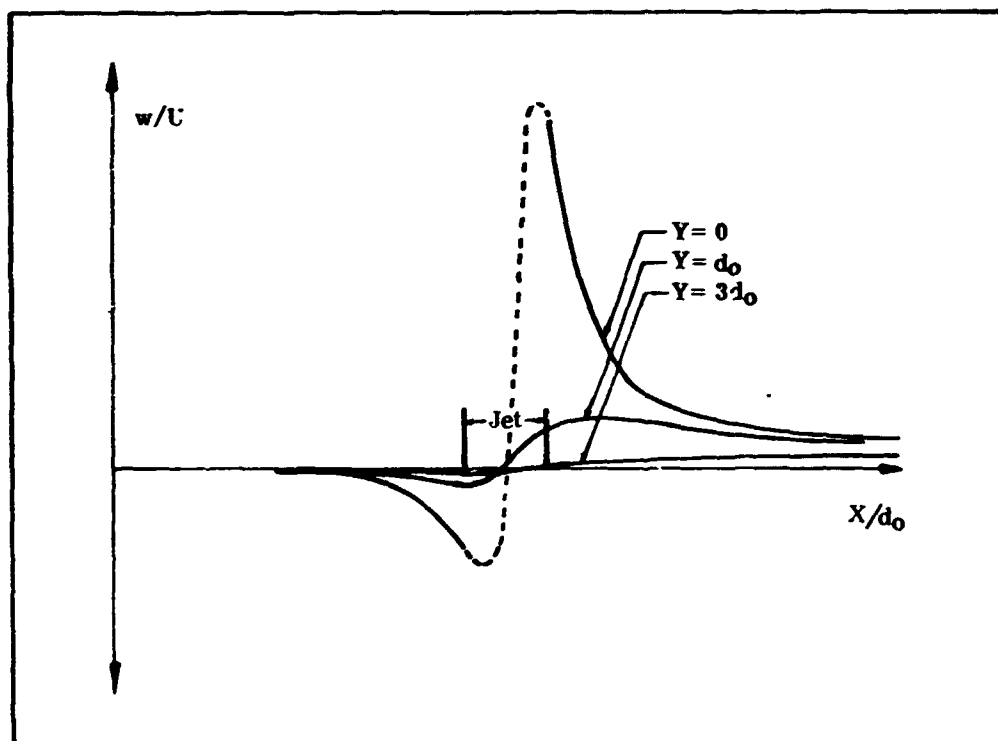


FIGURE 4. JET-INDUCED DOWNWASH VARIATION

The velocity potential for a sink element of length  $\delta\eta$

$$\phi = -\frac{\bar{m}}{4\pi r} d\eta$$

The induced velocity at a point P ( $X_p, Y_p, Z_p$ ) due to a sink element of length  $\delta\eta$  will be

$$\begin{aligned} V_i &= -\partial\phi/\partial r \\ &= -\frac{\bar{m}}{4\pi r^2} d\eta \\ &= \frac{-\bar{m} d\eta}{4\pi [(Z-Z_p)^2 + (X-X_p)^2 + (Y_p+\eta)^2]^{3/2}} \end{aligned} \quad (22)$$

The velocity component in the X direction is given by

$$u_s = -\partial\phi/\partial r = -(\partial\phi/\partial r)(\partial r/\partial X)$$

Performing differentiation with respect to  $X_p$

$$\begin{aligned} u_s &= -\frac{\bar{m}}{4\pi r^2} d\eta \frac{\partial r}{\partial X} \\ u_s &= \frac{\bar{m} d\eta (X-X_p)}{4\pi [(Z-Z_p)^2 + (X-X_p)^2 + (Y_p+\eta)^2]^{3/2}} \end{aligned} \quad (23)$$

Similarly the induced velocities in the direction of the axes Y and Z are obtained

$$v_s = -\frac{\bar{m} d\eta (Y_p+\eta)}{4\pi [(Z-Z_p)^2 + (X-X_p)^2 + (Y_p+\eta)^2]^{3/2}} \quad (24)$$

$$w_s = \frac{\bar{m} d\eta (Z-Z_p)}{4\pi [(Z-Z_p)^2 + (X-X_p)^2 + (Y_p+\eta)^2]^{3/2}} \quad (25)$$

Equation (23) represents the velocity component in the X-direction due to a sink element  $ds$ . Integration over the range  $-\frac{d}{2} \leq \eta \leq \frac{d}{2}$  will give the velocity induced by a jet element of length  $\delta s$ .

Integrating  $u_s$ :

$$\int_{-d/2}^{d/2} \frac{\bar{m} (X - X_p) d\eta}{4\pi [(Z - Z_p)^2 + (X - X_p)^2 + (Y_p + \eta)^2]^{3/2}} = \quad (26)$$

$$\frac{\bar{m}}{4\pi} (X - X_p) \int_{-d/2}^{d/2} \frac{d\eta}{[(Z - Z_p)^2 + (X - X_p)^2 + (Y_p + \eta)^2]^{3/2}}$$

Substituting in Equation (26) and evaluating from  $-d/2$  to  $d/2$  yields

$$\delta u_s = -\frac{\bar{m}}{4\pi} \frac{X - X_p}{[(Z - Z_p)^2 + (X - X_p)^2]} \times \left\{ \frac{Y_p - d/2}{[(Z - Z_p)^2 + (X - X_p)^2 + (Y_p - d/2)^2]^{1/2}} - \frac{Y_p + d/2}{[(Z - Z_p)^2 + (X - X_p)^2 + (Y_p + d/2)^2]^{1/2}} \right\} \quad (27)$$

Equations (24) and (25) can also be integrated to yield

$$\delta v_s = -\frac{\bar{m}}{4\pi} \left\{ \frac{1}{[(Z - Z_p)^2 + (X - X_p)^2 + (Y_p - d/2)^2]^{1/2}} - \frac{1}{[(Z - Z_p)^2 + (X - X_p)^2 + (Y_p + d/2)^2]^{1/2}} \right\} \quad (28)$$

$$\delta w_s = -\frac{\bar{m}}{4\pi} \frac{(Z - Z_p)}{[(Z - Z_p)^2 + (X - X_p)^2]} \times \left\{ \frac{Y_p - d/2}{[(Z - Z_p)^2 + (X - X_p)^2 + (Y_p - d/2)^2]^{1/2}} - \frac{Y_p + d/2}{[(Z - Z_p)^2 + (X - X_p)^2 + (Y_p + d/2)^2]^{1/2}} \right\} \quad (29)$$

Equations (27), (28), and (29) give the induced velocity components at  $X_p$ ,  $Y_p$ , and  $Z_p$  due to replacing a jet element of length  $\delta s$  by the sink distribution.

To this the blockage effect must be added. The strength of the doublet distribution utilized to represent the blockage effect of the jet is obtained from the complex velocity potential for the two-dimensional flow past an ellipse. By equating the strength of the doublet to the coefficient of the  $1/Z$  term, the flow past an equivalent circular cylinder is being considered.

For the two-dimensional flow past an ellipse

$$W(Z) = \frac{1}{2} U (a+b) \left[ \frac{e^{-i\alpha} [Z + (Z^2 - c^2)^{1/2}]}{a+b} + \frac{e^{i\alpha} [Z - (Z^2 - c^2)^{1/2}]}{a-b} \right] \quad (30)$$

for flow along  $a$ , the major semi-axis. Rotating flow 90 degrees makes  $a$  the minor semi-axis,  $b$  the major semi-axis,  $c = G$ .

$$\bar{W}(Z) = \frac{1}{2} U (a+b) \left[ \frac{Z + (Z^2 - c^2)^{1/2}}{a+b} + \frac{Z - (Z^2 - c^2)^{1/2}}{a-b} \right]$$

From binomial expansion, the leading two terms in a series of inverse powers are

$$\bar{W}(Z) = U Z + \frac{1}{2} U (a+b)(b)(1/Z)$$

the coefficient of the  $1/Z$  term is equated to the strength of the doublet,  $\mu$

In the coordinates of Figure 1

$$U = U_\infty \cos \theta$$

$a$  = minor axis of jet

$b$  = major axis of jet

$$\mu = \frac{1}{2} U_\infty \cos \theta (a+b)(b)$$



Considering the two geometric regions of the jet described in Equations (6) and (7) yields

$$\left. \begin{aligned} \mu &= \frac{\pi}{4} U_0 d^2 \cos \theta \left[ 1 - \frac{5}{4} \frac{z}{d} \frac{U_0}{U_{jc}} \right] \\ &\quad 0 \leq z^*/m \leq .3 \\ \mu &= \frac{5\pi U_0 d^2 \cos \theta}{32} \\ &\quad z^*/m > .3 \end{aligned} \right\} \quad (31)$$

With the notation of Figure 1 the induced velocity field at a given point P ( $\xi, \eta, \zeta$ ) due to a doublet of strength  $\mu$  at  $(\xi, \eta, \zeta) = (0, 0, 0)$  may be evaluated

The velocity potential of a doublet is given by

$$\phi = \frac{2\mu}{4\pi r^2} \cos \theta$$

$$\text{where } r = [\xi^2 + \eta^2 + \zeta^2]^{1/2}$$

$$\cos \theta = \zeta / r$$

then

$$\phi = \frac{2\mu}{4\pi} \frac{\zeta}{[\xi^2 + \eta^2 + \zeta^2]^{3/2}} \quad (32)$$

with the induced velocities in the  $\xi$ ,  $\eta$  and  $\zeta$  directions being given by

$$u_i = -\partial\phi/\partial\xi$$

$$v_i = -\partial\phi/\partial\eta$$

$$w_i = -\partial\phi/\partial\zeta$$

Equation (32) is differentiated to yield

$$u_i = -6\xi\mu/4\pi(\xi^2 + \eta^2 + \zeta^2)^{3/2} \quad (33)$$

$$v_i = -6\eta\mu/4\pi(\xi^2 + \eta^2 + \zeta^2)^{3/2} \quad (34)$$

$$w_i = \frac{2\mu}{4\pi(\xi^2 + \eta^2 + \zeta^2)^{3/2}} \left\{ 1 - \frac{3\xi}{(\xi^2 + \eta^2 + \zeta^2)} \right\} \quad (35)$$

From the relationship between  $\xi, \eta, \zeta$ , and  $X, Y, Z$  in Figure 1, it can be seen that

$$\left. \begin{aligned} \delta U_B &= u_i \sin\theta + w_i \cos\theta \\ \delta V_B &= -v_i \\ \delta W_B &= u_i \cos\theta - w_i \sin\theta \end{aligned} \right\} \quad (36)$$

and

$$\begin{aligned} \xi &= (x_p - x) \sin\theta + (z_p - z) \cos\theta \\ \eta &= -y_p \\ \zeta &= (x_p - x) \cos\theta + (z_p - z) \sin\theta \end{aligned}$$

where  $\delta U_B, \delta V_B, \delta W_B$  are the induced velocities at  $P(x_p, y_p, z_p)$  due to a jet element of length  $\delta s$  centered at  $(X, 0, Z)$ , and  $\mu$  is obtained from Equation (31).

The total interference velocity at a point may be determined by integrating Equations (27) - (29) and Equation (36) over the extent of the jet, giving the total induced sink and doublet component velocities. These component velocities are then summed to give the total interference velocity. In treating a jet exhausting from an infinite wall, an image system of the singularity distributions is utilized to satisfy the boundary condition at the wall. The flat plate pressure coefficients shown in Section II, 2 were computed in this manner. Boundary conditions for a wing or fuselage in the presence of a flow exiting from a nozzle are discussed in Sections IV and VIII.

In the treatment of the blockage effect discussed above, the jet curvature does not contribute anything to the doublet strength. Three-dimensional effects are

accounted for through the doublet position and orientation and by calculating the induced velocity field from the three-dimensional counterparts to the doublets.

For the lower velocity ratios ( $U_\infty/U_{jo}$ ), where the jet curvature is quite small, this model can be expected to be a good representation of the physical situation. As the jet curvature increases with increasing velocity ratio, the quasi-two dimensional approach becomes less valid. Calculations of induced surface static pressures for the higher velocity ratios ( $U_\infty/U_{jo} = .250$ ) did not correlate with test data as well as did calculations for the lower velocity ratios ( $U_\infty/U_{jo} = .125$ ).

Attempts were made to improve the correlation by changing the entrainment expression of Equation (i), without success. This suggested that some other mechanism was responsible for the lack of correlation between calculations and test data. It was thought that jet curvature had not been adequately included in the model. Also, it was argued that this curvature would allow relief for the crossflow fluid ahead of the jet and might be accounted for by applying a distribution of sources along the jet centerline. One would expect the strength of the sources to be a monotonically increasing function of the jet centerline curvature. Subsequently, it was learned that Werner and Chang (Reference 50), using a slender body matched asymptotic expansion technique, had deduced similar results. Calculations of jet-induced static pressures, using a source distribution, displayed markedly improved correlation with test data.

The source distribution has been made proportional to jet curvature and best correlation with test data, over the range of velocity ratios  $.1 \leq U_\infty/U_{jo} \leq .3$ , has been obtained by taking the source strength equal to three times the jet curvature.

The formulation for the induced velocity components at arbitrary points given in Equations (21) to (36) is, of course, not valid for points inside the jet. Figure 4 shows schematically, the variation of the downwash component induced in the plane of the jet exit by a flow exhausting from a nozzle located at  $Y=0$ . The large variation across the jet in the freestream direction is typical of the computed downwash distributions. Thus, a certain amount of care must be exercised in choosing the control points at which induced velocities are to be evaluated for use with the methods of computing forces and moments in Sections IV and VIII.

#### b. Arbitrary Jet Direction

Although the equations of motion for the jet model developed in the preceding discussion are written for a jet exhausting normally into a cross flow, they are valid

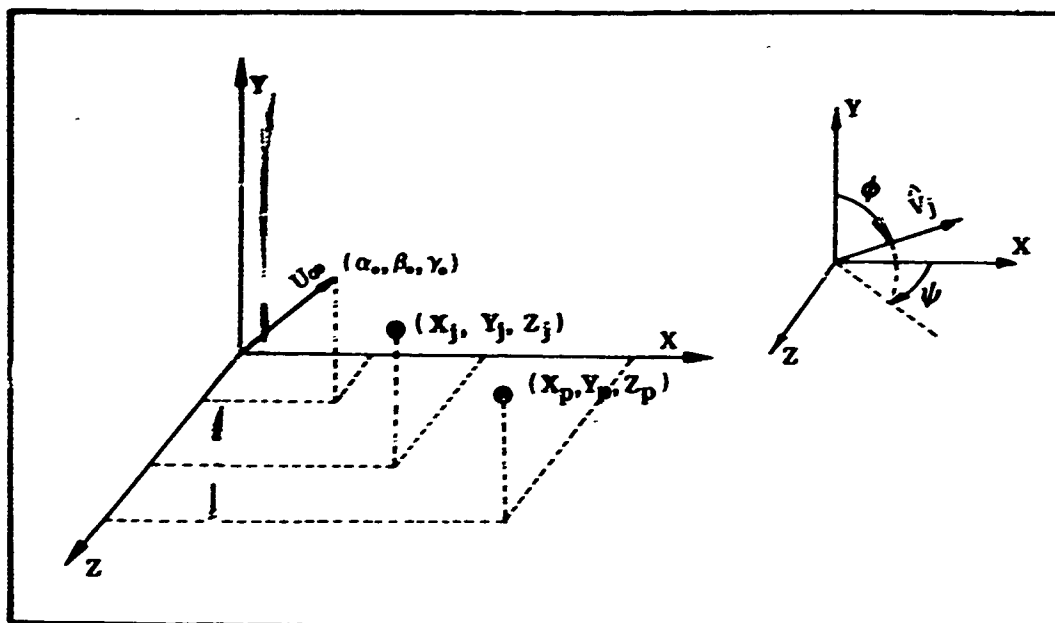


FIGURE 5. GENERAL COORDINATE SYSTEM

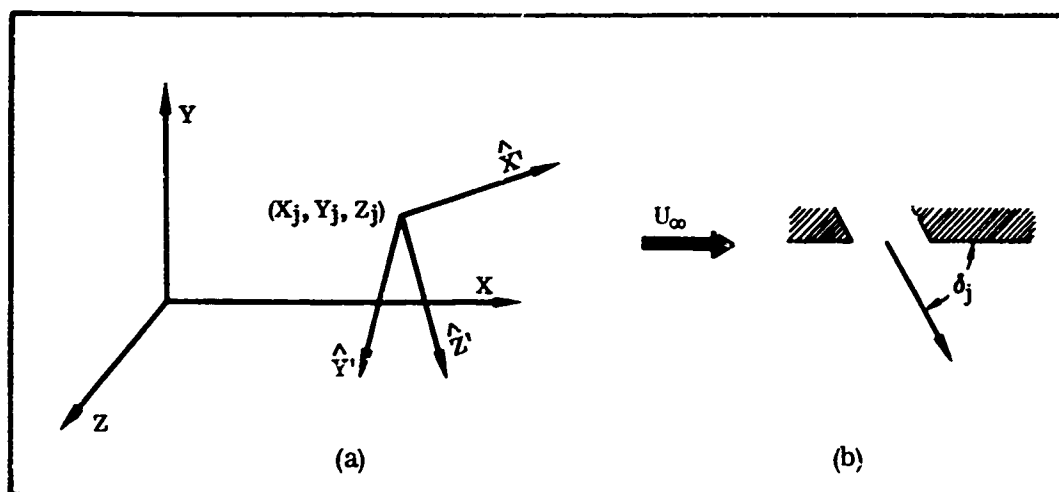


FIGURE 6. JET-CENTERED COORDINATE SYSTEM

for any jet in a local coordinate system, oriented with the  $X'$ -axis in the direction of the mainstream flow and the  $X'Z'$ -plane defined by the mainstream flow vector and the jet exhaust vector. The direction of the mainstream, the location of the center as well as the initial direction of the exhausting jet, and the position of the control points at which induced velocity components are to be evaluated may be arbitrarily specified in a general, fixed coordinate system as shown in Figure 5.

A local coordinate system, centered at  $X_j, Y_j, Z_j$  is then established as shown in Figure 6(a). The direction cosines of  $\hat{X}'$  with respect to the fixed coordinate system are  $\alpha_0, \beta_0, \gamma_0$  and the direction cosines for  $\hat{Y}'$  and  $\hat{Z}'$  are determined from the following relationships.

$$\begin{aligned}\hat{Y}' &= \hat{V}_j \times \hat{X}' \\ \hat{Z}' &= \hat{X}' \times \hat{Y}'\end{aligned}$$

where  $\hat{V}_j$  is the unit vector in the initial jet exhaust direction, obtained from  $\phi$  and  $\psi$ , the jet exhaust angles.

This establishes the co-planar relationship between the mainstream flow and the jet centerline required by the equations of motion formulated for the normally exhausting jet.

Initial conditions at the jet exit (shown schematically in Figure 6b) are now

$Z^* = 0., X^* = 0., U_j^* = 1., d^* = 1.,$  and  $dX^*/dZ^* = \left[ \frac{1 - \cos^2 \theta_0}{\cos^2 \theta_0} \right]^{1/2}$  where  $\cos \theta_0 = \hat{V}_j \cdot \hat{Z}'$ . Both  $\theta_0$  and the angle  $\delta_j$ , the angle specifying the exhaust direction in the exhaust plane, are shown in Figure 6(b).

Observations during the experimental investigation of Reference 3 showed that a jet exhausting into the direction of the crossflow,  $\delta_j > 90^\circ$ , appears to deform from its initial circular cross section more rapidly than a jet exhausting with the crossflow,  $\delta_j < 90^\circ$ . Consequently, the development region, in which the jet deforms to an elliptical cross section with a minor to major axis ratio of 1/4, has been made a function of the jet exhaust angle  $\delta_j$ . For  $\delta_j > 90^\circ$  the extent of the development region is defined to be  $H' = H (\cos \theta_0)$  and for  $\delta_j < 90^\circ$  the development region becomes  $H' = H / \cos \theta_0$  where  $H = .3 U_{j0} / U_\infty$  is the extent of the development region for a normally exhausting jet, defined previously.

The geometry of the jet and the jet-induced velocity components can now be computed in this local coordinate system, utilizing the equations developed for a jet exhausting normally into a crossflow.

## 2. COMPARISONS OF SINGLE JET COMPUTATIONS WITH TEST DATA

### a. Jet Centerlines

Figure 7 shows a comparison between computed and experimentally determined centerlines for normally exhausting jets, with velocity ratios of  $U_\infty/U_{j0} = .125, .250$  and  $U_\infty/U_{j0} = .123, .233$ . The correlations shown in Figure 7 were instrumental in the determination of the entrainment parameters  $E_1$  and  $E_3$ .

Extensive computations were carried out for jets at various velocity ratios and exhaust angles. A comparison of computed jet centerlines with an empirical equation for the centerlines of jets exhausting at angles other than 90 degrees to the mainstream is shown in Figure 8(a) through 8(d). These correspond to Figures 12(a), 13(a), 14(b), and 15(a) of Reference 9. The solid curves represent centerlines computed for the specified conditions. The broken curves represent the empirical equation

$$\frac{X}{d_0} = - \frac{(U_\infty/U_{j0})^2}{4 \sin^2 \delta_j} \left( \frac{Z}{d_0} \right)^3 - \frac{Z}{d_0} \cot \delta_j \quad (37)$$

The curves superimposed on the photographs of Figures 12 through 15 of Reference 9 show the fit of this equation. It should be emphasized that the broken curves represent an empirical rather than experimental determination of the centerlines. They are included in Figure 8 primarily to aid in orienting the computed centerlines with respect to the photographs of the jet wakes in Reference 9.

Figure 9 shows a comparison of experimental and theoretical jet centerlines for a jet of velocity ratio  $U_\infty/U_{j0} = .120$  exhausting at various angles into the mainstream. Since, in this figure, the agreement between theory and experiment is not as close as might be desired, a comment regarding the differences is in order. It is noted that the theoretical curves in Figure 9 employ values of entrainment coefficients based partly on correlation with the experimental data of Reference 7 (Figure 7). Comparison of the experimental centerline for the normally exhausting jet of Figure 9 with the test data of Figure 7(a) reveals differences which appear to be inconsistent with the small change in velocity ratio. In view of these experimental differences for the normally exhausting jet, the correlation for the jet centerlines shown in Figure 9 is considered to be adequate.

A further comparison of theory with experiment for jets exhausting at an angle other than 90 degrees is presented in Figure 10. Good agreement between theory and experiment can be observed.

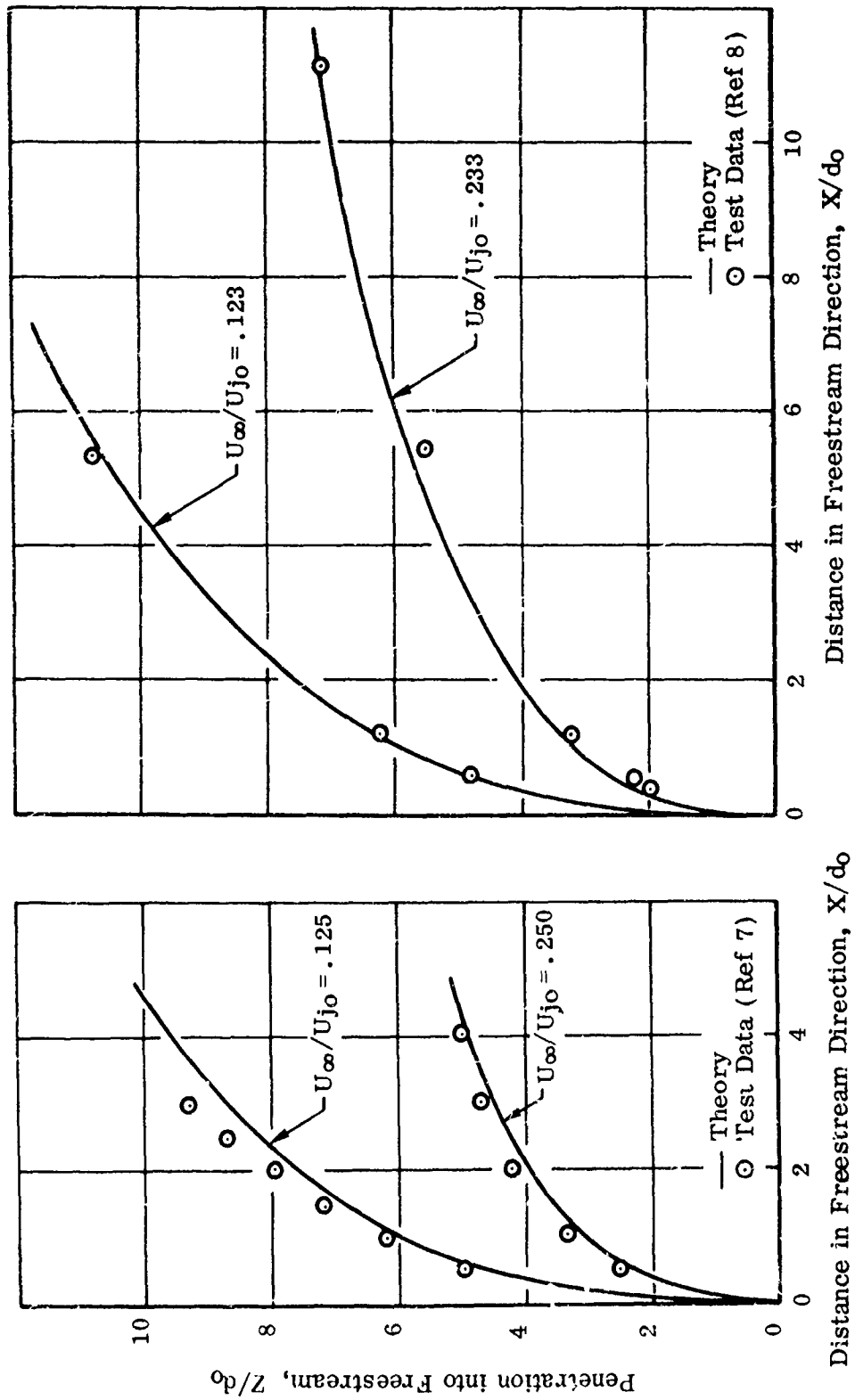


FIGURE 7. CENTERLINES OF JETS EXHAUSTING NORMALLY INTO THE FREESTREAM

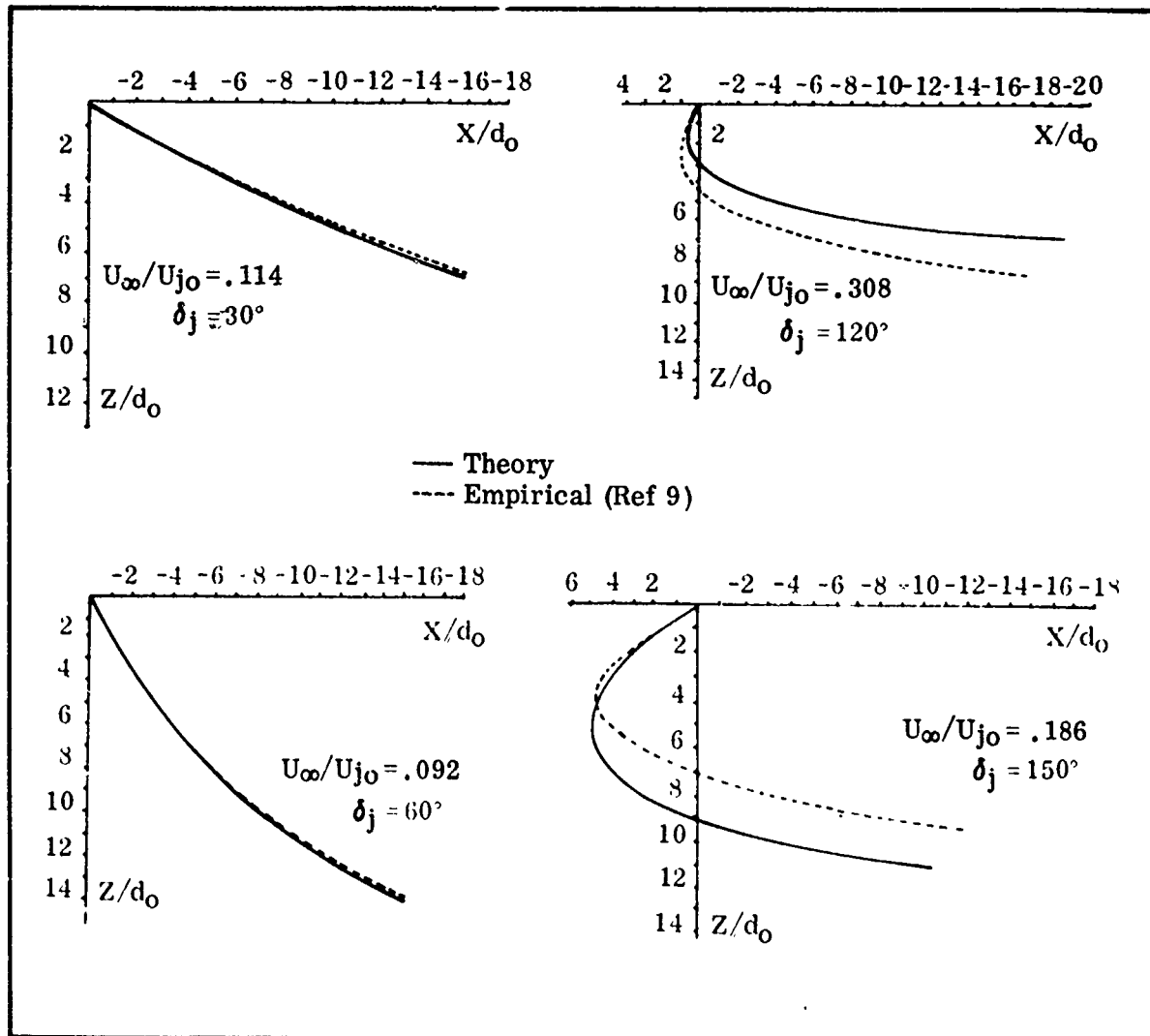


FIGURE 8. CENTERLINES OF JETS EXHAUSTING INTO THE FREESTREAM AT VARIOUS ANGLES



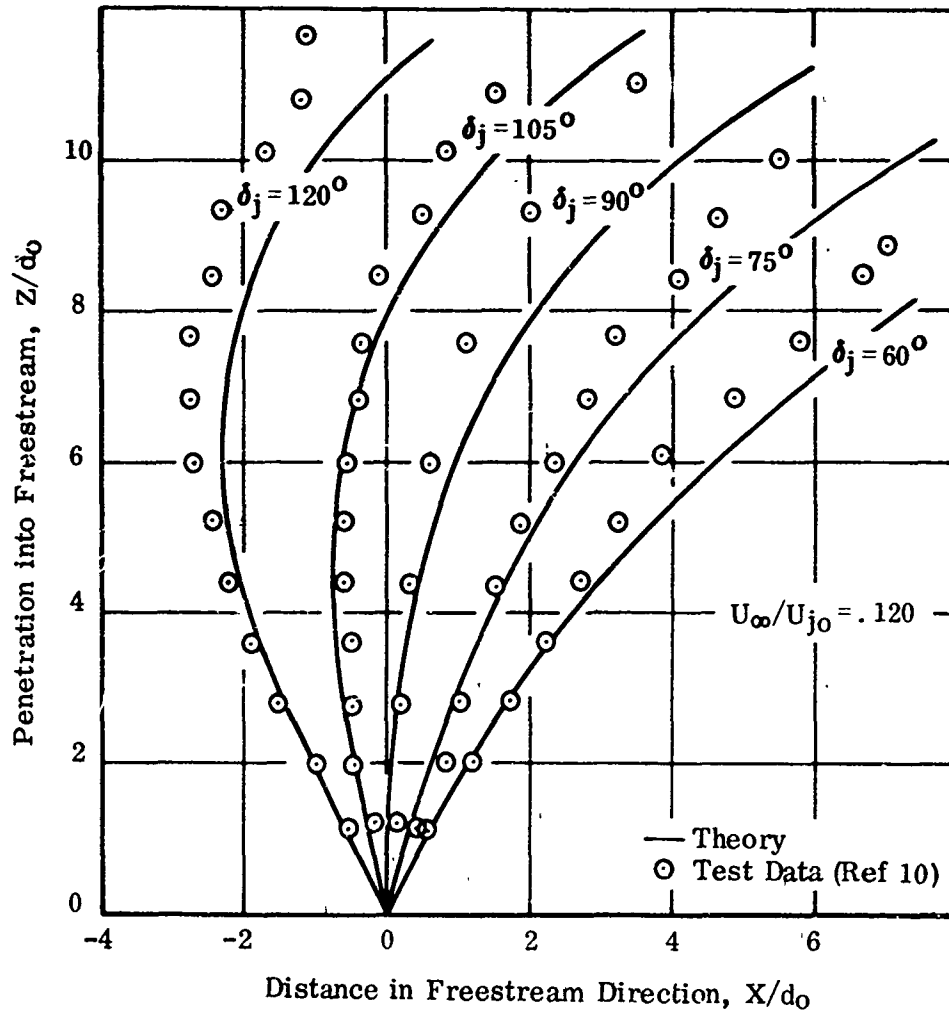


FIGURE 9. CENTERLINES OF A JET EXHAUSTING INTO THE FREESTREAM AT VARIOUS ANGLES

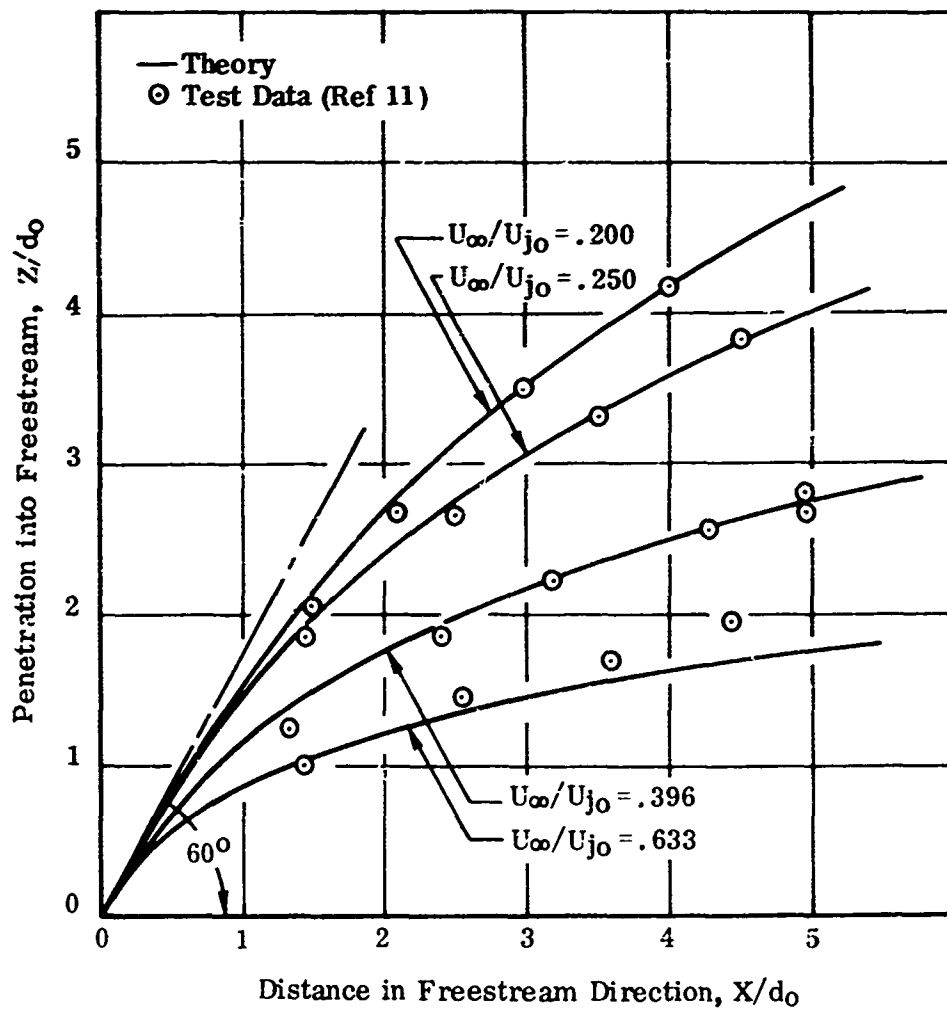


FIGURE 10. CENTERLINES OF JETS EXHAUSTING INTO THE FREESTREAM  
 AT AN ANGLE  $\delta_j = 60^\circ$

## b. Induced Pressures

Extensive computations to determine induced surface static pressure distributions due to single jets exhausting into a crossflow were carried out. Comparisons between theory and test data from References 3, 12, 13, and 14, are shown in Figures 12 through 18 for a number of jet configurations. Figure 11 is a schematic of the single jet arrangement, with surface pressure taps indicated, employed in the tests of Reference 3.

The surface static pressure variations with  $X/d_o$  at  $Y/d_o = 0$  and 1.5 are shown in Figure 12 for a jet with a velocity ratio  $U_\infty/U_{j0} = .125$ . Test data from References 3, 12, and 13 are plotted for comparison with the calculations. At  $Y/d_o = 0$ , the differences between the test data of References 3 and 12 are within experimental accuracy ahead of the jet, whereas the data from Reference 13 show significant differences. Behind the jet there are discernible differences in test data, due in part to the unsteady nature of the flow in this region. At  $Y/d_o = 1.5$ , the test data of References 3 and 12 are seen to be in good agreement. There is some discrepancy between these data and the data of Reference 13 in the region behind the jet.

The same static pressure variations for a jet with velocity ratio  $U_\infty/U_{j0} = .250$  are shown in Figure 13. At  $Y/d_o = 0$ , the data of References 3 and 12 are in good agreement ahead of the jet, while significant differences are noted for the data of Reference 13. Differences in the test data behind the jet are again evident. All three sets of test data show good agreement at  $Y/d_o = 1.5$ .

The purpose of making these comparisons was to determine whether there were discrepancies among data from different tests and, if so, the reasons for these discrepancies. The data of Reference 3 are in good agreement with the test data of Reference 12 except in the wake region behind the jet, where discrepancies might be expected because of the unsteady nature of the flow in this area. The differences between the data of Reference 13 and the data from the other tests could be due to boundary layer effects. The plate boundary layer was thicker for tests of Reference 13 than for the others. Boundary layer thickness has been shown to have a significant effect on the surface static pressure distribution (see Figure 5 of Reference 13). The correlation among the sets of test data also gives confidence in the data of Reference 3 for inclined jets and multiple jet configurations for which there are no other data available for comparison.

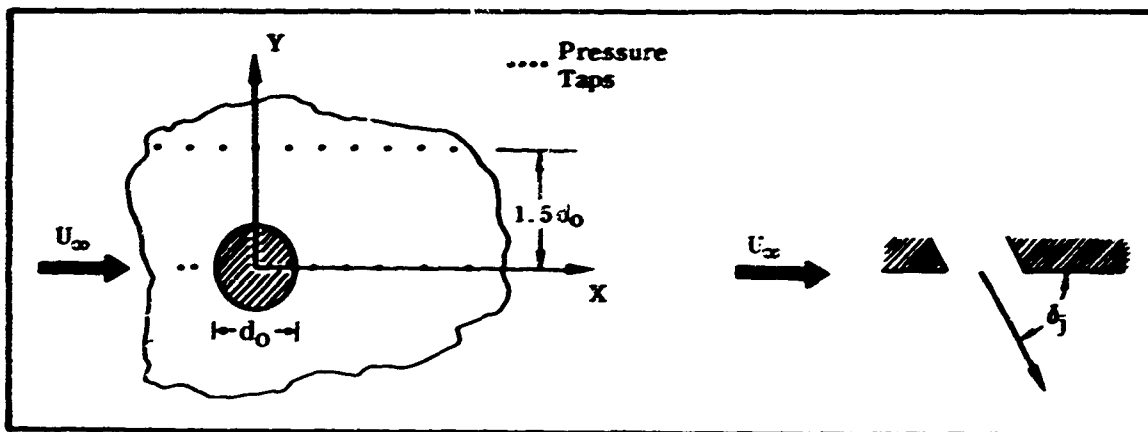
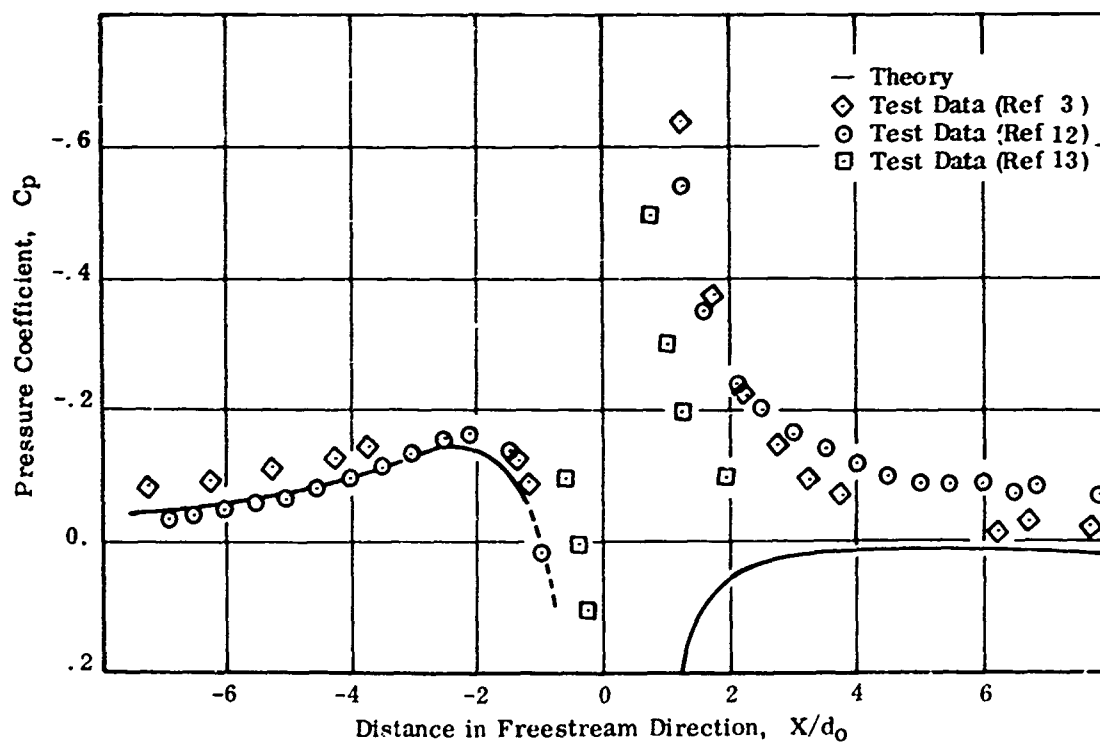
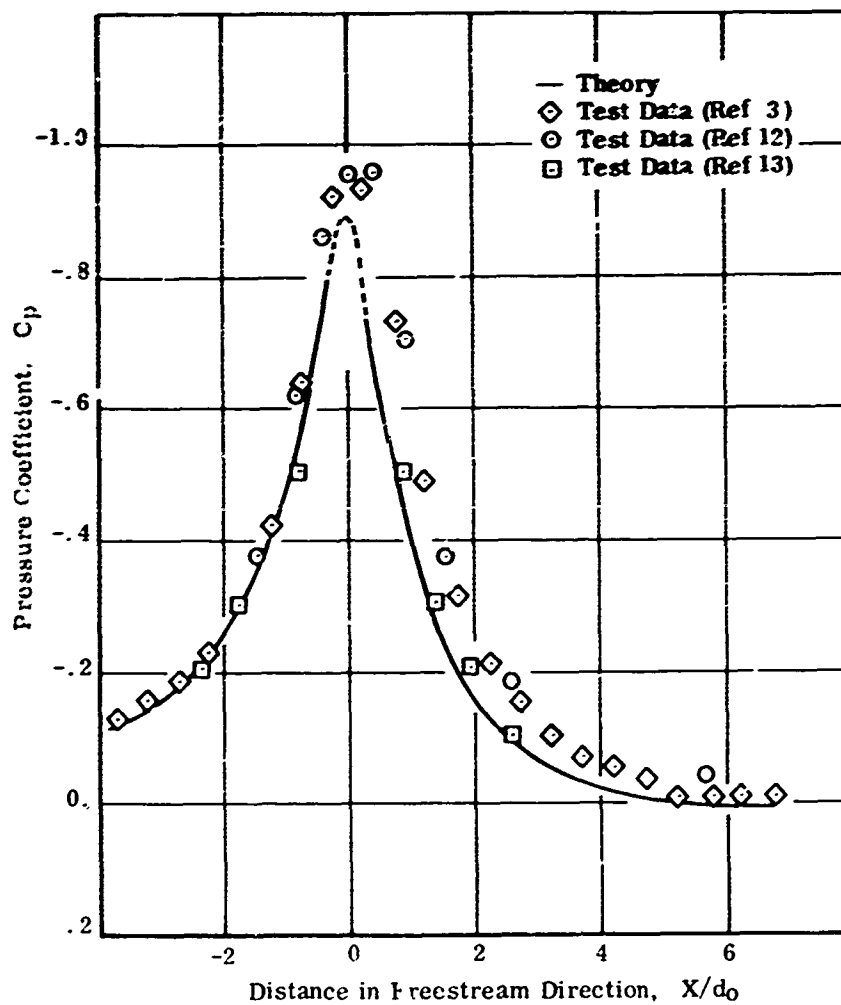


FIGURE 11. SINGLE JET CONFIGURATION



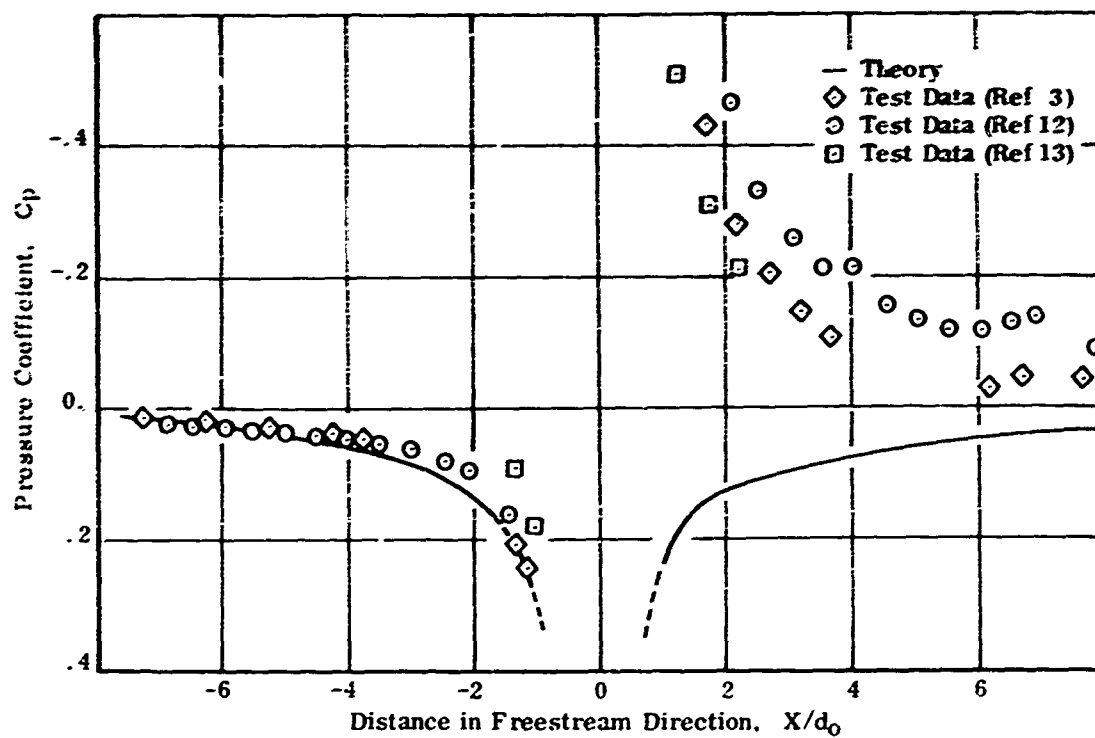
(a) Station  $Y/d_0 = 0$

FIGURE 12. INDUCED PRESSURE VARIATION DUE TO A SINGLE JET OF VELOCITY RATIO  $U_\infty/U_{j0} = .125$



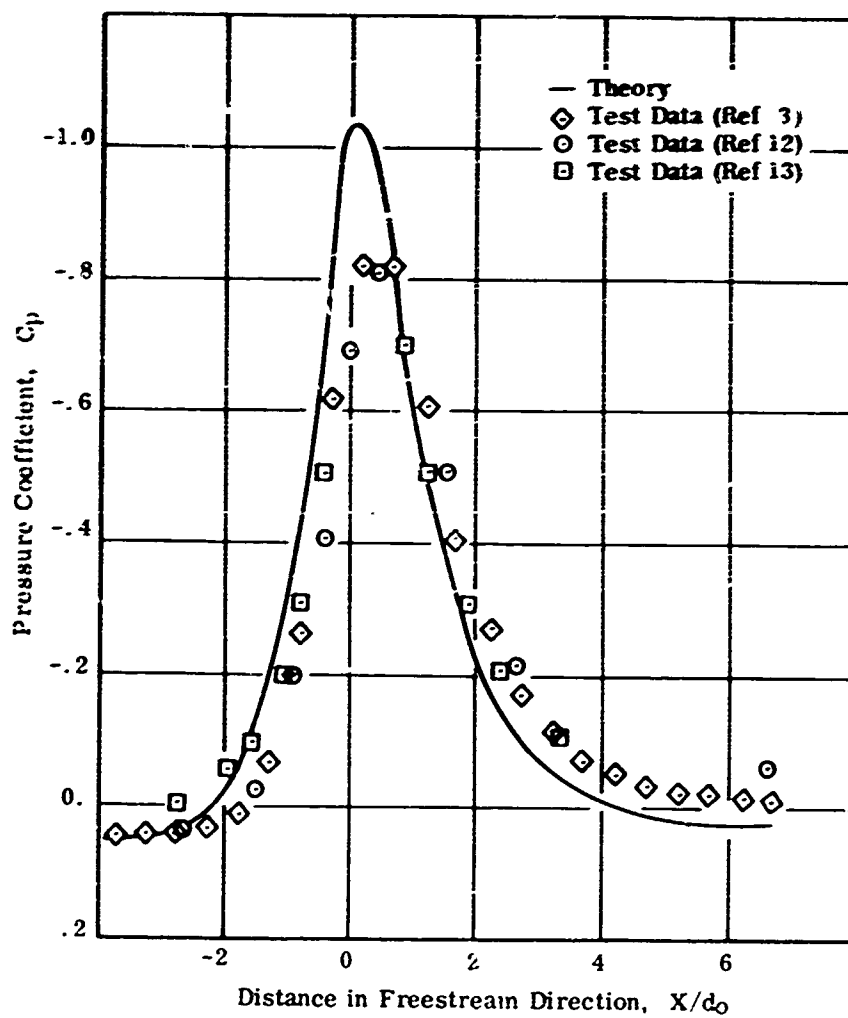
(b) Station  $Y/d_0 = 1.5$

FIGURE 12. (Concluded)



(a) Station  $Y/d_0 = 0$

FIGURE 13. INDUCED PRESSURE VARIATION DUE TO A SINGLE JET OF VELOCITY RATIO  $U_\infty/U_{j0} = .250$



(b) Station  $Y/d_0 = 1.5$

FIGURE 13. (Concluded)

The theoretical pressure variations show good agreement with test data in Figures 12 and 13 for the regions ahead of the jet exit. It might be noted that the agreement between theory and test data for the velocity ratio of .250 was greatly improved by utilization of the source distribution to account for the curvature of the jet, which was discussed on page 23.

There are significant differences between theory and test data in the wake regions behind the jet. The singularity representation of the jet used to compute the jet-induced pressure distribution assumes potential flow in the areas external to the jet. Physically meaningful results can only be expected in regions where the flow outside the boundary layer is potential. It is possible that a distribution of sources along the jet boundary may be used to represent the wake effects and to achieve better correlation with test pressures in the wake region. Also, it should be noted that the wake region is usually small with respect to the total area being investigated (see Figure 15 for example).

Figures 14, 15 and 16 show the pressure distributions in the plane of the jet exits around jets exhausting at angles of  $\delta j = 120^\circ$ ,  $90^\circ$  and  $60^\circ$  into the freestream. When the jet is directed against the crossflow ( $\delta j = 120^\circ$ ) extensive regions of negative pressure result primarily ahead of the jet. As the jet exhaust angle changes to  $90^\circ$  degrees and then to  $60^\circ$  degrees, these regions of negative pressure are observed to move downstream (Figures 15 and 16). Agreement between theory and test data is noted to be better for the  $\delta j = 90^\circ$  and  $\delta j = 60^\circ$  configurations than for the  $\delta j = 120^\circ$  configuration. In all three cases, discrepancies between theory and test data exist in the wake regions of the jets for reasons discussed previously.

Additional comparisons between computed and experimental induced pressure distributions around a single jet exhausting normally into the freestream are shown in Figures 17 and 18, for velocity ratios of .125 and .089. The experimental data of Figure 17 provide additional confirmation for the correlation between theory and experiment observed in Figure 15. They also indicate that the theoretical results lie within experimental differences. Very good agreement between theory and experiment is evident in Figure 18.



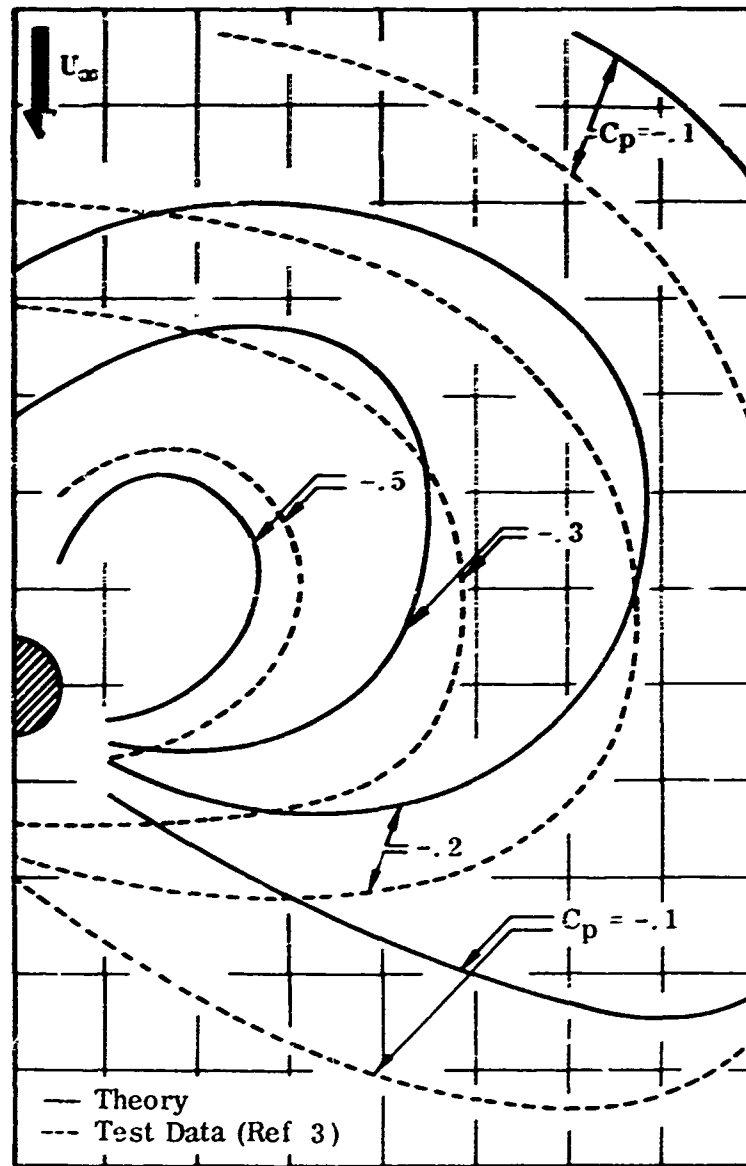


FIGURE 14. PRESSURE DISTRIBUTION AROUND A SINGLE JET EXHAUSTING AT AN ANGLE  $\delta_j = 120^\circ$  INTO THE FREESTREAM ( $U_\infty/U_{j0} = .125$ )

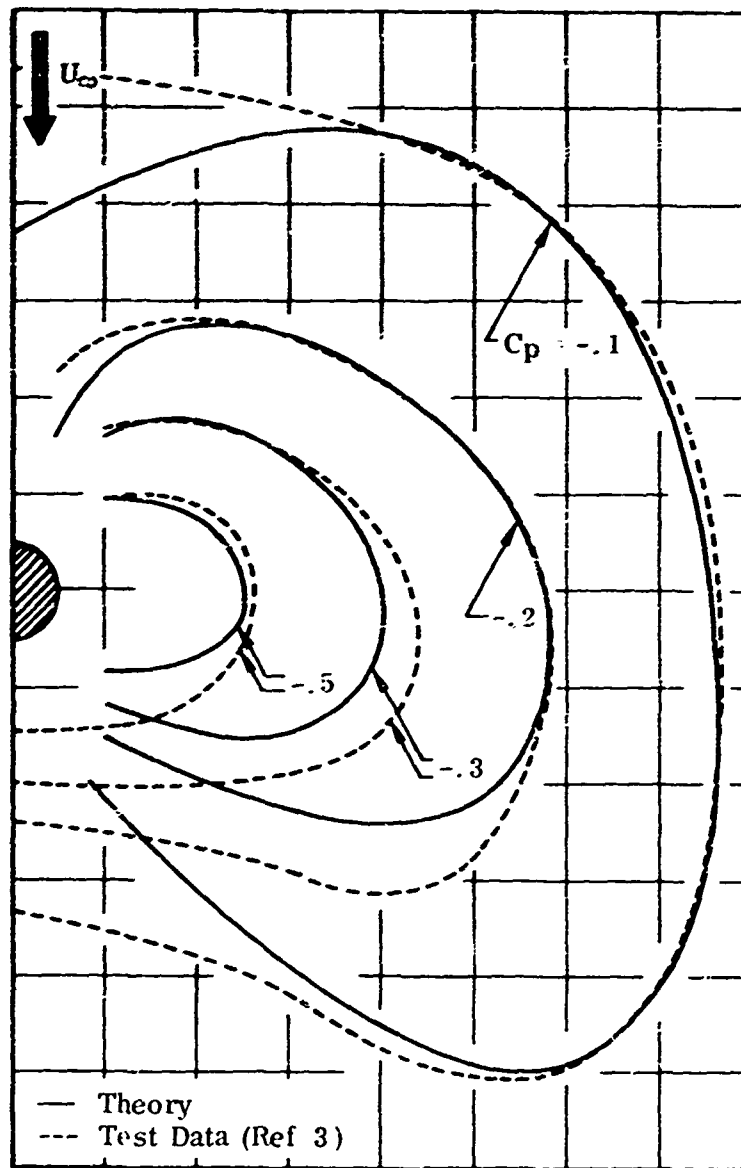


FIGURE 15. PRESSURE DISTRIBUTION AROUND A SINGLE JET EXHAUSTING AT AN ANGLE  $\delta_j = 90^\circ$  INTO THE FREESTREAM ( $U_\infty/U_{j0} = .125$ )

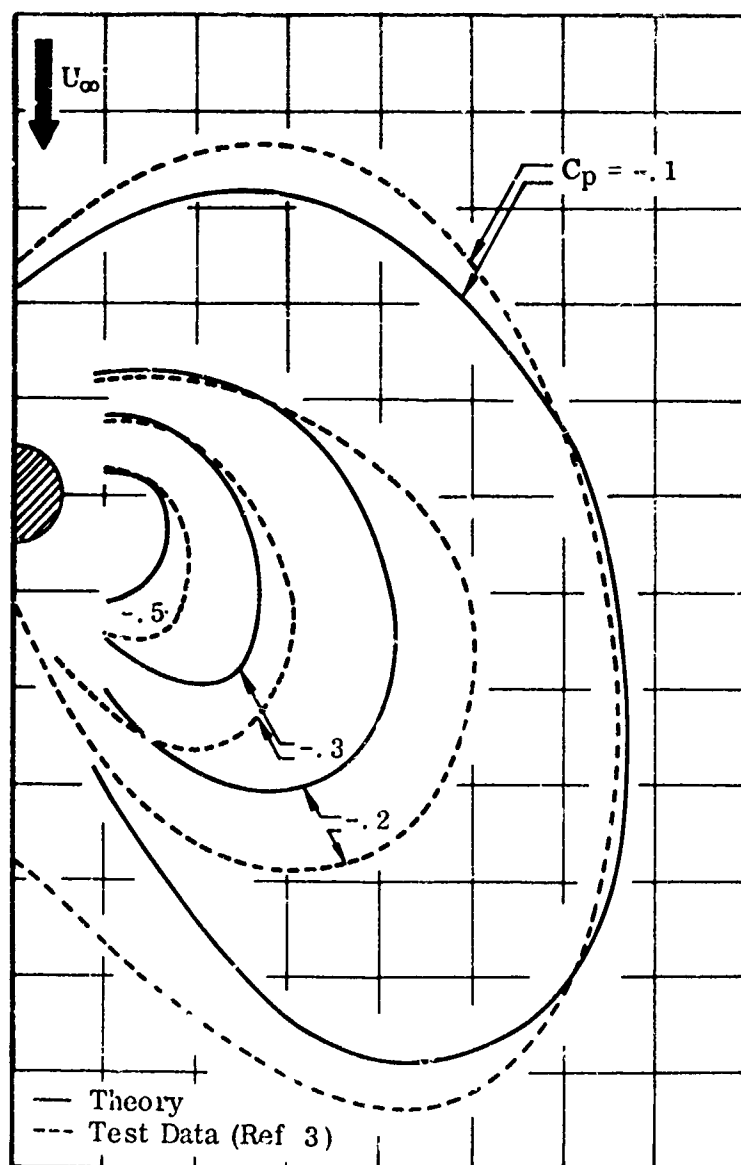


FIGURE 16. PRESSURE DISTRIBUTION AROUND A SINGLE JET EXHAUSTING AT AN ANGLE  $\delta_j = 60^\circ$  INTO THE FREESTREAM ( $U_\infty/U_{j0} = .125$ )

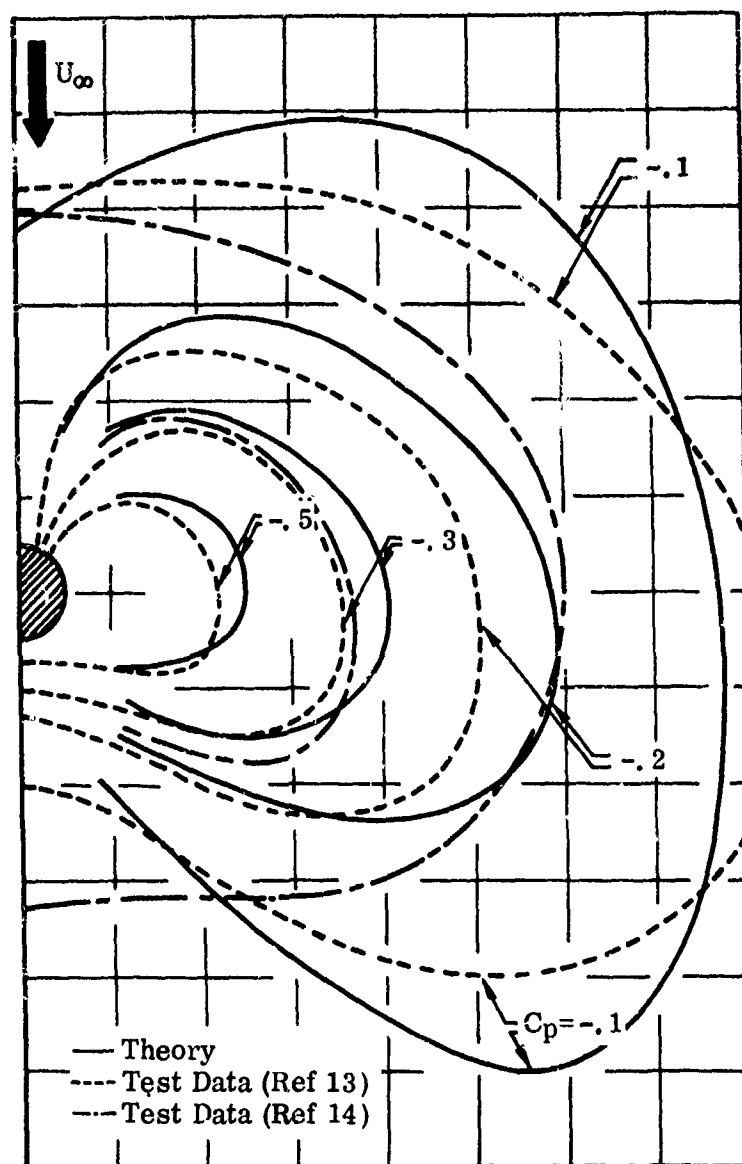


FIGURE 17. PRESSURE DISTRIBUTION AROUND A SINGLE JET EXHAUSTING AT AN ANGLE  $\delta_j = 90^\circ$  INTO THE FREESTREAM ( $U_\infty/U_{j0} = .125$ )

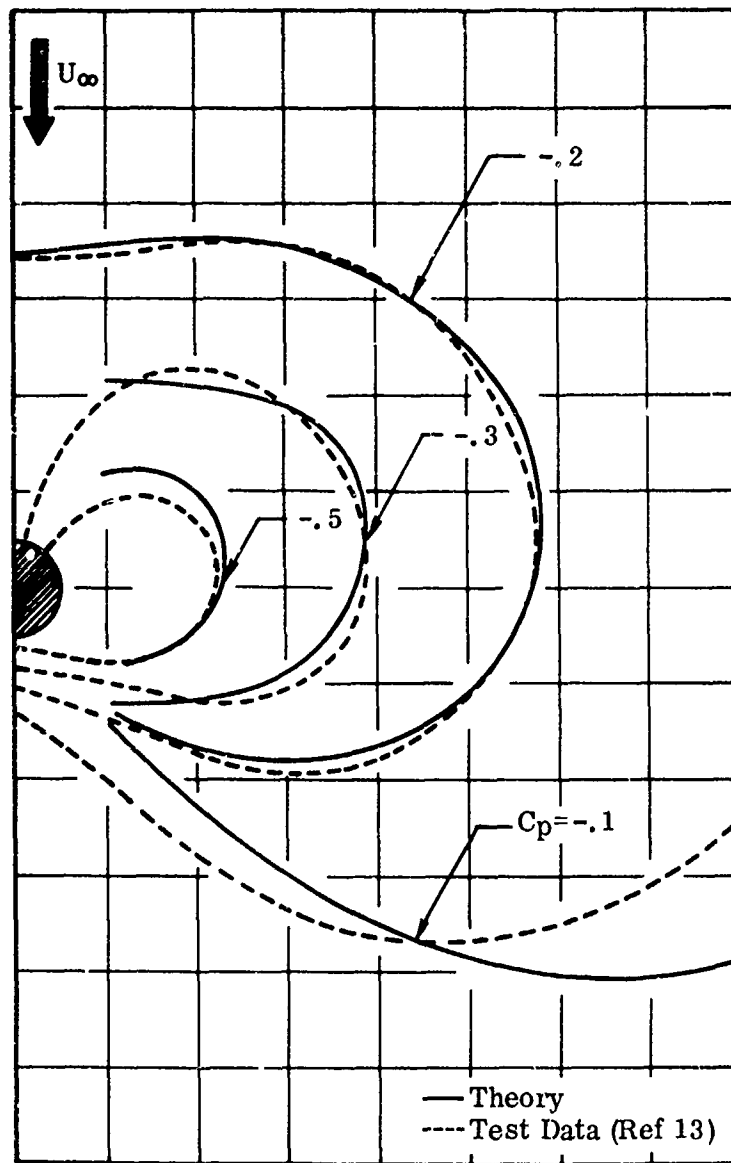


FIGURE 18. PRESSURE DISTRIBUTION AROUND A SINGLE JET EXHAUSTING AT AN ANGLE  $\delta_j = 90^\circ$  INTO THE FREESTREAM ( $U_\infty/U_{j0} = .089$ )

### 3. MULTIPLE JET ANALYTICAL MODEL

The basic single jet analytical model has been applied to the computation of the interaction flow field due to multiple exhausting jets. A multiple jet configuration is treated as a combination of discrete jets, with each jet (including jets resulting from the coalescence of other jets) being replaced by its representative singularity distribution to obtain the induced velocity field. In the development of the two-jet model described in detail in this section two assumptions were made

- The leading (or upstream) jet develops independently of the downstream jet
- The downstream jet exhausts into a freestream of reduced dynamic pressure which it sees as the result of blockage by the upstream jet.

Data from the wind tunnel investigation of Reference 3 have been analyzed to substantiate these assumptions and to establish quantitatively the empirical relationships utilized in the two-jet computations. Details of this analysis are also given in this section.

#### a. Two-Jet Computations

Figure 19 shows the planform of three jet configurations in relation to the mainstream flow. Arrangements (a) and (c) represent limiting cases. The arrangement of (a) allows each jet to develop independently to the point where the growth of the jets in the direction normal to the flow causes them to intersect. The configuration shown in (c) places the downstream jet entirely in the zone of influence of the upstream jet. The downstream jet is located partially in the zone of influence of the upstream jet in the arrangement depicted in (b).

Although Figure 19 shows the relationship of the jets in the plane of the jet exits, as an illustration, the determination of the degree of influence of the upstream jet (JET1) on the downstream jet (JET2) can be carried out for each element of JET1, as shown in the general case of Figure 20.

Plane L, defined by the mainstream flow vector and the diameter of JET1, identifies the element of JET2 influenced by a given element of JET1. Plane M, which contains the mainstream flow vector and the local jet velocity vector of the given element of JET1, is then established. The intersection of the plane M with the jet diameter of the appropriate element of JET2 is computed to determine the extent to which the two jets overlap.

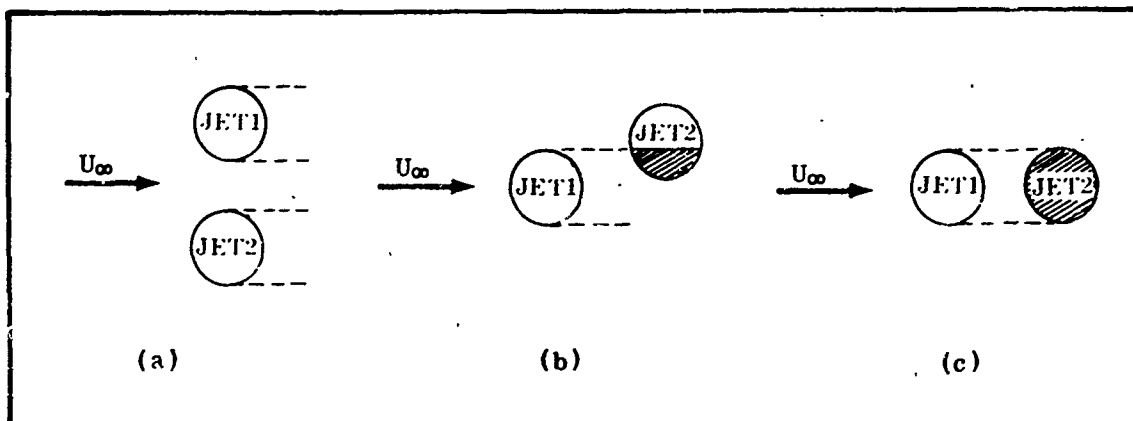


FIGURE 19. JET EXIT CONFIGURATIONS

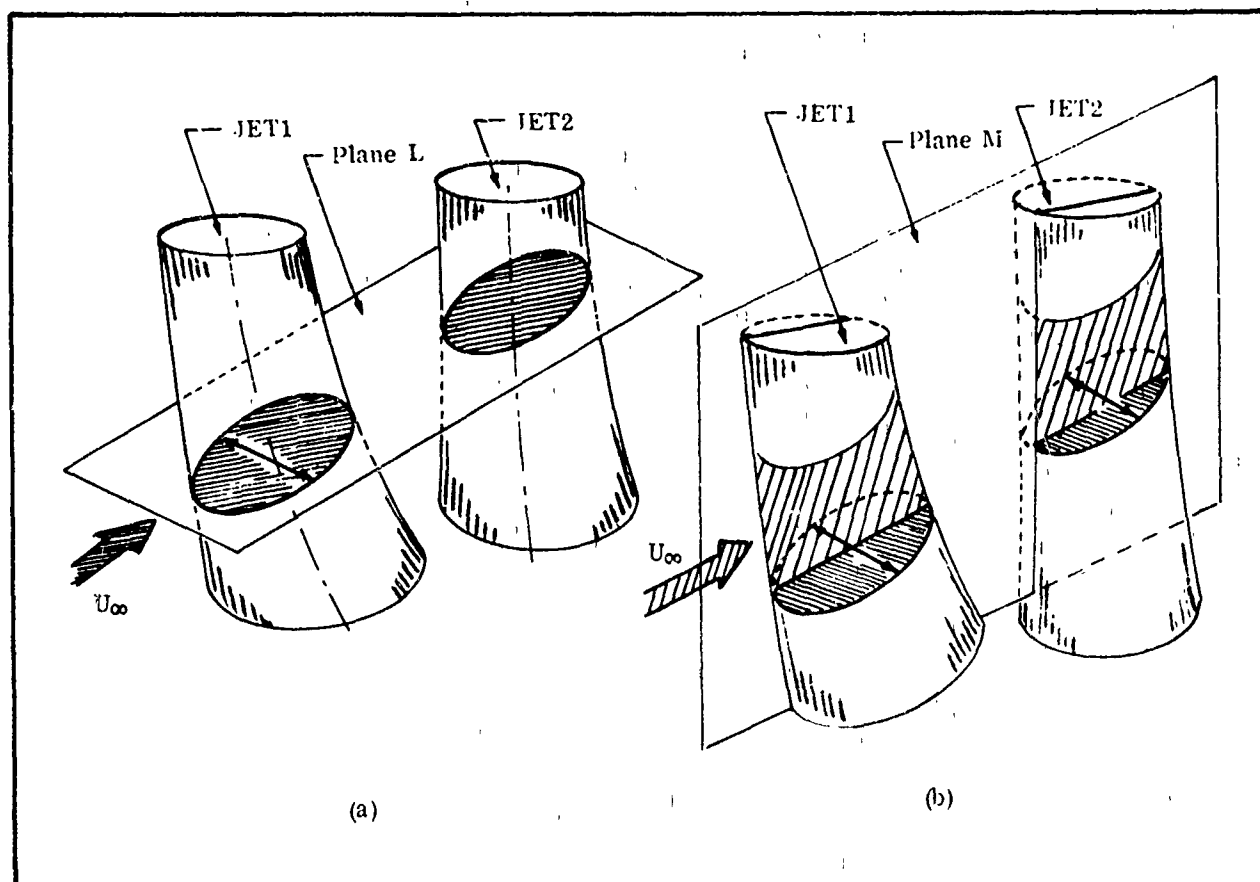


FIGURE 20. SCHEMATIC OF JET INFLUENCE

An expression for the effective dynamic pressure which the downstream jet "sees" as a result of the blockage by the upstream jet, based on analysis of experimental data will be derived in the following subsection. Configurations with complete overlap between the two jets (jets aligned in crossflow direction) and partial overlap will be considered, and the extent of overlap between the two jets will be a principal parameter. Thus the influence of the upstream jet on the downstream jet is introduced into the computations as a reduced freestream velocity,  $U_e/U_\infty = [q_c/q_\infty]^{1/2}$  in the continuity, momentum and force equations governing the development of the downstream jet.

When calculations of the distance between the two jet centerlines indicate that the jets have intersected, initial conditions for the merged jet which results are determined from the continuity and momentum considerations:

$$\begin{aligned} A_1 U_{j1} + A_2 U_{j2} &= A_3 U_{j3} \\ (A_1 U_{j1}) U_{j1x} + (A_2 U_{j2}) U_{j2x} &= (A_3 U_{j3}) U_{j3x} \\ (A_1 U_{j1}) U_{j1y} + (A_2 U_{j2}) U_{j2y} &= (A_3 U_{j3}) U_{j3y} \\ (A_1 U_{j1}) U_{j1z} + (A_2 U_{j2}) U_{j2z} &= (A_3 U_{j3}) U_{j3z} \end{aligned} \quad (38)$$

where

$A_1, A_2, A_3$  = area of JET1, JET2 and resulting merged jet, respectively  
 $U_{j1}, U_{j2}, U_{j3}$  = jet velocity of JET1, JET2 and resulting merged jet, respectively.

Initial conditions for the coalesced jet, in the local coordinate system centered at the point of intersection of the two jets (taken to be an average of the coordinates of the centerlines of JET1 and JET2 at intersection), are now

$$Z^* = 0., X^* = 0., U_j^* = 1., d^* = 1. \text{ and } dX^*/dZ^* = U_{j3x}'/U_{j3z}'$$

with the velocity ratio being given by  $U_\infty/U_{j0} = U_\infty/U_{j3}$ .

Subscripts  $x'$  and  $z'$  denote components in this local coordinate system.

These initial conditions are employed in integrating the set of differential equations for  $U_j^*, d^*$  and  $X^*$ .

The cross-sectional area of this coalesced jet is not taken to be circular as is normally specified for an exhausting jet at  $Z^* = 0$ . Experimental observations and correlation with test data were instrumental in establishing the geometrical features of the



initial cross section of the coalesced jet for different jet configurations. Details of the initial geometry of the merged jet will be discussed in the following subsection.

The velocity field induced by a two-jet configuration can now be determined by replacing each jet (including the coalesced jet) by its representative singularity distribution. The induced velocity components due to each singularity distribution are additive at every control point.

#### b. Determination of Empirical Parameters

Analysis to substantiate the assumptions made for the two-jet computations and to establish quantitatively the empirical relationships for the computational procedure described above was based on the experimental data from Reference 3.

##### (1) Effective Dynamic Pressure for Downstream Jets

The blockage effect of the leading jet in a two-jet configuration may be determined from the test data. The centerline of a single jet exhausting into a crossflow at a velocity ratio  $U_\infty/U_{j0} = .125$  together with test data from References 5 and 12 are shown in Figure 21. The data from the three tests are seen to be in close agreement. This is significant since all three tests were carried out using different values for the jet-exit dynamic pressure.

Data for the two-jet configurations, aligned in the crossflow direction, are plotted in Figures 22, 23 and 24 for the three different spacings between the jets. These data, together with the single jet data, may be used to derive "effective velocity ratios" for the downstream jets, making use of a similarity relationship derived in Reference 15. It was determined in Reference 15 that centerlines of single jets with different velocity ratios are similar and that for a given displacement in the crossflow direction,  $\Delta x/d_0$ , the penetration into the crossflow normal to the jet exit is inversely proportional to the velocity ratio ( $U_\infty/U_{j0}$ ). By applying this similarity relationship to a number of displacements,  $\Delta x/d_0$ , of the downstream jet, it is shown in Figure 25 that the centerline of the downstream jet in a two-jet configuration is the same as the centerline of a single jet exhausting into a crossflow of reduced dynamic pressure.

The information in Figure 25 has been used to obtain an empirical relationship for the dynamic pressure  $q_e$  which the downstream jet "sees," as the result of

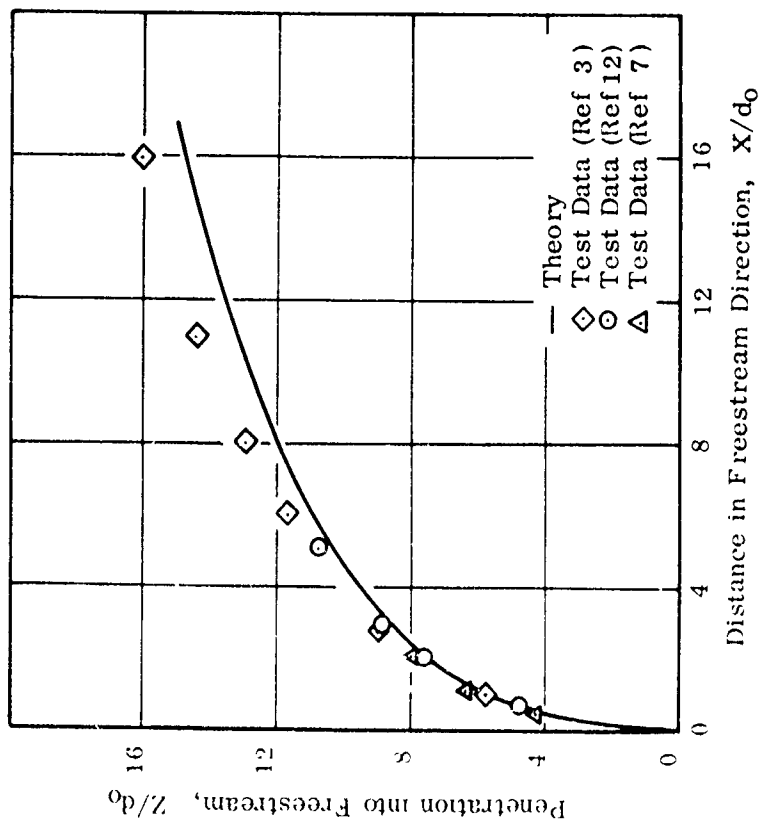


FIGURE 21. CENTERLINE FOR A SINGLE JET  
( $U_\infty/U_{j0} = .125$ )

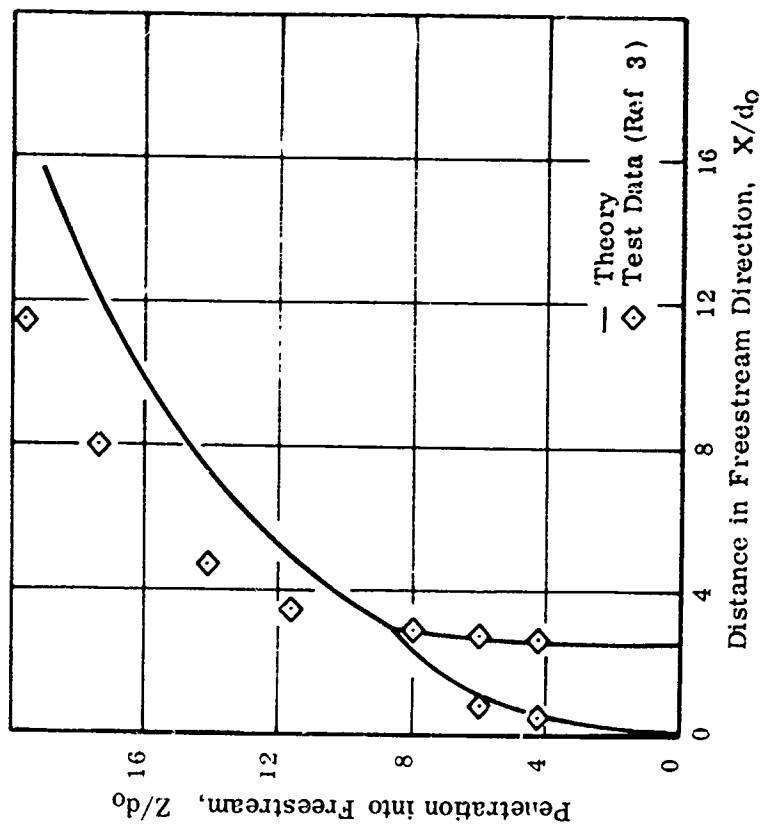


FIGURE 22. CENTERLINES FOR TWO JETS  
AT A SPACING OF 2.5 DIAMETERS  
( $U_\infty/U_{j0} = .125$ )

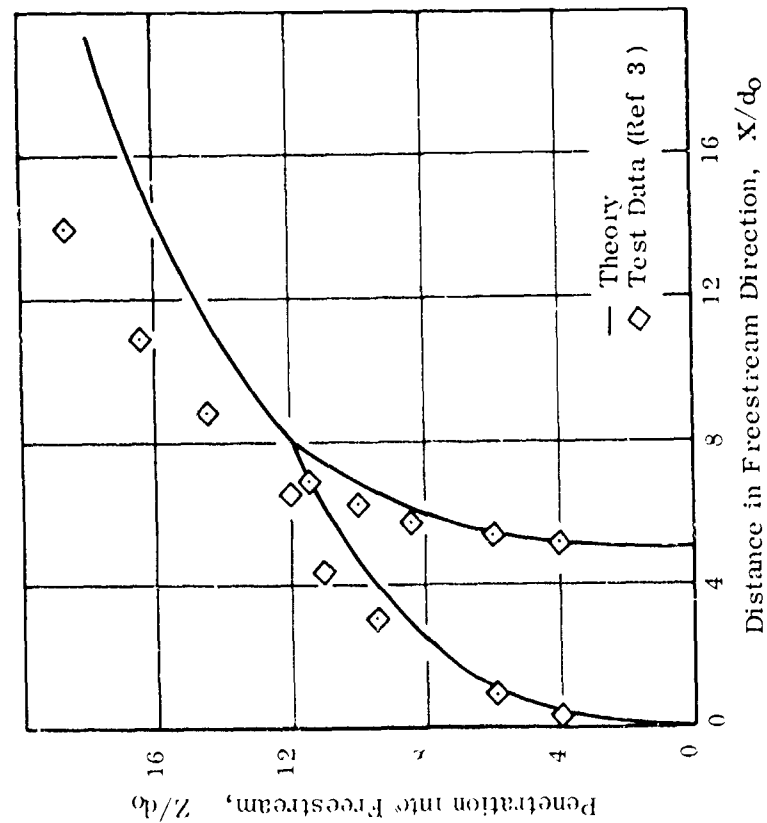


FIGURE 23. CENTERLINES FOR TWO JETS  
AT A SPACING OF 5 DIAMETERS  
( $U_\infty/U_{j0} = .125$ )

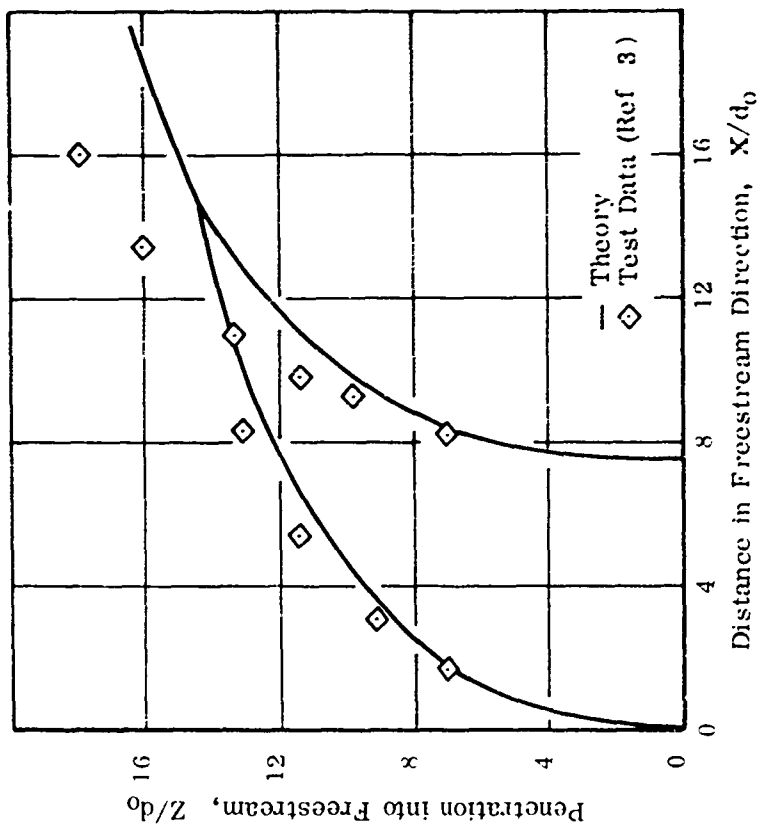


FIGURE 24. CENTERLINES FOR TWO JETS  
AT A SPACING OF 7.5 DIAMETERS  
( $U_\infty/U_{jc} = .125$ )

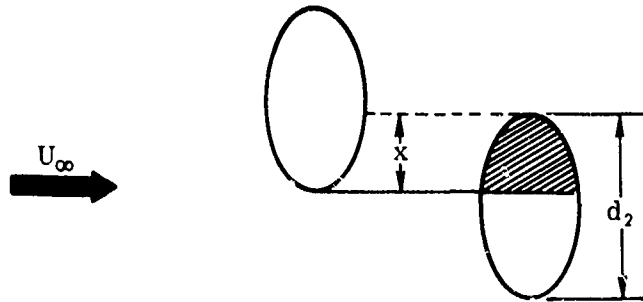
crossflow blockage by the upstream jet, in terms of the crossflow dynamic pressure,  $q_\infty$ , and spacing between the two jets,  $s$ . It is given by

$$\sqrt{\frac{q_e}{q_\infty}} = \frac{s/d_o - 1}{s/d_o + .75} \quad \left\{ s/d_o > 1 \right\} \quad (39)$$

The expression for  $[\alpha_e/\alpha_\infty]^{1/2}$  given in Equation (39) is now used as a limiting value when the two jets are aligned in the crossflow direction, when complete overlap between the two jets exists.

The above expression has been derived from test data for which the Reynolds number, based on freestream velocity and jet exit diameter, was approximately  $2 \times 10^3$ . Comparison with jet trajectories from References 7 and 12, in Figure 21, indicates that there is no measurable change in jet trajectory in the Reynolds number range  $10^3 \leq Re \leq 2 \times 10^3$ . However, it is possible that a large change in Reynolds number could affect the jet path and consequently influence the formulation for effective dynamic pressure given in Equation (39).

When the two jets are not aligned in the crossflow direction, an effective cross-flow dynamic pressure,  $q_\beta$ , which is a weighted mean of  $q_e$  and  $q_\infty$ , is utilized. The weighting of the dynamic pressure is determined from the degree of overlap between the upstream jet and the downstream jet (see sketch below)



Thus

$$\sqrt{q_\beta} = \frac{x \sqrt{q_e} + (d_2 - x) \sqrt{q_\infty}}{d_2} \quad (40)$$

## (2) Jet Decay Characteristics

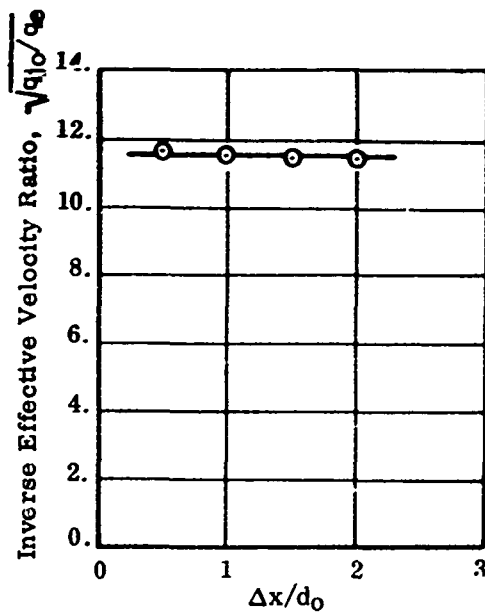
The decay characteristics of the single jet and the three two-jet configurations are shown in Figures 26 through 29. The information, obtained by analyzing the data of Reference 3, is presented in terms of the jet dynamic pressure rather than the impact pressure which has customarily been used. The reason for this is that the decay of jet momentum is due to entrainment of ambient or crossflow fluid. Thus, for jets of differing pressure ratios, the jet momentum flow parameter should be invariant rather than the impact pressure parameter. This observation is supported by the data presented in Reference 16.

Figure 26 illustrates that, in the presence of a crossflow, a jet decays at a greater rate than when it exhausts into a quiescent environment. Figures 27, 28 and 29 show the dynamic pressure decay for the two-jet configurations at three different jet spacings. The dynamic pressure has been obtained from the impact pressure by assuming that the static pressure throughout the jet is constant and equal to ambient pressure. Small variations in static pressure are expected but they should not affect the general conclusions. The distance,  $s$ , along the jet centerline is measured from the center of the jet orifice with the downstream jet exit used as the origin for the jet resulting from the coalescence of the upstream and downstream jet.

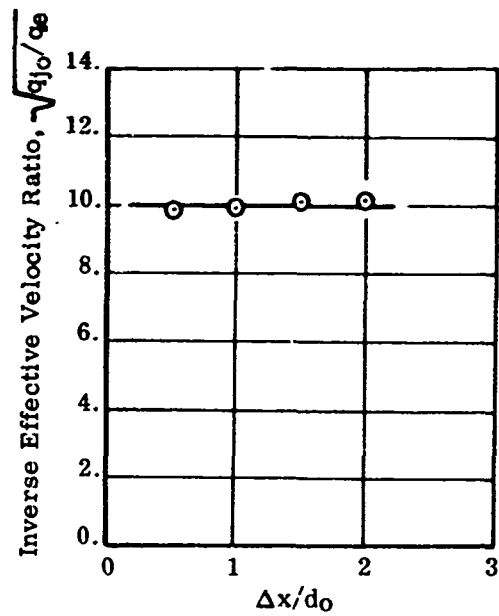
From the data in Figures 27 through 29 it is deduced that the rate at which downstream jet dynamic pressure decreases with distance along the jet centerline, increases with increased spacing between the two jets.

The decay characteristics of the upstream jet in each of the three two-jet configurations, together with data for the single jet, are shown in Figure 30. It is deduced that the decay of dynamic pressure for the leading jet in a two-jet configuration is independent of the spacing between the two jets. Since the centerline of the leading jet is also independent of the jet spacing (see Figures 22 through 24) and identical to that for the single jet, it is concluded that a leading jet in a two-jet configuration develops independently of the downstream jet.

This result, along with the finding that the downstream jet behaves as if it were exhausting into a crossflow of reduced dynamic pressure, is important in the application of the analytical model to the multiple jet problem since it permits a two-jet configuration to be treated as a combination of three discrete jets.



(a) Jet Spacing  $5 d_0$



(b) Jet Spacing  $7.5 d_0$

FIGURE 25. EFFECTIVE VELOCITY RATIOS OF DOWNSTREAM JETS IN TWO-JET CONFIGURATIONS ( $U_\infty/U_{j0} = .125$ )

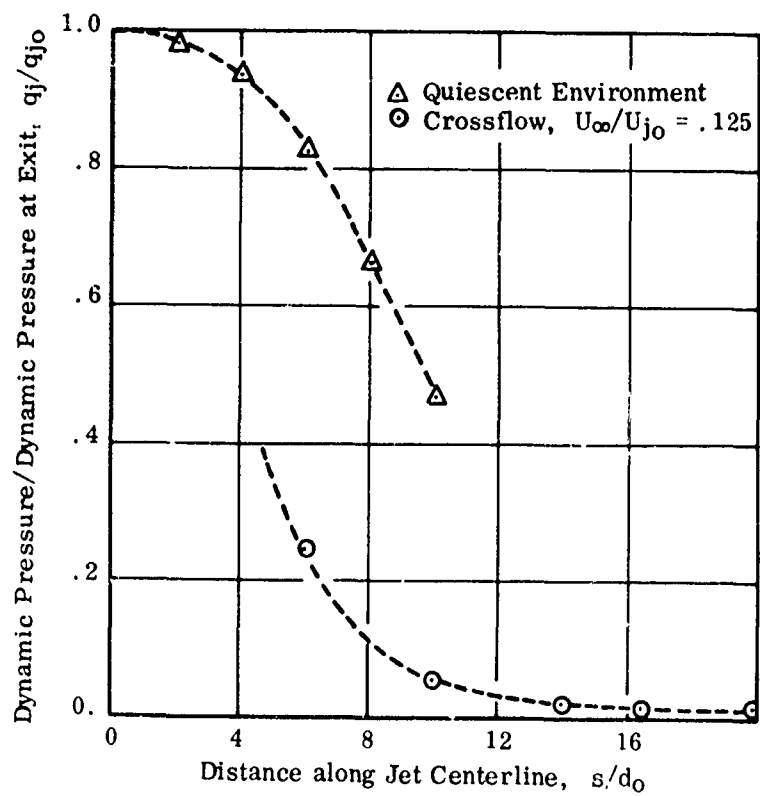


FIGURE 26. JET DYNAMIC PRESSURE DECAY FOR A SINGLE JET

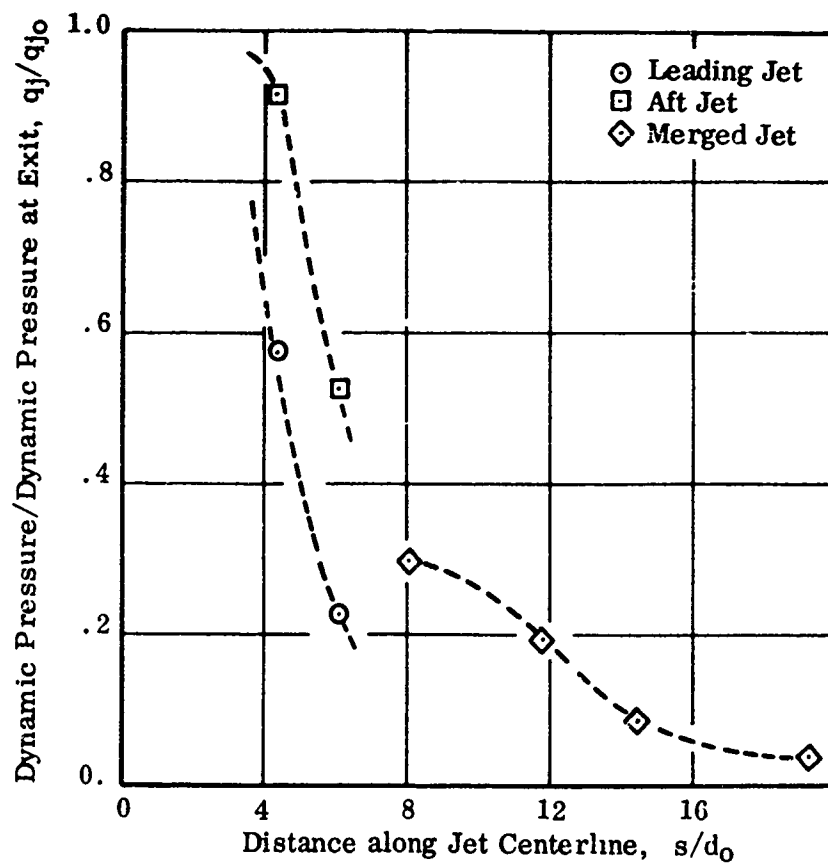


FIGURE 27. JET DYNAMIC PRESSURE DECAY FOR TWO JETS  
AT A SPACING OF 2.5 DIAMETERS  
( $U_\infty/U_{j0} = .125$ )

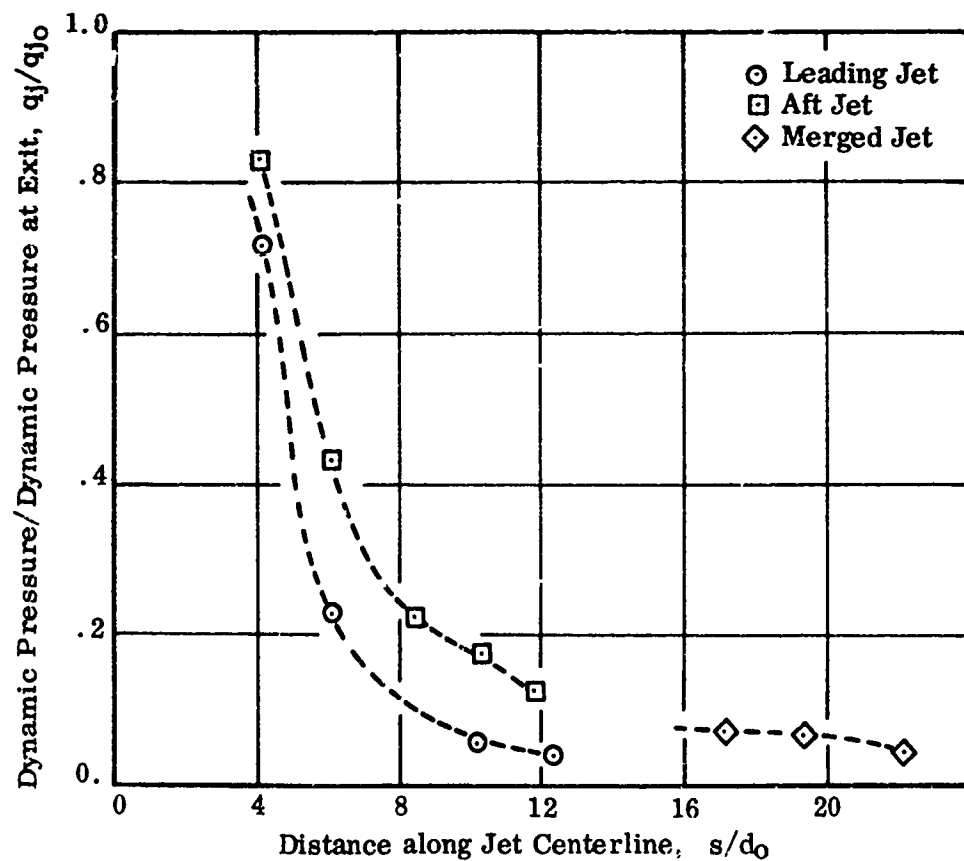


FIGURE 28. JET DYNAMIC PRESSURE DECAY FOR TWO JETS  
AT A SPACING OF 5 DIAMETERS  
( $U_\infty/U_{j0} = .125$ )



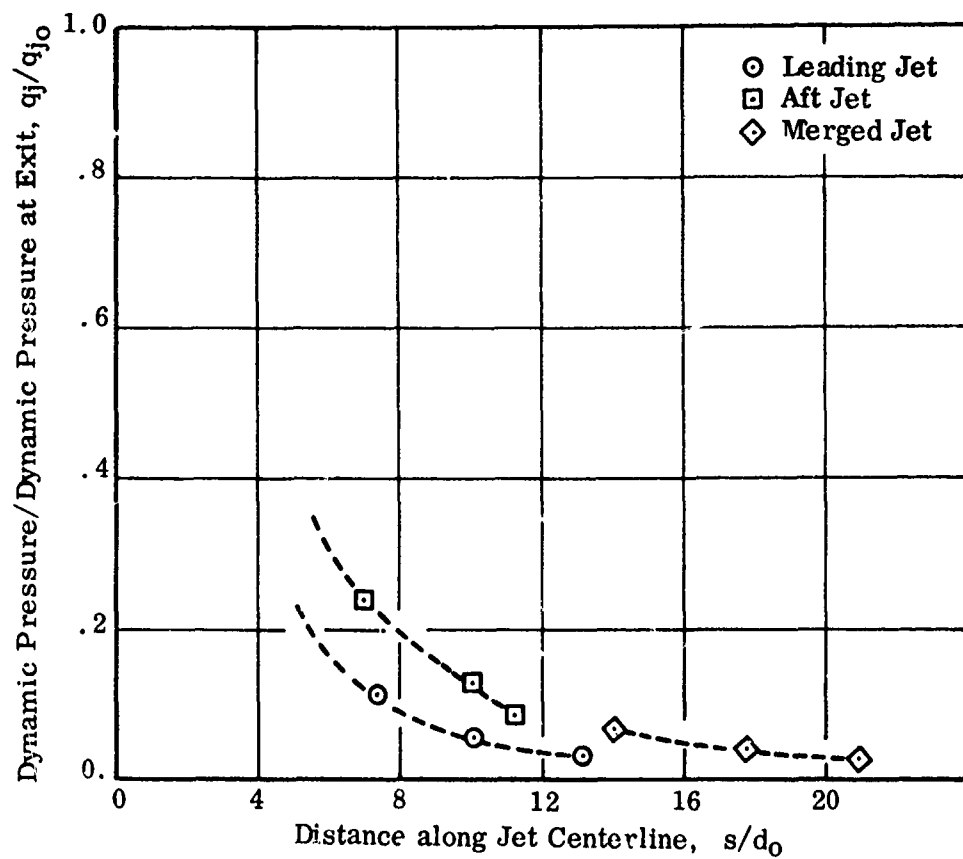


FIGURE 29. JET DYNAMIC PRESSURE DECAY FOR TWO JETS  
AT A SPACING OF 7.5 DIAMETERS  
( $U_\infty/U_{j0} = .125$ )

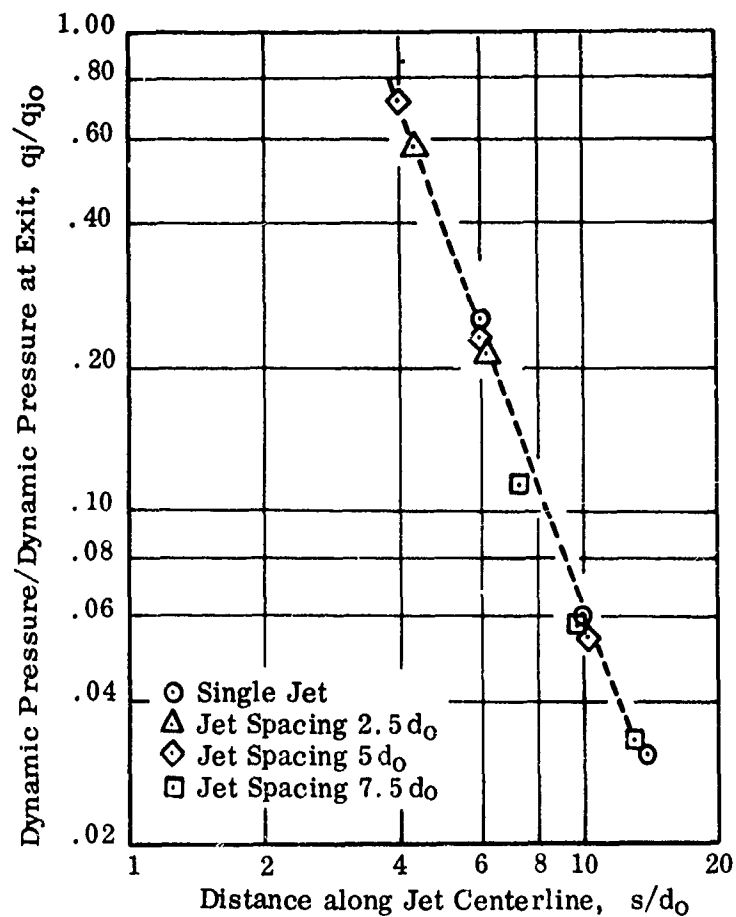


FIGURE 30. DECAY CHARACTERISTICS OF LEADING JETS  
IN TWO-JET CONFIGURATIONS  
( $U_\infty/U_{j0} = .125$ )

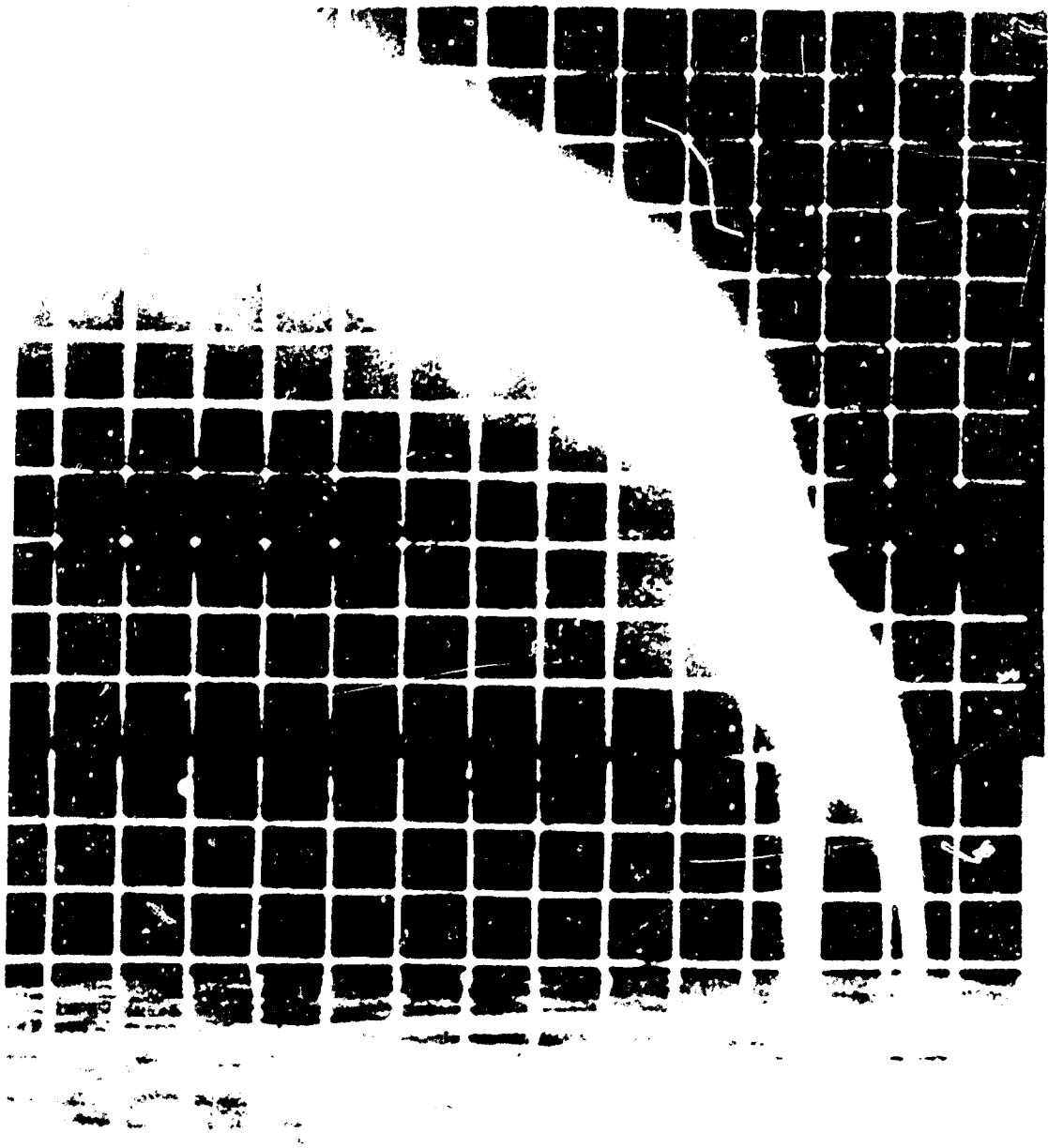


FIGURE 31. WATER VAPOR VISUALIZATION FOR TWO JETS  
AT A SPACING OF 2.5 DIAMETERS ( $U_{\infty}/U_{j0} = .125$ )

Best Available Copy

### (3) Geometry of Merged Jet

Test observations seemed to indicate that the downstream jet, being the stronger jet at the point of intersection, due to shielding by the upstream jet is the dominant jet.

This feature of the two-jet interaction is readily discernible in Figure 31. The dominant influence of the downstream jet on the characteristics of the coalesced jet results in the high degree of penetration exhibited by the coalesced jet. This same feature may be noted in Figures 22 through 24. As a result of these observations, geometrical features of the initial cross section of the coalesced jet are treated as a function of the jet orientation angle,  $\Omega$ . The jet orientation angle is defined as the enclosed angle between the freestream vector and the line joining the centers of the two jet exits.

For the jet spacings of the experimental investigation, it appears that best correlation between theory and test data is obtained by employing an initial circular cross section for the coalesced jet for jet orientation angles up to 20 degrees. For a jet orientation angle  $\Omega = 90^\circ$  (the jet configuration shown in Figure 36) the geometry of the jet cross section of the coalesced jet is initially represented by an ellipse, with a minor to major axis ratio of 1/2.

At this time the functional relationship of the coalesced jet cross section with orientation angle has not been established for the range  $20^\circ < \Omega < 90^\circ$ . It should also be noted that, while the above discussion is limited to jet configurations with a maximum spacing of 7.5 jet diameters, the importance of establishing a relationship between orientation angle and coalesced jet cross section decreases for large jet spacings, since the effect of the merged jet on induced pressures in the plane of the jet exit diminishes.

#### 4. COMPARISON OF TWO JET CALCULATIONS WITH TEST DATA

Computations for a range of two-jet configurations were effected. Comparisons between theory and test data from Reference 3 are presented in Figures 32 through 42.

Comparisons between predicted and experimentally determined pressure distributions in the plane of the jet exits around two-jet configurations with spacings of 2.5, 5 and 7.5 jet diameters are shown in Figures 32 through 34. In the computations shown in Figures 32 through 34, "effective velocity ratios" of .058, .087 and .098 were utilized for the downstream jets at the respective spacings of  $2.5 d_0$ ,  $5 d_0$  and  $7.5 d_0$ . These are based on an actual velocity ratio of .125 and the relationship between crossflow dynamic pressure,  $q_\infty$ , and the reduced dynamic pressure experienced by the downstream jet as given by Equation (39). For the spacing of 2.5 diameters it may be noted that the pressure distribution is similar to that induced by a single jet exhausting into a crossflow, although the regions of negative pressure are more extensive. As the jet spacing increases, the downstream jet is seen to have its own, discrete effect on the pressure distribution. Isobars of  $C_p = -.3$  are noted around the leading jet and the downstream jet in Figure 33; and in Figure 34, which shows the larger jet spacing, isobars of  $C_p = -.2$ ,  $-.3$ , are noted around each jet.

Generally good agreement between theory and test data is discernible for all three jet configurations. It should be pointed out that relatively small differences in measured pressure coefficients at stations of constant  $Y/d_0$ , when the variation with  $X/d_0$  is small (i.e., when the curve is very flat) can lead to what appear to be much larger discrepancies in the position of the isobars shown in the figures.

Theory and test data for the centerlines of the three two-jet configurations above are shown in Figures 22 through 24. Generally, the prediction for the centerline of the coalesced jet does not achieve the degree of penetration exhibited by the experimental data.

Figure 35 shows a sketch of a two-jet configuration, indicating the location of pressure taps, and defines the sideslip angle  $\beta$ . The variation of induced pressure with angle of sideslip for this configuration is shown in Figures 37 through 39.

Figure 37 shows comparison between theory and experimental data for induced pressure variation with  $X/d_0$  at  $Y/d_0 = 1.5$  and  $3.0$  for zero sideslip. Figure 38 shows the same comparison for a sideslip angle  $\beta = 20^\circ$ . The effects of positive sideslip are seen to be an increase in the magnitudes of the induced pressures in the region

ahead of the leading jet exit and a decrease in the region immediately behind it.

Figure 39 displays the effects of a sideslip angle  $\beta = -20^\circ$  on the above pressure distributions. Negative sideslip is seen to reverse the two effects discussed. It results in a decrease in the magnitudes of induced pressures in the region ahead of the leading jet exit and an increase in the region immediately behind it. These trends in the test data are also evident in the computed results. For both positive and negative sideslip, the downstream jet is discernible as a more discrete influence on the pressure distribution when compared to the zero sideslip configuration. This feature of the induced pressure distribution is predicted quite well by theory.

The correlation between theory and test data in Figures 37 through 39 and the effects of positive and negative sideslip are representative of results obtained for a two-jet configuration with a jet spacing of 7.5 diameters also. Figures 40 and 41 show the pressure variation with  $X/d_o$  at zero sideslip and at  $\beta = 20^\circ$  for a two-jet configuration with a spacing of 2.5 diameters. The correlation between theory and test data is seen to be very good for the zero sideslip condition of Figure 40. Noticeable differences between theory and test data exist for the  $\beta = 20^\circ$  case of Figure 41.

At zero sideslip,  $[q_c/q_\infty]^{1/2} = .46$  for the downstream jet, as computed from Eq. (39) with  $s = 2.5 d_o$ . This means the downstream jet "sees" a low crossflow dynamic pressure and, consequently, does not exert a strong influence on the induced flow field. The assumption that the upstream jet develops independently of the downstream jet is therefore justified, despite the close jet spacing. The good agreement between theory and test data in Figure 40 supports this conclusion.

At  $\beta = 20^\circ$ ,  $[q_c/q_\infty]^{1/2} = .93$  for the downstream jet, as given by Equation (40). The jet now has a stronger influence on the induced flow field. This strong influence, together with the close jet spacing, makes the assumption that the upstream jet develops independently of the downstream jet no longer representative of the physical situation. Further mutual interference effects between the two jets must be included to improve correlation between theory and test data.

Figure 36 shows a schematic representation of a two-jet configuration with a spanwise jet spacing of 7.5 diameters. Theoretical and experimental pressure variations with  $Y/d_o$  are shown for five stations of constant  $X/d_o$  in Figure 42. As expected, correlation between computed answers and test data is better at stations ahead of the jets than at stations immediately behind the jets. The wake region of the two jets is clearly defined at station  $X/d_o = 1.5$  in Figure 42(d). Correlation again improves farther behind the two jets where the importance of wake effects tends to diminish.

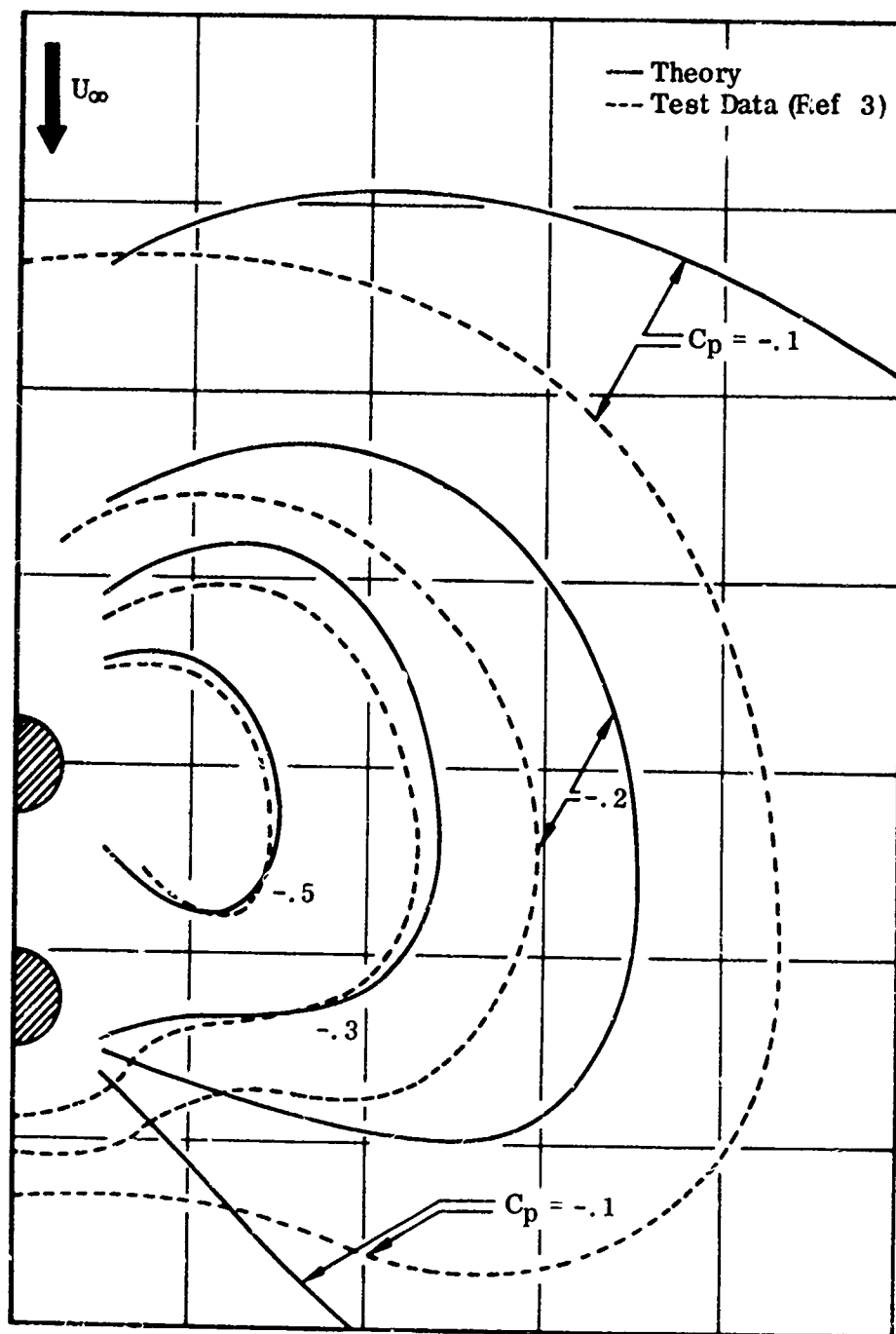


FIGURE 52. PRESSURE DISTRIBUTION AROUND TWO JETS  
 AT A SPACING OF 2.5 DIAMETERS  
 ( $U_\infty/U_{j0} = .125$ )

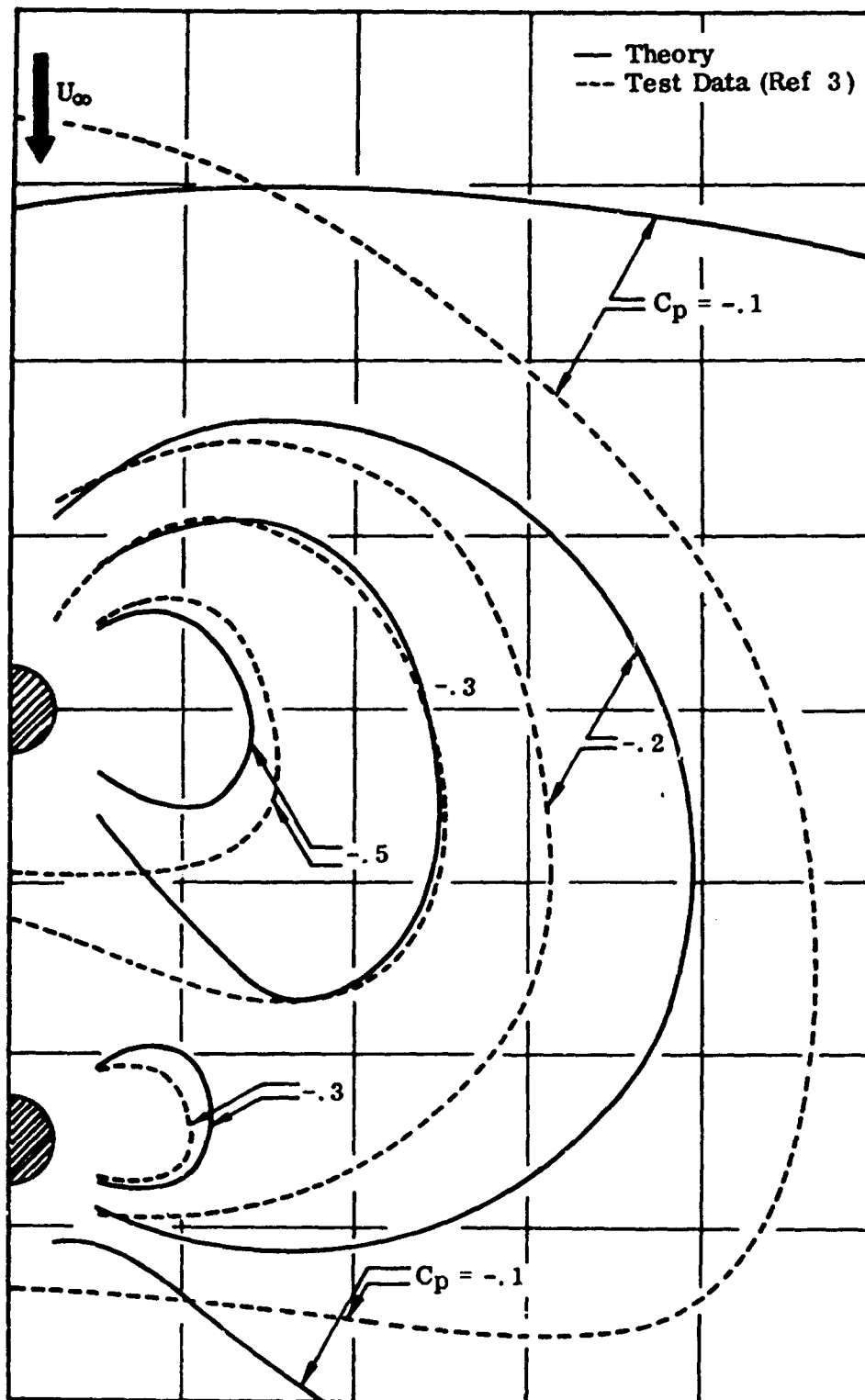


FIGURE 33. PRESSURE DISTRIBUTION AROUND TWO JETS  
AT A SPACING OF 5 DIAMETERS  
( $U_\infty/U_{j0} = .125$ )



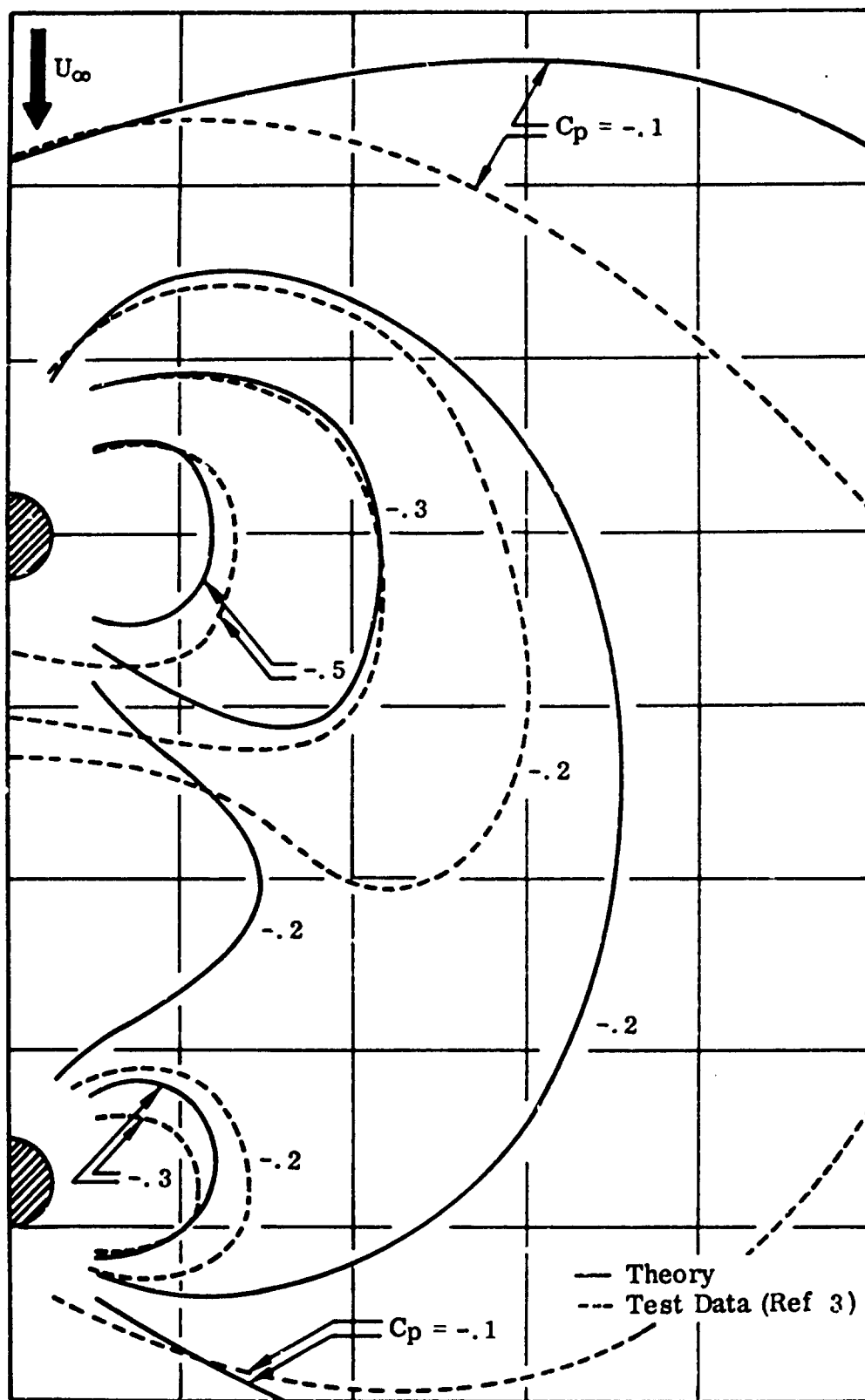


FIGURE 34. PRESSURE DISTRIBUTION AROUND TWO JETS  
AT A SPACING OF 7.5 DIAMETERS  
( $U_\infty/U_{j0} = .125$ )

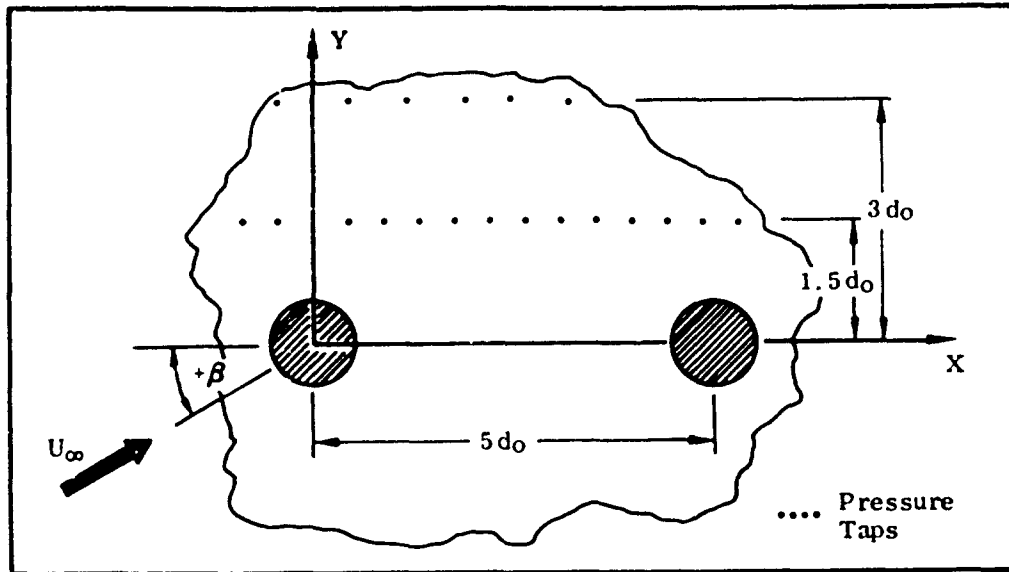


FIGURE 35. TWO-JET CONFIGURATION WITH SIDESLIP

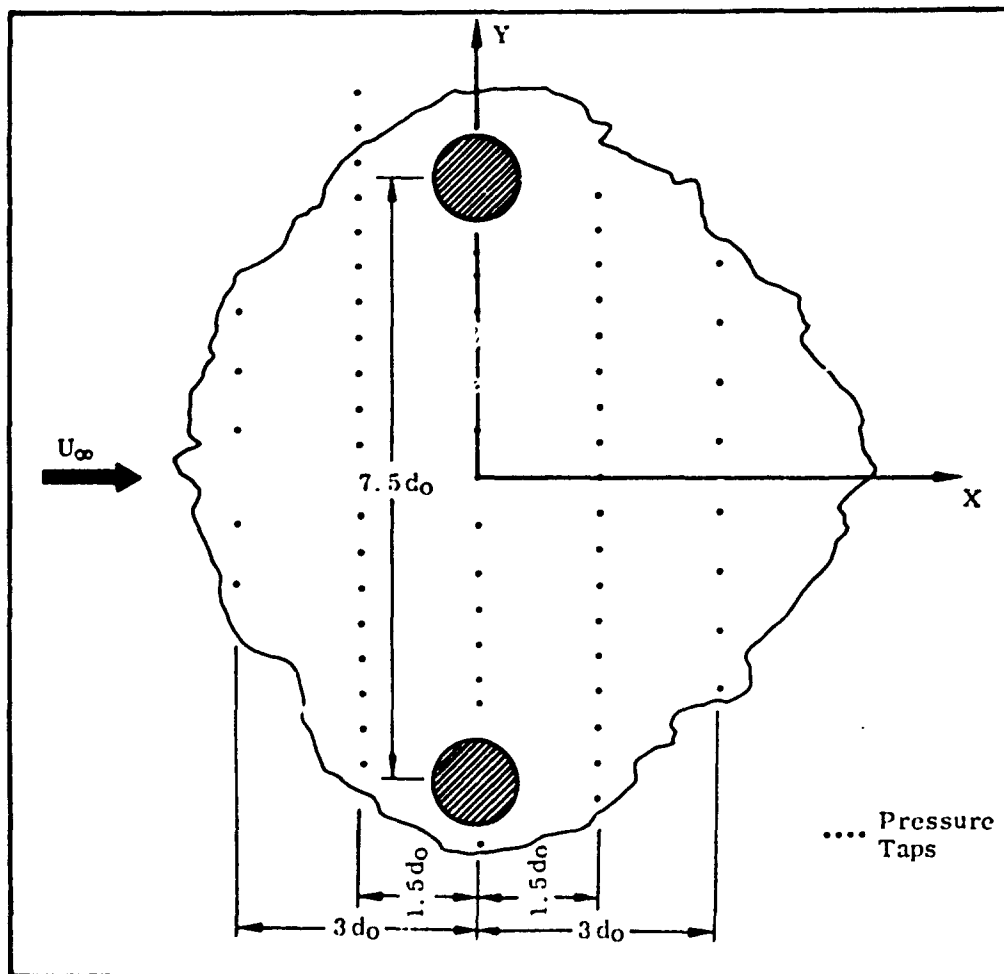
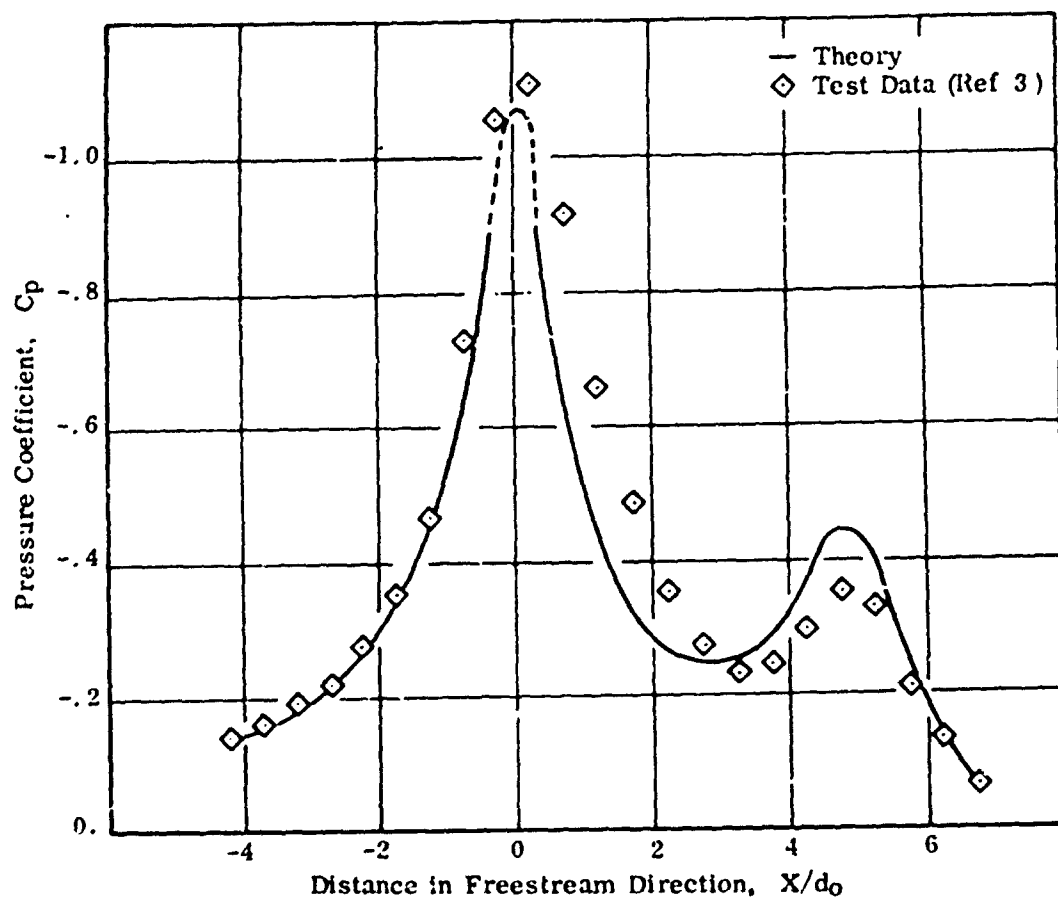
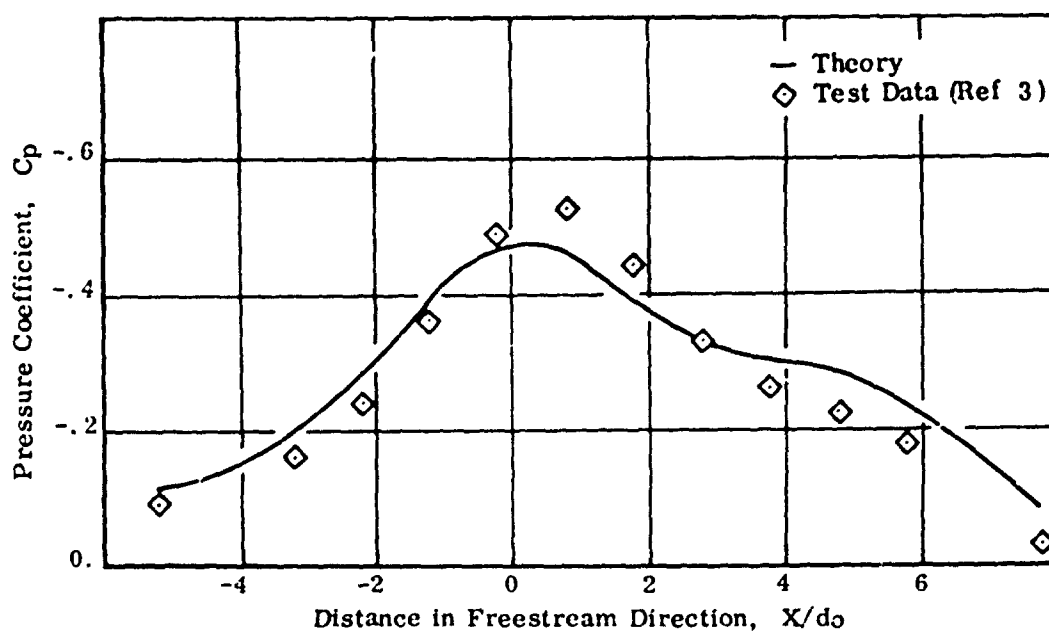


FIGURE 36. SPANWISE TWO-JET CONFIGURATION

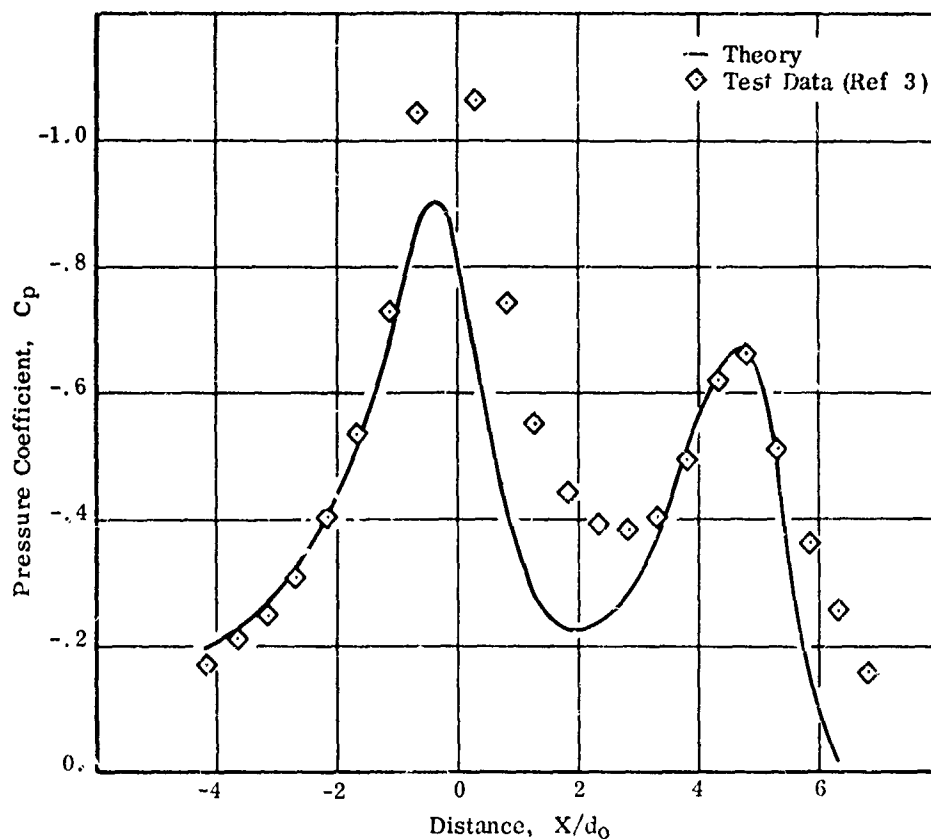


(a) Station  $Y/d_0 = 1.5$

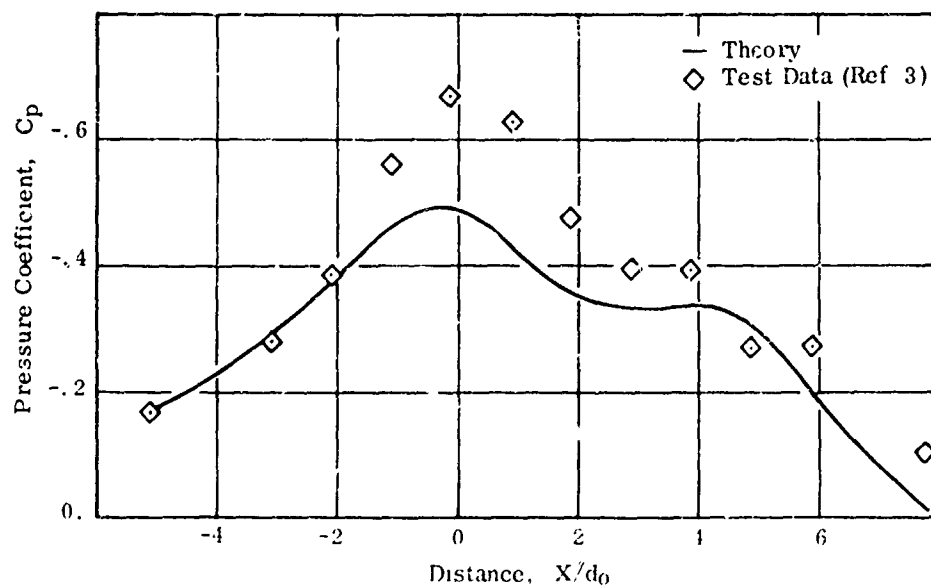


(b) Station  $Y/d_0 = 3$

FIGURE 37. INDUCED PRESSURE VARIATION FOR A TWO-JET CONFIGURATION AT ZERO SIDESLIP (Spacing =  $5 d_0$ ,  $U_\infty/U_{j0} = .125$ )

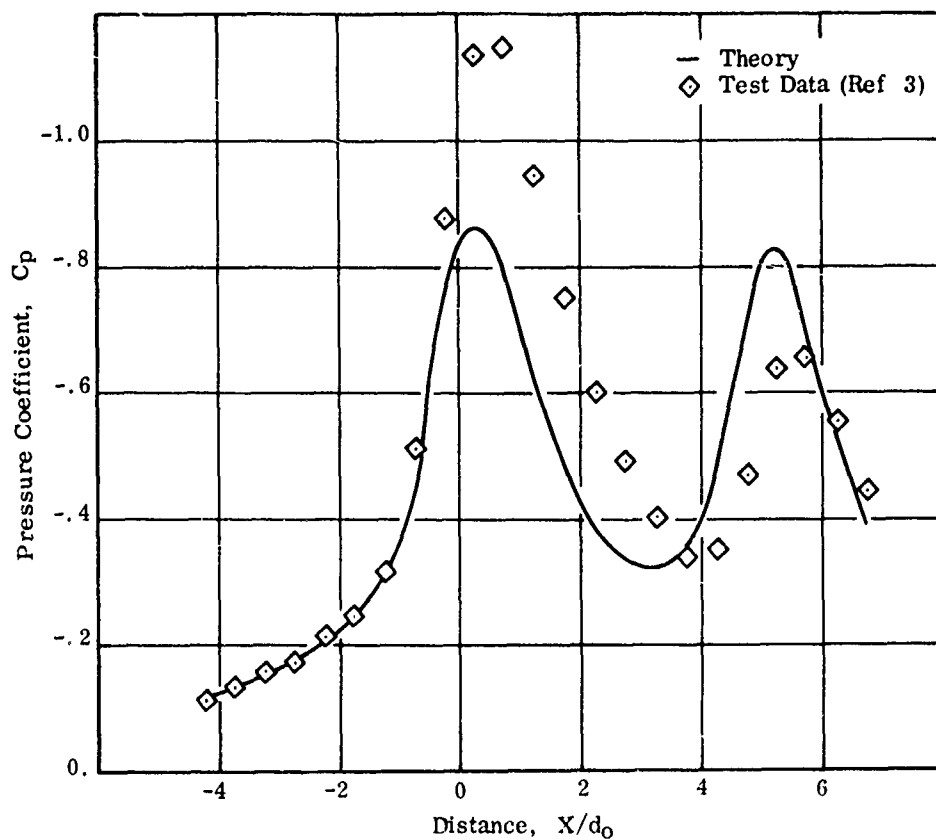


(a) Station  $Y/d_0 = 1.5$

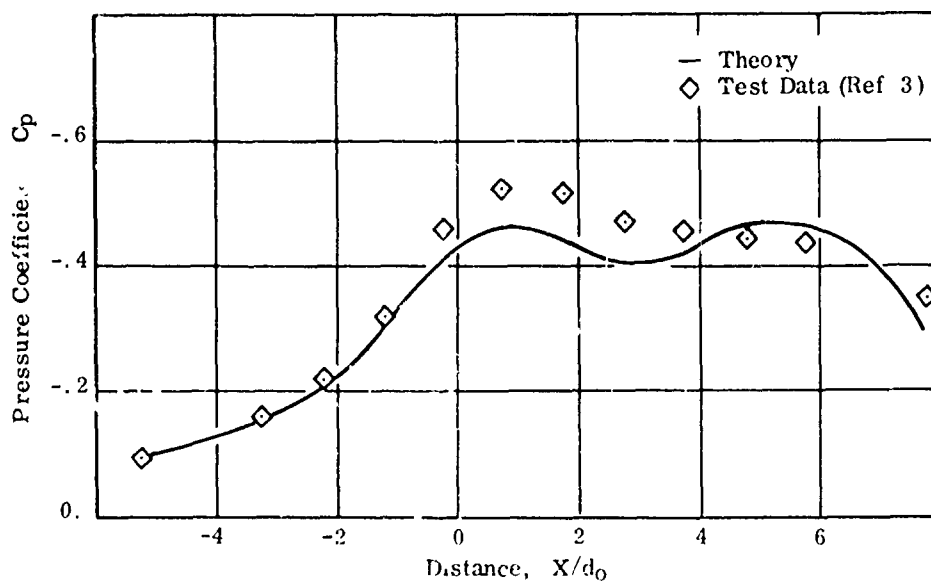


(b) Station  $Y/d_0 = 3$

FIGURE 38. INDUCED PRESSURE VARIATION FOR A TWO-JET CONFIGURATION  
 AT SIDESLIP  $\beta = 20^\circ$  (Spacing  $5d_0$ ,  $U_\infty/U'_{j0} = .125$ )

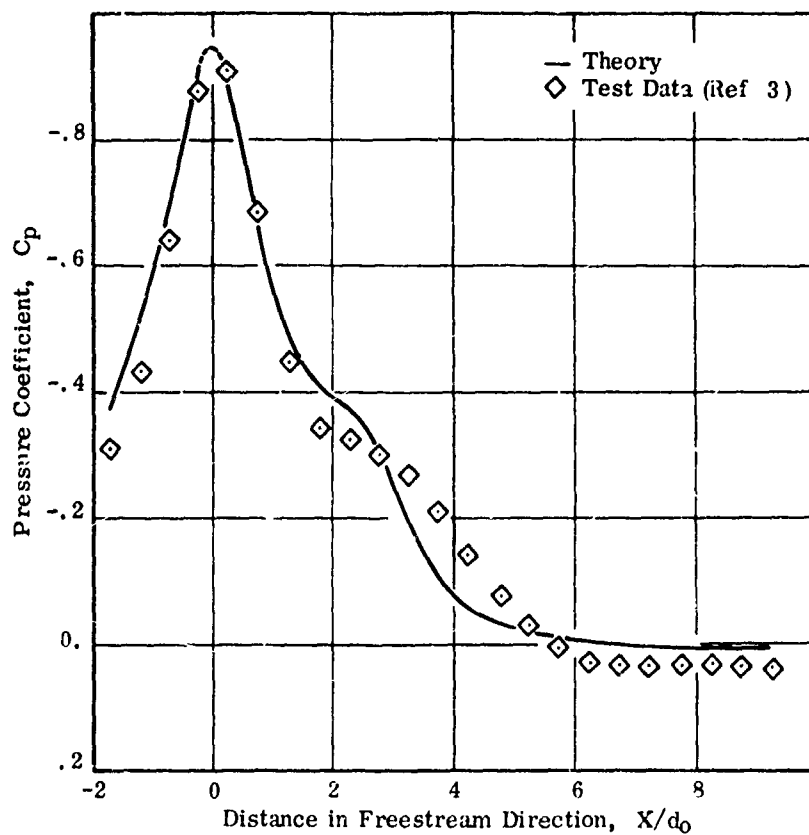


(a) Station  $Y/d_0 = 1.5$

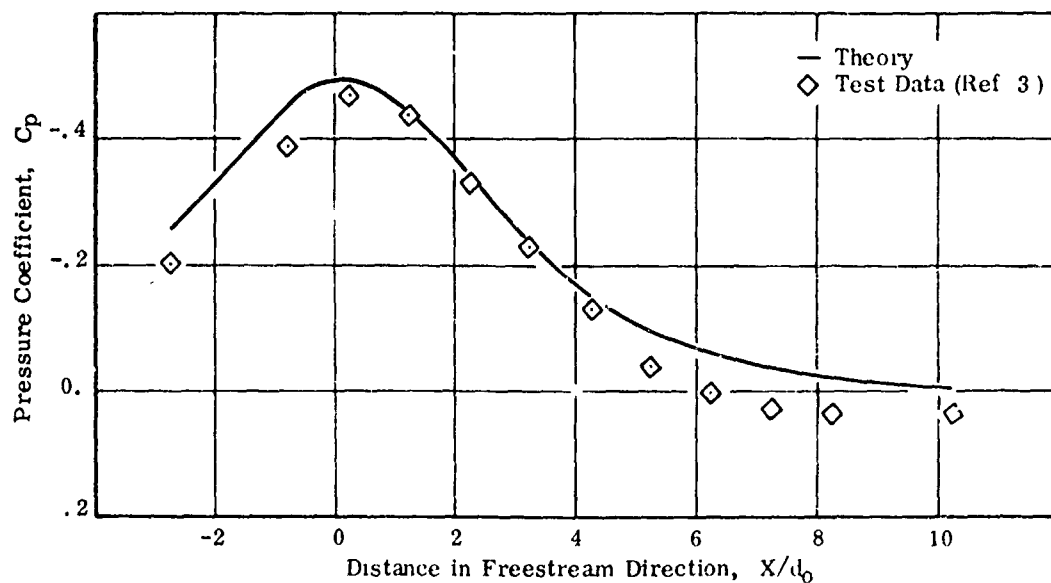


(b) Station  $Y/d_0 = 3$

FIGURE 39 INDUCED PRESSURE VARIATION FOR A TWO-JET CONFIGURATION  
 AT SIDESLIP  $\beta = -20^\circ$  (Spacing  $= 5 d_0$ ,  $U_\infty/U_{J0} = 0.125$ )

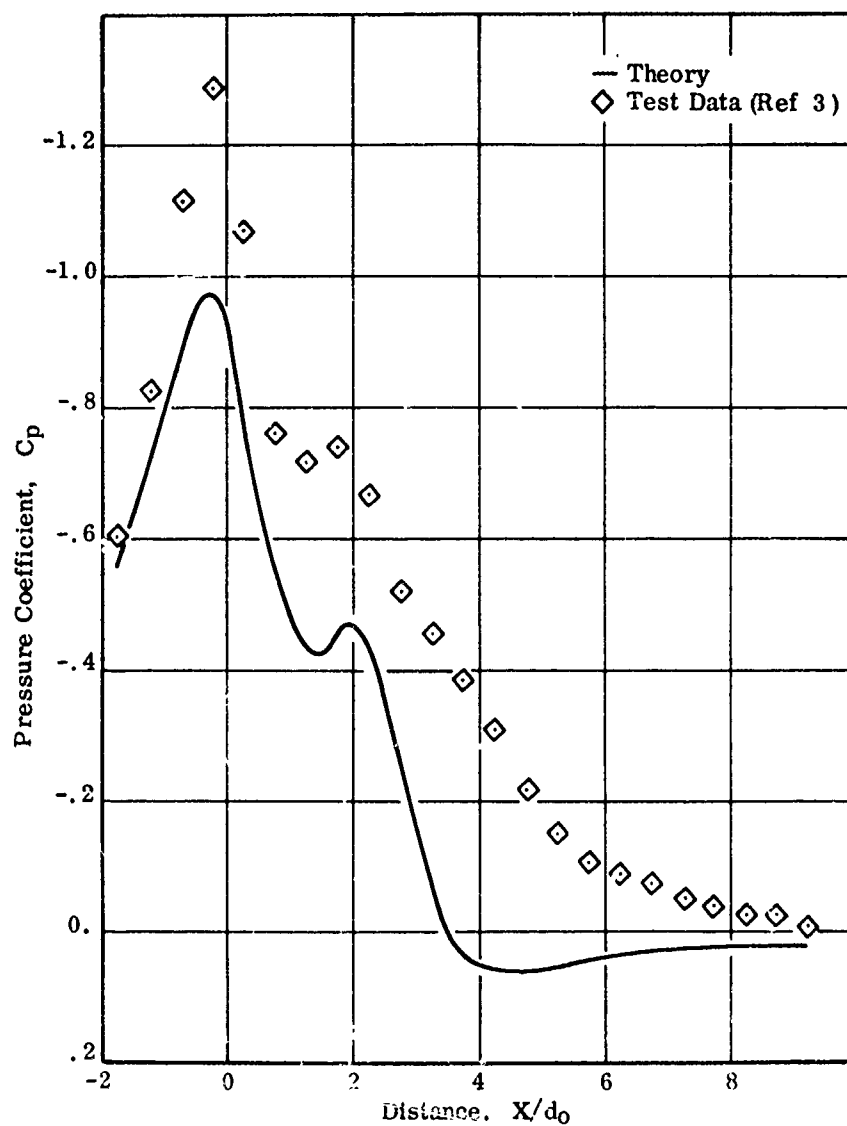


(a) Station  $Y/d_0 = 1.5$



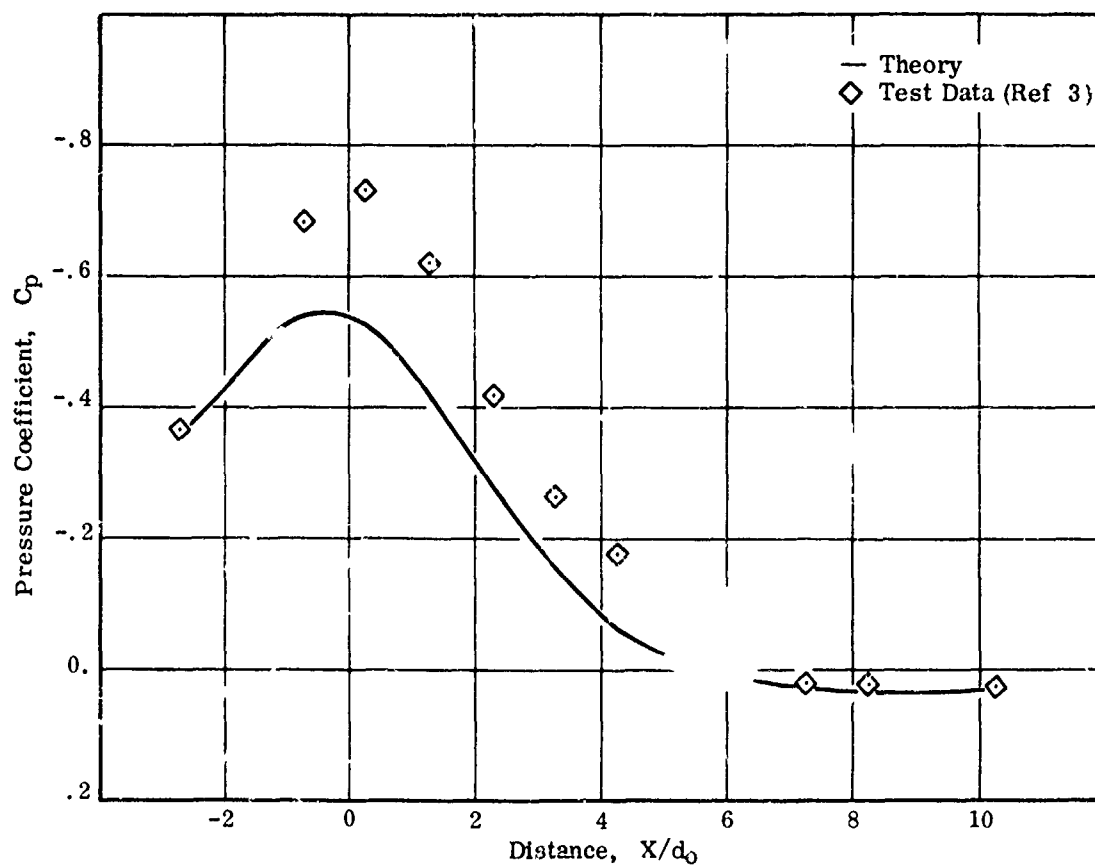
(b) Station  $Y/d_0 = 3$

FIGURE 40. INDUCED PRESSURE VARIATION FOR A TWO-JET CONFIGURATION AT ZERO SIDESLIP (Spacing =  $2.5 d_0$ ,  $U_\infty/U_{j0} = 0.125$ )



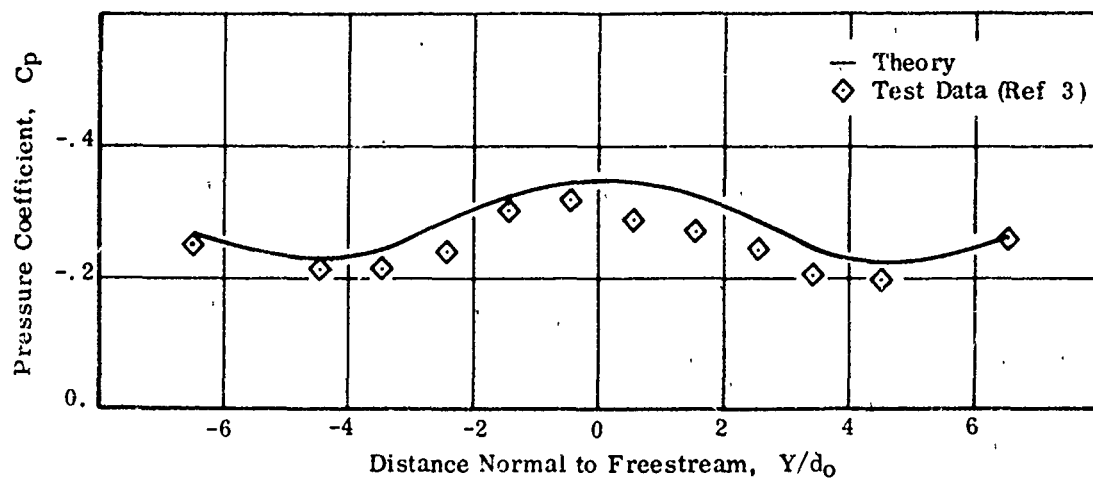
(a) Station  $Y/d_0 = 1.5$

FIGURE 41. INDUCED PRESSURE VARIATION FOR A TWO-JET CONFIGURATION  
AT SIDESLIP  $\beta = 20^\circ$  (Spacing =  $2.5 d_0$ ,  $U_\infty/U_{j0} = .125$ )

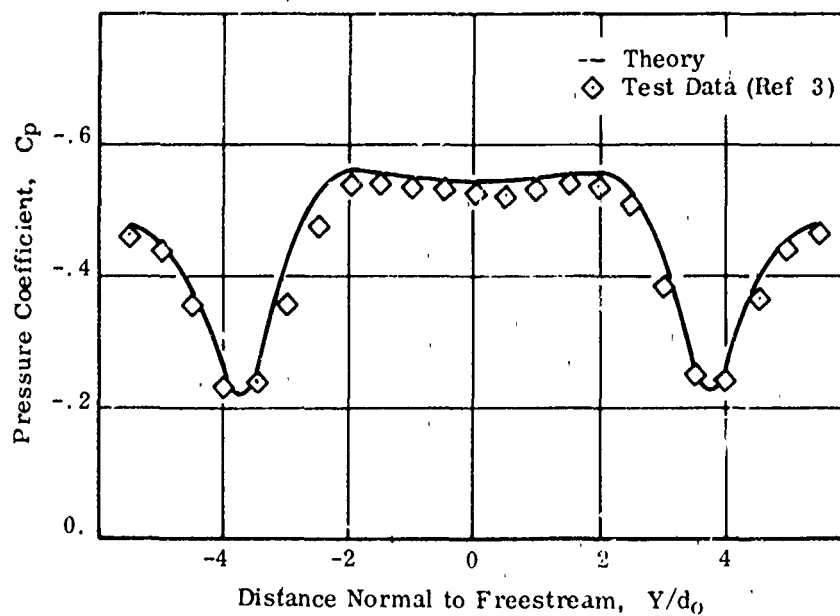


(b) Station  $Y/d_0 = 3$   
 FIGURE 41. (Concluded)



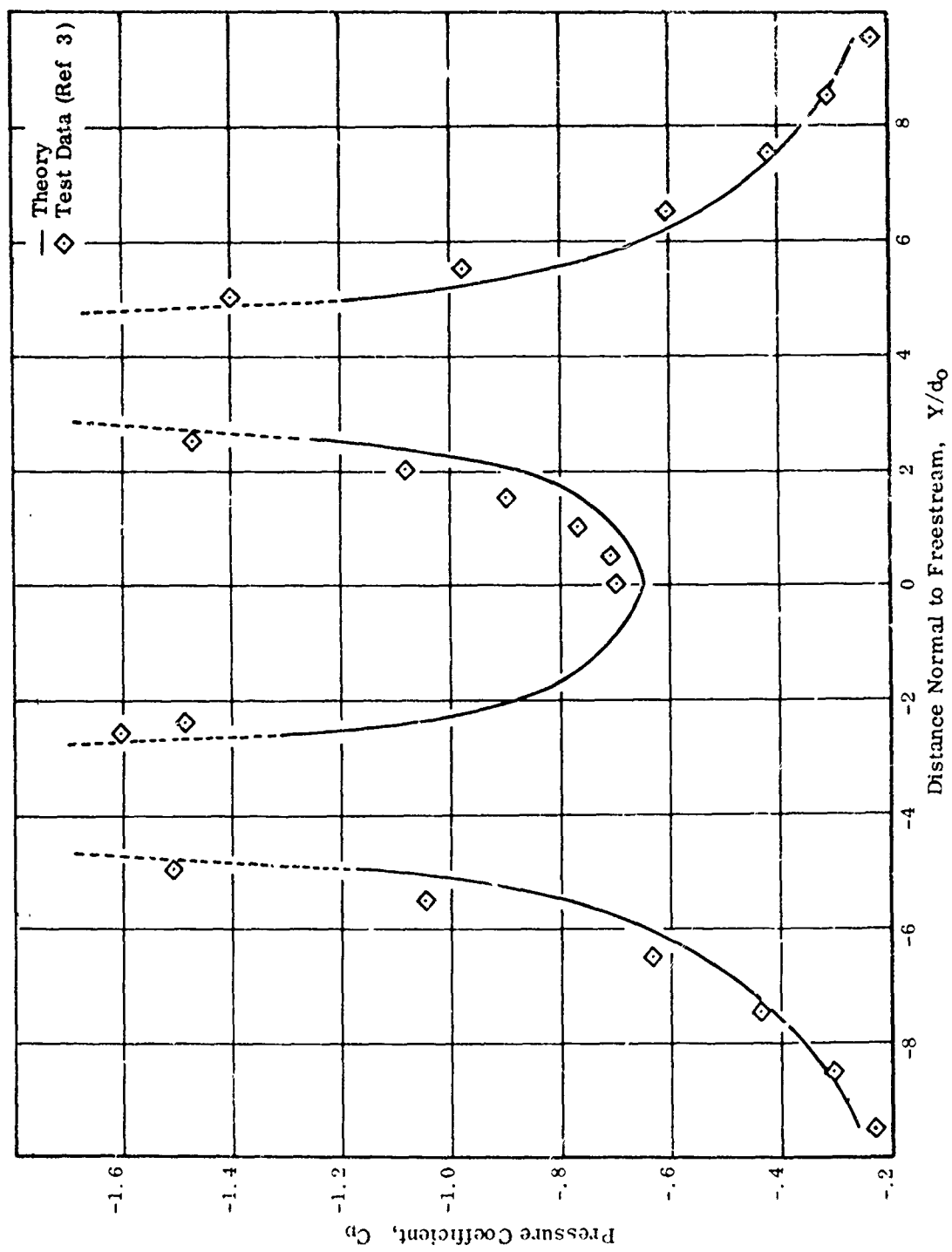


(a) Station  $X/d_0 = -3$



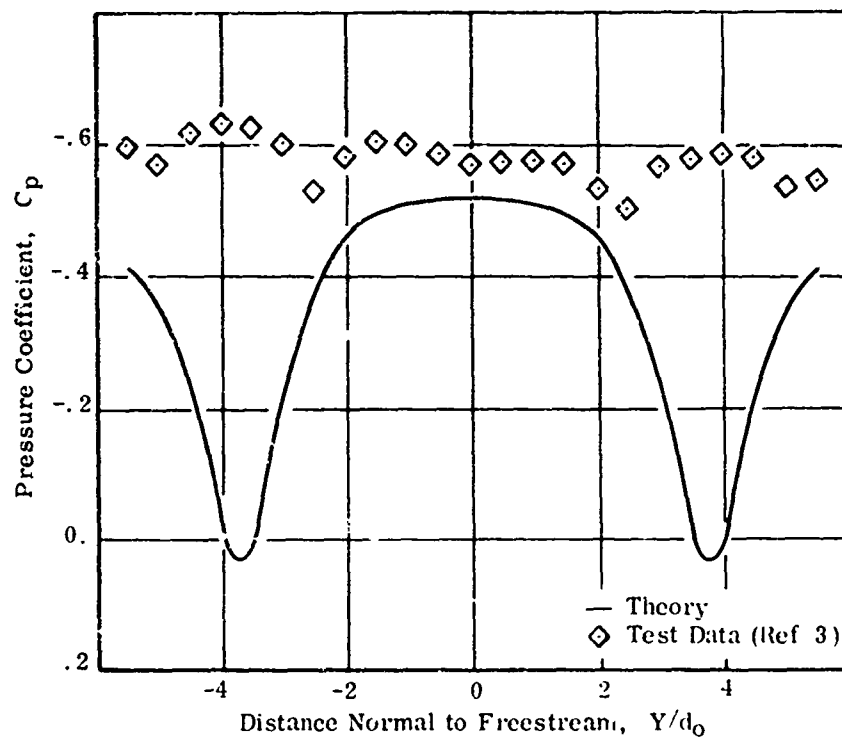
(b) Station  $X/d_0 = -1.5$

FIGURE 42. INDUCED PRESSURE VARIATION  
 FOR A SPANWISE TWO-JET CONFIGURATION  
 (Spacing =  $7.5 d_0$ ,  $U_\infty/U_{j0} = .125$ )

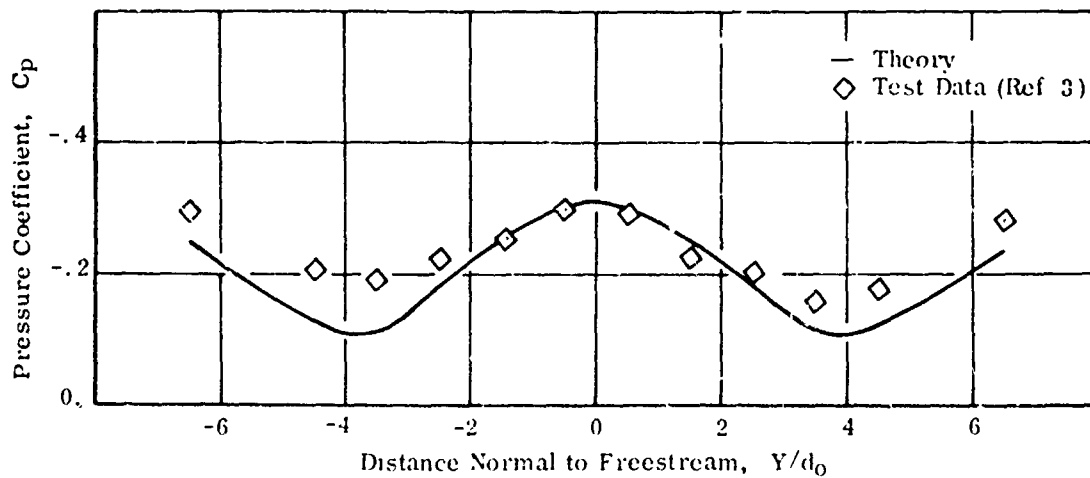


(c) Station  $X/d_0 = 0$

FIGURE 42. (Continued)



(d) Station  $X/d_0 = 1.5$



(e) Station  $X/d_0 = 3$

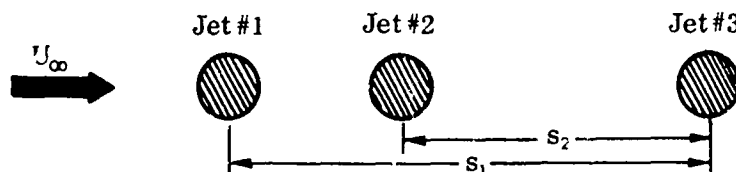
FIGURE 42. (Concluded)

## 5. APPLICATIONS TO MORE COMPLEX CONFIGURATIONS

As outlined previously, the computational procedure treats each jet in a multijet arrangement as a single jet, with shielded downstream jets exhausting into a cross-flow of reduced dynamic pressure.

This approach does not restrict jets in a multijet arrangement to have the same velocity ratios. Figure 43 shows the computed pressure distribution around a two-jet arrangement with the leading jet at a velocity ratio of .215 and the downstream jet at a velocity ratio of .150. Test data are also shown for comparison.

The extension of the computational procedure to the treatment of more complex jet configurations was effected for a three-jet arrangement. In the three-jet configuration sketched below,  $s_1$  is the distance between Jet No. 1 and Jet No. 3 and  $s_2$  is the distance between Jet No. 2 and Jet No. 3.



The effective freestream dynamic pressure into which Jet No. 2 exhausts is obtained from the relationship for the two-jet configuration given by Equation (39), where  $s$  is the spacing between Jet No. 1 and Jet No. 2 above. The crossflow dynamic pressure which Jet No. 3 "sees" is given by

$$\sqrt{\frac{q_e}{q_\infty}} = \left[ \frac{s_1/d_0 - 1}{s_1/d_0 + 1.75} \right] \left[ \frac{s_2/d_0 - 1}{s_2/d_0 + 1.75} \right] \{s_2/d_0\}^{1/2} \quad (41)$$

Equation (41) accounts for shielding by both of the leading jets on Jet No. 3. If  $s_2$  is very large, there is effectively no shielding and  $[q_e/q_\infty]^{1/2} \approx 1$ . If  $s_1$  is very large, only Jet No. 2 provides shielding, and

$$\sqrt{\frac{q_e}{q_\infty}} = \frac{s_2/d_0 - 1}{s_2/d_0 + 1.75}$$

Both jets contribute to the reduction in dynamic pressure when Jet No. 1 and Jet No. 2 are close to Jet No. 3.

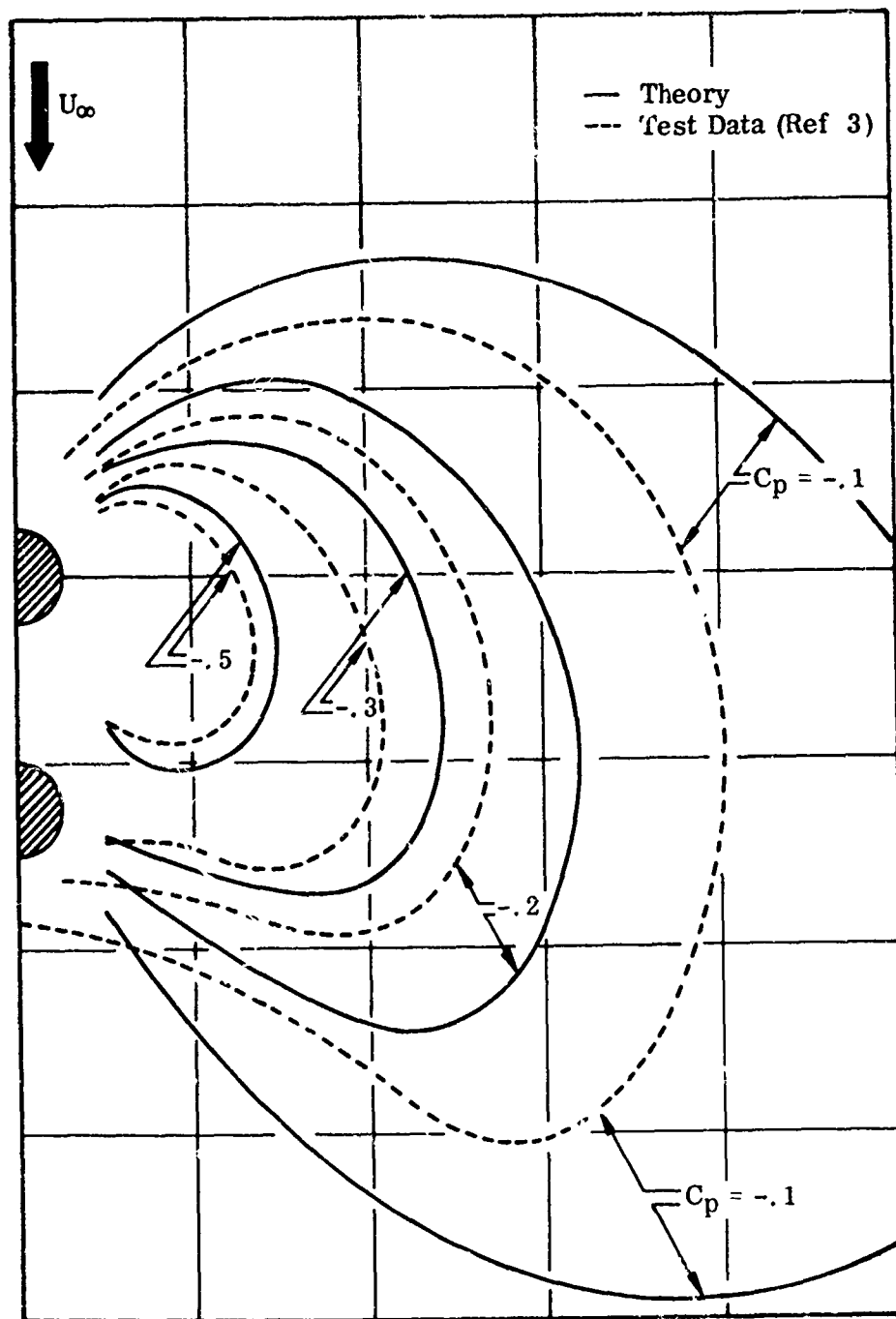


FIGURE 43. PRESSURE DISTRIBUTION AROUND TWO JETS  
 OF DIFFERENT THRUST LEVELS  
 (Upstream Jet,  $U_{\infty}/U_{j0} = .215$ )  
 (Downstream Jet,  $U_{\infty}/U_{j0} = .150$ )

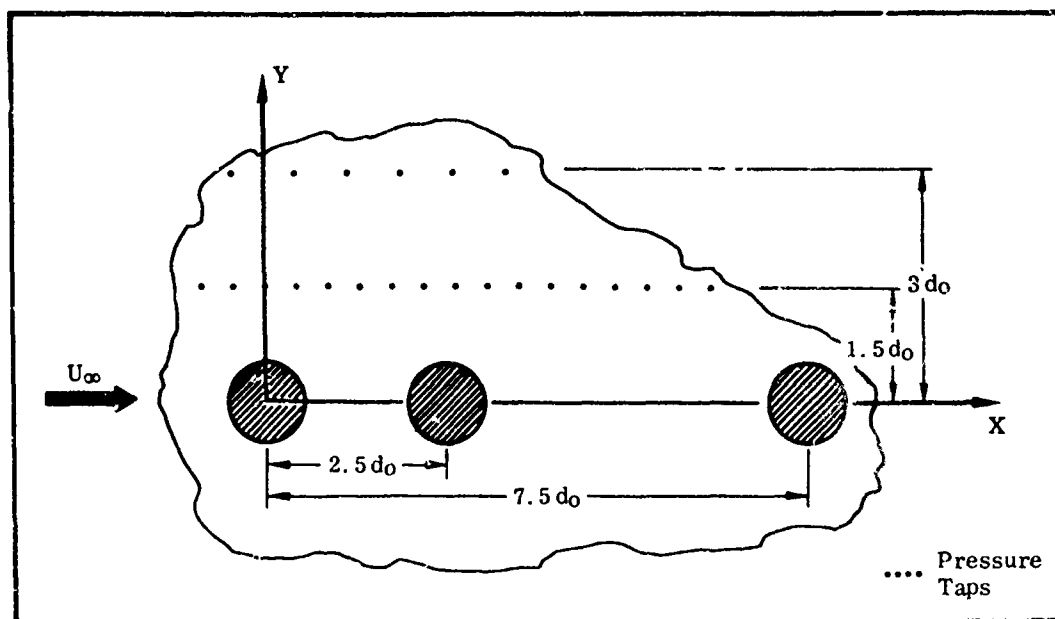


FIGURE 44. THREE-JET CONFIGURATION

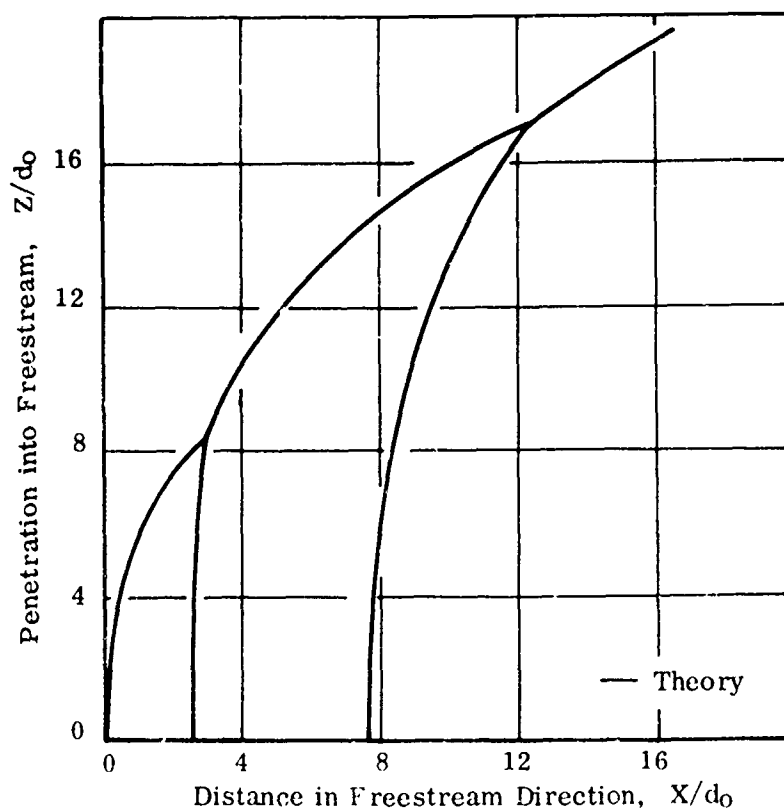
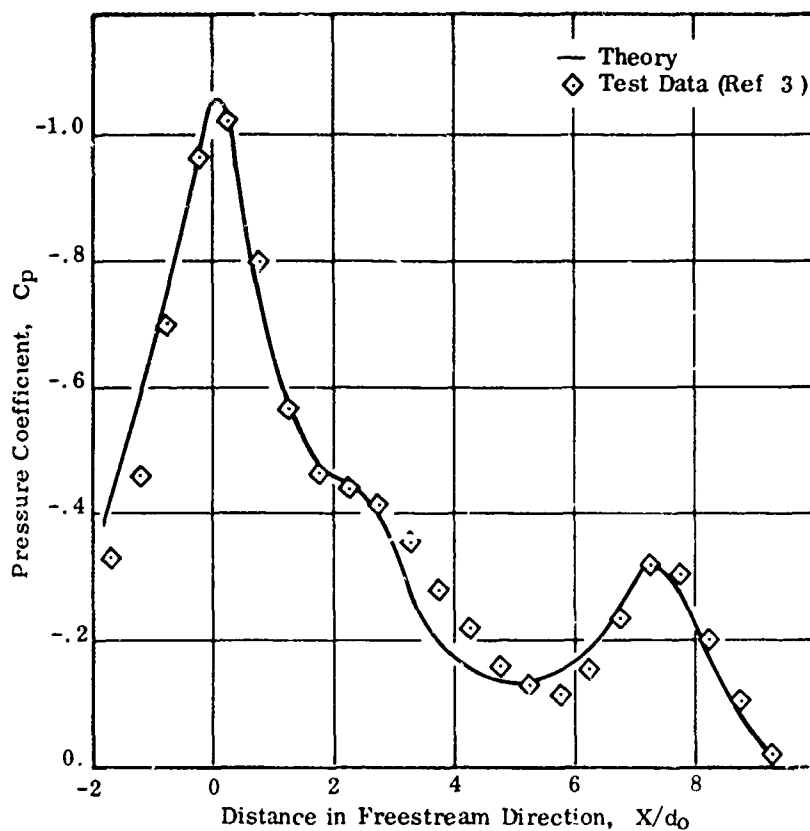
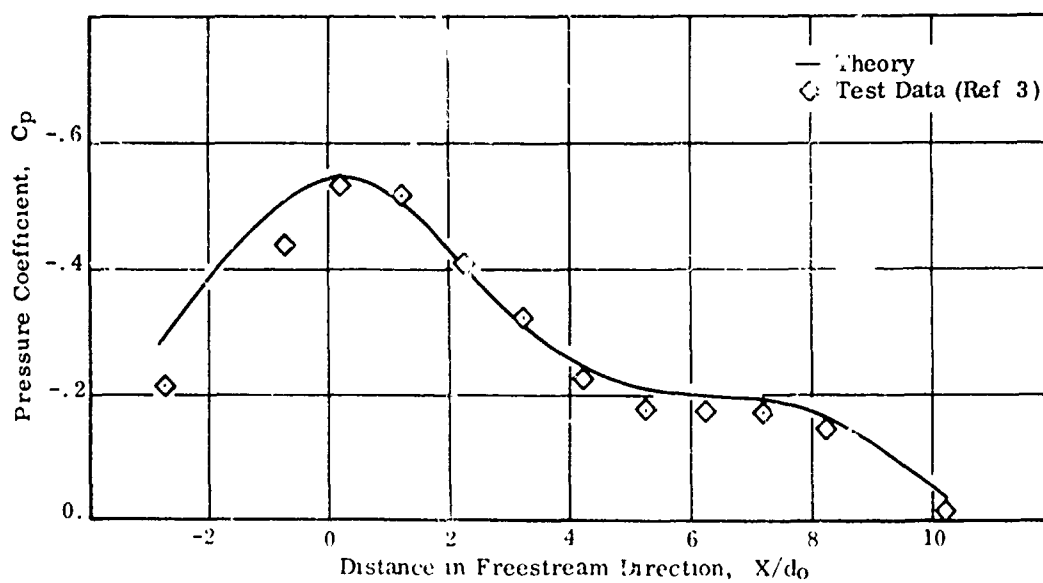


FIGURE 45. CENTERLINES FOR THREE-JET CONFIGURATION  
( $U_\infty/U_{j0} = .125$ )



(a) Station  $Y/d_0 = 1.5$



(b) Station  $Y/d_0 = 3$

FIGURE 46. INDUCED PRESSURE VARIATION FOR THREE-JET CONFIGURATION  
( $U_\infty/U_{j0} = .125$ )

Figure 44 shows a sketch of the three-jet configuration tested in Reference 3. The computed centerlines for this jet arrangement are shown in Figure 45. A comparison between predicted and experimental pressure variations at spanwise stations of 1.5 and 3.0 jet diameters is presented in Figure 46. In the computations shown in Figures 45 and 46, "effective velocity ratios" of .058 and .069 were utilized for the two downstream jets spaced at  $2.5 d_o$  and  $7.5 d_o$  from the leading jet, respectively. These are based on an actual velocity ratio of .125 and the relationships for reduced dynamic pressure of Equations (39) and (41). Good correlation between theory and data is noted.



### SECTION III

#### MAPPING METHOD FOR ARBITRARY CROSS SECTION

To use the transformation method and the nonlinear body aerodynamics method which are described in Sections IV and VI, it is necessary to have a method of mapping an arbitrary wing or body cross section into a unit circle. It is the purpose of this section to describe the method developed during this investigation to obtain such a mapping.

There are numerous methods available to map specific shapes into a unit circle such as the Joukowski transformation for wings. It is also possible to map polygons by the Schwarz-Christoffel transformation, but this transformation maps the polygon into a straight line, not into a circle.

The only suitable transformation for mapping an arbitrary section into a unit circle is that developed by Skulsky in Reference 46. This method uses a procedure similar to the Schwarz-Christoffel transformation. This method would be suitable for the mapping required by the programs developed during this study except for the following restrictions on the method. First, the method replaces the cross section by one made up of straight line segments giving only an approximation to the desired shape. Second, the mapping procedure is an iterative one and the question of convergence in the iteration arises. Third, a large number of terms in the mapping are required.

These restrictions are not so severe as to prevent the use of the Skulsky method for the present study program methods, but the method is restricted to symmetrical shapes and this restriction means that general airfoils could not be treated. For this reason, it was decided to develop a mapping function which would be more suitable for the present study.

The mapping method developed in this section presents an alternative approach to the computation of a mapping function. This method is not restricted to symmetrical sections and does not require any iterative procedure. The mapping is obtained by finding the potential for an arbitrary section which corresponds to a simple vortex flow about the corresponding circle. The potential is equated to that for a circle and equivalent points are located on the mapping circle. Knowing the point-to-point correspondence, the mapping function is then obtained.

## 1. COMPUTATION OF COMPLEX POTENTIAL FOR VORTEX FLOW

The method used to obtain a mapping function is to develop a potential function about an arbitrary shape which satisfies the boundary condition of no flow through the body and behaves as a simple vortex flow at large distances from the body. This expression is written in body plane coordinates (see Figure 47) and is compared to a similar flow about a circle expressed in circle plane coordinates, which is a well-known function.

The complex potential of a vortex flow about a circle is

$$W = \phi + i\psi = i \ln \zeta \quad (42)$$

The velocity in the circle plane is

$$\frac{dW}{d\zeta} = -u_c + i v_c = \frac{i}{\zeta} \quad (43)$$

To obtain the corresponding velocity about an arbitrary section it is necessary to obtain an analytic function of  $Z$  which satisfies the boundary conditions at the body and behaves like  $i/Z$  at large distances from the body. It is possible to obtain such a function by writing the velocity in the body plane

$$\frac{dW}{dZ} = -u_b + i v_b = \frac{i}{Z} f(Z) \quad (44)$$

where  $f(Z)$  is some function which approaches 1 as  $Z$  approaches infinity and which is chosen to satisfy the boundary conditions at the body. By writing the velocity in terms of polar coordinates i.e.,

$$-\frac{dW}{dZ} = V_b e^{-i\alpha} = -\frac{i}{Z} f(Z) \quad (45)$$

satisfying the boundary condition at the body reduces to finding a function  $f(Z)$  which matches a specified variation of  $\alpha$  around the section.

Assuming temporarily that the section to be mapped is smooth, that is has no corners, the log of Equation (45) can be taken to give

$$\ln V_b - i\alpha = -\frac{i\pi}{2} - \ln Z + \ln f(Z) \quad (46)$$

and  $\ln V_b$  and  $\alpha$  are conjugate functions. Thus, if  $\ln f(Z)$  is taken to be a Laurent series with no nonnegative powers, i.e.,

$$\ln f(Z) = \ln f(Z) = \frac{a_1 + ib_1}{Z} + \frac{a_2 + ib_2}{Z^2} + \frac{a_3 + ib_3}{Z^3} + \dots \quad (47)$$

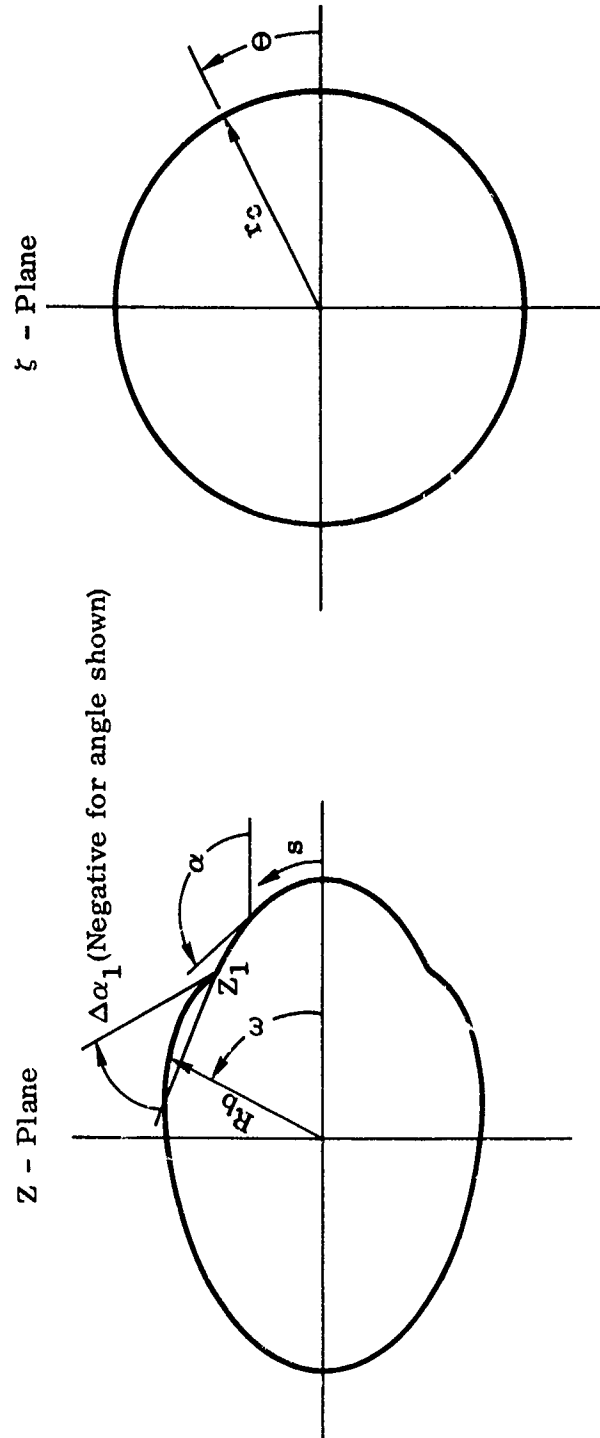


FIGURE 47. TERMINOLOGY FOR CROSS SECTION AND CIRCLE PLANES

the coefficients of this expansion can be chosen to obtain any desired variation of  $\alpha$  about the body.

This gives the expression for the complex velocity in the section plane as

$$V_b e^{-i\alpha_m - \frac{i}{Z} e^{g(Z)}} \quad (48)$$

When the section to be mapped has corners  $\alpha$  will be discontinuous and it is necessary to obtain an expression which has similar discontinuities. Assume that a corner exists

on the section to be mapped at  $Z = Z_m$ . Then, the factor  $\left(1 - \frac{Z_m}{Z}\right)^{k_m}$

where

$$k_m = -\frac{\Delta\alpha_m}{\pi + \Delta\alpha_m}$$

will have a singularity at  $Z_m$  with a discontinuity in angle of  $\Delta\alpha_m$ . This can be shown by comparing the limits on the two sides of the corner. Letting  $Z = Z_m - \Delta Z$

$$\left(1 - \frac{Z_m}{Z}\right)^{k_m} = \left(-\frac{\Delta Z}{Z}\right)^{k_m} = \left(-\frac{\Delta s e^{i\alpha}}{Z}\right)^{k_m} = \left[\frac{\Delta s}{R_b} e^{i(\alpha_m - \pi - \omega)}\right]^{k_m}$$

$$\ln \left(1 - \frac{Z_m}{Z}\right)^{k_m} = k_m \ln \left(\frac{\Delta s}{R_b}\right) + i k_m (\alpha_m - \pi - \omega)$$

Again, letting  $Z = Z_m + \Delta Z$

$$\left(1 - \frac{Z_m}{Z}\right)^{k_m} = \left(\frac{\Delta Z}{Z}\right)^{k_m} = \left[\frac{\Delta s}{R_b} e^{i(\alpha_+ - \omega)}\right]^{k_m}$$

$$\ln \left(1 - \frac{Z_m}{Z}\right)^{k_m} = k_m \ln \left(\frac{\Delta s}{R_b}\right) + i k_m (\alpha_+ - \omega)$$

subtracting these two expressions gives

$$i k_m (\alpha_+ - \alpha_m - \pi) = -i \Delta\alpha_m \quad (49)$$

which is the result sought. The magnitude of this factor gives an infinite velocity for an outside corner and zero velocity for an inside corner which is to be expected.

The complex velocity for an arbitrary section can thus be written

$$V_b e^{-i\alpha} = -\frac{i}{Z} \prod_{m=1}^M \left(1 - \frac{Z_m}{Z}\right)^{k_m} e^{g(Z)} \quad (50)$$

where M is the number of corners. This expression, being written wholly in terms of the section coordinate Z, can be evaluated directly.

Defining,

$$1 - \frac{Z_m}{Z} = \mu_m e^{i\beta_m}$$

the log of this function can be written

$$\ln V_b e^{-i\alpha} = \sum_{m=1}^M k_m \ln \mu_m - \ln R_b + i \left( \sum_{m=1}^M k_m \beta_m - \pi - \omega \right) + g(Z) \quad (51)$$

The imaginary part is

$$\alpha - \pi - \omega + \sum_{m=1}^M k_m \beta_m = -\mathcal{I}_m(g(Z)) \quad (52)$$

The left hand side of this equation is a continuous and periodic function of s and can be evaluated at any point on the body. This makes it possible to evaluate the coefficients of g(Z) to satisfy the boundary conditions to any degree of accuracy desired.

Letting

$$\epsilon = \alpha - \pi - \omega + \sum_{m=1}^M k_m \beta_m + \mathcal{I}_m(g(Z))$$

where

$$\mathcal{I}_m(g(Z)) = \sum_{n=1}^N \frac{b_n \cos n\omega - a_n \sin n\omega}{R_b^n}$$

and setting

$$E = \oint \epsilon^2 ds$$

E represents the least square error in fitting  $\alpha$ . Differentiating with respect to each of the a's and b's and setting the results to zero

$$\frac{\partial E}{\partial a_j} = 0$$

$$\frac{\partial E}{\partial b_j} = 0$$

gives a set of linear equations solvable for the a's and b's.

Once these coefficients are determined, the real part of Equation (51) can be evaluated and  $V_b$  obtained. Then, comparing the potential functions in the circle plane with that about the section gives

$$\theta = \frac{2\pi \int V_b ds}{\oint V_b ds} \quad (53)$$

where  $\theta$  is the angular distance about the circle. This gives a relationship between the points on the section and points on the mapping circle which permits a mapping to be obtained.

## 2. COMPUTATION OF DERIVATIVE OF MAPPING FUNCTION WITH CORNERS

Once it is known which point on the section maps into which point on the circle it is relatively simple to obtain the mapping function, and this relationship has been obtained above.

The derivative of the mapping function can be written as a Laurent's series in  $\zeta$  as

$$\frac{dZ}{d\zeta} = 1 + \frac{d_2}{\zeta^2} + \dots + \frac{d_n}{\zeta^n} + \dots \quad (54)$$

the  $1/\zeta$  term being zero for a closed section. It can also be shown that

$$\frac{dZ}{d\zeta} = \frac{ds}{r_c d\theta} e^{i(\alpha - \theta - \pi/2)} \quad (55)$$

when the mapping is evaluated at the mapping circle. Then the coefficients of the mapping can be evaluated as follows. The radius of the mapping circle can be determined by setting,

$$\oint \frac{1}{\zeta} \frac{dZ}{d\zeta} d\zeta = 2\pi i$$

or

$$2\pi i = \oint \frac{1}{r_c^2 e^{i\theta}} e^{i(\alpha - \theta - \pi/2)} \frac{ds}{d\theta} d(r_c e^{i\theta})$$

$$2\pi i = \frac{i}{r_c} \oint e^{i(\alpha - \theta - \pi/2)} ds$$

or

$$r_c = \frac{1}{2\pi} \oint e^{i(\alpha - \theta - \pi/2)} ds \quad (56)$$

similarly

$$\oint \zeta^{n-1} \frac{d\bar{z}}{d\zeta} d\zeta = 2\pi i d_n$$

$$2\pi i d_n = \oint r_c^{n-1} e^{i(n-1)\theta} \frac{ds}{r_c d\theta} e^{i(\alpha-\theta-\pi/2)} i r_c e^{i\theta} d\theta$$

$$d_n = \frac{r_c^{n-1}}{2\pi} \oint e^{i[\alpha+(n-1)\theta-\pi/2]} ds \quad (57)$$

Since it has been shown above how to evaluate  $\theta$  as a function of  $s$  it is possible to obtain the derivative of the mapping function.

It is possible at this point to integrate  $dZ/d\zeta$  directly and to obtain the mapping function. When the section to be mapped has corners, however, the region in the vicinity of the corners is not mapped accurately unless an extremely large number of terms in the mapping function is retained. For this reason, it is desirable to rewrite  $dZ/d\zeta$  in such a manner that the corner singularities are expressed explicitly. This requires that  $dZ/d\zeta$  be written as

$$\frac{dZ}{d\zeta} = \prod_{m=1}^M \left(1 - \frac{\zeta_m}{\zeta}\right)^{\frac{\Delta\alpha_m}{\pi}} \left(1 + \sum_{n=1}^N \frac{A_n}{\zeta^n}\right) \quad (58)$$

It is now possible to expand the product factors of Equation 58 by binomial expansion, complete the expansion by further multiplication and the terms equated with like terms of Equation (54). This results in a set of expressions which can be solved for the  $A$ 's. Equation (58) allows a satisfactory mapping near the corner points with a limited number of terms but cannot be integrated directly to give the mapping function analytically. It is possible to integrate (58) numerically, however.

### 3. COMPUTATION OF MAPPING FUNCTION

The computer programs written for the transformation method and the nonlinear body aerodynamics method do not permit the use of the derivative of the mapping function but require that the mapping function itself be known and be written in the form.

$$z = \zeta + C_0 + \frac{C_1}{\zeta} + \dots + \frac{C_n}{\zeta^n} \quad (59)$$

To obtain the mapping function in this form, the expression of Equation (58) is expanded to obtain the derivative of the mapping by expanding each of the terms

$$\left(1 - \frac{\zeta_m}{\zeta}\right)^{\frac{\Delta\alpha_m}{\pi}}$$

by a binomial expansion. These expressions are then multiplied together and also multiplied by the summation term in Equation (58). This results in an expression for  $dZ/d\zeta$  which can immediately be integrated analytically into the form of Equation (59).

This integration allows calculation of all the coefficients of Equation (59) except for  $c_0$ . To obtain  $c_0$  it is necessary to compare the original and the mapped section and shift the mapped curve to best reproduce the original cross section. The amount of shift required is then the value of  $c_0$ .

#### 4. SAMPLE CALCULATIONS OF MAPPINGS

This method has been used to map several sections. Figure 48 for example is a mapping of an extremely thick Joukowski airfoil which was mapped since the exact point-to-point mapping correspondence could be determined. Shown on the figure are both a complete mapping from the physical coordinates of the airfoil giving an excellent reproduction of the airfoil with the exception that some error is introduced near the trailing edge, and a mapping starting with the true  $\theta$  distribution which shows even better agreement. In the complete mapping twenty terms of the expansion for  $g(Z)$  were used.

Figure 49 shows a mapping of a 65-010 airfoil using the above method. In this case only ten terms of the expansion were used so that the agreement in this case is not quite so good, although still satisfactory. To obtain this mapping it was necessary to place a singularity within the airfoil at the center of the leading edge radius. Without this additional singularity an unsatisfactory mapping was obtained.

Figure 50 shows a mapping of a much more difficult section, the section being that of a T-38 section in the region where the jet inlets are adjacent to the body. This section, which is symmetrical, has five discontinuities on each side. The mapping was made using twenty terms in the expansion for  $g(Z)$ . The resultant agreement between the true section and the mapped section is very good.



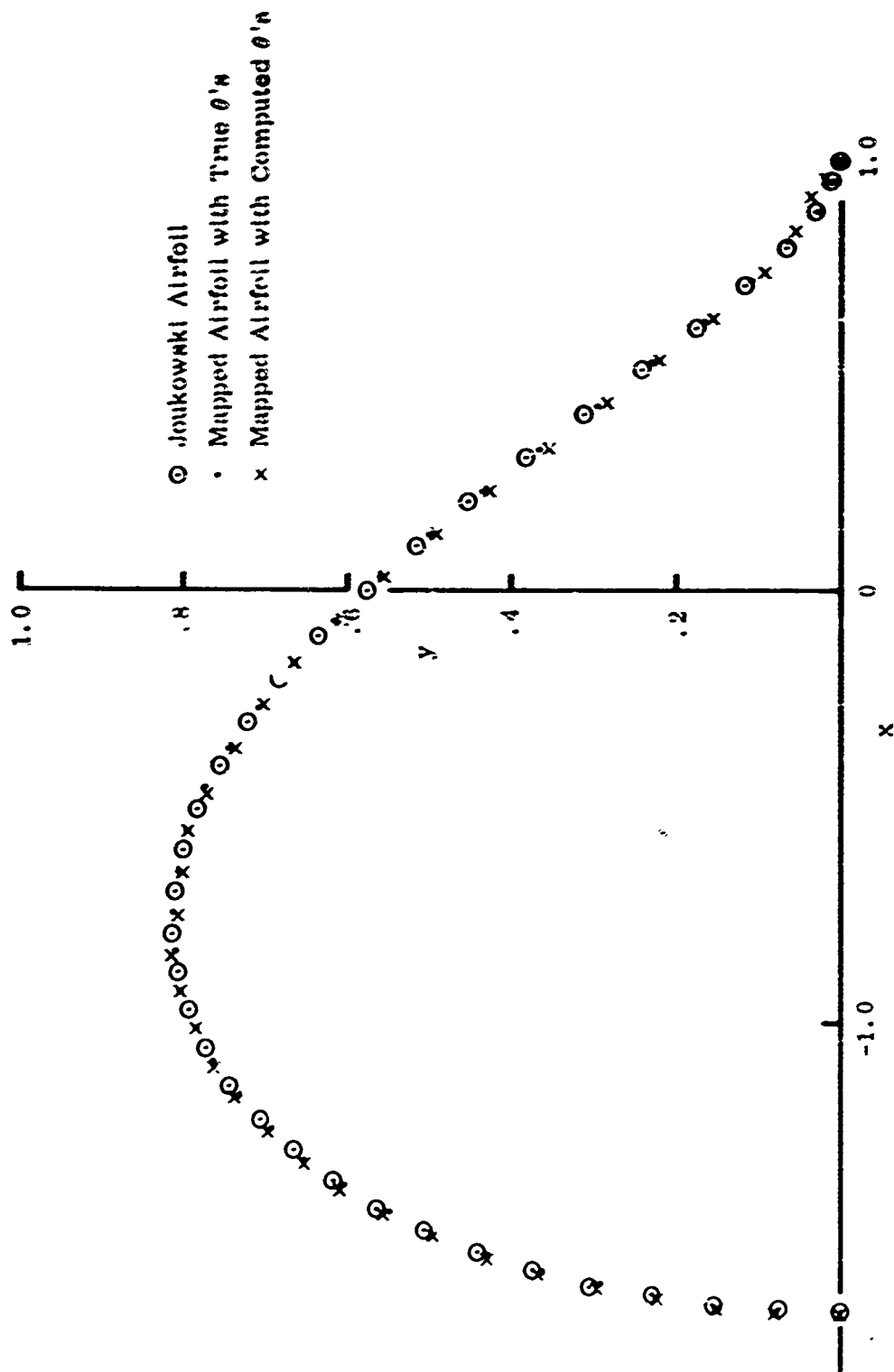


FIGURE 48. MAPPING OF JOUKOWSKI AIRFOIL.

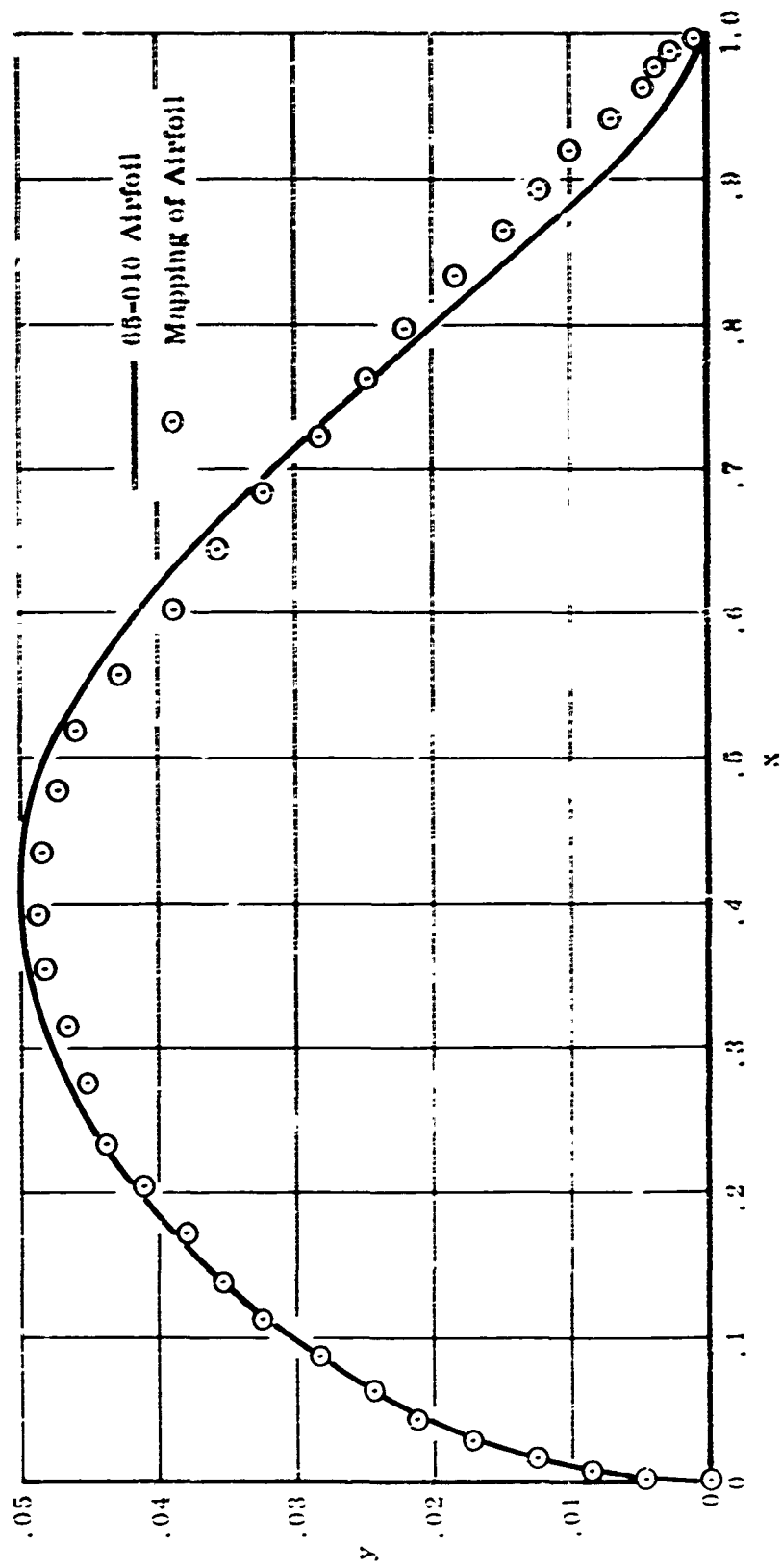


FIGURE 49. MAPPING OF 65-010 MOD. AIRFOIL.

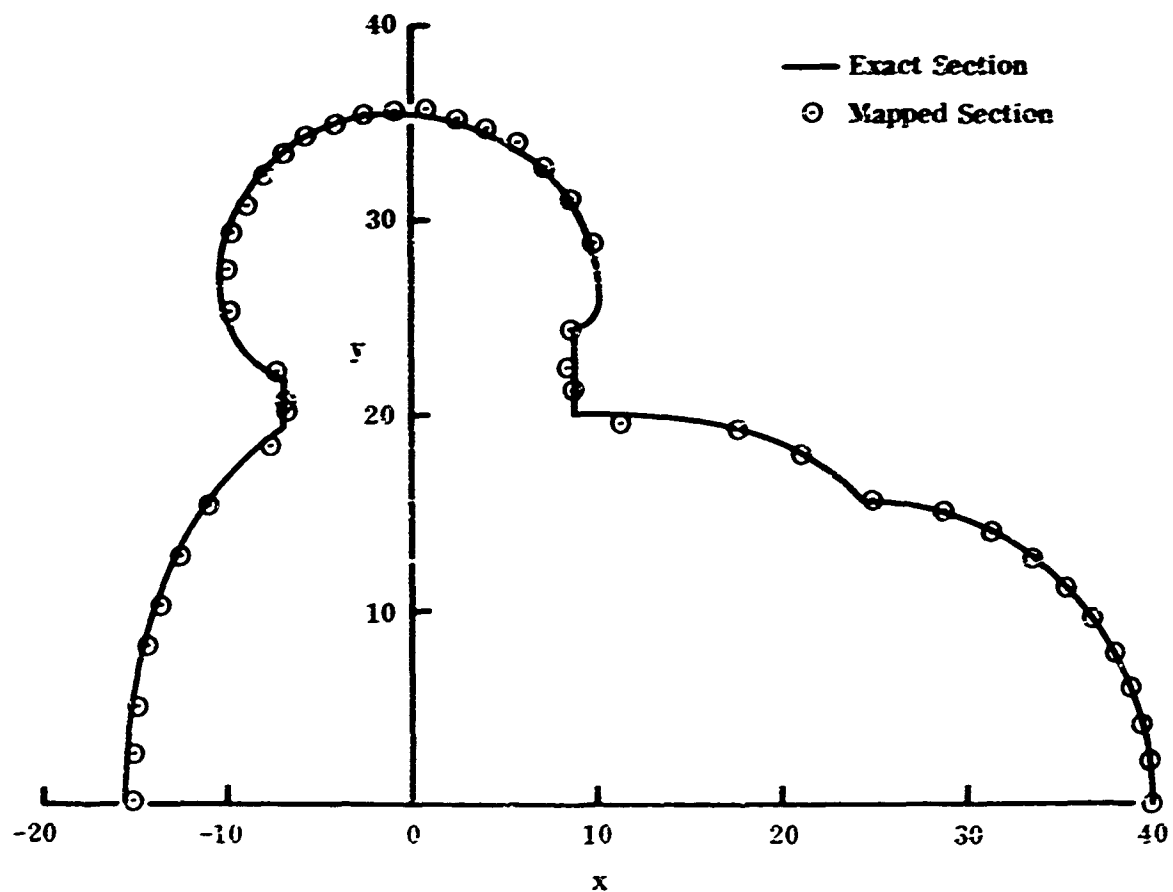


FIGURE 50. MAPPING OF T-38 SECTION AT STA. 291.5

## SECTION IV

### TRANSFORMATION METHOD

#### 1. INTRODUCTORY REMARKS

Under the assumption of inviscid flow, the force and moment on an immersed body arise from the pressure alone. Thus, the problem is that of determining the pressure distribution on a wing or fuselage with one or more jets exhausting into a uniform crossflow. The flow is assumed to be inviscid, incompressible and irrotational. The wing or body configuration can be fairly general as long as its cross sectional profile can be mapped into a circle on a two-dimensional space. The governing differential equation for the motion is the three-dimensional Laplace equation (viscosity has been implicitly included in the jet model). The boundary condition is the usual flow tangency condition.

In addition to these assumptions, we further assume that the presence of the body has negligible influence on the jet. Thus, the jet flow field,  $\vec{q}_j$ , may be computed independently and used in the formulation of the boundary conditions for the present problem.

The total velocity vector,  $\vec{q}$ , may then be written as

$$\vec{q} = \vec{U}_\infty + \vec{q}_j + \vec{q}_1 + \vec{q}_2 \quad (60)$$

where  $\vec{U}_\infty$  is the freestream velocity,  $\vec{q}_j$ , the perturbation velocity due to the presence of the body in the freestream, and  $\vec{q}_2$  is the perturbation velocity due to the body presence in the jet induced flow field. The problem of determining  $\vec{q}$  is here termed the power-on problem, that of determining  $\vec{U}_\infty + \vec{q}_1$ , the power-off problem and that of determining  $\vec{q}_j + \vec{q}_2$ , the power-effect problem. Emphasis will be placed on determining the power effect since we assume that methods already exist for determining the power-off pressure distribution.

Thus, the problem is reduced to that of solving for the perturbation velocity  $\vec{q}_2$ , in the presence of a body and a given jet induced flow field,  $\vec{q}_j$ . The governing differential equation, as mentioned above, is the three-dimensional Laplace equation

$$\frac{\partial^2 \phi}{\partial x^2} + \frac{\partial^2 \phi}{\partial y^2} + \frac{\partial^2 \phi}{\partial z^2} = 0, \quad (61)$$

where  $x$ ,  $y$  and  $z$  are body-oriented coordinates (Figure 51) and  $\phi$  is the perturbation velocity potential. The perturbation velocity components are  $u_2 = -\frac{\partial \phi}{\partial x}$ ,  $v_2 = -\frac{\partial \phi}{\partial y}$ ,  $w_2 = -\frac{\partial \phi}{\partial z}$ . The perturbation velocity vector may then be written as:

$$\vec{q}_2 = u_2 \vec{i} + v_2 \vec{j} + w_2 \vec{k} \quad (62)$$

The problem is then to find a solution of Equation (61), subject to the boundary conditions that

$$(\vec{q}_j - \text{grad } \phi) \cdot \vec{n} = 0 \quad \text{on the body surface,} \quad (63)$$

and  $\text{grad } \phi$  vanishes at infinity. The vector  $\vec{n}$  refers to the body surface outward normal.

It is possible to obtain a numerical solution to the problem by applying Green's Theorem using distributed singularities on the body surface. The basic formulation of the problem would be similar to that given by Hess and Smith in Reference 17. This approach, although giving a numerically exact solution, is not convenient for the present investigation for two reasons. The first reason is that a large amount of computing time is required to generate solutions for practical problems. The second reason is that a large number of control points are required to describe the body geometry.

Thus, in this investigation a quasi-two-dimensional method has been developed which is an approximate solution to Equation 61 and satisfies the boundary conditions in an approximate way. The technique consists of essentially two parts which correspond to two steps in the computation and are called the segment method and the three-dimensional modification. Step (1), or the segment method, consists of obtaining an approximate three-dimensional velocity potential by determining exact solutions of the two-dimensional Laplace Equation at a number of body stations. In Step (2), this velocity potential is modified to better satisfy the three-dimensional Laplace Equation.

Step (1), or the segment method, is an application of slender body theory in which the x-derivatives are neglected in favor of derivatives in the other two directions. Thus, the governing differential equation reduces to

$$\frac{\partial^2 \phi}{\partial y^2} + \frac{\partial^2 \phi}{\partial z^2} = 0 \quad (64)$$

The boundary conditions are then

$$\frac{\partial \phi}{\partial \vec{\nu}} = \vec{q}_j \cdot \vec{\nu} \quad \text{on each } y-z \text{ section} \quad (65)$$

and  $\text{grad}_{2D} \phi$  vanishes at infinity, where  $\vec{\nu}$  is an outward normal to each y-z section. This boundary value problem may now be solved by first mapping the contour of every y-z section into a circle and then using the method described in the following subsection. The potential so determined involves x as a parameter and may be written symbolically as  $\phi(y, z; x)$ . These potentials could, however, be consolidated to form a three-dimensional velocity potential. This latter potential will not, in general, satisfy the three-dimensional Laplace equation. To remedy this, a technique is developed as Step (2).

Step (2) is, in effect, an alternative method of including some three-dimensional effects in the problem in place of the usual procedure employed in the slender-body theory. (A general description of the slender-body theory may be found in Reference 18.) The present technique is based on the fact that failure of the consolidated potential to satisfy the three-dimensional Laplace Equation implies local violation of conservation of mass. To remedy this deficiency, a distribution of residual sources and sinks are included.

Inclusion of these residual sources and sinks supplements the old velocity field,  $\vec{q}_j = \text{grad}_{2D} \phi(y, z; x)$ , and is denoted by  $\vec{q}_s$ . The existence of the body will also have to be recognized in this supplementary field. To do this, we again use the segment method. The new flow field after Step (2) may then be written as:

$$\vec{q}' = \vec{q}_j - \text{grad}_{2D} \phi(y, z; x) + \vec{q}_s - \text{grad}_{2D} \phi_s(y, z; x) \quad (66)$$

This process could, in principle, be repeated. Each time when the process of three-dimensional modification is involved, two more terms, similar to  $\vec{q}_s$  and  $\text{grad}_{2D} \phi_s$ , would be added to the above expression.

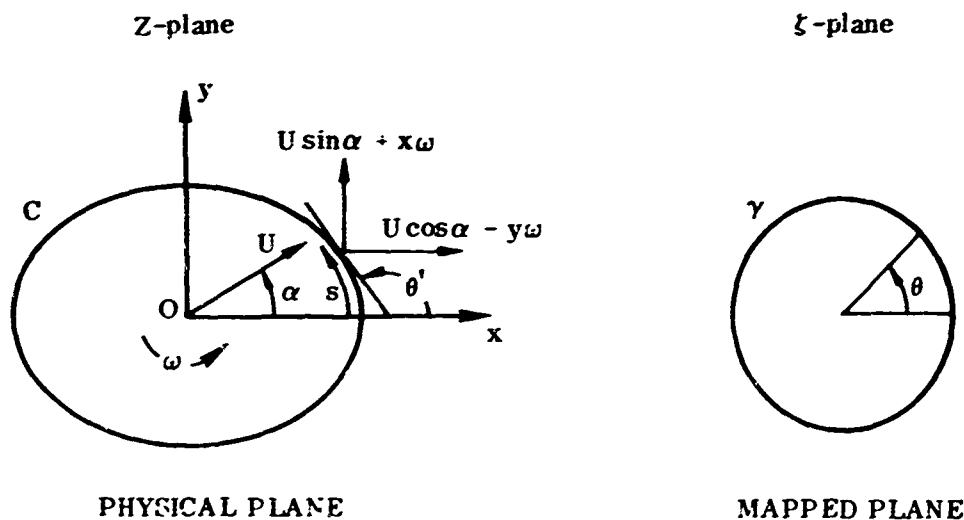
## 2. COMPUTATION OF FUSELAGE PRESSURE DISTRIBUTION

As stated above, the present technique comprises two steps, the segment method and the three-dimensional modification. The former can be used independently, whereas the latter, being a modification procedure, must be used in conjunction with the first step. Some details of these two steps will now be discussed.

### a. Segment Method

#### (1) The Boundary Function

The method is, in effect, a numerical extension of the procedure described in Reference 19. The problem considered in Reference 19 is that of determining the complex velocity potential for a cylinder moving two-dimensionally in infinite fluid at rest at infinity. The motion of the cylinder is described by a velocity of translation  $U$  and an angular velocity  $\omega$ . Let  $C$  be the contour of the cylinder cross-section and  $O$  the origin of coordinates about which the cylinder is rotating.



Suppose the region outside  $C$  in the  $Z$ -plane is mapped conformally on the outside of the unit circle  $|\zeta| = 1$  in the  $\zeta$ -plane by the relation

$$Z = f(\zeta) \quad (67)$$

with the points at infinity in the  $z$  and  $\zeta$ -plane corresponding. Again, following Reference 19, the normal velocity of the cylinder along the outward normal is

$$(U \cos \alpha - y \omega) \sin \theta' - (U \sin \alpha + x \omega) \cos \theta'$$

in which  $\theta'$  is the inclination of the tangent to the  $x$ -axis. Thus,

$$-\frac{\partial \psi}{\partial s} = (U \cos \alpha - y \omega) \frac{dy}{ds} - (U \sin \alpha + x \omega) \frac{dx}{ds} \quad (68)$$

Integrating along the cylinder boundary, we get

$$\psi = Ux \sin \alpha - Uy \cos \alpha + \frac{1}{2} \omega (x^2 + y^2) + B \quad (69)$$

where  $B$  is an arbitrary constant which, without loss of generality, may be set equal to zero.

Thus,  $\psi$  is equal to the imaginary part of the function

$$f(z, \bar{z}) = -Uz e^{-i\alpha} + \frac{1}{2} i \omega z \bar{z}$$

so that finally, on the boundary of the cylinder, the stream function  $\psi$  is such that

$$2i\psi = -U\bar{z} e^{-i\alpha} + U\bar{z} e^{i\alpha} + i\omega z \bar{z} \quad (70)$$

Let  $\sigma = e^{i\theta}$  denote a general point on the unit circle in the  $\zeta$ -plane. Then, on the unit circle, Equation (70) gives

$$2i\psi = B(\sigma) = -Uf(\sigma) e^{-i\alpha} + U\bar{f}(\frac{1}{\sigma}) e^{i\alpha} + i\omega f(\sigma) \bar{f}(\frac{1}{\sigma}) \quad (71)$$

This function,  $B(\sigma)$ , is called the boundary function by Milne-Thomson.



If the boundary function is expanded in a power series in  $\sigma$ , we can write

$$B(\sigma) = B_1(\sigma) + B_2(\sigma)$$

where  $B_1(\sigma)$  contains the negative powers of  $\sigma$  only so that  $B_1(\sigma)$  is holomorphic ( $B_2(\sigma)$  is finite, single valued and has a finite single valued differential coefficient) outside the unit circle and vanishes at infinity.

Thus, in terms of the complex velocity potential function  $W(\sigma)$ , Equation (71) may be written in the form

$$W(\sigma) - \overline{W}\left(\frac{1}{\sigma}\right) = B_1(\sigma) + B_2(\sigma) \quad (72)$$

Let  $\gamma$  be the circumference of the unit circle. Then Equation 72 may be used to obtain

$$\frac{1}{2\pi i} \int_{\gamma} \frac{W(\sigma) d\sigma}{\sigma - \xi} - \frac{1}{2\pi i} \int_{\gamma} \frac{\overline{W}\left(\frac{1}{\sigma}\right) d\sigma}{\sigma - \xi} = \frac{1}{2\pi i} \int_{\gamma} \frac{B_1(\sigma) d\sigma}{\sigma - \xi} + \frac{1}{2\pi i} \int_{\gamma} \frac{B_2(\sigma) d\sigma}{\sigma - \xi}$$

Now,  $W(\xi)$  and  $B_1(\xi)$  are holomorphic outside  $\gamma$ , while  $\overline{W}\left(\frac{1}{\xi}\right)$  and  $B_2(\xi)$  are holomorphic inside  $\gamma$ . Therefore, if  $\xi$  is outside  $\gamma$ , application of Cauchy's Theorem shows that the second and fourth integrals vanish and the first and third give

$$W(\xi) = B_1(\xi) \quad (73)$$

Thus, Equation (73) gives the complex velocity potential as a function of  $\xi$ . Elimination of  $\xi$  between Equations 67 and 73 yields the complex potential as a function of  $Z$ .

In summary, to determine the complex potential  $W(Z)$ , it is necessary to know the mapping function of Equation 67 and the stream function on the boundary of the cylinder (Equation (70)). The boundary function in the circle plane may then be determined and, hence, that part which contains only negative powers of  $\xi$ . The complex potential is then immediately determined.

## (2) Application of Boundary Function to the Segment Method

Although a cylinder under translation and rotation was given as an example of the boundary function, this approach may be used to solve more general problems in which  $\psi$  may be determined around a contour for which the mapping into a unit circle is known.

Consider an elongated body with its longitudinal axis aligned in the direction of the freestream (Figure 51). Let the velocity components in the x, y and z direction be denoted by u, v, and w respectively. The body is divided by cuts as shown and the volume adjacent to each cut represents a segment.

From the computation of the jet flow field (see Section II), we know what the jet induced velocity components of u, v and w along the cross sectional boundary of each cut would be if the body were not present. Due to the presence of the body segment, we must satisfy the boundary condition that no fluid penetrates the surface of the body segment. In the method of segments, this boundary condition is not, in general, satisfied exactly. It is satisfied approximately by moving the cross section of each cut in such a way that the velocity component normal to the cut is equal and opposite to that induced by the jet. Thus, application of the boundary condition does not account for growth of the body in the x-direction.

The method developed in Section III may be used to determine the mapping function of Equation 67 so that the problem of obtaining the complex potential and, hence, velocity and pressure distribution, is reduced to one of determining the stream function on the given boundary.

Following the procedure for determining a boundary function, we first transform the cross sectional area of each cut to a circle by the mapping function

$$Z = \zeta + b_0 + \frac{b_1}{\zeta} + \frac{b_2}{\zeta^2} + \dots + \frac{b_n}{\zeta^n} ,$$

where  $Z = y + iz$  (physical plane),  $\zeta = re^{i\theta}$  (mapped plane).

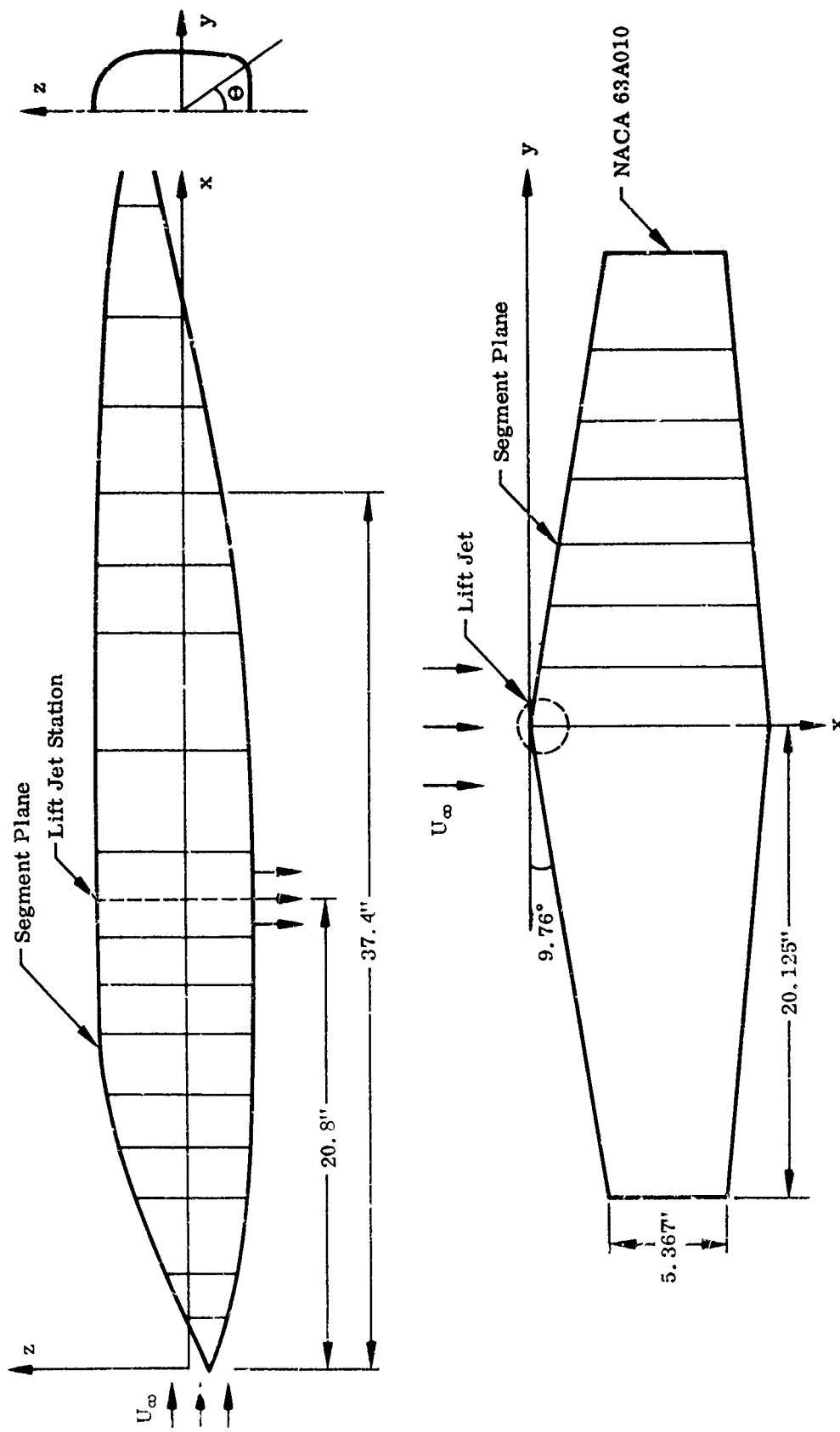


FIGURE 51. REPRESENTATIVE CONFIGURATIONS FOR WING AND FUSELAGE

The complex constants  $b_0, b_1, \dots, b_n$ , which signify the geometry of the cut, are determined by the procedure discussed in Section III of this volume. The complex potential on the mapped plane due to the motion of each cut is assumed to be

$$W = \Phi + i\Psi = a_0 \ln \xi + \frac{a_1}{\xi} + \frac{a_2}{\xi^2} + \dots + \frac{a_n}{\xi^n} \quad (74)$$

To compute the boundary function for every cut, we write

$$d\Psi = \frac{\partial \Psi}{\partial r} dr + \frac{\partial \Psi}{\partial \theta} d\theta.$$

When we perform the integration of this formula along a circle where the variable  $r$  remains unchanged, it reduces to

$$\Psi = \int_0^\theta \frac{\partial \Psi}{\partial \theta} d\theta.$$

Putting  $\psi$  in a form convenient for computation yields

$$\Psi = \int_0^\theta \left( \frac{\partial \Psi}{\partial y} \frac{\partial y}{\partial \theta} + \frac{\partial \Psi}{\partial z} \frac{\partial z}{\partial \theta} \right) d\theta = - \int_0^\theta \left( w_j \frac{\partial y}{\partial \theta} - v_j \frac{\partial z}{\partial \theta} \right) d\theta, \quad (75)$$

where  $v_j$  and  $w_j$  are the jet induced velocity components.

If we set the upper limit to  $2\pi$ , this integral gives the net flow of fluid through the boundary. This may not be zero, due to the fact that only two velocity components have been accounted for instead of three. This source or sink inside the boundary is accounted for by the logarithmic term in Equation 74.

We first determine the coefficients  $a_1, \dots, a_n$  in Equation (74) by considering the periodic part of Equation (75). Thus, we form

$$\Psi_1 = \Psi + \frac{\theta}{2\pi} \int_0^{2\pi} \left( w_j \frac{\partial y}{\partial \theta} - v_j \frac{\partial z}{\partial \theta} \right) d\theta$$

The boundary function  $\phi_1$  can now be expanded in the form of a Fourier series by the usual method

$$\psi_1 = \sum_{n=0}^n A_n \cos n\theta + \sum_{n=1}^n B_n \sin n\theta.$$

The boundary function may now be used to determine the coefficients  $a_1, \dots, a_n$  in Equation (74) and, hence, determine the potential for the flow which will cancel the normal component of velocity calculated by the jet program.

The first term in Equation (74) represents the source and circulation potential, and will be considered later. The coefficients,  $a_1, a_2, \dots, a_n$ , of the remaining terms may be determined by equating them to  $A_n$  and  $B_n$ . Setting  $a_1 = a'_1 + i a''_1$ ,  $a_2 = a'_2 + i a''_2, \dots$ , we obtain

$$A_1 = \frac{a''_1}{r_b}, B_1 = -\frac{a'_1}{r_b}; A_2 = \frac{a''_2}{r_b^2}, B_2 = -\frac{a'_2}{r_b^2}; \dots \quad (76)$$

or

$$a_1 = -r_b B_1 + i r_b A_1,$$

$$a_2 = -r_b^2 B_2 + i r_b^2 A_2,$$

$$a_n = -r_b^n B_n + i r_b^n A_n.$$

where  $r_b$  is the radius of the mapped circle.

To evaluate the coefficient of the logarithmic term in Equation (74), we write

$$a_0 \ln \zeta = a_0 \ln r + i a_0 \theta.$$

For a body without circulation,  $a_0$  is real and is given by

$$a_0 = a'_0 = -\frac{1}{2\pi} \int_0^{2\pi} \left( \omega_j \frac{\partial \psi}{\partial \theta} - v_j \frac{\partial \phi}{\partial \theta} \right) d\theta.$$

Thus far, the complex coefficients in Equation (74) have all been determined, which sets the flow through every cross section of the cut to zero in a predetermined external flow field. The complete complex potential is then the summation of Equation 74 and the potential induced by the exhausting jets. Once this potential is known, it is a relatively simple matter to write a computer program to calculate the pressure distributions along the boundary of every cut, which result in the power effect by the segment method. Sample calculations are discussed in Volume II.

#### b. Three-Dimensional Modification

By establishing the real part of the complex potential in the physical plane, we obtain the velocity potential at every point exterior to the body on the planes passing through the cuts. These velocity potentials all exhibit the same form except that their coefficients are different from one plane to another. In other words, every coefficient is actually a function of  $x$ . To show this parameter  $x$  explicitly in Equation 74, we write the velocity potential at station  $x$ , with the help of Equation (76)

$$\begin{aligned} \phi(y, z; x) = & a'_0(x) \ln r + \frac{r_0(x)}{r} [A_1(x) \sin \theta - B_1(x) \cos \theta] \\ & + \frac{r_0^2(x)}{r^2} [A_2(x) \sin 2\theta - B_2(x) \cos 2\theta] + \dots + \frac{r_0^n(x)}{r^n} [A_n(x) \sin n\theta - B_n(x) \cos n\theta] \end{aligned} \quad (77)$$

in which  $r$  and  $\theta$  are functions of  $y$  and  $z$  given by the mapping function. By consolidating these expressions from every station, we could construct a three-dimensional velocity potential. This potential does not, however, satisfy the three-dimensional Laplace equation. To remedy this deficiency, we proceed to Step (2).

In Step (2), we first divide the region of the flow field into a network of small parallelepipeds whose "centers" are situated on the planes passing through each cut (Figure 52) and then compute the flux through the surfaces of each parallelepiped by using the available velocity potential. To account for this flux approximately, we have

$$Q_i = \left( \frac{\partial u}{\partial x_i} + \frac{\partial v}{\partial y_i} + \frac{\partial w}{\partial z_i} \right) \Delta V$$

in which the partial derivatives are evaluated at the center of the parallelepiped and

$\Delta V$  refers to its volume. Upon denoting the potentials at this and its neighboring stations to be  $\phi_i, \phi_{i-1}, \phi_{i+1}$ , and the velocity components to be  $u = -\frac{\partial \phi}{\partial x}$ ,  $v = -\frac{\partial \phi}{\partial y}$  and  $w = -\frac{\partial \phi}{\partial z}$ , we obtain

$$Q_i = -2 \left[ \frac{\phi_{i-1}}{(x_{i-1} - x)(x_{i-1} - x_{i+1})} - \frac{\phi_i}{(x_{i-1} - x)(x - x_{i+1})} + \frac{\phi_{i+1}}{(x_{i-1} - x_{i+1})(x - x_{i+1})} \right] \Delta V$$

The quantities in the bracket represent an approximation for the partial derivative  $\frac{1}{2} \frac{\partial^2 \phi}{\partial x^2}$ . These reduce to the central difference formula for stations of equal intervals. The sum  $\frac{\partial u}{\partial x} + \frac{\partial v}{\partial y} + \frac{\partial w}{\partial z}$  is always equal to zero, since  $\phi_i$  is the potential obtained by the segment method. However, the net flux  $Q_i$ , computed in this manner, is not in general equal to zero. This implies that fluid has been created or destroyed within the parallelepiped. In other words, the Laplace equation has a residual term, since the continuity equation and the Laplace equation are equivalent. To counter-balance this residual term, a source of the same strength but of opposite sense is placed at the center of the parallelepiped, so that the three-dimensional Laplace equation is approximately satisfied in its neighborhood. Repeating the process for each parallelepiped yields a network of residual sources and sinks in the space. These sources and sinks create a new field which will modify the old one.

A schematic diagram for the parallelepiped network is shown in Figure 52. Though there are only two layers and few parallelepipeds indicated, it is understood that for computational purposes we need at least four or five layers to cover a space extending several body diameters outward. To illustrate the effects of residual sources and sinks, let A be an arbitrary point on the body surface (Figure 52) with the coordinates  $x_0, y_0$  and  $z_0$ . Let the centers of the surrounding parallelepipeds be  $x_i, y_i$ , and  $z_i$ . The residual velocity components at Point A are then given by

$$u(x_0, y_0, z_0) = \frac{1}{4\pi} \sum_{i=1}^M \frac{m_i (x_0 - x_i)}{[(x_0 - x_i)^2 + (y_0 - y_i)^2 + (z_0 - z_i)^2]^{3/2}}$$

$$v(x_0, y_0, z_0) = \frac{1}{4\pi} \sum_{i=1}^M \frac{m_i (y_0 - y_i)}{[(x_0 - x_i)^2 + (y_0 - y_i)^2 + (z_0 - z_i)^2]^{3/2}}$$

$$w(x_0, y_0, z_0) = \frac{1}{4\pi} \sum_{i=1}^M \frac{m_i (z_0 - z_i)}{[(x_0 - x_i)^2 + (y_0 - y_i)^2 + (z_0 - z_i)^2]^{3/2}}$$

in which  $m_i = -Q_i$  and M refers to the total number of the residual singularities whose presence may affect the velocity distributions at Point A. A schematic arrangement

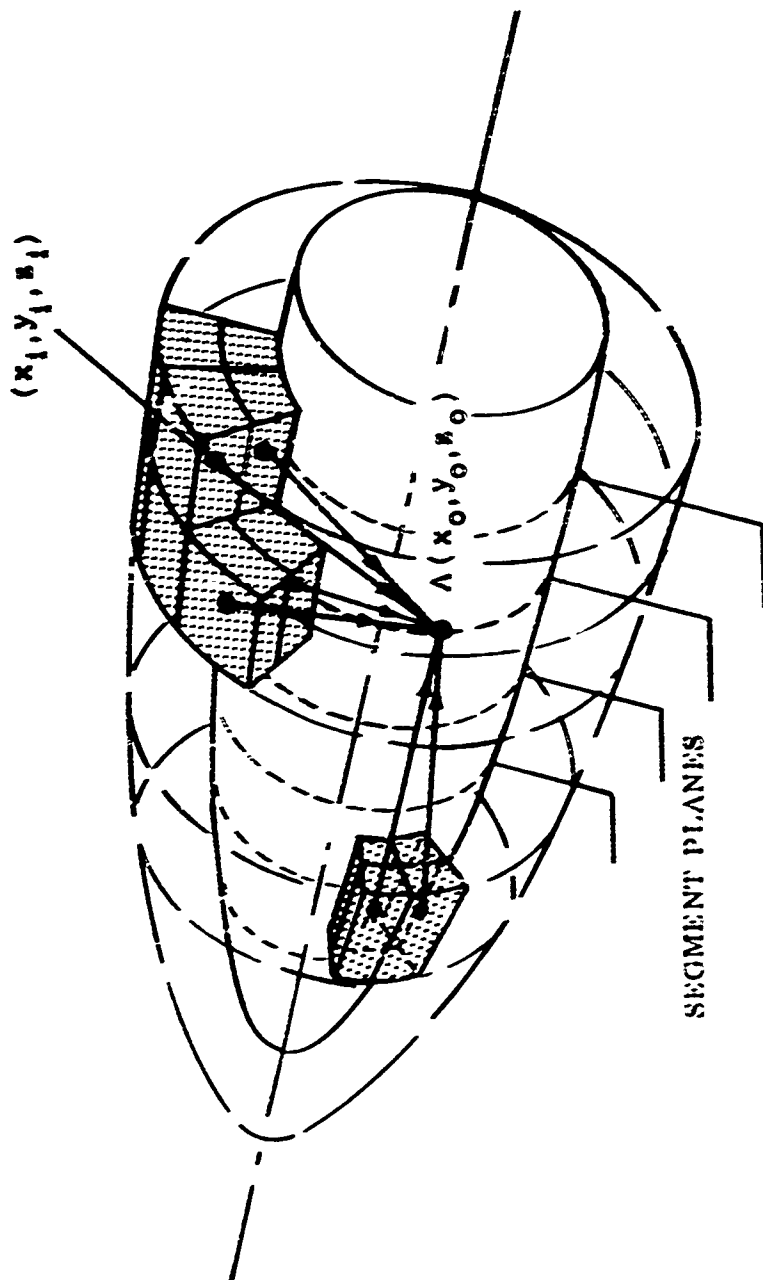


FIGURE 52. PARALLELEPIPED NETWORK



is shown in Figure 33 and the arrows indicate the influences of neighboring singularities to Point A.

Owing to the fact that this is a linear problem, we can solve the residual field separately, which upon superposition with the velocity potential obtained in Step (1) gives a modified velocity potential. The computational procedure is essentially the same as in Step (2), except that prior to Step (1) we calculate the velocity components induced by the residual sources and sinks along the boundary of each cut. This step again results in a set of velocity potentials defined on the planes passing through the cuts. Consolidating these potentials in a similar manner as for Equation (77) gives a three-dimensional potential due to the residual sources and sinks. This potential added to the potential found in the segment method forms a new potential. This new potential should better satisfy the three-dimensional Laplace equation. If the accuracy is still not acceptable, we can usually repeat Steps (1) and (2) to perform a second iteration. This procedure can be, in principle, carried out indefinitely. However, inasmuch as this is a quasi-two-dimensional method and the flow field involves inaccurate quantities in and near the exhausting jet, higher iterations may not be very meaningful.

### 3. COMPUTATION OF WING PRESSURE DISTRIBUTION

A finite wing is also a three-dimensional body, but it has a distinct property of generating lift in a uniform flow. Consequently, the above procedure is applicable with the additional requirement that the Kutta-Joukowski condition be satisfied at the trailing edge. To accomplish this, consider the following:

$$\begin{aligned} \frac{dW}{d\xi} &= \frac{a_0}{\xi} - \frac{a_1}{\xi^2} - \dots - \frac{na_n}{\xi^{n+1}} \\ &= \frac{a_0}{r} \cos \theta - \sum_{j=1}^n \frac{j a_j \cos(j+1)\theta}{r^{j+1}} - i \frac{a_0}{r} \sin \theta + i \sum_{j=1}^n \frac{j a_j \sin(j+1)\theta}{r^{j+1}} \end{aligned}$$

If it is assumed that the trailing edge occurs at  $\theta = 0$ , it becomes necessary to set the tangential velocity component equal to zero here, i.e., to set the imaginary part

of the equation to zero at  $\theta = 0$ . Referring  $\alpha_j'$  to the imaginary part of  $\alpha_j$ , we have

$$a_2'' = \sum_{j=1}^n \frac{j^2 \alpha_j'}{j^2} = \sum_{j=1}^n \alpha_j'.$$

Thus the first term in Equation (16) is defined.

Since the computational procedure in step (1) disregards the variation of the circulation along the wing span due to the wing planform, the computed lift is likely to be larger than it should be. To better estimate the wing lift, we apply the lifting line theory in a reverse manner. In other words, we make some attempt to reduce the magnitude of the "downwash" components (actually upwash for the usual adverse lift caused by the exhausting jet), so that the over-prediction in step (1) could be partially compensated for. The procedure is to represent the circulation  $\Gamma$ , obtained in step (1) in a Fourier series in the wing spanwise direction. We next use the equation

$$w'(y) = \frac{1}{3} \frac{1}{4\pi} \int_{-\frac{b}{2}}^{\frac{b}{2}} \frac{d\Gamma}{d\eta} \frac{1}{y-\eta} d\eta. \quad (78)$$

to compute the downwash components at every section. The symbol  $b$  denotes the span length or that portion of the span length over which the power effect is significant. Then a new flow field on the fictitious wing is constructed by subtracting  $w'$  from the modified  $w$  components in step (2). This constitutes the modification to account for the spanwise variation of the circulation around the wing after inclusion of the residual source distribution.

It is noted here that there are two arbitrary elements involved in the above procedure. These are:

- (a) The factor  $1/3$  in Equation 78 is an added empirical factor to the original equation.
- (b) Since only the lifting line theory is invoked, all the components at any given section, regardless of the chordwise position, are reduced by an equal amount equal to  $w'(y)$ .

#### 4. COMPUTATIONS AND RESULTS

On the basis of the above analysis, computer programs have been written to calculate the pressure distributions on a wing or body. These pressure distributions can be integrated to give force and moment on the wing or body.

To recapitulate, the sequence of the computational procedure is:

- (a) Sever the wing or body into a number of sections.
- (b) Obtain the mapping function for each section.
- (c) Transform the sectional contour into a circle.
- (d) Acquire the velocity distribution along the boundary of each section by means of the jet flow field program.
- (e) Find the boundary function at each section.
- (f) Expand these boundary functions in Fourier series.
- (g) Determine the coefficients of the complex potential at each section from the Fourier coefficients.
- (h) Compute the pressure distribution from the complex potential.
- (i) Determine the force and moment by integrating the pressure distribution.

If the three-dimensional modification is needed, we skip step (i) and include the following steps:

- (j) Form a network of parallelepipeds in the exterior space.
- (k) Compute the net flux in each parallelepiped.
- (l) Place a source of the same strength but of opposite sense at the center of each parallelepiped.
- (m) Determine the velocity distributions along the sectional boundaries induced by the residual sources and sinks.
- (n) Repeat steps (e) through (i) to obtain the force and moment.

Extensive calculations have been carried out for two wings and two bodies with lifting jets in a uniform crossflow. The parameters involved in these computations are: freestream to the jet velocity ratio, angle of attack, sideslip angle, location of the jets and the number of lifting jets. The calculated results have been compared with wind tunnel test data. The agreement has been fairly

satisfactory. Some examples can be found in Volume II. A general feature from these investigations indicates that the power effect is a strong function of the velocity ratio but is rather insensitive to angle of attack.

## SECTION V

### INLET FLOW FIELD

Inlet flow models are developed which allow lift, drag, and moment estimation for bodies containing inlets normal to the free stream. A propulsion model for lifting fans is developed relating internal and external flows.

#### 1. ANALYSIS

The basis of the inlet flow field analysis is the assumption that the flow about an inlet normal to the free stream may be approximated by the potential flow produced by a concentrated sink embedded in an infinite plane above which passes a uniform flow. The force produced on the surface containing the inlet is assumed to be the force acting on that portion of the infinite plane obtained by projecting the planform of the surface onto the infinite plane. For purposes of calculation, the force upon the affected portion of the infinite plane is divided into two portions: a lip force acting in the immediate vicinity of the inlet, and a surface force acting on the remaining planform area.

##### a. Lip Forces

The lip forces and moments are calculated by establishing a control surface of radius  $R_1$  about the inlet centroid and applying the law of conservation of momentum (Figure 53).

The lip force in the free stream direction is expressed as shown below.

$$D_L = \rho \int u_x v_n dS + \int p dS_x$$

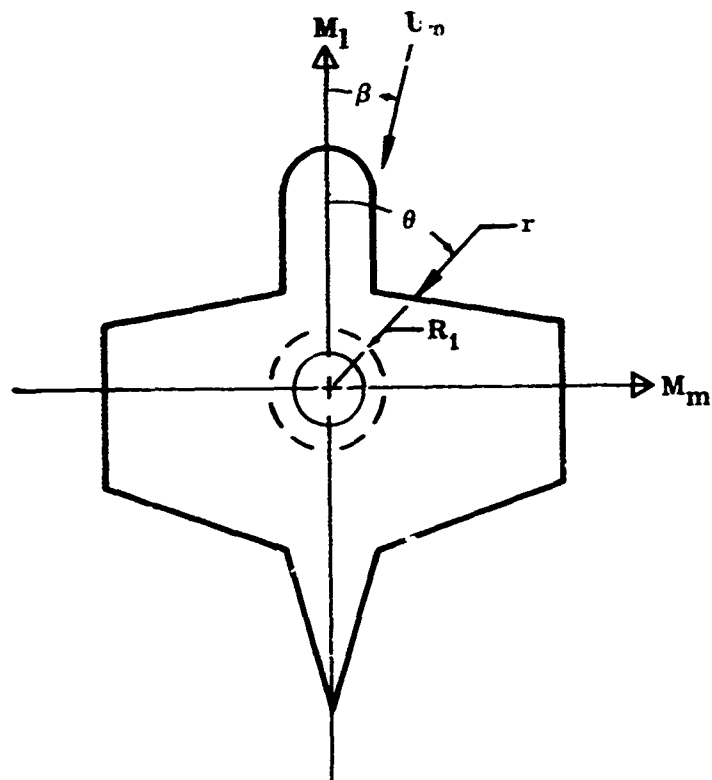
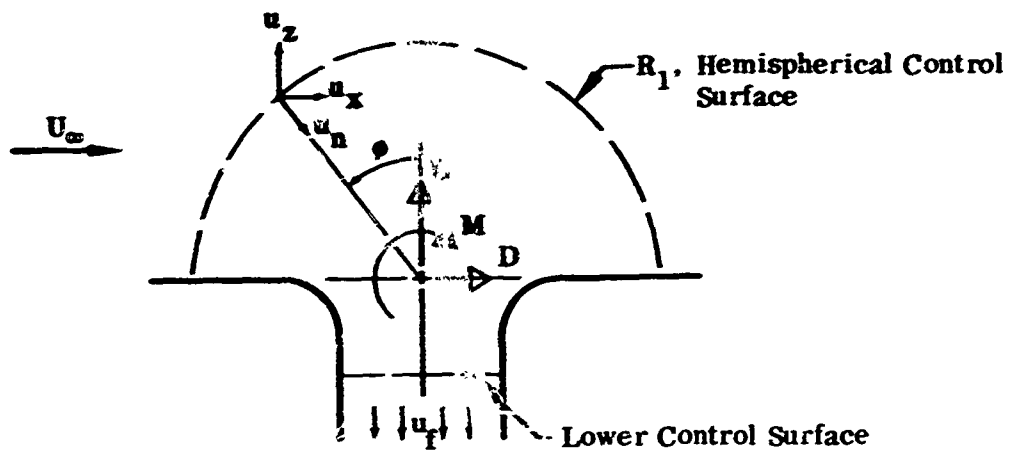


FIGURE 53. COORDINATE SYSTEM FOR INLET MODEL

The pressure and velocity at the hemispherical control surface may be expressed in terms of the sink induced velocity,  $u_s$ .

$$P_{R_1} = P_{T_\infty} - \frac{\rho}{2} (U_\infty^2 + 2 U_\infty u_s \sin \phi \cos \theta + u_s^2)$$

$$u_n = u_s + U_\infty \sin \phi \cos \theta$$

$$u_x = U_\infty + u_s \sin \phi \cos \theta$$

$$u_z = -u_s \cos \phi$$

The velocity  $u_s$  is obtained from the sink strength or fan flow rate.

$$u_s = m / 4 \pi R_1^2$$

$$m = 2 A_f U_f$$

The conditions at the lower control surface are shown below. The constant  $K$  is defined as shown and the constant  $\eta$  is a dynamic head recovery factor for the inlet.

$$P = P_\infty + \eta \frac{\rho}{2} U_\infty^2 - \frac{\rho}{2} (u_n^2 + u_x^2)$$

$$u_n = -U_f$$

$$u_x = K U_\infty$$

The drag is then found.

$$D_L = \rho A_f U_f U_\infty (1-K)$$

As the free stream velocity component is reduced to zero or near zero in passing through the fan, we may calculate the total drag by assuming the turning to take place in the inlet.

$$D_L = \rho A_f U_f U_\infty$$

The moment about the centroid, and normal to the free stream is found as shown below.

$$M_L = \rho \int (\bar{U} \times \bar{r}) u_n dS + \int p (\bar{n} \times \bar{r}) dS$$

$$M_L = \rho A_f U_\infty U_f (R_i/2 + K \Delta z)$$

$$M_L = \rho A_f U_\infty U_f R_i/2$$

$$M_{mL} = M_L \cos \beta$$

$$M_{xL} = -M_L \sin \beta$$

As in the drag calculation, the parameter  $K$  has been set equal to zero for consistency.

The lift may be calculated from the expression

$$L_L = \rho \int u_z u_n dS + \int p dS_z$$

Thus,

$$L_L = \frac{\rho}{2} A_f \left[ U_f^2 (1 - A_f/4\pi R_i^2) + U_\infty^2 (\eta - K^2) \right]$$

The parameter,  $K$ , is retained in the expression as the change flow direction in passage through the fan does not affect the pressure at the lower control surface, the source of the term. In the equations for drag and pitching moment, the parameter  $K$  reflects an unremoved freestream momentum flux and later elimination of this component, in the fan or nozzle, will cancel the terms containing  $K$ .



## b. Surface Forces

The forces and moments on the remaining effective area are calculated by integration of the pressure distribution created by the sink. The pressure coefficient at any point is described by the expression shown below.

$$C_p = \frac{U_f}{U_\infty} \frac{A_f}{\pi r^2} \cos(\theta - \beta) - \left( \frac{U_f}{U_\infty} \frac{A_f}{\pi r^2} \right)$$

The lift can then be expressed as the following integral.

$$L_s = -\frac{1}{2} \rho U_\infty^2 \int_0^{2\pi} \int_{R_1}^r C_p r dr d\theta$$

Integrating with respect to  $r$  yields the intermediate result which may be used in conjunction with a body description to obtain the force.

$$\begin{aligned} L_s = \frac{1}{2} \rho U_\infty U_f \frac{A_f}{\pi} & \left[ \cos \beta \int_0^{2\pi} \ln \left| \frac{r}{R_1} \right| \cos \theta d\theta \right. \\ & \left. + \sin \beta \int_0^{2\pi} \ln \left| \frac{r}{R_1} \right| \sin \theta d\theta \right] \\ & + \frac{\rho}{4} U_f^2 \left( \frac{A_f}{2\pi R_1} \right)^2 \int_0^{2\pi} \left[ 1 - \left( \frac{R_1}{r} \right)^2 \right] d\theta \end{aligned}$$

In a similar manner the pitching and rolling moments are found.

$$\begin{aligned} M_{ms} = \frac{\rho}{2} U_\infty U_f \frac{A_f R_1}{\pi} & \left[ \cos \beta \int_0^{2\pi} \left( \frac{r}{R_1} - 1 \right) \cos^2 \theta d\theta \right. \\ & \left. + \sin \beta \int_0^{2\pi} \left( \frac{r}{R_1} - 1 \right) \cos \theta \sin \theta d\theta \right] \\ & + \frac{\rho}{2} U_f^2 \frac{\left( \frac{A_f}{2\pi} \right)^2}{R_1} \int_0^{2\pi} \left( 1 - \frac{R_1}{r} \right) \cos \theta d\theta \end{aligned}$$

$$M_{\lambda s} = \frac{\rho}{2} U_{\infty} U_f \frac{A_f R_i}{\pi} \left[ \cos \beta \int_0^{2\pi} (1-r/R_i) \cos \theta \sin \theta d\theta \right. \\ \left. + \sin \beta \int_0^{2\pi} (1-r/R_i) \sin^2 \theta d\theta \right] \\ + \frac{\rho}{2} U_f^2 \frac{(A_f/2\pi)^2}{R_i} \int_0^{2\pi} (R_i/r - 1) \sin \theta d\theta$$

It must be noted that the effects of the body edges on the pressure distribution created by the inlet have been neglected, and that the forces and moments due to edge effects are not included in the analysis.

## 2. LIFT-FAN PROPULSION MODEL

A simple expression has been obtained relating the flow parameters to propulsion parameters for lift-fan units. The model is based upon the assumption that the pressure difference across the fan may be represented by the following relation.

$$\Delta P = \frac{1}{2} \rho C_t U_t^2$$

If the exit static pressure is assumed to be that of the free stream, and if allowance is made for loss of dynamic head at the inlet and for nonaxial flow at the fan entrance, the pressure differential may be related to flow conditions.

$$\Delta P = \frac{1}{2} \rho \left[ U_f^2 + (K^2 - \eta) U_{\infty}^2 \right]$$

The fan flow rate may then be described in terms of free stream conditions and fan speed.

$$U_f^2 = C_t U_t^2 + (\eta - K^2) U_{\infty}^2$$

The fan flow rate is often expressed in terms of flow ratio and tip speed ratio.

$$\frac{U_{\infty}}{U_f} = \frac{U_{\infty}}{U_t} \left[ \frac{1}{C_t + (\eta - K^2)(U_{\infty}/U_t)^2} \right]^{0.5}$$

The thrust carried by the fan blades may be obtained in terms of fan flow or tip speed parameters.

$$T_f = A_f \Delta P$$

$$\begin{aligned} T_f &= \frac{1}{2} \rho A_f [U_f^2 + (K^2 - \eta) U_{\infty}^2] \\ &= \frac{1}{2} \rho A_f C_t U_t^2 \end{aligned}$$

The effect of the presence of a fan centerbody may be considered by assuming it to produce a base drag force, or momentum loss.

$$\begin{aligned} T_f &= A_f \Delta P - \frac{1}{2} \rho U_f^2 C_D S_{CB} \\ &= \frac{\rho}{2} A_f \left[ \frac{C_t}{1 + C_D S_{CB}/A_f} \right] U_t^2 - \frac{\rho}{2} \frac{(\eta - K^2) C_D S_{CB}}{1 + C_D S_{CB}/A_f} U_{\infty}^2 \end{aligned}$$

where:

$$U_f^2 = \frac{1}{1 + C_D S_{CB}/A_f} [C_t U_t^2 + (\eta - K^2) U_{\infty}^2]$$

### 3. COMPARISON WITH PREVIOUS RESULTS

If the preceding relations are applied to the case of a simple fan in an infinite plane, having an inlet which turns the flow by ninety degrees with no flow losses, the results of the present expressions may be compared with previous work (20, 21).

The lip and surface forces become:

$$L_{L+S} = \frac{\rho}{2} A_f [U_f^2 + U_\omega^2]$$

The fan thrust reduces to:

$$T_f = \frac{\rho}{2} A_f [U_f^2 - U_\omega^2]$$

And the total lift may be expressed as:

$$\begin{aligned} L &= L_{L+S} + T_f \\ &= \rho A_f U_f^2 \end{aligned}$$

a result in agreement with Theodorsen (20).

The expression for the fan flow rate is then found to be

$$\begin{aligned} U_f^2 &= C_t U_t^2 + U_\omega^2 \\ &= U_{f_{U_\omega=0}}^2 + U_\omega^2 \quad \text{for } U_t = \text{constant} \end{aligned}$$

This result is in agreement with Grahame (21), who derived the expression by other means.

#### 4. DEVELOPMENT OF HANDBOOK METHOD

The simplicity of the empirical model outlined above enables estimation of inlet effects without resort to sophisticated computer techniques. The lip force and fan flow equations are applied in the form given. The integrals used to describe the surface forces may be easily integrated by finite summation using a work sheet as shown in Table 1. Because the induced forces are concentrated in the immediate vicinity of the inlet, large angular increments may often be used with little loss of accuracy. Semigraphical integration is often a convenient alternate.

TABLE 1  
INLET-SURFACE FORCE AND MOMENT CALCULATIONS

1	2	3	4	5	6	7	8	9	10	11	12
$\theta$	$\Delta\theta$	$R/R_1$	$\ln R/R_1$	$\cos\theta$	$\sin\theta$	$F_1$	$F_1\Delta\theta$	$F_2$	$F_2\Delta\theta$	$F_3$	$F_3\Delta\theta$
						$4 \times 5$	$7 \times 2$	$4 \times 3$	$9 \times 2$	$3^2 - 1$	$11 \times 2$

1	2	3	4	5	6	7	8	9	10	11	12
$\theta$	$\Delta\theta$	$R/R_1$	$R/R_1 - 1$	$\cos\theta$	$\sin\theta$	$M_1$	$M_1\Delta\theta$	$M_2$	$M_2\Delta\theta$	$M_3$	$M_3\Delta\theta$
						$4 \times 5^2$	$7 \times 2$	$4 \times 5 \times 6$	$9 \times 2$	$4 \times 5/3$	$11 \times 2$

1	2	3	4	5	6	7	8	9	10	11	12
$\theta$	$\Delta\theta$	$R/R_1$	$R/R_1 - 1$	$\cos\theta$	$\sin\theta$	$L_1$	$L_1\Delta\theta$	$L_2$	$L_2\Delta\theta$	$L_3$	$L_3\Delta\theta$
						$4 \times 5 \times 6$	$7 \times 2$	$4 \times 6^2$	$9 \times 2$	$4 \times 6/3$	$11 \times 2$

$$L_s = 0.5 \rho U_\infty U_f \frac{A}{\pi} f \left( \sum F_1 \Delta\theta \cos\beta + \sum F_2 \Delta\theta \sin\beta \right) - 0.25 (A_f/2\pi R_1)^2 U_f^2 \sum F_3 \Delta\theta$$

$$M_s = 0.5 \rho U_\infty U_f \frac{A R_1}{\pi} \left( \sum M_1 \Delta\theta \cos\beta + \sum M_2 \Delta\theta \sin\beta \right) + 0.5 \rho U_f^2 R_1^{-1} (A_f/2\pi)^2 \sum M_3 \Delta\theta$$

$$M_1 = -0.5 \rho U_\infty U_f \frac{A R_1}{\pi} \left( \sum L_1 \Delta\theta \cos\beta + \sum L_2 \Delta\theta \sin\beta \right) - 0.5 \rho U_f^2 R_1^{-1} (A_f/2\pi)^2 \sum L_3 \Delta\theta$$

## SECTION VI

### NONLINEAR BODY AERODYNAMICS

To evaluate the body contribution to the aerodynamic derivatives of V/STOL aircraft it is necessary to include the range of flight conditions which is likely to be encountered in operation. This requires the aircraft to operate at extensive angle of attack and sideslip since the flight altitude near hovering flight is not determined by aerodynamic forces but rather from the application of power. There is, however, an area of flight where the aerodynamic and power effects will tend to be of the same order of magnitude and where neither component can be safely neglected.

It is to treat the aircraft behavior in the region where both aerodynamic forces and power are important in supporting the aircraft weight that nonlinear aerodynamics is important.

To obtain the total aerodynamics of bodies at large angles of attack and sideslip it is necessary to treat both the potential flow contribution and the viscous effects. This study has utilized slender body theory for the potential contributions, while two methods of treating the viscous effects have been examined. The first method using vortex tracking was found to be unreliable within the present state of the art and to be too unwieldy for use as a handbook procedure. The second method, using the viscous crossflow concept appears to be quite suited for a handbook procedure.

#### 1. SLENDER BODY THEORY

To completely represent the aerodynamic forces and moments on a body it is necessary to combine both the potential and the viscous contributions. To obtain the potential contribution, slender body theory is used. The development of the equations representing the slender body solutions is an adaptation of the methods of Sacks<sup>(22)</sup>. The basic equations have been modified to permit large angles of attack and sideslip to be accounted for. The ability to handle arbitrary body shapes has been attained by introducing a method of obtaining a mapping function for an arbitrary body shape.

A computer program has been written which computes five component force and moment coefficients as functions of resultant angle of attack, roll angle, yaw velocity and pitching velocity. From these coefficients the aerodynamic derivatives can be easily obtained.

The equation for the forces and moments given by Reference 22 when modified to eliminate the rolling velocity, the effect of which can be considered negligible for a body, and the time derivatives, can be written in complex form:

$$Y-iL = 2\pi\rho U_0 \bar{A}_1 \Big|_{x=l} + \rho U_0 \left[ S\bar{R} + U_0 \frac{d}{dx} (SZ_c) \right]_{x=l} \quad (79)$$

$$N-iM = -2\pi\rho U_0 \int_0^l (x-x_{cg}) \frac{\partial \bar{A}_1}{\partial x} dx - \rho U_0 \int_0^l (x-x_{cg}) \frac{\partial}{\partial x} \left[ S\bar{R} + U_0 \frac{d}{dx} (SZ_c) \right] dx \quad (80)$$

$$L' = \frac{1}{2} \rho U_0 R \oint_{x=l} F_d(z\bar{z}) - 2\pi\rho U_0 \int_0^l \bar{R} \bar{A}_1 dx - \rho U_0 \int_0^l \bar{R} \frac{d}{dx} (SZ_c) dx \quad (81)$$

The evaluation of these equations requires that the complex potential

$$F = B(x) \ln Z + \sum_{n=1}^{\infty} A_n(x) / Z^n + D(x) \quad (82)$$

be known. When the residue of the potential  $A_1(x)$  is known, the only difficulty in evaluating the total forces and moments arises in evaluating the first term of the moment equation above:

$$R \oint F_d(z\bar{z})$$

The rest of the terms are readily evaluated.

Sacks<sup>(22)</sup> has shown that

$$B(x) = \frac{U_0}{2\pi} \frac{dS}{dx} \quad (83)$$



It remains to evaluate the coefficients  $A_n(x)$  since the coefficient  $D(x)$  is not required.

The coefficients  $A_n(x)$  can be evaluated by re-expressing Equation (82) in terms of the mapping circle plane coordinate  $\zeta$ , i.e.,

$$F = B(x) \ln \zeta + \sum_{n=1}^{\infty} A_n(x) / \zeta^n \quad (84)$$

Reference 22, Appendix B, shows that this expression can be evaluated from the coefficients of the mapping from the circle plane.

$$Z = \zeta + a_0 + \sum_{n=1}^{\infty} a_n / \zeta^n \quad (85)$$

and is expressible as

$$F = \bar{R} \sum_{n=1}^{\infty} a_n / \zeta^n - R r_c^2 / \zeta + T_N(\zeta) \quad (86)$$

where

$$\zeta = r e^{i\theta} \quad (87)$$

and  $T_N(\zeta)$  is the portion of the potential required to satisfy the boundary conditions of the body and is equivalent to the expression of Equation (25) of Reference 23:

$$T_N(\zeta) = r_c^2 U_0 \left\{ - \sum_{n=0}^N (a'_n - 2n \frac{r_c'}{r_c} a_n) \frac{\zeta^{-(n+1)}}{n+1} \right. \quad (88)$$

$$+ \sum_{m=0}^N \sum_{n=0}^N \left[ m \left( \frac{nr_c'}{r_c} a_m \bar{a}_n - a_m \bar{a}_n' \right) + n \left( \frac{mr_c'}{r_c} \bar{a}_n a_m - \bar{a}_n a_m' \right) \right] \frac{\zeta^{(n-m)}}{(n-m)r_c^2(n+1)} \Big\}$$

$$+ H \ln \zeta$$

The coefficient H by comparison with the coefficient B(x) can be shown to be

$$H = \frac{U_0}{2\pi} \frac{dS}{dx} \quad (85)$$

A comparison of the two expressions for F gives the expression

$$A_1(x) = \bar{R} a_1 - R r_c^2 - r_c^2 U_0 \left[ \bar{a}'_0 + \sum_{m=1}^N \left\{ m \left( \frac{(m-1)r_c'}{r_c} \bar{a}_m \bar{a}_{m-1}' - \bar{a}_m \bar{a}_{m-1}' \right) / r_c^{2m} \right. \right. \\ \left. \left. + (m-1) \left( \frac{m r_c'}{r_c} \bar{a}_{m-1} \bar{a}_m - \bar{a}_{m-1} \bar{a}_m' \right) / r_c^{2m} \right\} \right] - \frac{d_0 U_0}{2\pi} \frac{dS}{dx} \quad (86)$$

$$U_0 = U_\infty \cos \alpha \quad (87)$$

with this expression and the definition of P (again with  $\rho = \frac{\partial}{\partial t} = 0$ )

$$R = -[r \cos \phi + q \sin \phi](x - x_{c0}) - i[U_\infty \sin \alpha + (q \cos \phi - r \sin \phi)(x - x_{c0})] \quad (88)$$

This expression for R has been modified from the definition of reference 22 to utilize resultant angle of attack and roll angle instead of angle of attack and sideslip.

All of the necessary information is now available to solve Equations (79) and (80) if it is assumed that the coefficients of the mapping function (Equation (85)) are known. The expression

$$R \oint_{x=L} F d(z \bar{z})$$

can be evaluated by integration by parts to be

$$R \oint_{x=L} F d(z \bar{z}) = R \left[ F z \bar{z} \right]_{|z_0|e^{i(2\pi+\omega_0)}}^{|z_0|e^{i\omega_0}} - \oint_{x=L} z \bar{z} dF \\ = -R \left[ \oint_{x=L} z \bar{z} dF \right] \\ = -R \left[ \oint_{x=L} z(\zeta) \bar{z}(\zeta) \frac{dF}{d\zeta} d\zeta \right] \quad (89)$$

since the first term of the integration by parts is imaginary. On the surface of the body  $\bar{Z}$  can be represented by the expression

$$\bar{Z}_B = \bar{Z}_C + \bar{a}_0 + \sum_{n=1}^N \frac{\bar{a}_n}{\bar{z}_C^n} = \frac{r_C^2}{\bar{z}_C} + \bar{a}_0 + \sum_{n=0}^N \bar{a}_n \frac{\bar{z}_C^n}{r_C^{2n}} \quad (94)$$

and the expression for  $F$  can be differentiated with respect to  $\bar{z}$  and the residue of the integral can be obtained.

Thus, assuming that a mapping function is available, it is possible to solve Equations (79), (80) and (81) for  $Y$ ,  $L$ ,  $N$ ,  $M$  and  $L'$  as functions of  $\alpha$ ,  $\phi$ ,  $q$  and  $r$ . Also by direct differentiation or by perturbing either  $\alpha$ ,  $\phi$ ,  $q$  or  $r$ , it is possible to obtain the derivatives of the coefficients as well. The above analysis can also be readily extended to include either the rolling velocity or the time-dependent behavior of the coefficients should these be desired. In the treatment of these equations it has been assumed that the forward velocity can be resolved into an axial and a crossflow component which permits the equations to be solved at angles of attack up to 90 degrees.

#### a. Simplified Method of Obtaining Major Mapping Coefficients

Section III has described the method which has been developed under this study for determining the coefficients of the mapping function. This solution makes the problem of solving for the slender body aerodynamics solvable. It is desirable, however, to simplify the procedure for treating the body aerodynamics by eliminating the need for mapping the body since this requires a great amount of work.

To obtain a method of using slender body theory for a handbook method, it is necessary to find an approximate method for estimating the most important coefficients of the mapping function in a simplified fashion. An examination of Equations (79) and (80) shows that except for the term  $A_1$  all the variables are independent of the mapping, i.e., they can be obtained directly from the body geometry and flight attitude. In addition, it can generally be assumed that the rolling moment of the body can be considered negligible. It can also be shown that the derivatives of  $Y$ ,  $L$ ,  $N$  and  $M$  with respect to  $q$  and  $r$  are dependent only on the radius of the mapping circle and the coefficient  $a_1$ . The other coefficients enter into the derivatives with respect to angle of attack and sideslip (or resultant angle of attack) through the  $\cos \alpha$  terms appearing in Equation (90). It appears from this expression that coefficients other than  $r_C$ ,  $a_0$ , and  $a_1$  may be neglected in treating the body. This would imply the simplification of Equation (90) to the form

$$A_1(x) \approx \bar{R}a_1 - Rr_c^2 - r_c^2 U_0 a_0' \frac{a_0 U_0}{2\pi} \frac{dS}{dx} \quad (95)$$

This approximation and a suitable method of estimating  $r_c$ ,  $a_0$  and  $a_1$  would permit a relatively simple procedure to be outlined for treating the potential contribution to the body aerodynamics. The most suitable method of approximating these three coefficients is to treat  $a_0$  as if it were equivalent to the centroid of the cross section, and to estimate  $r_c$  and  $a_1$  from the maximum vertical and lateral dimensions of the body. If  $2a$  is the maximum lateral dimension and  $2b$  is the maximum vertical dimension, then by letting

$$r_c = \frac{a+b}{2} \quad (96)$$

$$a_1 = \frac{b-a}{2} \quad (97)$$

a relatively good approximation for these coefficients is obtained. These approximations have been made for the T-38 body and their values are compared with those obtained from an analog mapping method and shown in Figures 54 through 56. Considering the complexity of the chosen body, it is considered that the agreement obtained is quite good. The effects on the coefficients of using these approximate values and neglecting all other coefficients are shown in Figure 57.

It is felt that this is an adequate demonstration of the capabilities of predicting this portion of the body aerodynamics.

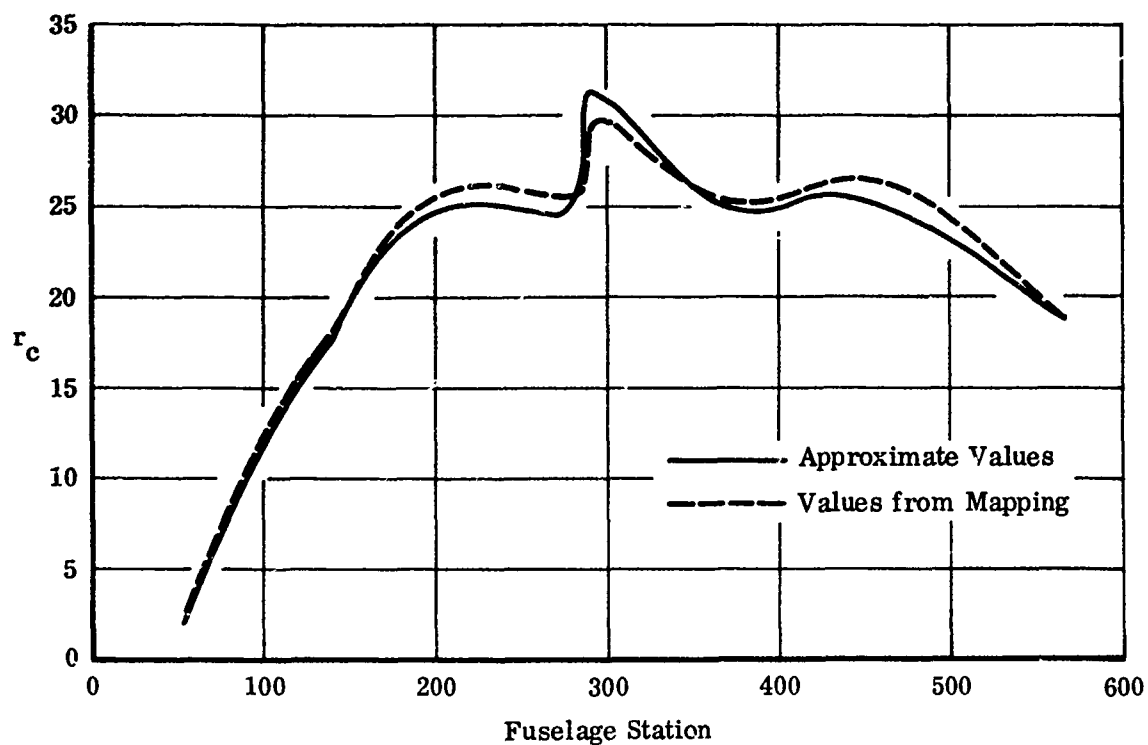


FIGURE 54. EXACT AND APPROXIMATE CALCULATION OF MAPPING CIRCLE RADIUS

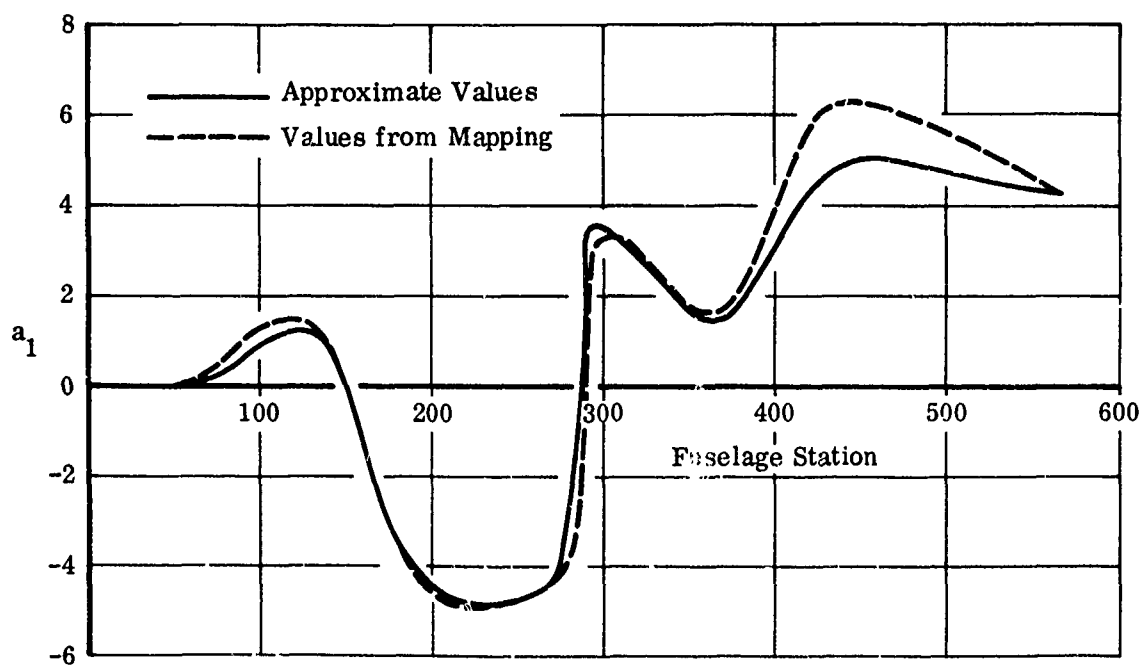


FIGURE 55. EXACT AND APPROXIMATE CALCULATION OF MAPPING COEFFICIENT  $a_1$

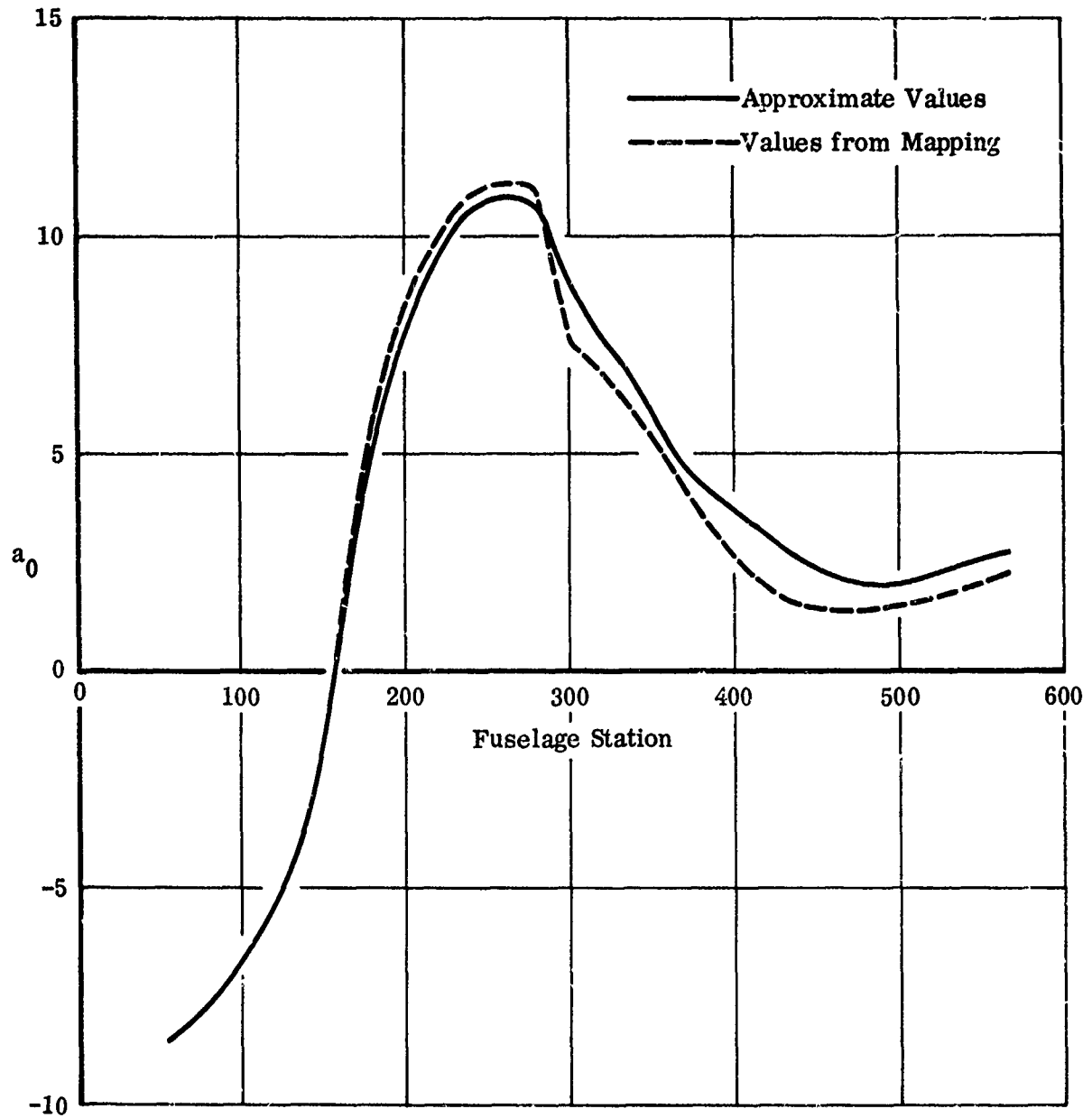


FIGURE 56. EXACT AND APPROXIMATE CALCULATION OF  
MAPPING COEFFICIENT  $a_0$

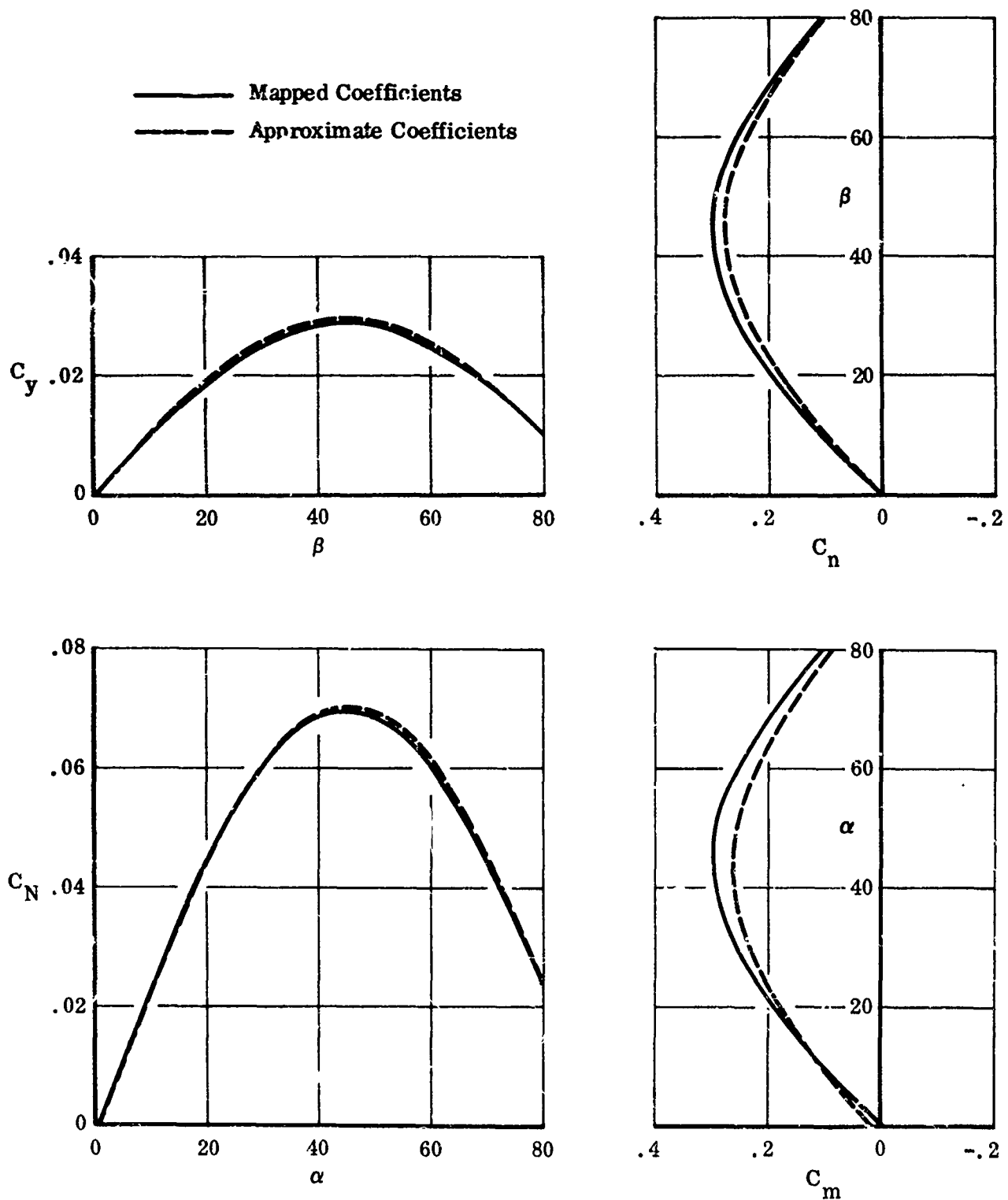


FIGURE 57. COMPARISON OF COEFFICIENTS USING EXACT AND APPROXIMATE MAPPING COEFFICIENTS

## 2. VORTEX TRACKING

One method of obtaining the nonlinear characteristics of bodies is to treat the viscous flow as if the vorticity were collecting in a single vortex pair. Under this assumption the paths of the concentrated vortices are traced and the effects of these vortices on the body are computed.

This computational model requires several simplifications to the true flow pattern about a body and the degree of success in predicting the aerodynamics is dependent upon obtaining a satisfactory set of assumptions. Reference 23 presents in detail a procedure which has been used in an attempt to obtain a valid model for arbitrary bodies at angles of attack. The basic model used is that of Bryson<sup>(24)</sup> which balances the forces between the concentrated vortex and a "feeding sheet" to obtain the equation

$$\dot{\zeta}_1 + (\zeta_1 - \zeta_0) \frac{\dot{r}}{r} = W_1 \quad (98)$$

which relates the vortex path to the local potential and to the rate of growth of the vortex strength. This equation differs from that for a free vortex ( $\dot{\zeta}_1 = W_1$ ) in that an additional velocity  $(\zeta_1 - \zeta_0) \frac{\dot{r}}{r}$ , is imposed on the vortex due to the presence of the feeding sheet.

The Bryson model also postulates the existence of a stagnation line on the body which in effect permits the strength of the vortex to be computed when used in conjunction with Equation (98).

The method of Reference 23 is a generalization of the Bryson model which permits the introduction of an arbitrary body with unsymmetrical flow conditions in the crossflow plane. This formulation retains the major features of the Bryson model but generalizes the method by relating the flow in the body plane back to a similar flow about a body of revolution by means of a mapping function. Other modifications are made as required to permit a more general flow pattern and to permit more flexibility in specifying the stagnation line.

The method was used on the T-38 body, and doing so showed several limitations in the model, the most serious of which was caused by the feeding sheet force. This force at times became exceedingly large which, in turn, produced an unrealistic path for the vortex.

During the present study, modifications were made to the above model with the intent of improving the accuracy of the method. The most satisfactory modification



consisted of two changes in the model. First, the effect of the feeding sheet was neglected. That is, the vortices were assumed to move freely with the potential flow field including the effects of the other vortex of the pair and both image vortices but assuming no feeding sheet force. The second modification was to relax the stagnation line requirement. Originally, the selection of a pair of separation lines together with the requirement that the cross flow velocity went to zero there, permitted the specification of the vortex strengths. This condition was replaced by the assumption that the rate at which the vortex was being fed was equal to the crossflow velocity at the separation line. This condition, which may be stated as

$$\frac{d\Gamma}{dx} = U_p + U_\Gamma \quad (99)$$

is more realistic as a condition from a consideration of the buildup of vorticity in the boundary layer. It also has the advantage of permitting a gradual change of vortex strength buildup regardless of the location of the separation line. With the original assumption, an abrupt change in the separation line would cause an abrupt change in the vortex strength.

Figure 58 shows a comparison of the results obtained with this modified model and test data. The agreement at angles of attack up to 40 degrees is quite good but the theoretical results begin to act erratically at higher angles. Further attempts to extend the results to higher angles of attack were unsuccessful. Additional calculations were made with this model in sideslip. In sideslip the flow pattern in the crossflow plane is unsymmetrical and the path of each vortex is different. Calculations made under these circumstances showed a very erratic behavior and did not agree at all well with available test data. The apparent reason for this was the unsymmetrical vortex location which tended to exaggerate the asymmetry.

This model has several drawbacks due to the simplifications necessary to permit a solution to be obtained. Among these are separation, a quasi two-dimensional flow field and the assumption that the vorticity behaves as a rectilinear vortex with the rotation confined to the crossflow plane.

It was decided that it would not be possible to refine the model sufficiently to allow realistic aerodynamic loads to be computed within the program time limitations so the alternative viscous crossflow model was studied and utilized to account for the viscous effects instead.

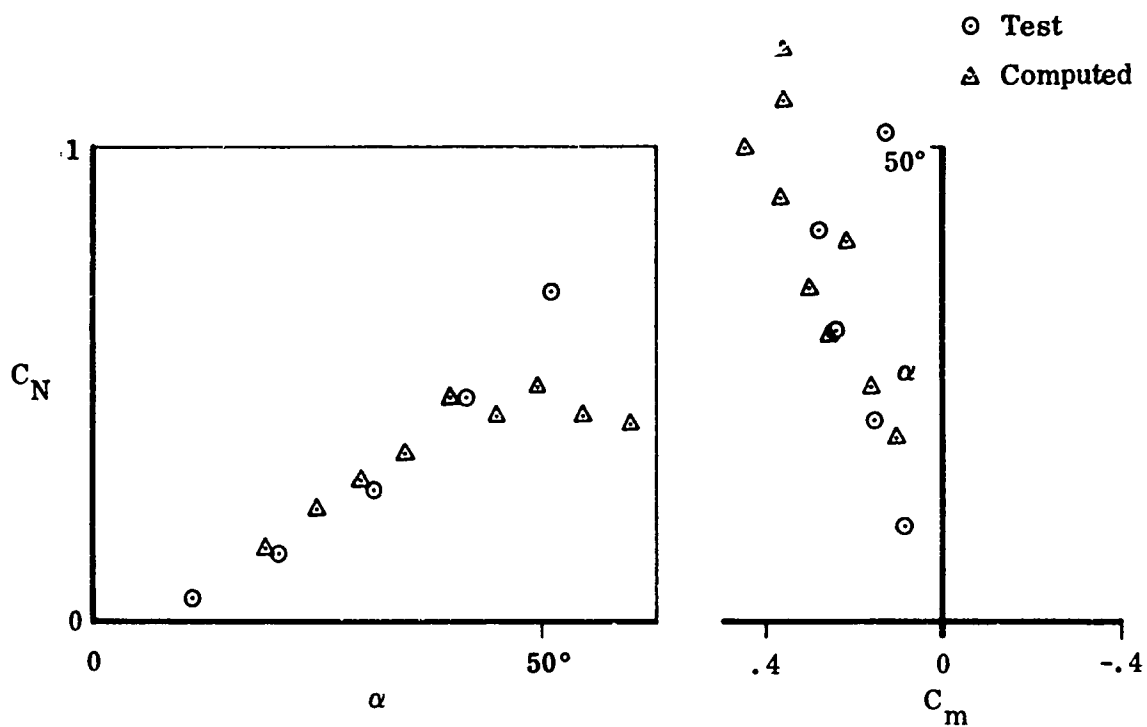


FIGURE 58. COMPARISON OF COMPUTED AND TEST NORMAL FORCE AND MOMENT COEFFICIENTS FOR F-5B BODY

### 3. VISCOUS CROSSFLOW

The viscous crossflow concept assumes that the effects of an angle of attack or sideslip can be estimated by treating only the component of dynamic pressure in the crossflow plane, and that the forces exerted at each segment of the body are independent of those sections forward or aft of this segment. This treats the body by what is essentially a strip theory based on local two-dimensional values of the body drag.

Using this concept, the incremental force on any segment can be written in the form

$$\frac{d}{dx}(\gamma - iL)_{visc} = \frac{\rho}{2} \left[ C_{D_y} c_y V_0 |V_0| - i C_{D_z} c_z W_0 |W_0| \right] \quad (100)$$

where  $(C_{D_y} c_y)$  and  $(C_{D_z} c_z)$  are local values of the crossflow drag areas per unit length in the yaw and pitch directions respectively.

To include the effects of pitching and yawing velocity, it is necessary to define the crossflow velocity components  $V_0$  and  $W_0$  as

$$V_0 = U_\infty \sin \alpha \sin \phi - r(x - x_{cg}) \quad (101)$$

$$W_0 = -U_\infty \sin \alpha \sin \phi - q(x - x_{cg}) \quad (102)$$

With these definitions and Equation (100), the viscous contributions to the forces and moments can be written

$$\left[ \gamma - iL \right]_{visc} = \frac{\rho}{2} \int_0^l \left[ C_{D_y} c_y V_0 |V_0| - i C_{D_z} c_z W_0 |W_0| \right] dx \quad (103)$$

$$\left[ N - iM \right]_{visc} = -\frac{\rho}{2} \int_0^l (x - x_{cg}) \left[ C_{D_y} c_y V_0 |V_0| - i C_{D_z} c_z W_0 |W_0| \right] dx \quad (104)$$

The above formulations permit the viscous contributions to  $Y$ ,  $L$ ,  $N$  and  $M$  to be computed as functions of  $\alpha$ ,  $\phi$ ,  $q$  and  $r$ . No attempt has been made to include a viscous contribution to rolling moment since it does not seem to be a significant contribution to the overall aircraft aerodynamics. Nor is it possible to formulate a model which

would include acceleration effects of the body. It is believed that the above formulations give the most significant effects due to viscosity.

The values for the crossflow drag coefficients can be obtained by considering two-dimensional section data for the shape under consideration or a similar shape. Calculations made thus far have shown that treating the body as an equivalent ellipse will give reasonable values for the viscous forces and moments.

Calculations were made for the T-38 body using for the crossflow drag coefficient Equation (20) of Reference 25, Chapter III.

$$C_{D_0} = 2C_f \left(1 + \frac{a_e}{b_e}\right) + 1.1 \left(\frac{b_e}{a_e}\right) \quad (105)$$

with

$$C_f = .0075$$

$a_e$  and  $b_e$  which in Equation (105) are the ellipse semi-axes parallel and perpendicular to the crossflow respectively were assumed to be the maximum dimensions of the local T-38 cross section.

The results obtained with this equation, together with the slender body values, are shown in Figure 59 as compared with test data.

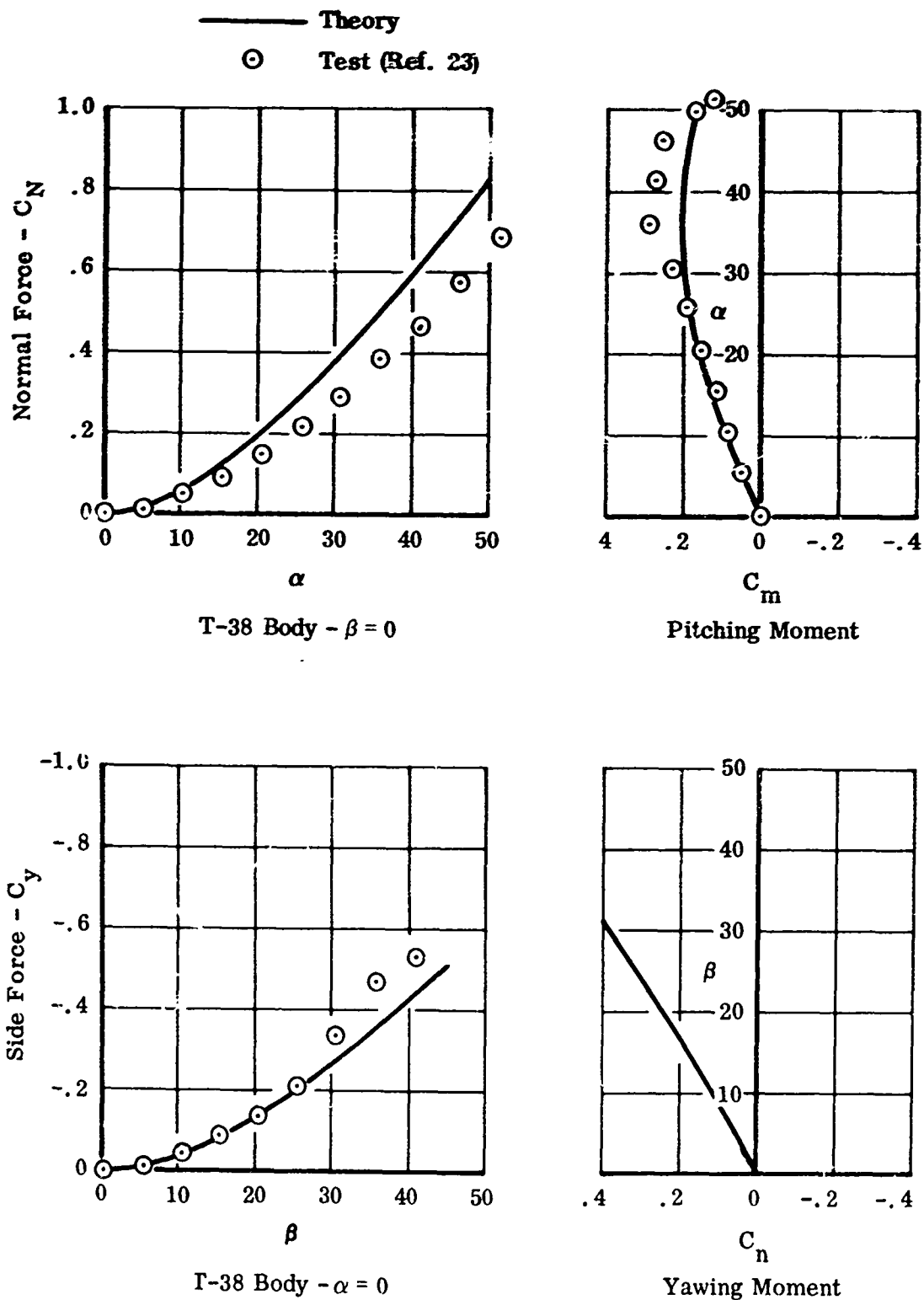


FIGURE 59. COMPARISON OF TEST AND THEORETICAL COEFFICIENTS FOR T-38 FUSELAGE

## SECTION VII

### NONLINEAR WING AERODYNAMICS

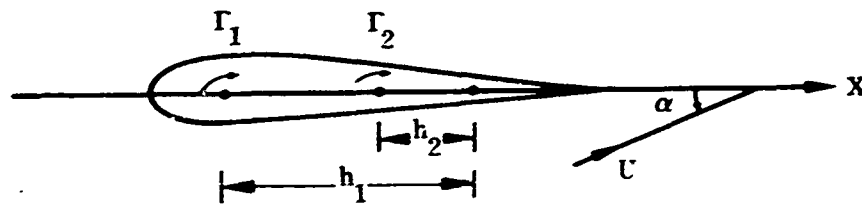
When a V/STOL aircraft is operating in the hover or transition speed regime, there will be occasions when either the aircraft angle of attack or sideslip angle are of such a magnitude as to necessitate an investigation of the nonlinear aerodynamics of the vehicle. This section deals with the problem of determining the nonlinear aerodynamic characteristics of a wing.

The method which has been developed is a modification and extension of the Weissinger method. Weissinger<sup>(26)</sup> replaced the wing by a concentrated vortex at the quarter chord position, and, by determining the downwash due to this vortex and associated trailing vortex system at a number of control points on the three quarter chord line, was able to determine the strength of this vortex. To do this he balanced the downwash due to the vorticity with the upwash due to the attitude of the wing at the control points on the wing. This procedure is effectively one of taking theoretical section data and including aspect ratio effects by accounting for the trailing vorticity. Choice of the quarter chord line for the vortex implies  $C_{m_{j/4}} = 0$  and satisfying the downwash boundary condition at the three quarter chord line results in a limit of  $2\pi$  per radian for the lift curve slope for rectangular wings as the aspect ratio is increased indefinitely. Or equivalently the section lift curve slope is  $2\pi$  per radian.

The model for the nonlinear wing problem is similar in that nonlinear section data are used to generate information for finite wings. The variation of the section lift curve slope throughout the angle-of-attack range is accounted for by locating two lifting lines at appropriate locations on the section chord and the relative strengths of the vortices are determined from test or estimated section characteristics. The problem of predicting wing lift and pitching moment characteristics is then one of solving for the induced downwash angle associated with the planform under consideration and of evaluating the lift and moment contributions at an effective angle of attack as determined from the induced downwash.

## 1. NONLINEAR SECTION MODEL

The analytical model used to represent nonlinear wing section data assumes that at an angle of attack of 90 degrees the normal force on the section is entirely due to a viscous drag, and that there is a contribution to the normal force at an arbitrary angle of attack  $\alpha$  proportional to  $\sin^2 \alpha$ . The circulation effect of the section is represented by two vortices as illustrated in the sketch below. The boundary condition for no flow through the airfoil surface is set at .75 of the chord.



Satisfying this boundary condition, we obtain

$$\frac{\Gamma_1}{2\pi h_1} + \frac{\Gamma_2}{2\pi h_2} = U \sin \alpha \quad (106)$$

The normal force contribution due to circulation effects  $C_{NIND}$  is given by

$$C_{NIND} = C_N - (C_N)_{\alpha=90} \sin^2 \alpha \quad (107)$$

in which  $(C_N)_{\alpha=90}$  is the normal force at  $\alpha = 90^\circ$ .

The contribution to the normal force coefficient due to circulation effects is assumed to be represented by

$$2 \left( \frac{\Gamma_1}{Uc} + \frac{\Gamma_2}{Uc} \right) = C_{NIND} \quad (108)$$

Equations (106), (107), and (108) may be solved for  $\Gamma_1/Uc$ ,  $\Gamma_2/Uc$  from given section data for any combination of  $h_1/c$  and  $h_2/c$ . As in the case of the linearized model of Weissinger<sup>(26)</sup>, the positions of the two vortices are found by considering the section pitching moment data.

The pitching moment about the 1/4 chord position  $C_{m_{1/4}}$  is

$$C_{m_{1/4}} = 2 \frac{\Gamma_1}{Uc} \left( \frac{h_1}{c} - .5 \right) + 2 \frac{\Gamma_2}{Uc} \left( \frac{h_2}{c} - .5 \right) + (C_N)_{\alpha=90} \sin^2 \alpha \left( .25 - \frac{\bar{x}}{c} \right) \quad (109)$$

in which  $\bar{x}$  is distance on the airfoil chord through which the viscous force acts. Substituting for  $\Gamma_1/Uc$ ,  $\Gamma_2/Uc$  from Equations (106), (107), and (108) we obtain

$$C_{m_{1/4}} = \left( \frac{h_1}{c} + \frac{h_2}{c} - .5 \right) C_{NIND} - 4\pi \frac{h_1}{c} \frac{h_2}{c} \sin \alpha + (C_N)_{\alpha=90} \sin^2 \alpha \left( .25 - \frac{\bar{x}}{c} \right) \quad (110)$$

The positions of the vortices represented by  $h_1$  and  $h_2$  in Equation (110) are chosen to give good correlation between the pitching moment calculated from Equation (110) and the section test data. The strength of the two vortices may then be obtained from Equations (106), (107), and (108) using the section normal force data.

This procedure has been checked against data from a NACA 0012 airfoil<sup>(27)</sup>. With the two vortices positioned so that  $h_1/c = .546$  and  $h_2/c = .053$ , calculations of the pitching moment against angle of attack are compared with test data in Figure 60.



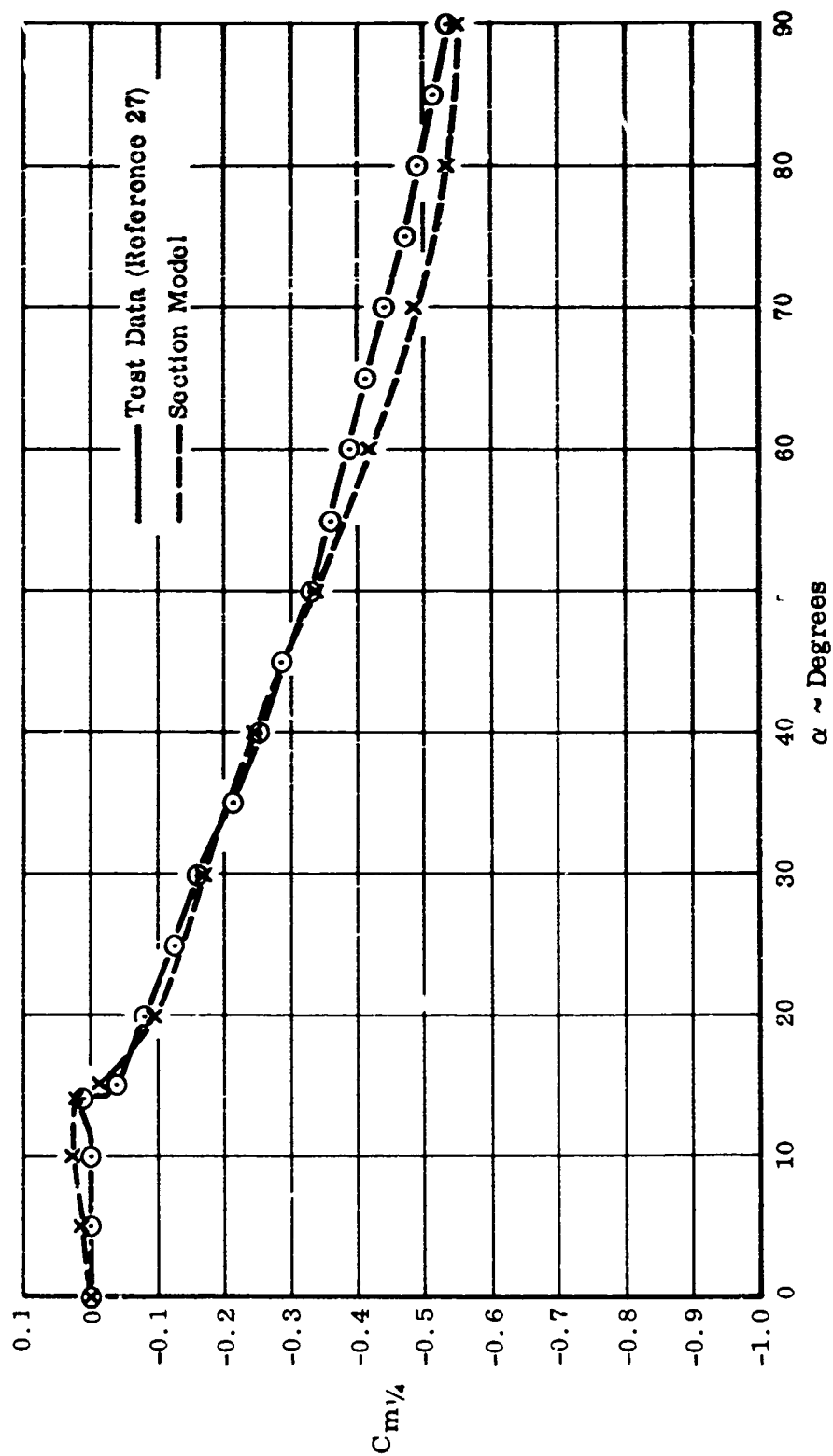


FIGURE 60. SECTION MOMENT COEFFICIENT TEST AND CALCULATED DATA

The strengths of the two vortices  $\Gamma_1$  and  $\Gamma_2$  which will give the required section normal force (given in Figure 61) are shown in Figure 62.

The capability of the section model to fit the normal force and pitching moment data very closely suggests that this section model may be used to calculate wing characteristics.

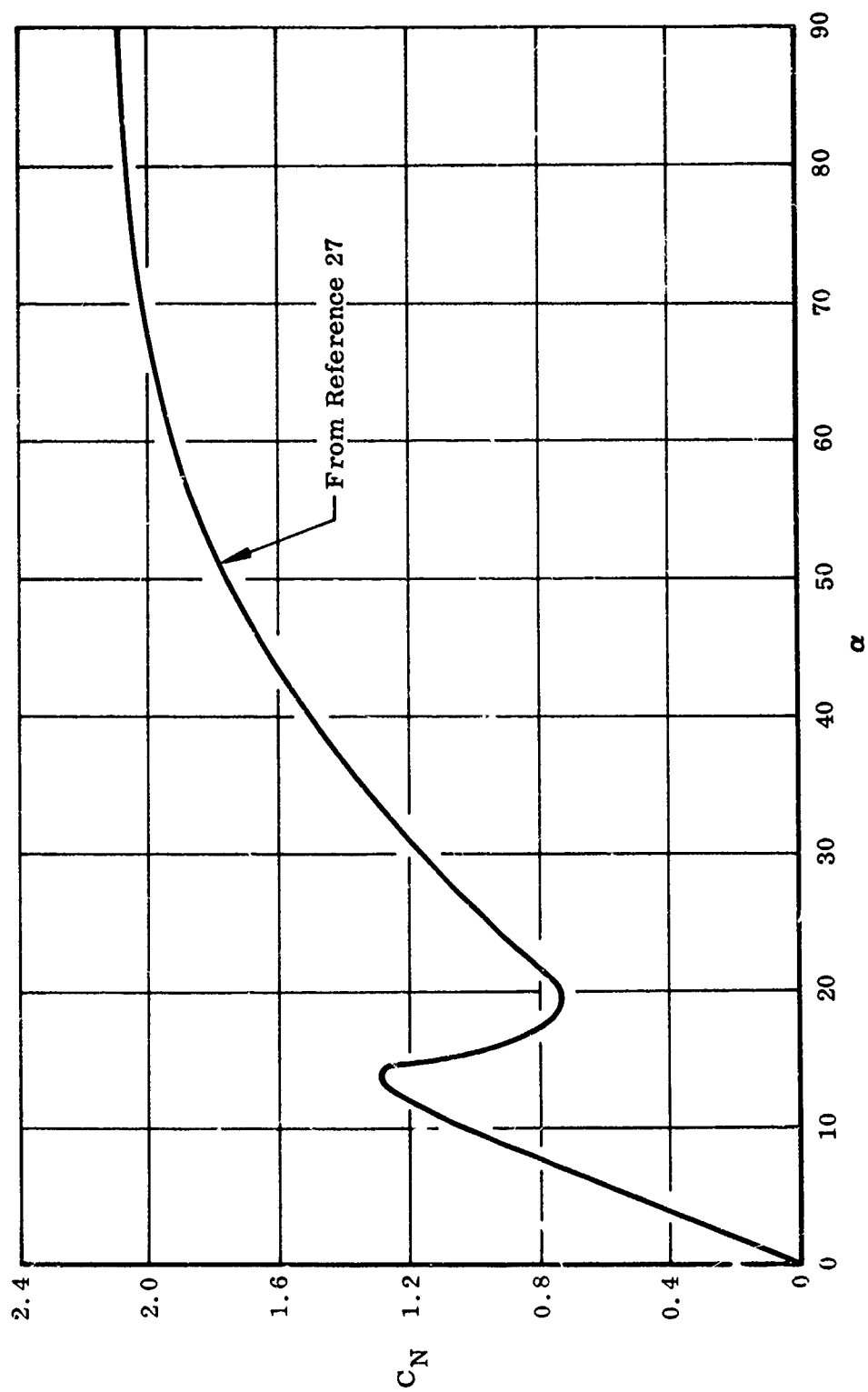


FIGURE 61. SECTION NORMAL FORCE COEFFICIENT FOR NACA 0012 AIRFOIL

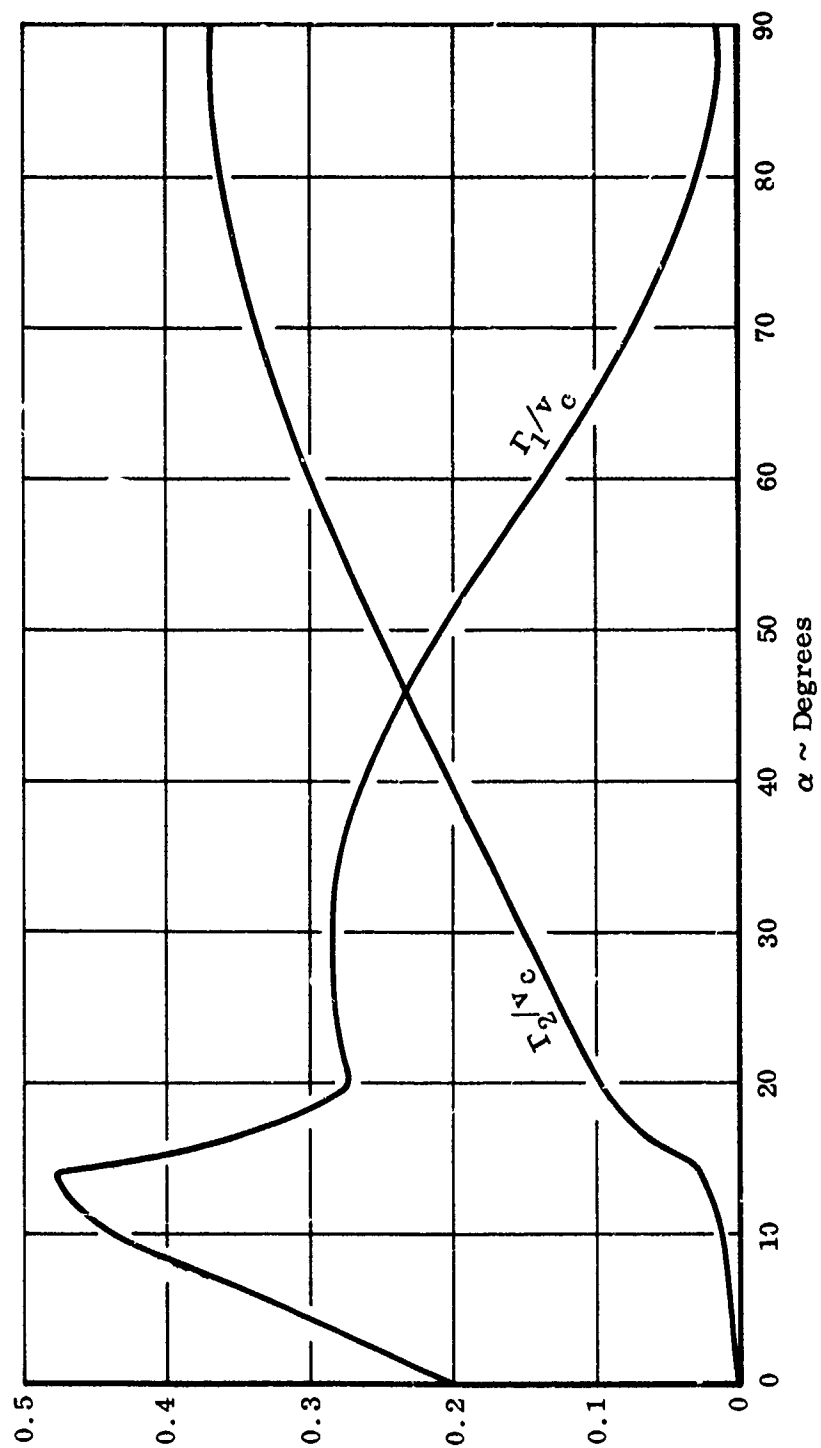


FIGURE 62. CIRCULATION STRENGTHS OF TWO LIFTING LINES FOR NACA 0012 AIRFOIL

## 2. APPLICATION OF THE SECTION MODEL TO WING CALCULATIONS

The method used to determine finite wing characteristics involves determining the effective angle of attack at a number of reference stations on the wing, using the section model. The weighting of the circulation at these sections may then be deduced, and from this weighting of circulation, the total circulation around the sections determined by satisfying the no-flow boundary condition at appropriate points on the wing. Since the circulation is not a linear function of angle of attack, an iterative procedure is necessary. First an effective angle-of-attack distribution is assumed. The weighting of the circulation between the two vortices is then determined. The circulation across the wing span may then be calculated and a new effective angle-of-attack distribution determined, and this procedure is repeated until convergence of effective angle of attack is achieved.

### a. Downwash Due to the Bound Vorticity

It is necessary to determine the downwash at the control points due to bound and trailing vorticity. We first consider the downwash due to the bound vorticity.

Consider a bound vortex line of strength  $\Gamma(\eta)$  extending from  $(\xi_i, \eta_i)$  to  $(\xi_{i+1}, \eta_{i+1})$ . Let the downwash control point be at  $P(x, y, 0)$ . This arrangement is shown in Figure 63.

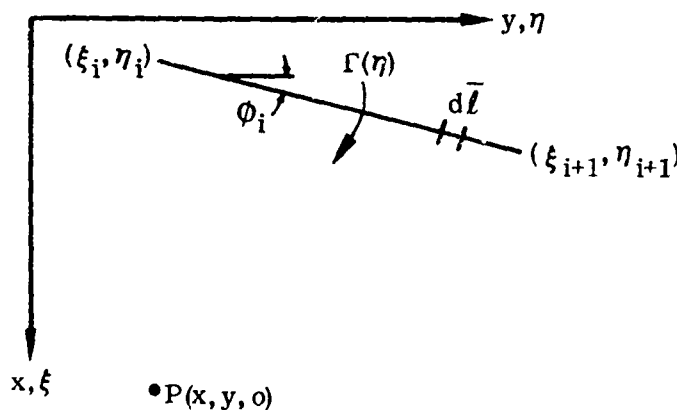


FIGURE 63. GEOMETRY FOR BOUND VORTICITY

Let  $\bar{V}_L$  be the velocity induced by the bound vorticity from  $(\xi_i, \eta_i)$  to  $(\xi_{i+1}, \eta_{i+1})$  at P then

$$\bar{V}_L = \frac{1}{4\pi} \int_{\xi_i, \eta_i}^{\xi_{i+1}, \eta_{i+1}} \Gamma(\eta) \frac{d\bar{z} \wedge \bar{r}}{R^3} \quad (111)$$

in which

$$\bar{r} = (x - \xi) \hat{i} + (y - \eta) \hat{j}, \quad R^2 = |\bar{r}|^2$$

and

$$d\bar{z} = \sqrt{d\xi^2 + d\eta^2} \left( \frac{|\eta|}{\eta} \sin \phi_i \hat{i} + \cos \phi_i \hat{j} \right)$$

Thus

$$d\bar{z} \wedge \bar{r} = \begin{vmatrix} \frac{|\eta|}{\eta} \tan \phi_i d\eta & d\eta & 0 \\ x - \xi & y - \eta & 0 \\ \hat{i} & \hat{j} & \hat{k} \end{vmatrix} \quad (112)$$

The downwash due to this piece of the lifting line  $w_L$  follows as

$$w_L = \frac{1}{4\pi} \int_{\eta_i}^{\eta_{i+1}} \frac{\Gamma(\eta)}{[(x - \xi)^2 + (y - \eta)^2]^{3/2}} \left[ \frac{|\eta|}{\eta} \tan \phi_i (y - \eta) - (x - \xi) \right] d\eta \quad (113)$$

Now  $\xi = \xi_i + (\eta - \eta_i) \frac{|\eta|}{\eta} \tan \phi_i$

so that

$$w_L = \frac{1}{4\pi} \int_{\eta_i}^{\eta_{i+1}} \left[ (x - \xi_i - (\eta - \eta_i) \frac{|\eta|}{\eta} \tan \phi_i)^2 + (y - \eta)^2 \right]^{3/2} \times \left[ \frac{|\eta|}{\eta} \tan \phi_i (y - \eta) - (x - \xi_i - (\eta - \eta_i) \frac{|\eta|}{\eta} \tan \phi_i) \right] d\eta \quad (114)$$

Equation (114) enables the downwash to be calculated in terms of  $\Gamma(\eta)$  for a given downwash control point and wing geometry.

b. Downwash Due to the Trailing Vorticity

Let  $\bar{V}_t$  be the velocity induced by the trailing vortex system at the point  $P(x, y, z)$ . Then with the aid of Figure 64 we obtain

$$d\bar{V}_t = - \frac{i}{4\pi} \frac{d\Gamma}{d\eta} d\eta \int_{LL}^{\infty} \frac{d\bar{\ell} \wedge \bar{r}}{R^3} \quad (115)$$

The lower limit in the integral, LL, represents the point on the bound vortex from which the vorticity  $d\Gamma$  has been shed,

when 
$$\bar{r} = (x - x_1)\hat{i} + (y - y_1)\hat{j} + (z - z_1)\hat{k} \quad (116)$$

and 
$$d\bar{\ell} = dx_1\hat{i} + dy_1\hat{j} + dz_1\hat{k} \quad (117)$$

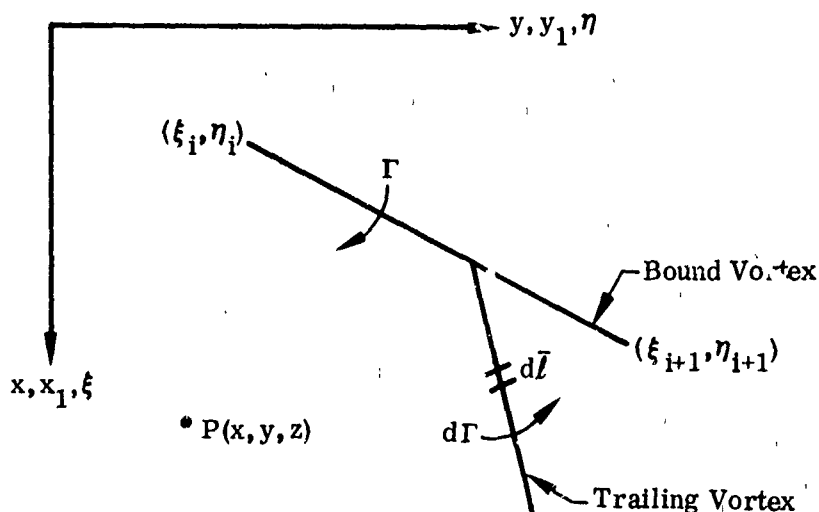


FIGURE 64. GEOMETRY OF TRAILING VORTICITY

If we assume that the trailing vorticity follows the effective angle of attack and sideslip directions we obtain

$$dx_1 = \cos \beta_e \cos \alpha_e \sqrt{dx_1^2 + dy_1^2 + dz_1^2}$$

$$dy_1 = -\sin \beta_e \sqrt{dx_1^2 + dy_1^2 + dz_1^2}$$

$$dz_1 = \cos \beta_e \sin \alpha_e \sqrt{dx_1^2 + dy_1^2 + dz_1^2}$$

Thus equation (117) gives

$$d\bar{e} = \left[ \hat{i} - \frac{\tan \beta_e}{\cos \alpha_e} \hat{j} + \tan \alpha_e \hat{k} \right] dx_1 \quad (118)$$

Substituting for  $y_1$ , and  $z_1$ , in Equation (116) we get

$$\bar{r} = (x - x_1) \hat{i} + \left[ y - z + \frac{\tan \beta_e}{\cos \alpha_e} (x_1 - \xi) \right] \hat{j} + \left[ z - \xi - \tan \alpha_e (x_1 - \xi) \right] \hat{k} \quad (119)$$

Equations (118) and (119) may be used to deduce

$$d\bar{e} \wedge \bar{r} = \begin{vmatrix} 1 & -\frac{\tan \beta_e}{\cos \alpha_e} & \tan \alpha_e \\ x - x_1 & y - z + \frac{\tan \beta_e}{\cos \alpha_e} (x_1 - \xi) & z - \xi - \tan \alpha_e (x_1 - \xi) \\ \hat{i} & \hat{j} & \hat{k} \end{vmatrix} dx_1 \quad (120)$$

Writing

$$d\bar{V}_t = du_t \hat{i} + dv_t \hat{j} + dw_t \hat{k}$$

we obtain

$$d\omega_t = \frac{1}{4\pi} \left[ y - z + \frac{\tan \beta_e}{\cos \alpha_e} (x - \xi) \right] d\Gamma \int_{\omega}^{\infty} \frac{dx_1}{R^3} \quad (121)$$



in which

$$R = \left[ (x - x_1)^2 + \left( y - \eta - \xi \frac{\tan \beta_e}{\cos \alpha_e} + \frac{\tan \beta_e}{\cos \alpha_e} x_1 \right)^2 + \left( z - \zeta + \xi \tan \alpha_e - \tan \alpha_e x_1 \right)^2 \right]^{1/2} \quad (122)$$

From Equation (122) we may obtain  $R^3$  in the form

$$R^3 = \left\{ a + bx_1 + cx_1^2 \right\}^{3/2} \quad (123)$$

in which

$$a = x^2 + \left( y - \eta - \xi \frac{\tan \beta_e}{\cos \alpha_e} \right)^2 + \left( z - \zeta + \xi \tan \alpha_e \right)^2$$

$$b = -2 \left[ x - \frac{\tan \beta_e}{\cos \alpha_e} \left( y - \eta - \xi \frac{\tan \beta_e}{\cos \alpha_e} \right) + \left( z - \zeta + \xi \tan \alpha_e \right) \tan \alpha_e \right]$$

$$c = \frac{\sec^2 \beta_e}{\cos^2 \alpha_e}$$

The integral  $\int_{-\infty}^{\infty} \frac{dx_1}{R^3}$  in Equation (121) may be

integrated in closed form and an integral expression deduced for  $w_t$ . The analysis, given in Appendix II, results in the following expression for  $w_t$

$$w_t = \frac{1}{4\pi} \int_{\eta_i}^{\eta_{i+1}} \left\{ \frac{(H\eta + I)(F\eta + G)}{\sqrt{(1 + \tan^2 \phi_i)(\eta^2 + D\eta + E)}} - \sqrt{1 + a_i^2 + b_i^2} (H\eta + I) \right\} \frac{d\eta}{d\gamma} \frac{d\gamma}{A\eta^2 + B\eta + C} \quad (124)$$

Equation (114) with Equation (124) are the basic expressions for determining the downwash at a control point for a given wing geometry and flight condition.

### 3. METHOD FOR CALCULATION OF WING CHARACTERISTICS

The downwash at a control point  $P(x, y, z)$  due to the bound vorticity in the interval  $(\eta_i, \eta_{i+1})$  together with the associated trailing vorticity is  $w_L + w_t$  which is given by the integrals in Equations (114) and (124). By determining similar integral expressions for the other bound and trailing vortex segments, it is possible to determine a series of integrals whose sum will represent the downwash at a general control point. The problem we are faced with is the indirect one of being given the downwash at the control points, and being required to determine the  $\Gamma(\eta)$  distribution which will give this specified downwash. Since  $\Gamma(\eta)$  is to be integrated to determine the downwash we have an integral equation for  $\Gamma(\eta)$ . The procedure which has been taken to solve this equation is to choose a number of circulation control points, say  $\eta_0, \eta_1, \dots, \eta_n$ , and to write  $\Gamma(\eta)$  as a Lagrangian polynomial in terms of the circulation at these control points.

$$\text{Thus } \Gamma(\eta) = \frac{(\eta - \eta_1)(\eta - \eta_2) \dots (\eta - \eta_n)}{(\eta_0 - \eta_1)(\eta_0 - \eta_2) \dots (\eta_0 - \eta_n)} \Gamma(\eta_0) + \dots + \frac{(\eta - \eta_0) \dots (\eta - \eta_{n-1})}{(\eta_n - \eta_0) \dots (\eta_n - \eta_{n-1})} \Gamma(\eta_n) \quad (125)$$

This representation for  $\Gamma(\eta)$  permits the integral for  $W_L$  and  $W_t$  to be evaluated in terms of the coefficients  $\Gamma(\eta_i)$ ,  $i = 0, 1, \dots, n$ . The total circulation at a given wing station is distributed between the two lifting lines by weighting the vorticity. This weighting of vorticity, which is a function of effective angle of attack, is determined from the section model. An example of the weighting function calculated for the NACA 0012 airfoil is shown in Figure 65. The expression for the downwash may be written in matrix form as follows:

$$[AW + B(I - W)]\Gamma = D \quad (126)$$

in which **A**, **B** are the matrices for the leading and aft lifting lines representing the coefficients of the circulation column vector  $\Gamma$ . **W** and **I - W** are matrices which give the weighting of the vorticity between the leading and aft lifting lines. **D** is the downwash column vector.

The procedure has been first checked for the linear angle-of-attack range. Calculations of the spanwise loading for an aspect ratio 5 rectangular wing with sweep

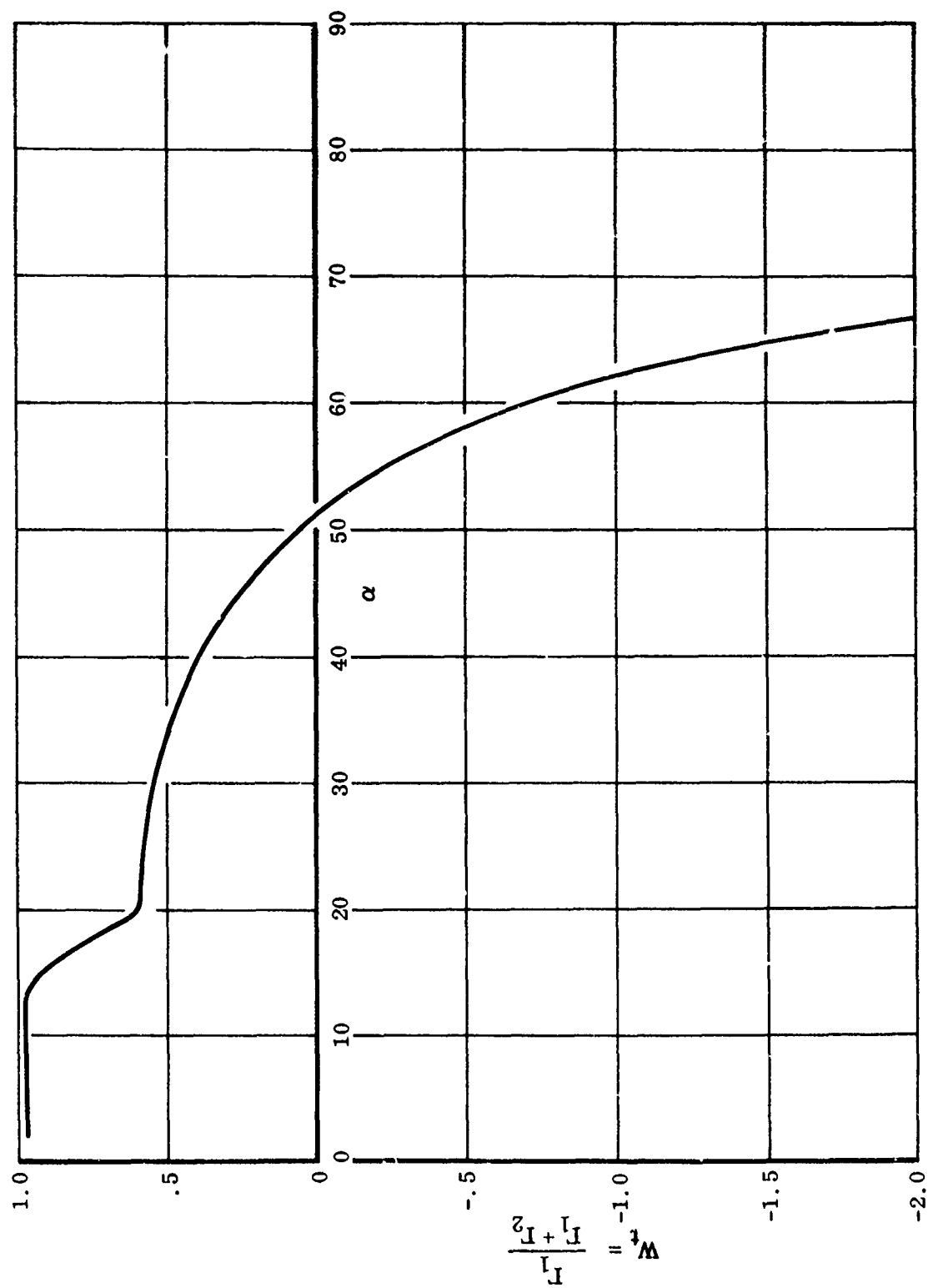


FIGURE 65. WEIGHTING OF CIRCULATION BETWEEN THE LIFTING LINES

back angles of  $0^\circ$  and  $45^\circ$  are shown in Figure 66. These calculations compare favorably with the calculation of Reference 26 and test data of Reference 28. Further calculations for nonlinear  $\alpha$  will be given in Volume II.

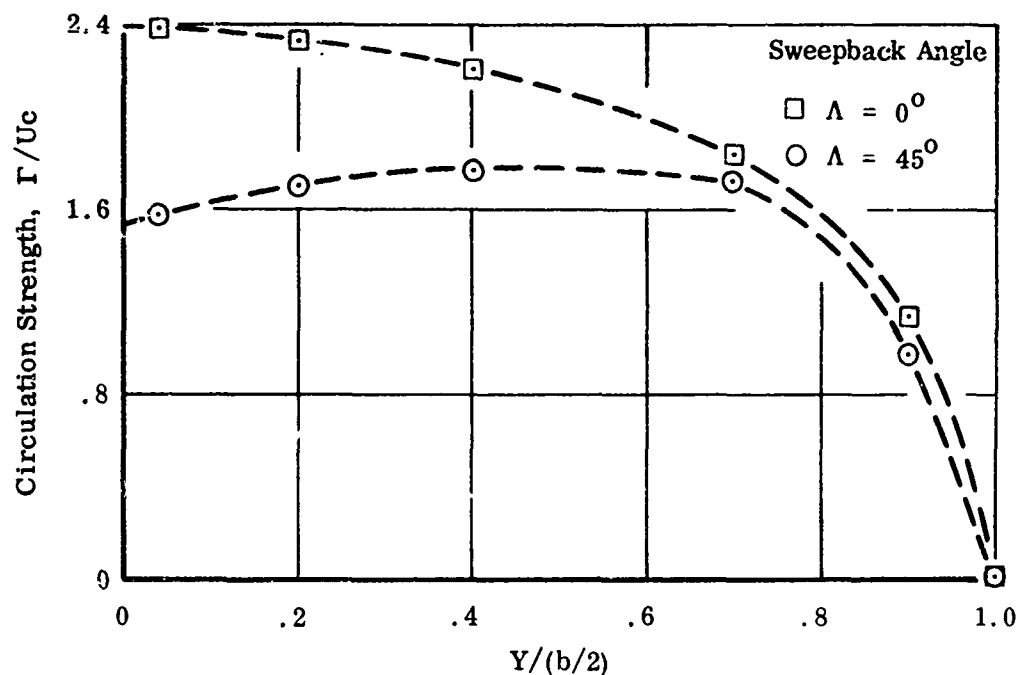


FIGURE 66. SPANWISE LOADING FOR ASPECT RATIO 5 RECTANGULAR WING

It is possible, using this approach, to make calculations for a wing with a flap. The section lift and pitching moment would be changed depending on flap deflection angle, flap chord, etc. The change in section characteristics would, in turn, change the circulation weighting function. No calculations have been made for wings with flaps. It may be necessary to include two more lifting lines to represent the flap for more satisfactory correlation with test data.

## SECTION VIII

### EMPIRICAL METHODS USING JET FLOW FIELD THEORY

The computer program which calculates the induced velocity field due to single or multiple jets exhausting into an arbitrarily directed mainstream, developed in Section II, may be utilized in the development of handbook methods for estimating induced forces and moments on supporting structures adjacent to the exhausting jets. In this section, methods for the wing and fuselage are presented to illustrate the utility of the jet flow field program for the development of handbook methods.

#### 1. EMPIRICAL METHODS FOR THE WING

Three different approaches, each utilizing the jet flow field program, have been used to obtain empirical methods for the wing. The first approach taken was to substitute an equivalent area circle for a wing to evaluate the induced forces and moments. The second approach considered the wing planform geometry ( $\Delta\theta$  method). In the third method an equivalent plain wing is constructed so that classical methods for calculating wing force and moment may be used. A discussion of the methods and results follows.

##### a. Equivalent Area Circle

The major part of the lift loss experienced by a VTOL vehicle is due to adverse pressure distributions on the lower surface of the vehicle <sup>(18), (29)</sup>. This suggests that a good estimate of these lift losses might be obtained by determining the lift losses on an equivalent circular area of an infinite flat plate from which the jet or jets are exhausting.

Pressure coefficients computed by the Jet Flow Field Program were integrated numerically to obtain total induced forces in the plane of the jet exit. Figure 67 shows the computed variation of the induced force on a flat plate around a normally exhausting jet with velocity ratio for two values of the parameter  $\sqrt{\frac{S_j}{S}}$ , where  $S_j$  is the jet exit area and  $S$  the portion of the infinite flat plate area over which the induced force is evaluated. The lift increment due to jet operation,  $\Delta L$ , is defined as  $\Delta L = F + T$

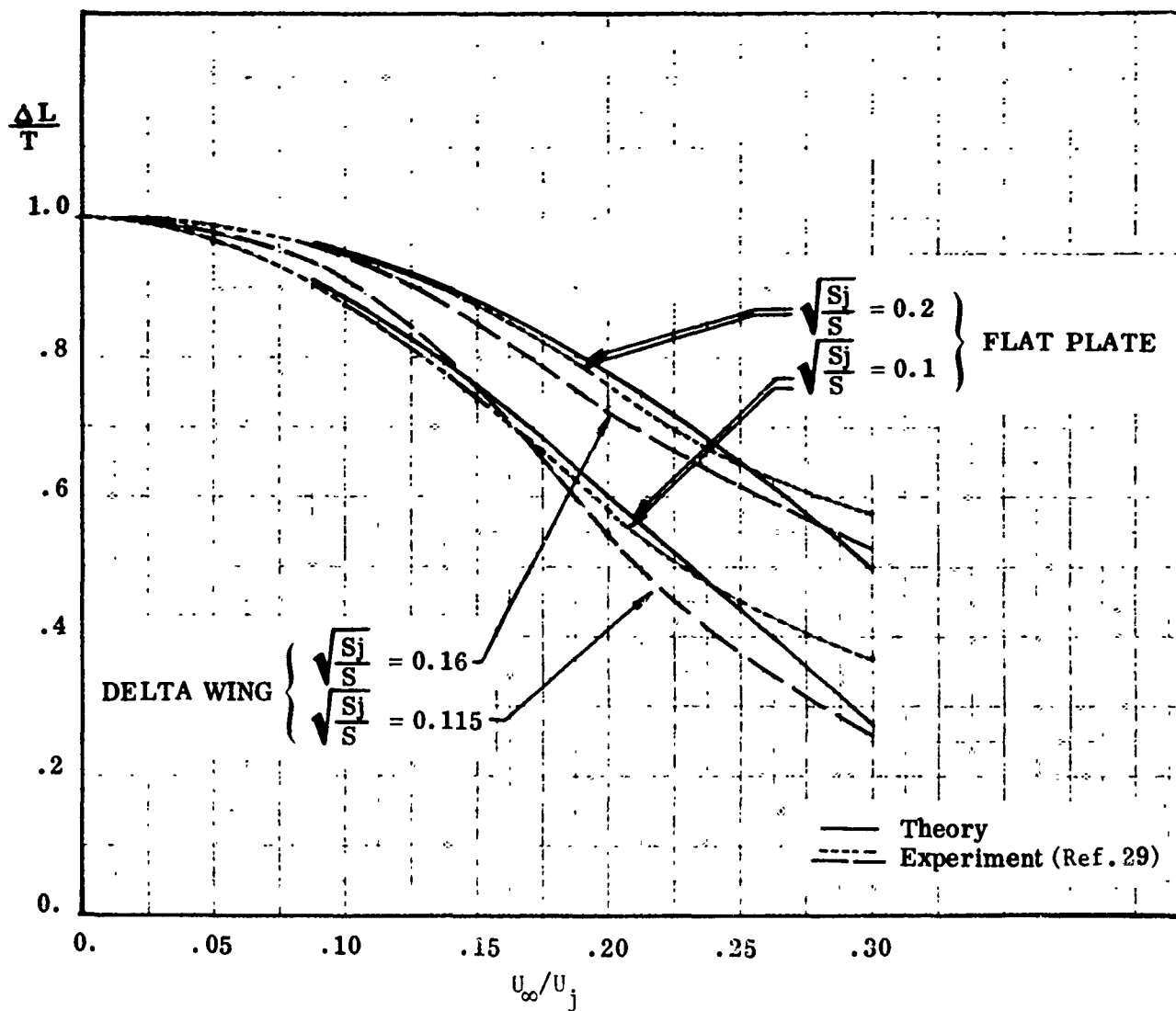


FIGURE 67. INDUCED FORCES ON FLAT PLATE AND DELTA WING

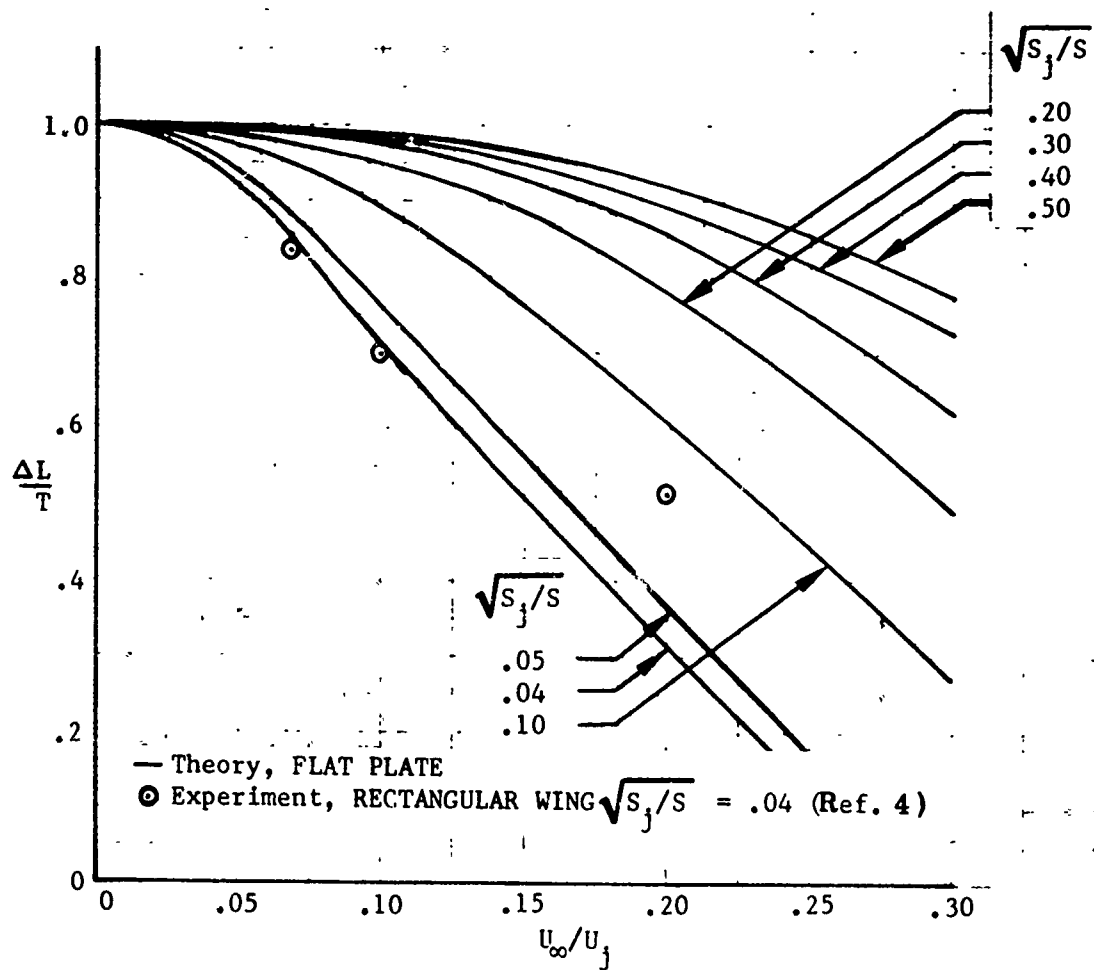


FIGURE 68. INDUCED FORCES ON FLAT PLATE AND RECTANGULAR WING,  $x_j/c = 0.5$ , EQUIVALENT AREA CIRCLE

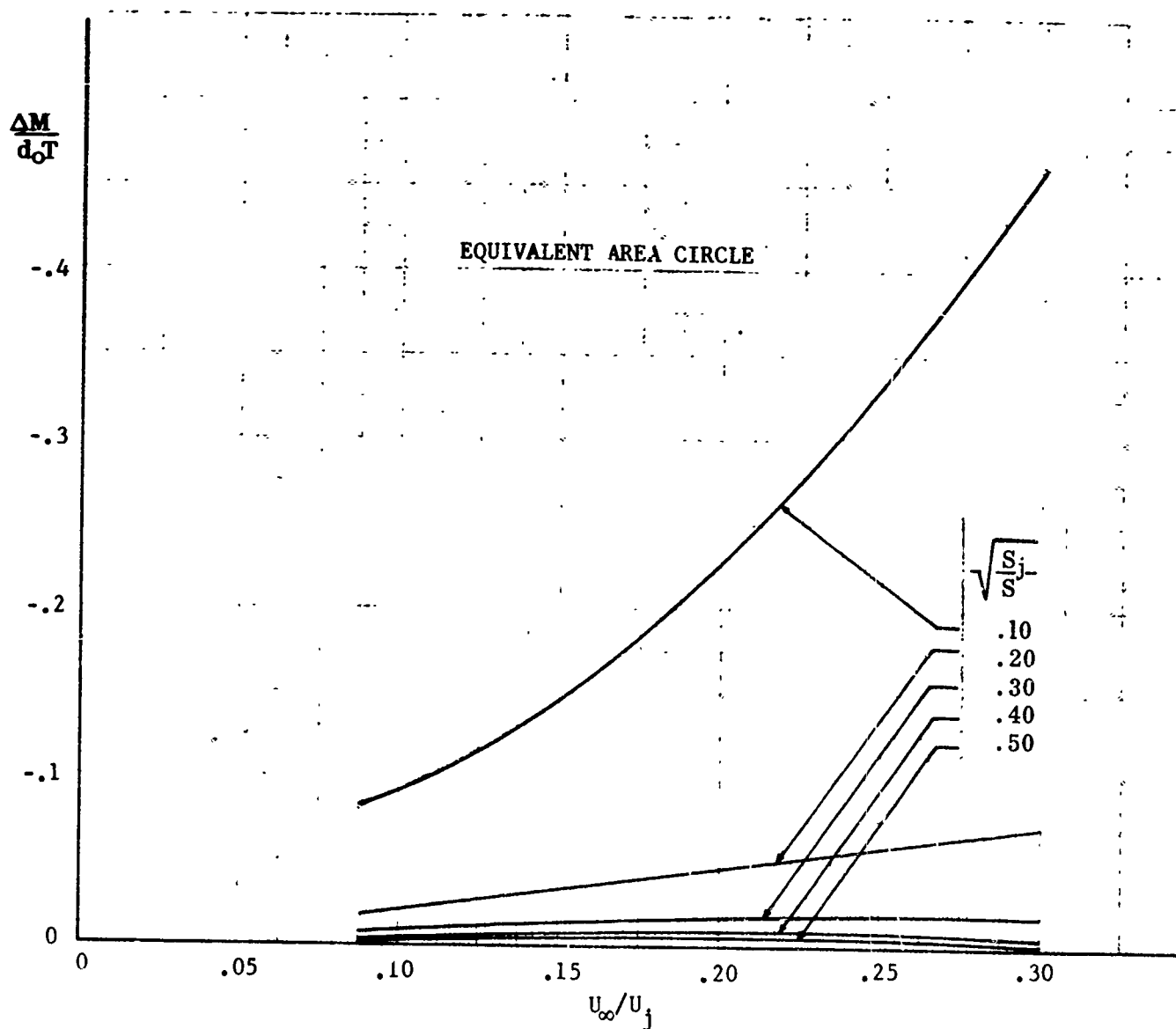


FIGURE 69. INDUCED MOMENTS ABOUT AXIS OF JET



where  $F$  is the jet-induced force and  $T$  the static thrust of the jet. Good correlation with the experimental data of Reference 29 is discernible. Experimental data on induced forces for delta wings with similar  $\sqrt{\frac{S_j}{S}}$  values indicate the utility of the jet model and the associated computer program in estimating forces induced by exhausting jets on finite wings. The variation of induced force with velocity ratio for a range of the parameter  $\sqrt{\frac{S_j}{S}}$  is shown in Figure 68. Figure 69 shows the induced moments computed about the axis of the jet as a function of velocity ratio for a range of the parameter  $\sqrt{\frac{S_j}{S}}$ .

Experimental data points obtained for a rectangular wing with an aspect ratio of 3.0 are shown in Figure 68 for comparison with computations for a flat plate with the same  $\sqrt{\frac{S_j}{S}}$  value. Very good agreement for the low velocity ratio data points is evident. The error incurred in the computed values, by letting a circle of equivalent area represent the rectangular wing, becomes significant for the high velocity ratio data point.

This substitution of an equivalent area circle for the purpose of evaluating induced forces, as shown schematically in Figure 70(a), disregards induced forces on the shaded portions of the rectangular wing and replaces them with the induced forces on the cross-hatched portions of the circle. For the rectangular wing of Reference 2, this affects approximately 36 percent of the total area of the wing. By comparison, Figure 70(b) shows the relationship between a delta wing, sweep back angle of  $60^\circ$ , and the circle of equivalent area. The shaded area which is replaced by the cross-hatched area now represents approximately 16 percent of the total wing area. The shaded and cross-hatched areas are also seen to constitute a better substitution, in terms of respective distances from the centrally located jet exit, for the delta wing configuration as compared to the rectangular wing.



FIGURE 70. EQUIVALENT CIRCULAR AREAS FOR RECTANGULAR AND DELTA WINGS

b.  $\Delta\theta$  Method

Due to the need for improved accuracy a method was developed which includes the wing planform in greater detail. The contribution to the

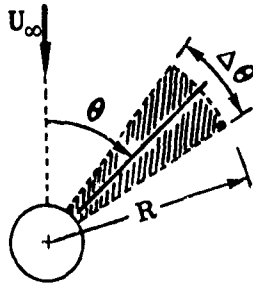


FIGURE 71. SCHEMATIC OF SAMPLE WING

ratio of total induced force to installed thrust on a wing of the shaded segment of Figure 71 can be evaluated if

$$\int_{1/2}^{R/d_0} c_p(r/d_0) d(r/d_0)$$

is known as a function of  $\theta$ , for a given velocity ratio and deflection angle of the exhausting jet. Then the ratio of induced force to thrust ratio on the segment,

$$\frac{F}{T} = \frac{2}{\pi} \left( \frac{U_\infty}{U_j} \right)^2 \int_{\theta - \Delta\theta/2}^{\theta + \Delta\theta/2} \int_{1/2}^{R/d_0} c_p(r/d_0) d(r/d_0) d\theta \quad (127)$$

$$\frac{F}{T} = \frac{2}{\pi} \left( \frac{U_\infty}{U_j} \right)^2 \Delta\theta \int_{1/2}^{R/d_0} c_p(r/d_0) d(r/d_0) \quad (128)$$

By employing numerical integration of the pressure coefficients computed by the jet flow field program in the plane of the jet exit, curves of

$$\int_{1/2}^{R/d_0} c_p(r/d_0) d(r/d_0)$$

versus  $R/d_0$  at constant  $\theta$  can be generated for a range of velocity ratios and jet deflection angles. Figures III-1 through III-6 in Appendix III are examples of sets of curves that can be utilized in the method.

A wing of arbitrary planform can be broken down into a number of segments as illustrated in Figure 72. The ratio of induced force to thrust is

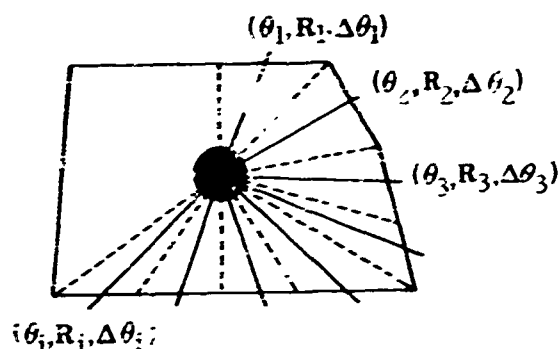


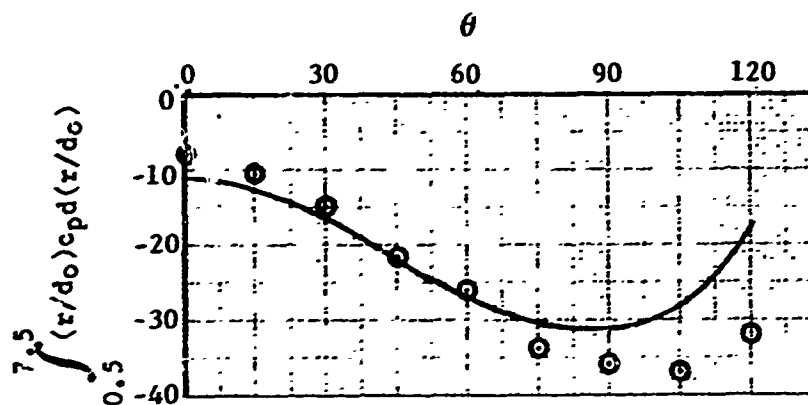
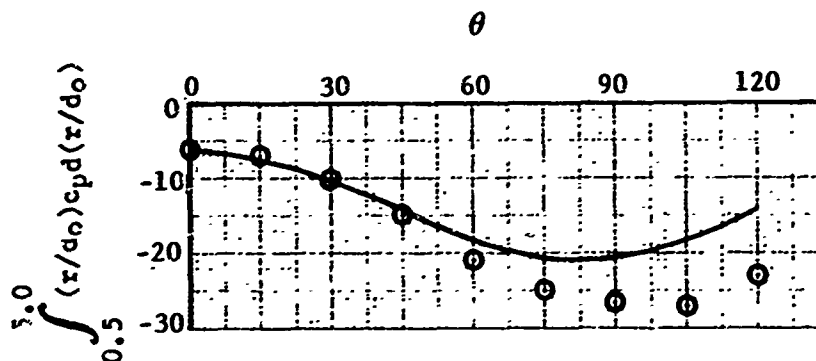
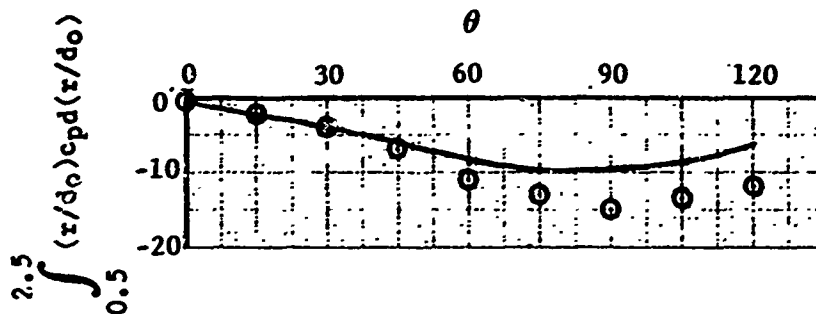
FIGURE 72. SEGMENTATION OF SAMPLE WING

evaluated by obtaining the appropriate value of

$$\int_{1/2}^{R/d_0} c_p(r/d_0) d(r/d_0)$$

from the curves and multiplying by the appropriate  $\Delta\theta$  and coefficient. The contributions are then added to obtain the total induced force to thrust ratio on the wing.

A comparison of experimental and calculated values of surface force on a flat plate is shown in Figure 73. The results of a delta wing and a rectangular wing are shown in Figure 74 and Table 2.



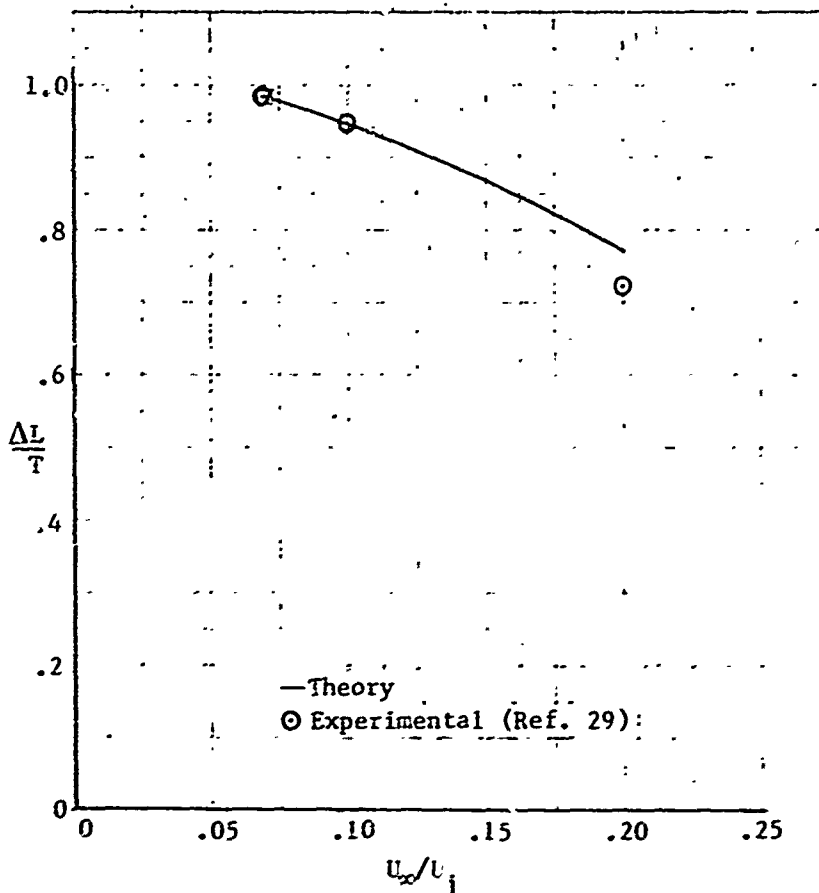
⊙ Experimental data for  $U_j/U_\infty = 8$ , Ref 12.

— Calculated values by jet flow field program for  $U_j/U_\infty = 8$ .

FIGURE 73. DISTRIBUTION OF SURFACE FORCE AROUND THE JET

TABLE 2. INDUCED FORCES ON A RECTANGULAR WING ( $\Delta\theta$  METHOD)

Jet Location	$U_j/U_\infty$	$(\Delta L/T)_{\text{exp.}}$	$(\Delta L/T)_{\text{emp.}}$
0.2	5	0.43	0.40
0.2	10	0.70	0.75
0.2	15	0.85	0.89
0.5	5	0.52	0.21
0.5	10	0.66	0.68
0.5	15	0.82	0.84
0.8	5	1.00	0.18
0.8	10	0.81	0.67
0.8	15	0.82	0.83

FIGURE 24. INDUCED FORCES ON A DELTA WING,  
 $\Delta\theta$  METHOD

### c. Equivalent Plain Wing

A jet exhausting into a freestream will induce a downwash component of velocity over the wing planform. The surface boundary condition will be satisfied, in a linearized form, when this downwash velocity component is cancelled by some mechanism. A convenient way of producing a downwash to cancel that produced by the jet is to construct an equivalent plain wing with an appropriate camber distribution. Classical methods may then be used to calculate the power induced force and moment on the wing.

Power induced section characteristics may be determined using linearized thin airfoil theory as follows.

Consider the problem of determining the lift and pitching moment on a wing section in the presence of a jet exhausting into a uniform freestream  $U_\infty$  directed along the positive x-axis. Let the jet induced downwash over the wing section,  $0 \leq x \leq c$  be  $w(x)$ . Let  $z$  be the displacement normal to the x-axis of the equivalent airfoil section as defined above. Then,  $\frac{dz}{dx} = \frac{w}{U_\infty}$ , and so

$$z(x) = \int_0^x \frac{w(x)}{U_\infty} dx \quad (129)$$

Thus, writing

$$\frac{dz}{dx} = \frac{w}{U_\infty} = \sum_{n=0}^{\infty} B_n \cos n\phi \quad (130)$$

in which  $\phi$  is given by  $x = c/2 (1 + \cos \phi)$ , (131)

we obtain 
$$B_0 = \frac{1}{\pi} \int_0^\pi \frac{w}{U_\infty} d\phi, \quad B_n = \frac{2}{\pi} \int_0^\pi \frac{w}{U_\infty} \cos n\phi d\phi, \text{ for } n \geq 1 \quad (132)$$

The section lift and pitching moment coefficients may be determined as functions of  $B_0$ ,  $B_1$ , and  $B_2$  (details may be found in Reference 47). Thus,

$$C_L = -2\pi \left( B_0 + \frac{1}{2} B_1 \right) \quad (133)$$

and

$$C_m = \frac{\pi}{4} (B_1 + B_2) - \frac{1}{4} C_L \quad (134)$$

Finite wing lift and pitching moment coefficients may be determined using the methods described in References 48 and 49.

Examples of equivalent section camber lines are shown in Figures 75, 76 and 77.

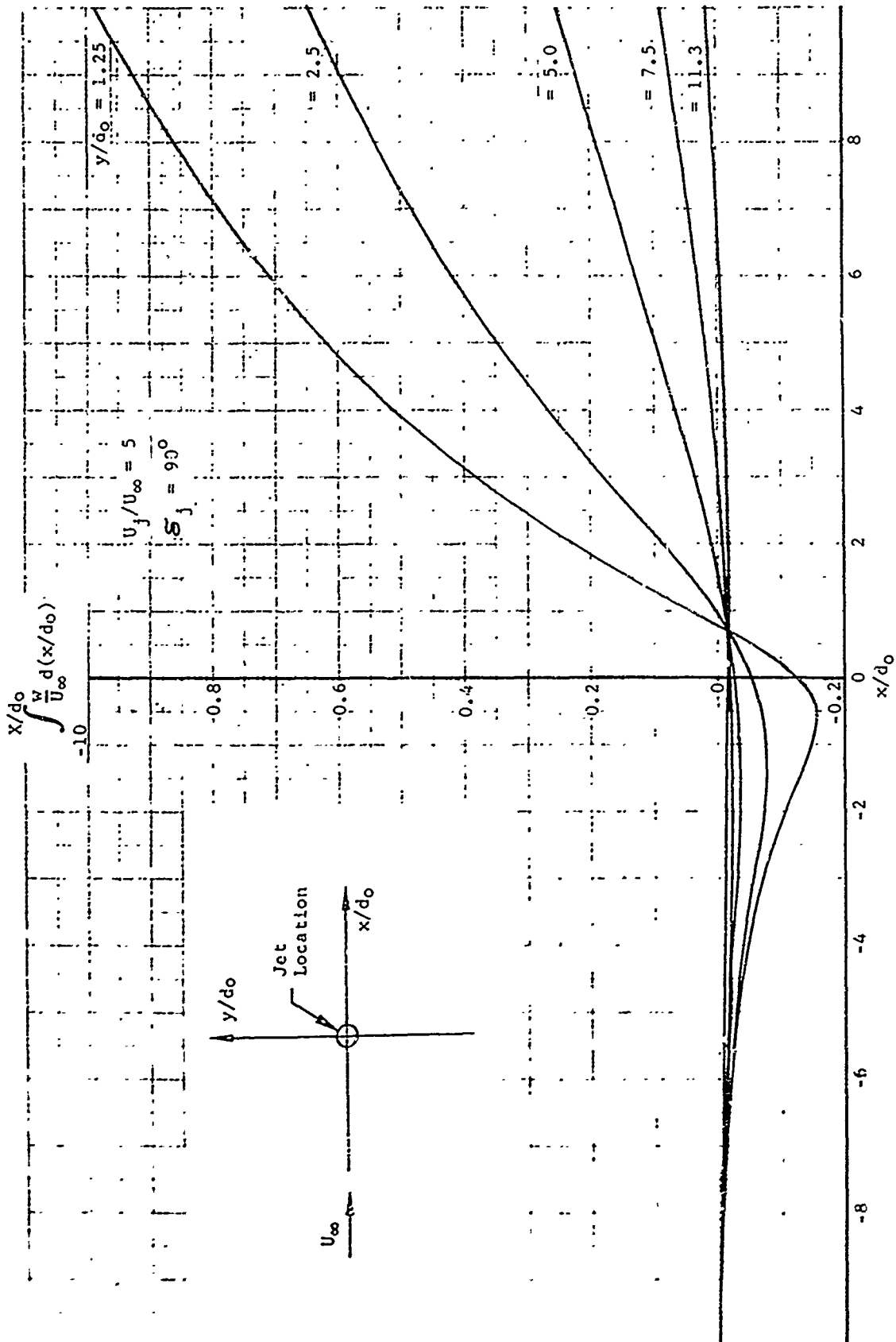


FIGURE 75. CURVES FOR EFFECTIVE ANGLE OF ATTACK AND CAMBER CALCULATION

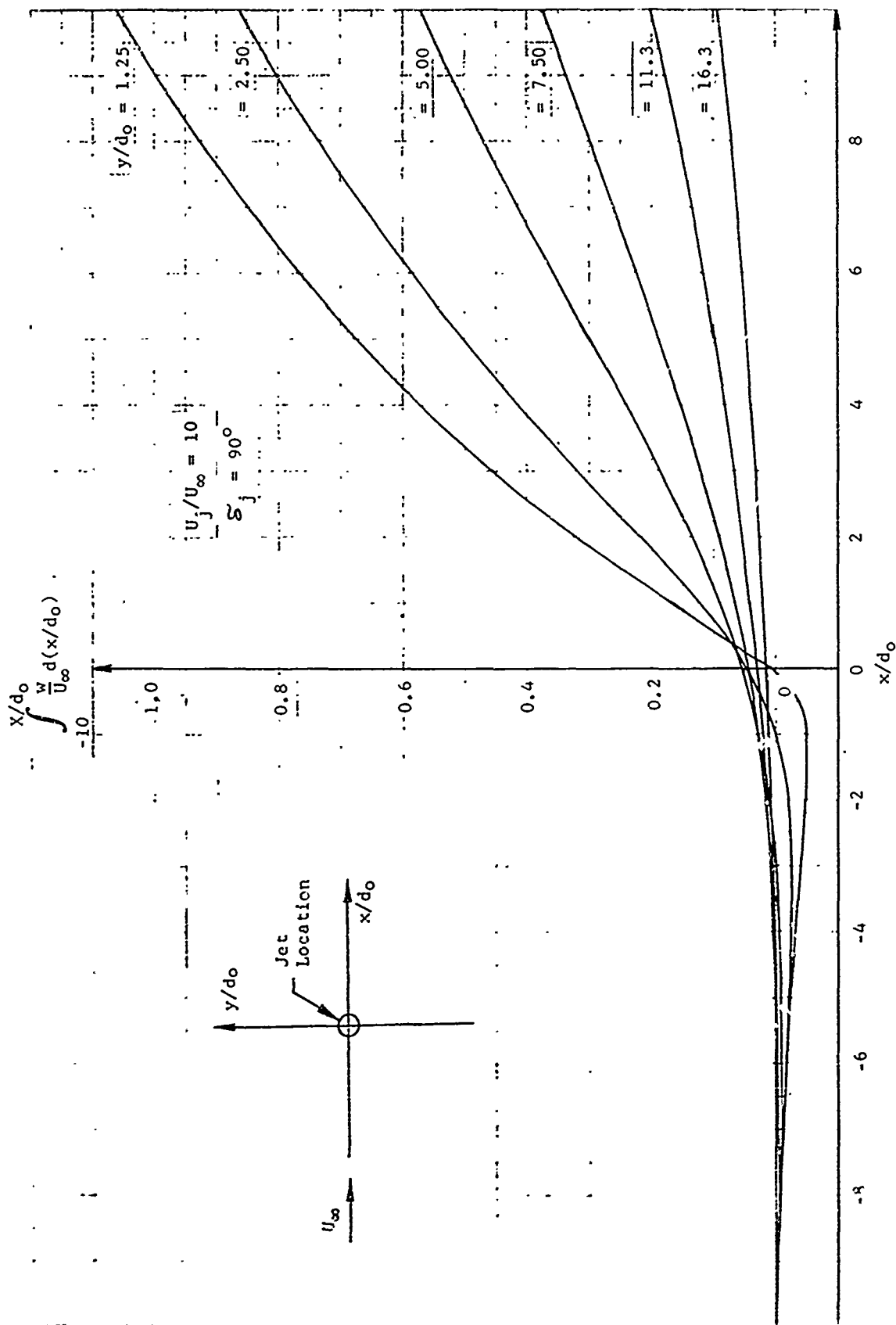


FIGURE 76 . CURVES FOR EFFECTIVE ANGLE OF ATTACK AND CAMBER CALCULATION



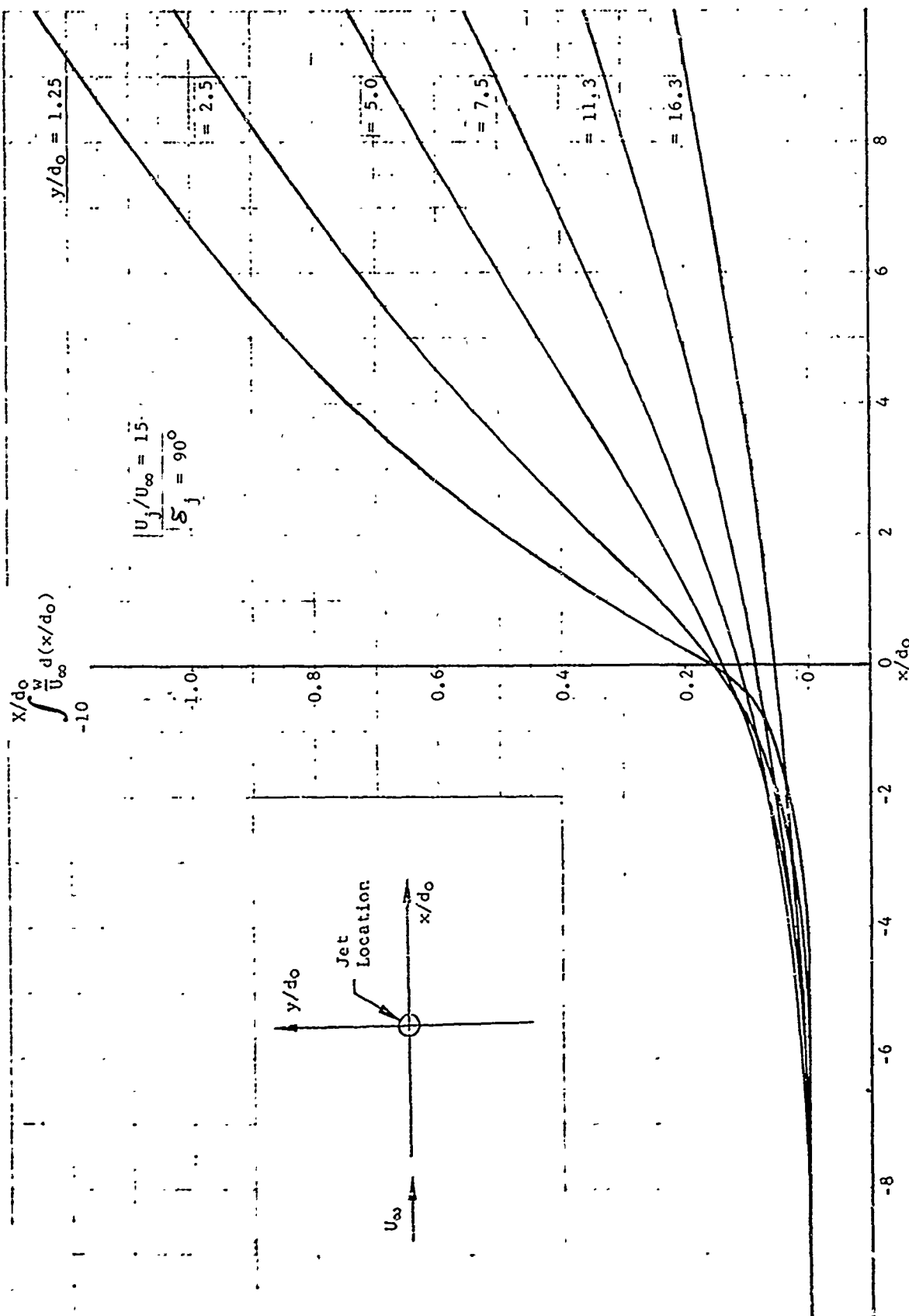
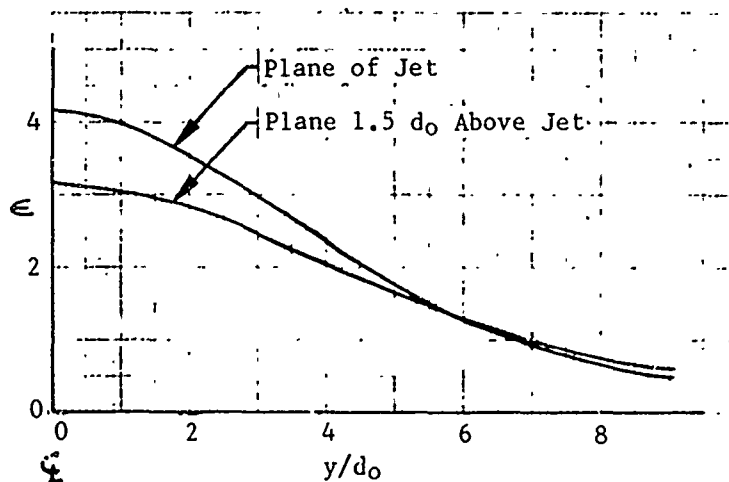


FIGURE 77. CURVES FOR EFFECTIVE ANGLE OF ATTACK AND CAMBER CALCULATION

#### d. Application to Calculations of Downwash at Tail Surface

The jet flow field program may be used to compute the velocity components induced by exhausting jets at arbitrary points in space. Thus, the program has the capability of determining the jet induced downwash in the vicinity of the horizontal tail. The power induced contribution to the pitching moment due to the presence of the horizontal tail may then be deduced.

The results of a typical calculation are shown in Figure 78. The jet induced downwash,  $\epsilon$ , is shown for two tail stations.



13 Jet Diameters Aft,  $\xi_j = 90^\circ$ ,  $U_j/U_\infty = 5$

FIGURE 78 . JET EXHAUST EFFECTS ON TAILPLANE

## 2. BODY METHOD

### a. Application of Lagally's Theorem in Relation to the Present Problem.

The most fundamental information in the present study is the knowledge of the induced velocity field due to the powered lift system. Based on this, alternative procedures may be found to predict the power induced forces and moments on an immersed body. Such alternative methods provide not only competing approaches but often an understanding of the problem derived from taking a different viewpoint.

The end result of the present jet model is a distribution of sinks and doublets along the jet path. A source, a sink, or a doublet will all induce a force to attract the submerged body towards the singularity on the basis of incompressible inviscid flow theory. This explains in part the loss in lift of a V/STOL aircraft in the presence of a downward jet. If instead of a single source, a system of sources (sinks are considered to be negative sources) and doublets is introduced, the total force and moment are the additive forces and moments induced by individual singularities. This is, in effect, Lagally's theorem and holds true in two-dimensional as well as in three-dimensional cases (References 30 and 31). It applies, in principle, to a submerged body of arbitrary shape in a uniform stream with arbitrary number of sources, doublets, and higher order singularities. Using this theorem for the present problem, the task is then to determine the velocities and their gradients "induced" by the fuselage and the image systems for singularities outside the immersed body, since these velocities and gradients represent the force and moment exerted on the fuselage by the jet.

For a two-dimensional body, finding such an image system is possible, as long as it can be mapped into a unit circle on the transformed plane. Thus, the power-effect forces and moments may be calculated for a general class of bodies. Unfortunately, there is no corresponding procedure for a three-dimensional body. The image of a singularity in that boundary is usually a complex one. Only for the special case of a sphere, may the image system be found conveniently and exactly. Since a fuselage is a three-dimensional body of complicated geometry, it is virtually a hopeless task to determine the image system for this kind of body. However, if we can approximate the fuselage by a prolate spheroid of equal volume, the possibilities are improved. On the strength of this simplification, we propose to employ Lagally's theorem as a possible empirical method for the fuselage.

Before we dwell on the main aspect, some explanation seems to be pertinent in regard to the justification of this simplification. Lagally's theorem is derived by

means of the integral equations in which the force and moment are expressed in terms of momentum flux through an enclosing control surface. The process of integrating the detailed surface pressure has in effect been circumvented. The details of the fuselage geometry, which reveals in the form of velocity potential, become increasingly indistinct as the distance from the surface increases. For a two-dimensional body, the general complex potential at large distances can be expressed in terms of a Laurent series. The leading term is proportional to  $1/(x + iy)$ , which behaves like a doublet. The higher order terms signify more refined details. By the same token, the disturbance potential of a three-dimensional body decays like  $1/(x^2 + y^2 + z^2)$  at great distances. This is recognized to be a doublet. Thus, the total force and moment on an immersed body by all singularities will be insensitive to the detailed geometry, provided that we can show that a substantial portion of the forces and moments are derived from the "induced" velocities and their gradients at positions of singularities sufficiently far from the fuselage. By examining the outputs from the jet model in which the strength of singularities increases with the distance away from the exit and using a simple body, say a sphere, one could confirm this conjecture.

#### b. Lagally's Theorem and Computation of a Sphere as a Test Case

Since the computation is based on inviscid flow, the forces acting on the surface of a fuselage arise from the pressure alone. Thus, the components of the force are given by

$$F_i = - \int_{(S)} p n_i dS, \quad i = 1, 2, 3 \quad (135)$$

where  $p$  is the pressure, and  $n_i$  are the cartesian components of a unit normally drawn outward to the element  $dS$  of the fuselage surface  $S$ . This equation may be reduced by Bernoulli's equation and Green's theorem to

$$F_i = \sum_{a=1}^{N_1} \rho \int_{(S_a)} \left( u_i u_j n_j - \frac{1}{2} u_j u_j n_i \right) dS, \quad i, j = 1, 2, 3 \quad (136)$$

where the repeated indices  $j$  refer to summation,  $u_i$  are the velocity components, and  $S_a$  are the surfaces of spheres of infinitesimal radii which surrounds  $N_1$  singularities at the positions  $\hat{r}_a$  ( $a = 1, 2, \dots, N_1$ ). This is a general expression. To specify the nature of the singularities, we shall make distinction between a source and a doublet.

For a source of strength  $m_a$  located at the position  $\vec{r}_a$ , the velocity components on the surface of the infinitesimal sphere  $a$ , after the series expansion, may be written as

$$u_i = q_{ia} + \frac{m_a(x_i - x_{ia})}{r^3} + \left(\frac{\partial q_i}{\partial x_j}\right)_a x_j + \frac{1}{2} \left(\frac{\partial^2 q_i}{\partial x_j \partial x_k}\right)_a x_j x_k + \dots, \quad i, j, k = 1, 2, 3$$

where the subscript  $a$  indicates the position of singularity, and  $q_{ia}$  are the velocity components at the point  $\vec{r}_a$  induced by all causes except the singularity there. The second term represents the velocity components by the singularity, in which  $r$  refers to the radius of the infinitesimal sphere. The third, fourth and the rest of the terms are members of the Taylor series. Upon substitution of this expression into Equation (136), we obtain

$$F_{ia} = 4\pi m_a \rho q_{ia} \quad (137)$$

This may be looked upon as a force  $\vec{F}_a$  acting on a fuselage in a line through the source at  $\vec{r}_a$ . Thus, the moment on the fuselage due to  $m_a$  is the vector product of  $\vec{r}_a$  and  $\vec{F}_a$  and is given by

$$M_{ia} = 4\pi m_a \rho \epsilon_{ijk} x_{ja} q_{ka}, \quad i, j, k = 1, 2, 3 \quad (138)$$

where  $\epsilon_{ijk}$  is the permutation symbol,  $\epsilon_{123} = \epsilon_{231} = \epsilon_{312} = 1$ ,  $\epsilon_{213} = \epsilon_{132} = \epsilon_{321} = -1$ , and  $\epsilon_{ijk} = 0$ , if  $i, j, k$  are not all different. For a doublet of strength  $\mu_b$  situated at the point  $\vec{r}_b$ , the force and moment may be obtained by a similar but somewhat more complex procedure. For details, one is referred to the above mentioned references.

The total force and moment on the fuselage are the summation of individual contributions and are given by

$$F_i = 4\pi \rho \left[ \sum_{a=1}^{N_1} m_a q_i + \sum_{b=1}^{N_2} \mu_b \frac{\partial q_i}{\partial x_j} \right], \quad i, j = 1, 2, 3 \quad (139)$$

$$M_i = 4\pi \rho \epsilon_{ijk} \left[ \sum_{a=1}^{N_1} m_a x_{ja} q_{ka} + \sum_{b=1}^{N_2} (\mu_b q_{kb} + x_{jb} \mu_b \frac{\partial q_{kb}}{\partial x_l}) \right], \quad i, j, k, l = 1, 2, 3$$

The subscripts a and b have been dropped for convenience. The quantities  $m$ ,  $\vec{\mu}$ ,  $\vec{r}$  are known from the jet flow field program, but the velocity components  $q_i$  must be determined according to the given configuration. Thus, to use Lagally's theorem, the problem is that of determining these components.

As stated above, the quantities  $q_i$  at the point in question are the velocity components induced by all causes except the singularity there. But the contributions due to other singularities outside the body may be neglected without affecting the final result, because the force and moment induced at one singularity by another are equal and opposite to those at the latter singularity by the former. This is sometimes referred to as the reciprocal relation. Consequently, the relevant induced velocities  $q_i$  resulting from a body in a uniform crossflow with an exhausting jet may be classified as: (a) the velocity induced by the body, (b) the velocity induced by the image system of sources, and (c) the velocity induced by the image system of doublets. These velocities are all functions of body geometry. A general expression for an arbitrary body is not known at present. The velocities of type (a) can be determined, if we assume that a fuselage be replaced by an ellipsoid of equal volume. The solution to this is known and can be found in many books. Unfortunately, it is still difficult to obtain velocities of types (b) and (c) even under this assumption. Thus, it appears that some further approximation is needed. Before exploring possible approaches, it seems worthwhile to know the magnitude of these velocities and the relative importance of each type. To do this, we shall work out a simple example.

The only known three-dimensional configuration for which all three types of the induced velocities can be determined exactly is a sphere. For this reason, we choose this as our test case. The power effect may be calculated with the singularity distribution given by the jet flow field. It turns out that type (a) contributes roughly 80 percent of the total effect. For an elongated body such as a fuselage, it is conceivable that this percentage may be somewhat reduced. Nevertheless, the evidence seems to point out the fact that the effect of the image system is relatively small as compared to that due to the body and may be neglected for the first approximation.

Prior to this finding, attempts were made by the trial-and-error methods to get approximate image systems for a source outside a prolate spheroid, using the image system of an ellipse and the correspondence between a circle and a sphere as the guide. This effort did not persist long enough to examine various approaches, but it appears that some useful approximation should result, depending on the accuracy required.

(c) Application of Method to Fuselage

By choosing elliptic coordinates  $\nu, \xi, \omega$ , the velocity potential at a field point for flows past a prolate spheroid at an angle of attack  $\alpha$  is given by

$$\phi = -U_{\infty} \cos \alpha k \nu \xi - U_{\infty} \sin \alpha k (1 - \nu^2)^{\frac{1}{2}} (\xi^2 - 1)^{\frac{1}{2}} \cos \omega - A \nu \left[ \frac{1}{2} \xi \ln \frac{\xi + 1}{\xi - 1} - 1 \right] \\ - A' (1 - \nu^2)^{\frac{1}{2}} (\xi^2 - 1)^{\frac{1}{2}} \left[ \frac{1}{2} \ln \frac{\xi + 1}{\xi - 1} - \frac{\xi}{\xi^2 - 1} \right] \cos \omega,$$

$$A = \frac{U_{\infty} k \cos \alpha}{\frac{\xi_0}{\xi_0^2 - 1} - \frac{1}{2} \ln \frac{\xi_0 + 1}{\xi_0 - 1}}, \quad A' = \frac{-U_{\infty} k \sin \alpha}{\frac{1}{2} \ln \frac{\xi_0 + 1}{\xi_0 - 1} - \frac{\xi_0^2 - 2}{\xi_0(\xi_0^2 - 1)}}$$

$$k = ae, \quad e = \frac{1}{\xi_0}, \quad k(\xi_0^2 - 1)^{\frac{1}{2}} = c.$$

where  $U_{\infty}$  is the freestream velocity,  $a$  and  $c$  are the polar and equatorial radii of the given spheroid that is a member of the confocal family  $\xi = \xi_0$ . The relationship between this and the cartesian coordinate system is

$$x = k \nu \xi, \quad y = -w \sin \omega, \quad z = w \cos \omega, \\ w = k (1 - \nu^2)^{\frac{1}{2}} (\xi^2 - 1)^{\frac{1}{2}}$$

in which the surfaces  $\xi = \text{constant}$  and  $\nu = \text{constant}$  are confocal ellipsoids and hyperboloids with the common foci of  $(\pm k, 0, 0)$  as illustrated in Figure 79. By knowing the velocity potential and this coordinate transformation, we can determine  $q_i$  and  $\partial q_i / \partial x_j$  at every position of the sources and doublets in the jet flow field. Application of Equation (139) then gives the force and moment on the given body caused by the induced velocities of type (a). These are assumed to equal approximately the force and moment on the fuselage. Calculations were subsequently made for the test fuselage with a lift jet at freestream to jet velocity ratios equal to 0.2 and 0.3. The results are shown in Figure 80, along with the test data and those computed by the transformation method.

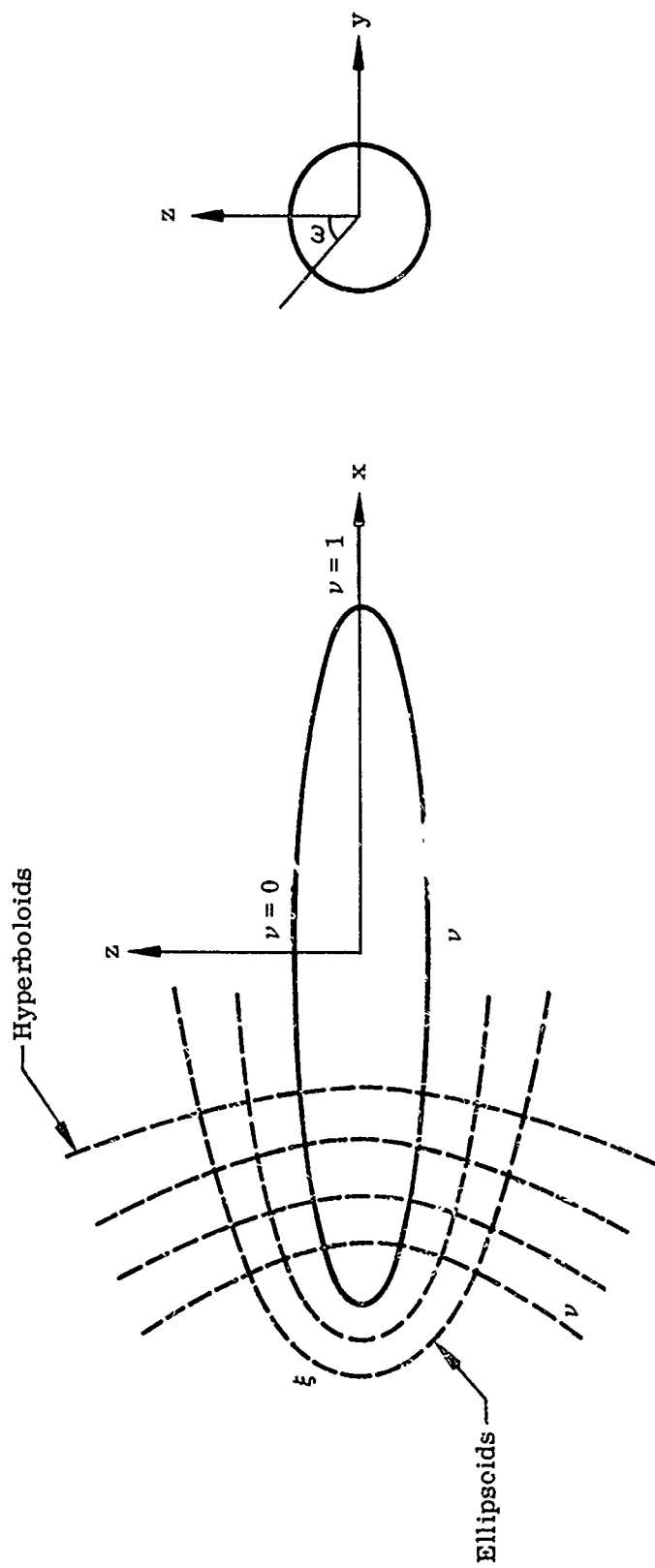


FIGURE 79. PROLATE SPHEROID AND ELLIPTIC COORDINATES



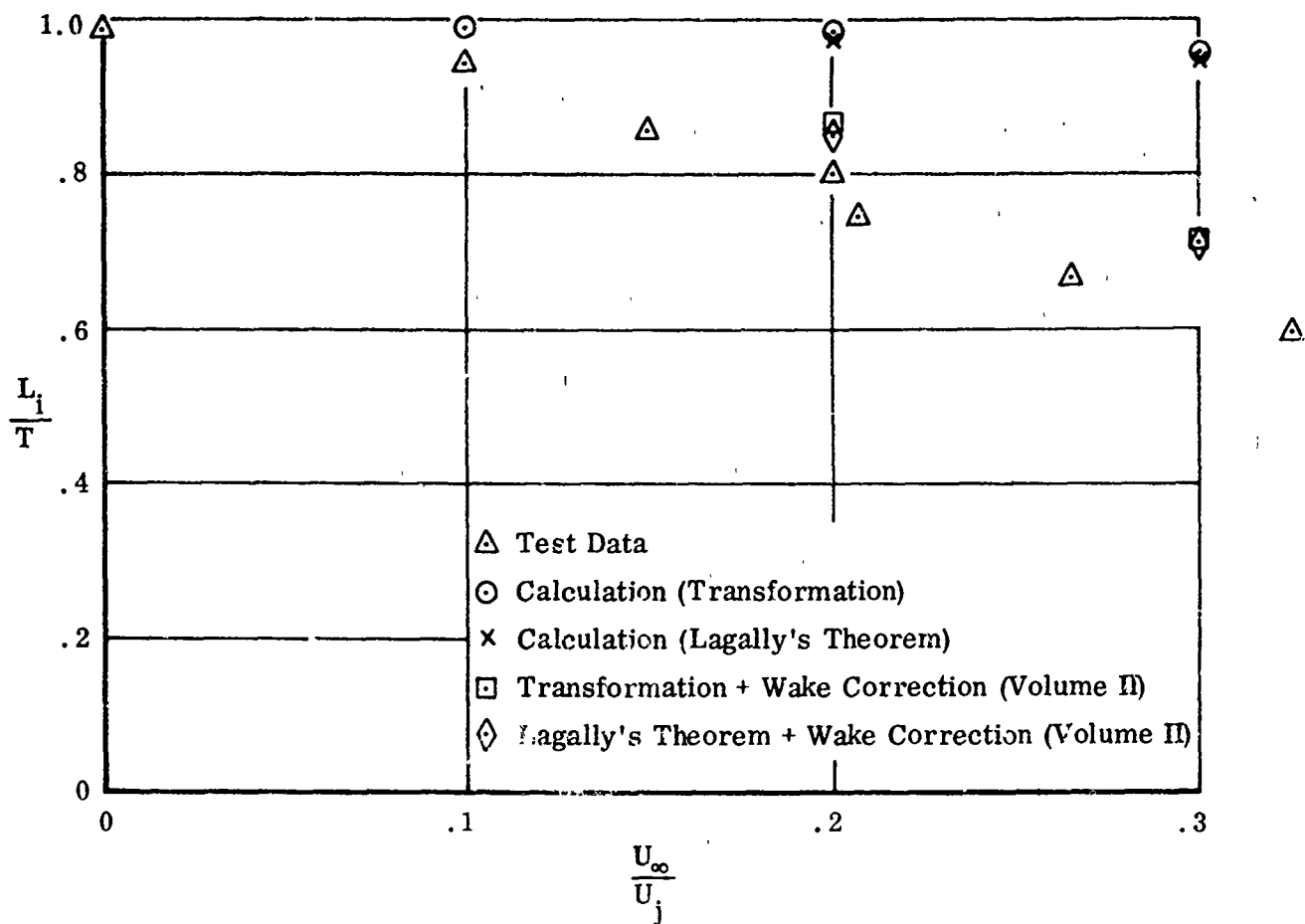


FIGURE 80. POWER-EFFECT LIFT FOR LIFT JET WITH FUSELAGE  
CALCULATED BY LAGALLY'S THEOREM AND ITS COMPARISON  
WITH TRANSFORMATION METHOD AND TEST DATA

## SECTION IX

### HOVER AERODYNAMICS

The hover region of V/STOL flight requires special treatment due to the lack of steady freestream conditions. Two areas of special treatment for this flight regime have been studied. The first deals with the power effects in a state of true hover. The second treats nonlinear and nonsteady power off aerodynamics at near hover condition. These studies provide a limit point for the transition aerodynamics and permit an approach to V/STOL hover flight analysis.

## 1. POWER EFFECTS IN HOVER

A number of experimental, empirical, and theoretical investigations have been devoted to the problem of determining the forces exerted on a stationary body from which a jet exhausts. Particular attention has been devoted to thrust losses of lifting jet configurations both in and out of ground effect; a good summary of these efforts may be found in Reference (32).

The most pertinent results to date are contained in an empirical relation for lift loss out of ground effect,

$$\left[\frac{G}{T}\right]_{\infty} = 0.009 \sqrt{\frac{S}{A_j}} \left[ \frac{\partial(q_x / P_{T,p} - p) / \partial(x/d)}{x_i/d} \right]^{0.5} \quad (140)$$

from Reference (33), or

$$\left[\frac{G}{T}\right]_{\infty} = K \left[ \frac{P_{T,p}}{p} \right]^{-0.64} \sqrt{\frac{S}{A_j}} \left[ \frac{\partial(q_x / P_{T,p} - p) / \partial(x/d)}{x_i/d} \right]^{0.5} \quad (141)$$

from Reference (34), and in an empirical correlation for the change in force due to the presence of the ground plane,

$$\frac{G}{T} - \left[\frac{G}{T}\right]_{\infty} = 0.012 \left[ \frac{\bar{D}/d - 1}{h/d} \right]^{2.3}, \text{RAE data}^{(35)} \quad (142)$$

or,

$$\frac{G}{T} - \left[\frac{G}{T}\right]_{\infty} = 0.025 \left[ \frac{\bar{D}/d - 1}{h/d} \right]^{2.02}, \text{NACA data}^{(36)} \quad (143)$$

The preceding results are primarily applicable to single or closely spaced, centrally located jets. Although derived from small-scale, cold-jet tests, Equations (140) and (141) have been shown to apply to more complicated configurations.<sup>(34,37)</sup> Equation (142) has been applied with reasonable success to full-scale configurations having closely spaced turbojet propulsion.<sup>(37,38)</sup>

Equations (140) and (141) differ because of the addition of a jet pressure parameter by a later investigator.

Equations (142) and (143) vary because different data were used in determining the constants. A cursory examination of later NASA data<sup>(33)</sup> indicated a preference for Equation (143) and a brief effort was made to determine if the empirical constants of Equations (142) and (143) could be related to the area ratio, jet decay rate, or out-of-ground effect loss.

The nature of Equations (140) thru (143) indicates that knowledge of jet decay rate, out-of-ground effect loss, and true jet thrust for simple configurations is required for such an effort. A requirement for this data group greatly reduces the amount of useful data available. As can be seen in the data summary of Table 3, only data from References (33) and (39) remain, and Reference (39) does not consider ground effect. References (34) and (37) contain the proper data group but involve more complex body geometry.

During early attempts to correlate Equations (142) and (143), nonlinearities of log-log plots of  $G/T - (G/T)_{\infty}$  versus  $h/d$  led to the plotting of  $G/T$  versus  $h/d$  in semi-log form. One such plot is shown in Figure 81. As the quality of the correlation seemed remarkable, additional data was correlated in this manner. Figure 82 indicates that correlation is possible for circular flat plates with an error band of 20 percent. Datum outside this band and much of the scatter within this band may be attributed to errors in transcribing information from Reference (33).

An expression of the form

$$\frac{G}{T} = \left[ \frac{G}{T} \right]_{\infty} e^{B \frac{\sqrt{S/A} - 1}{h/d}} \quad (144)$$

is therefore suggested. The value of B obtained from the data of Figure 81 differed from that obtained from Figure 82; B was found to be 0.97 and 1.23, respectively. The difference may be attributable to the different jet turbulence levels produced by a rectangular plenum (Figure 81) and a cylindrical plenum (Figure 82). For the two configurations that have been examined, it is noted that the constant B is inversely proportional to the square root of the out-of-ground effect loss.

$$\frac{B'}{B} = \left[ \frac{(G/T)_{\infty}}{(G/T)'_{\infty}} \right]^{0.5} \quad (145)$$

TABLE 3 Jet Hover Data Summary

REF	JET	MODEL	FORCE	MOMENT	$C_{\infty}$	JET DECAY	TEMP	PRESSURE
2	S,M	C,R,T	G/T		X	X		L
3	M	A	G/T		X	X		
4	S	C,R,T	G/T		L			
5	S	C,R,T,A	L/L $_{\infty}$					
6	M	A	G/T		X	X		
7	S	R	L/T $_m$					X
8	S,M	R	G/T		X	X		
9	S,M	R,A	L/T $_m$					
10	M	F				X	X	L
11	M	C	T/T $_m$			X	X	X
12	M	A	G/L $_{\infty}$	L			X	
13	S,M	A	L/T	X	X			

symbols: A - aircraft

C - circular plate

F - pod or fuselage

G - lift loss

L - limited data, lift

M - multiple jets

R - rectangular or square plate

S - single jet

T - jet thrust; triangular plate

T $_m$  - calculated jet momentum thrust

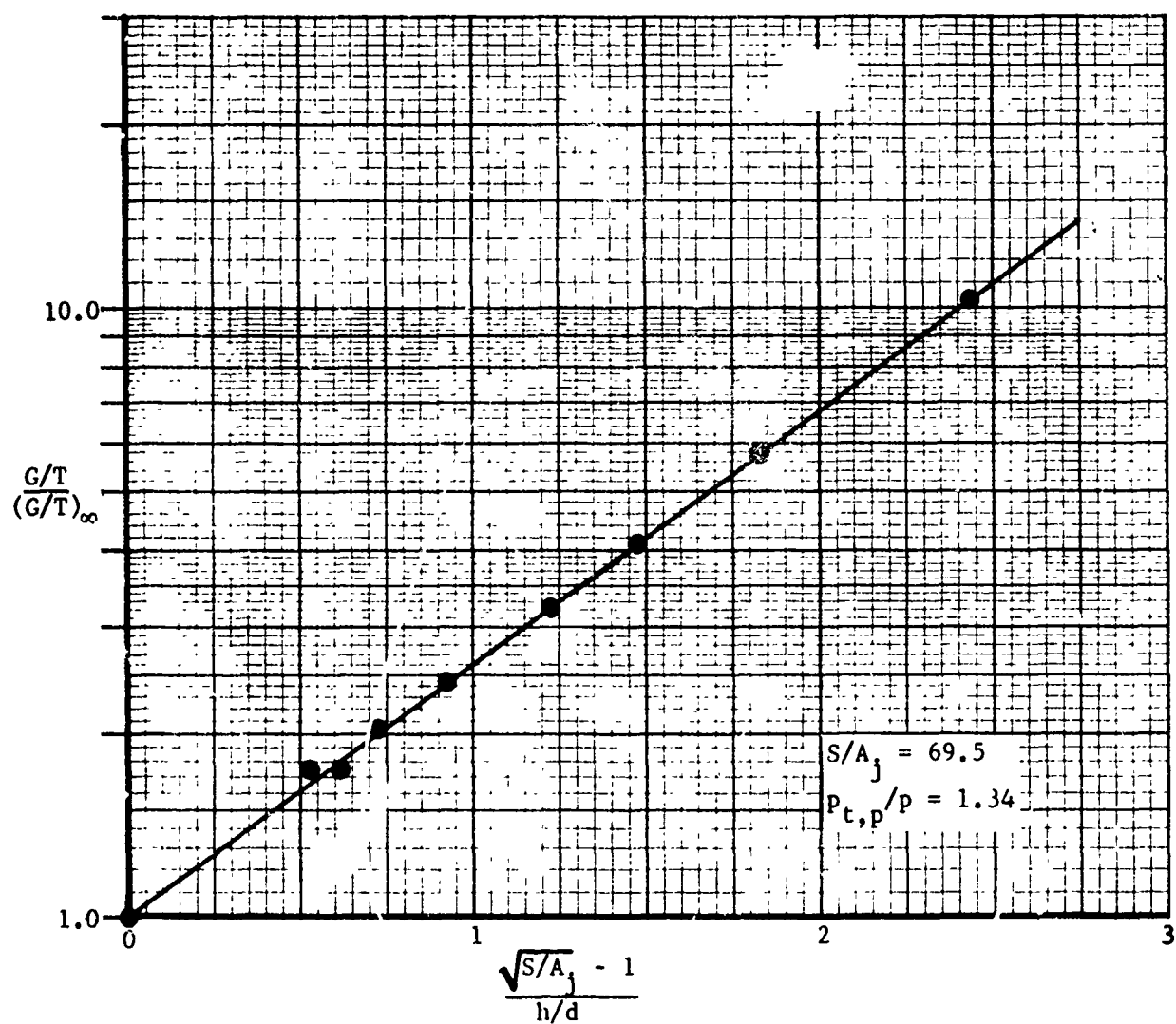


FIGURE 81. LIFT LOSS FOR CIRCULAR FLAT PLATES, RECTANGULAR PLENUM (Ref.33)

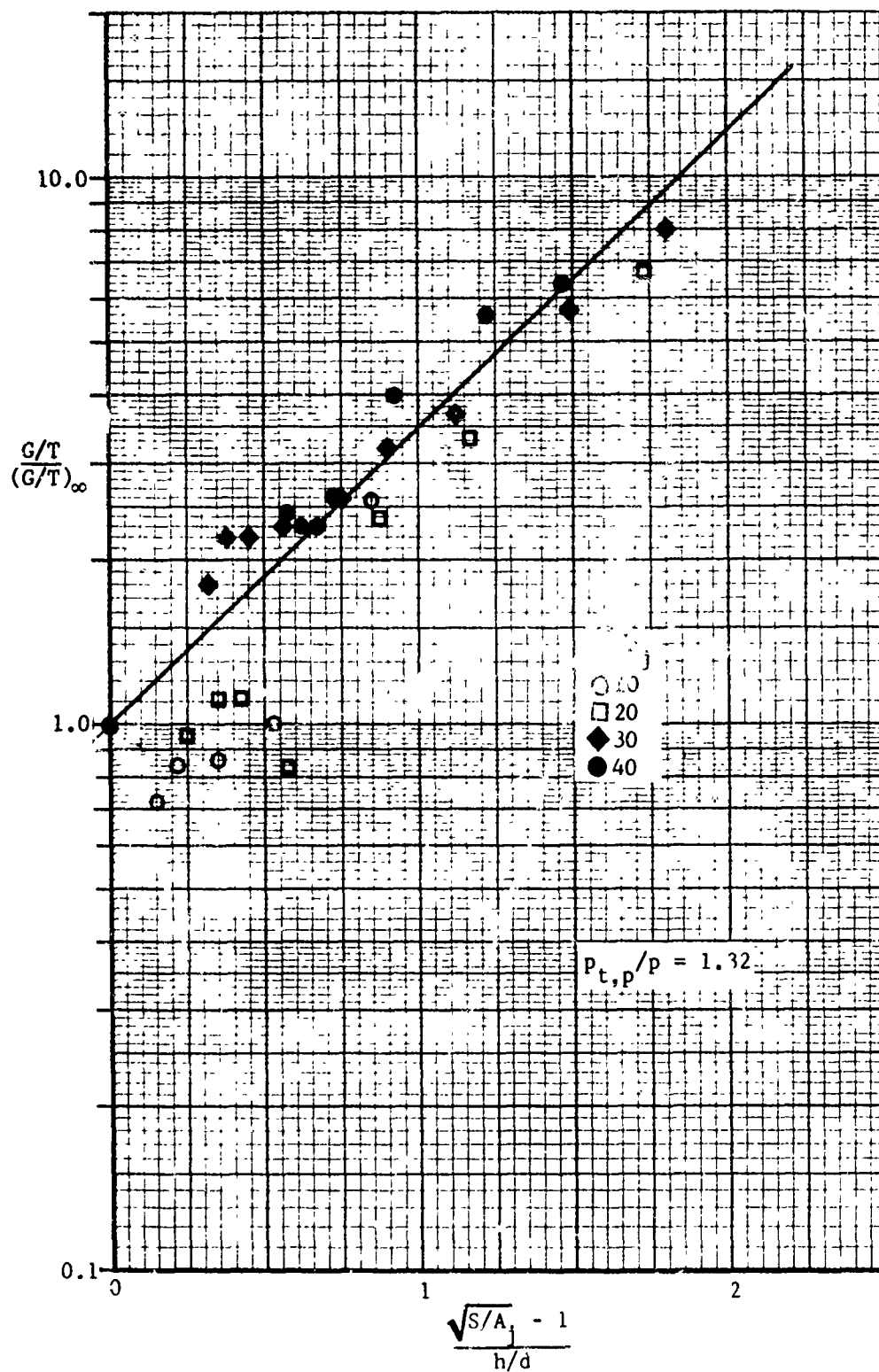


FIGURE 82. LIFT LOSS FOR CIRCULAR FLAT PLATES, CIRCULAR PLENUM (Ref.33)

Equation (145) in combination with relations (140) and (141) may be used to relate the constant B to the rate of jet (impact) pressure decay.

$$\frac{B'}{B} = \left| \frac{\partial (q_x / P_{T,p} - p) / \partial (x/d)}{x_i/d} \right| \left/ \left( \frac{\partial (q_x / P_{T,p} - p) / \partial (x/d)}{x_i/d} \right)' \right|^{0.25} \quad (146)$$

Relation (146) in combination with Equation (144) suggests Equation (147).

$$\frac{G}{T} = \left[ \frac{G}{T} \right]_{\infty} \exp \left\{ B'' \frac{\sqrt{S/A_j} - 1}{h/d} \left[ \frac{\partial (q_x / P_{T,p} - p) / \partial (x/d)}{x_i/d} \right]^{-0.25} \right\} \quad (147)^*$$

However, further analysis is necessary before conclusions can be drawn regarding the validity of Equation (147) which has been developed using limited data for centrally located jets in circular plates.

It should be noted that a correlation similar to that of Equation (144) may be found in the form

$$\frac{G}{T} = \left[ \frac{G}{T} \right]_{\infty} e^{B''' [(G/T)_{\infty} / (h/d)]} \quad (148)$$

This suggests that  $(G/T)_{\infty}$  is proportional to  $\sqrt{S/A_j} - 1$  and not to  $\sqrt{S/A_j}$  as indicated in Equations (140) and (141). This seems intuitively correct as one would desire the calculated load on the plate to go to zero if no plate is present,  $S/A_j = 1$ . A comparison is shown in Figure 83. Thus,  $\sqrt{S/A_j} - 1$  is a significant parameter both in and out of ground effect.

It is probable that relations of the type listed above will not be useful for a body very near to the surface where small details of specific body and jet geometry become significant. Additional terms will be required in this region.

\*Note: For circular planforms,  $\sqrt{S/A_j} = \bar{D}/d$ .



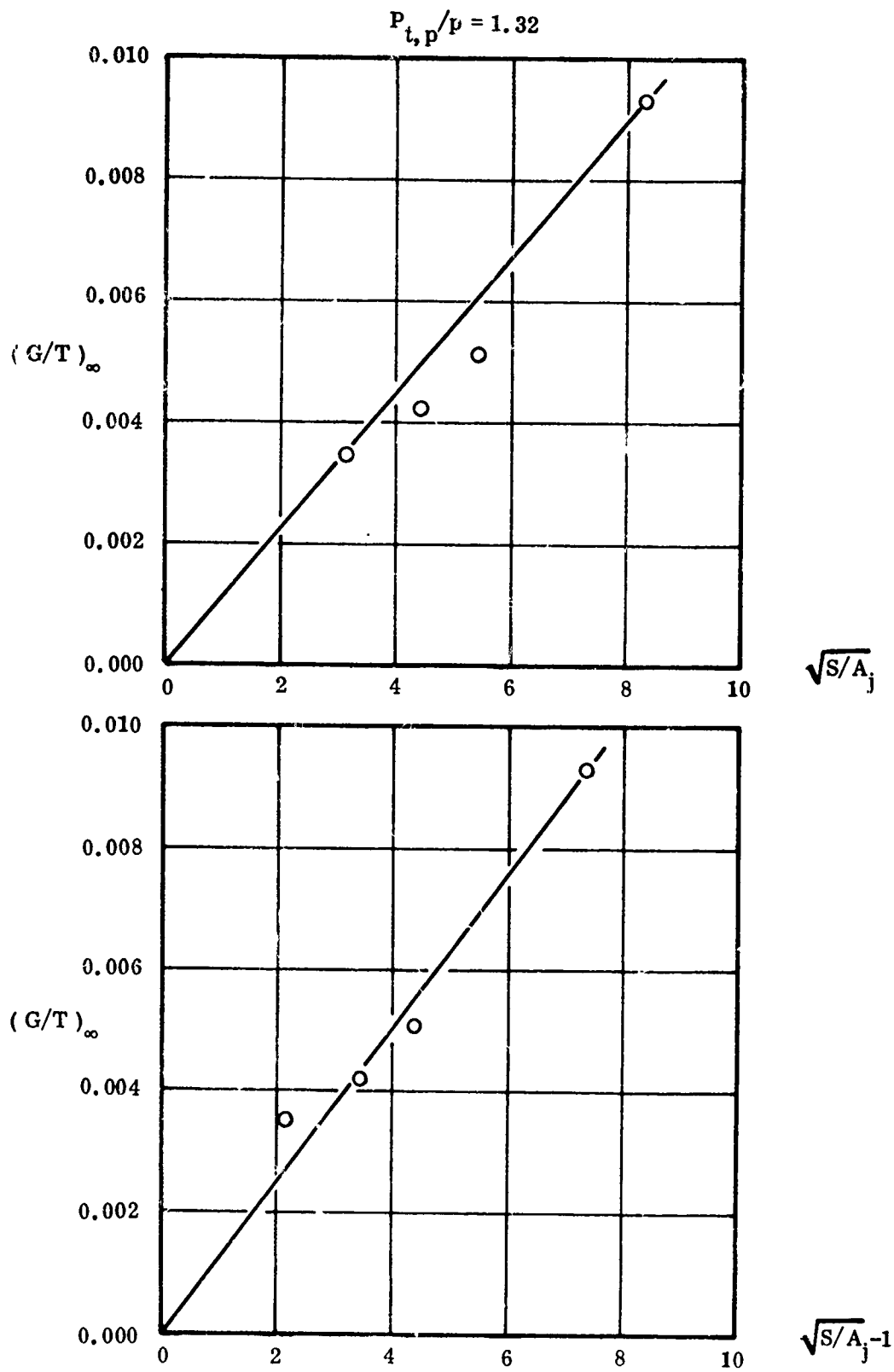


FIGURE 83. OUT OF GROUND EFFECT LIFT LOSSES, CIRCULAR PLENUM, REF(33)

## 2. PERTURBATION METHOD

To attack the problem of nonlinear and nonsteady aerodynamics at near hover condition, a study combining theoretical analysis and water tank tests was undertaken to determine the feasibility of obtaining a method for predicting stability derivatives under flight conditions.

A small existing water tank was used to try out possible techniques of obtaining test data for further study. This tank and the arrangements used for these tests are shown in Figure 84. The model was suspended from a beam that was free to roll across the tank. Motive power was supplied by unbalancing the weights on the two weight pans. Weights were shifted from the aft side to the forward side, providing an incremental loading while keeping the total mass of the system constant. An accelerometer attached to the beam supplied a force trace versus time plot. Strain gages were mounted on the supporting rod to provide moment measurements.

Acceleration and moment plots were obtained for the model, and measurements were made both with the model in water and in air. Typical plots are shown in Figure 85 for different incremental weight loadings. The initial accelerations in both cases were plotted against incremental weight, and straight lines were faired through the points. From these straight lines, it was possible to determine the apparent mass of the model in water. (The apparent mass in air was assumed to be negligible compared to that in water.)

The acceleration curves were integrated, and the values of force and moment versus velocity then were obtained for three different incremental weights. The force due to the acceleration (apparent mass multiplied by acceleration) was subtracted from the total force, and a net force was obtained which was assumed to be due to viscous effects. The results of this data reduction, reduced to drag coefficient and plotted against velocity multiplied by time, are shown in Figure 86. The shape of the three incremental weight curves shows good correlation throughout the test range. The four-pound curve is somewhat low, but this could be attributed to inaccuracies in the data reduction.

Since both accelerometers and strain gages were not only measuring the linear motion of the rigid body but also were picking up elastic transients and other spurious inputs, isolation of the reduced data was somewhat difficult. This problem was further increased by the use of strip chart recorders which contributed their own noise and pen-arm inertia to the plots. Of the models tested — rectangular plate, cylindrical

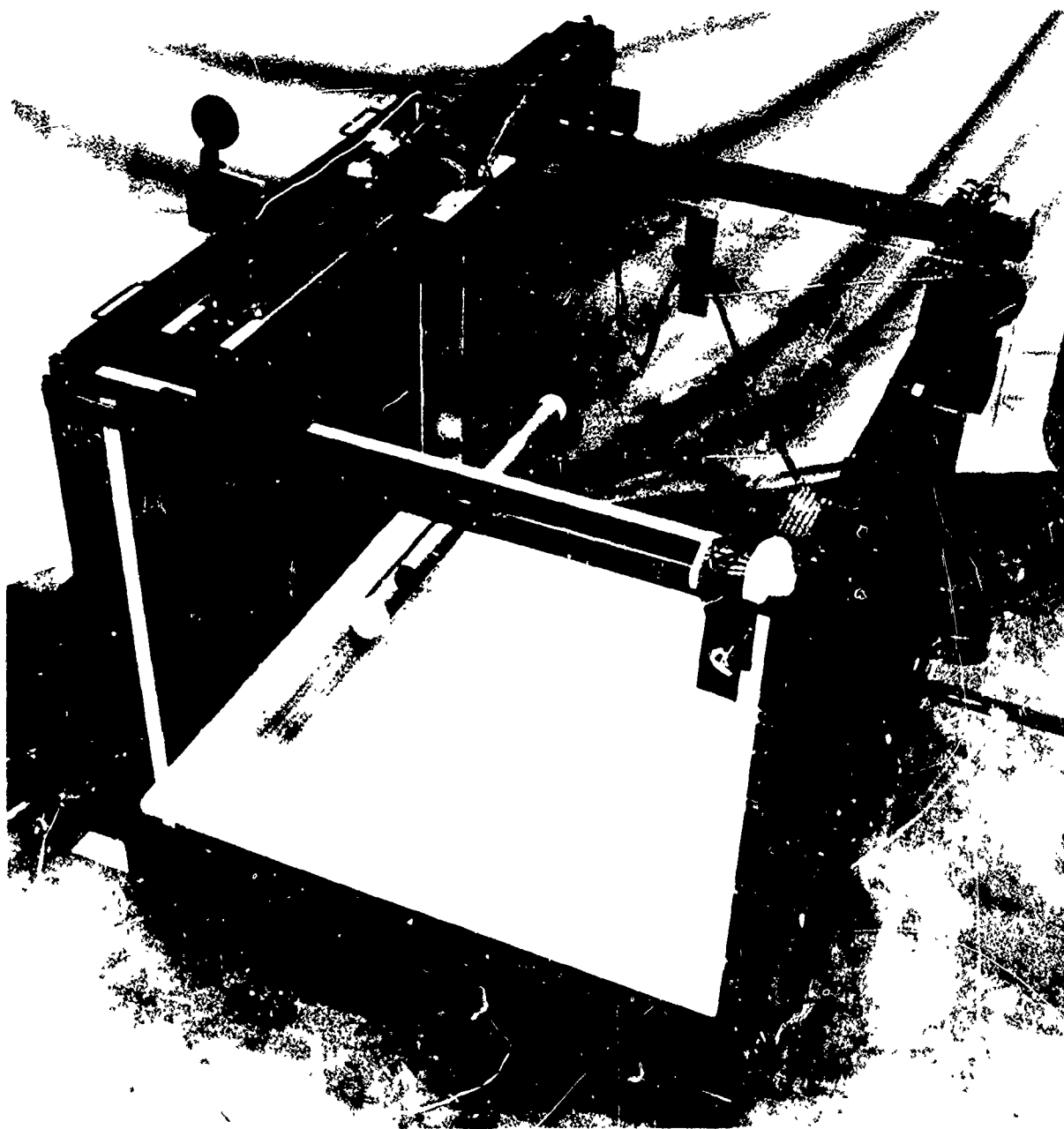


FIGURE 84. PRELIMINARY HYDRODYNAMIC TESTBED

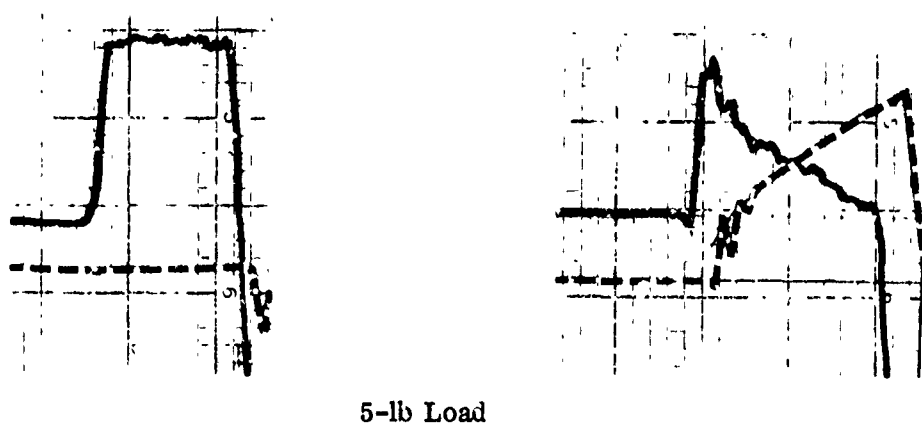
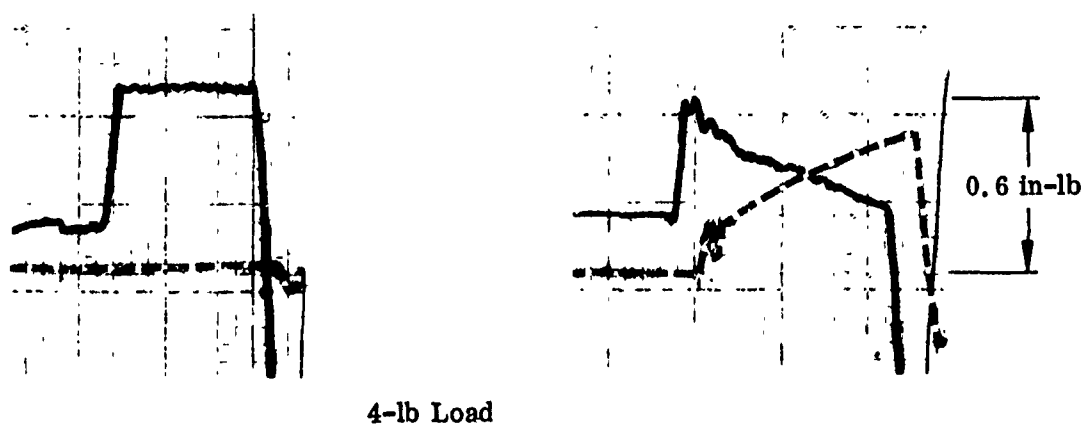
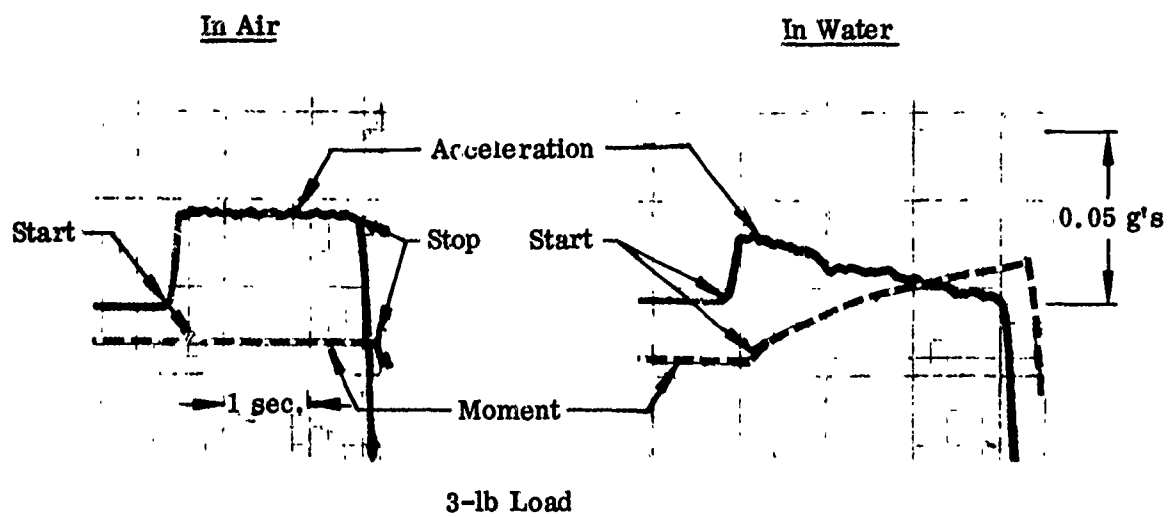


FIGURE 85. TYPICAL TIME HISTORIES

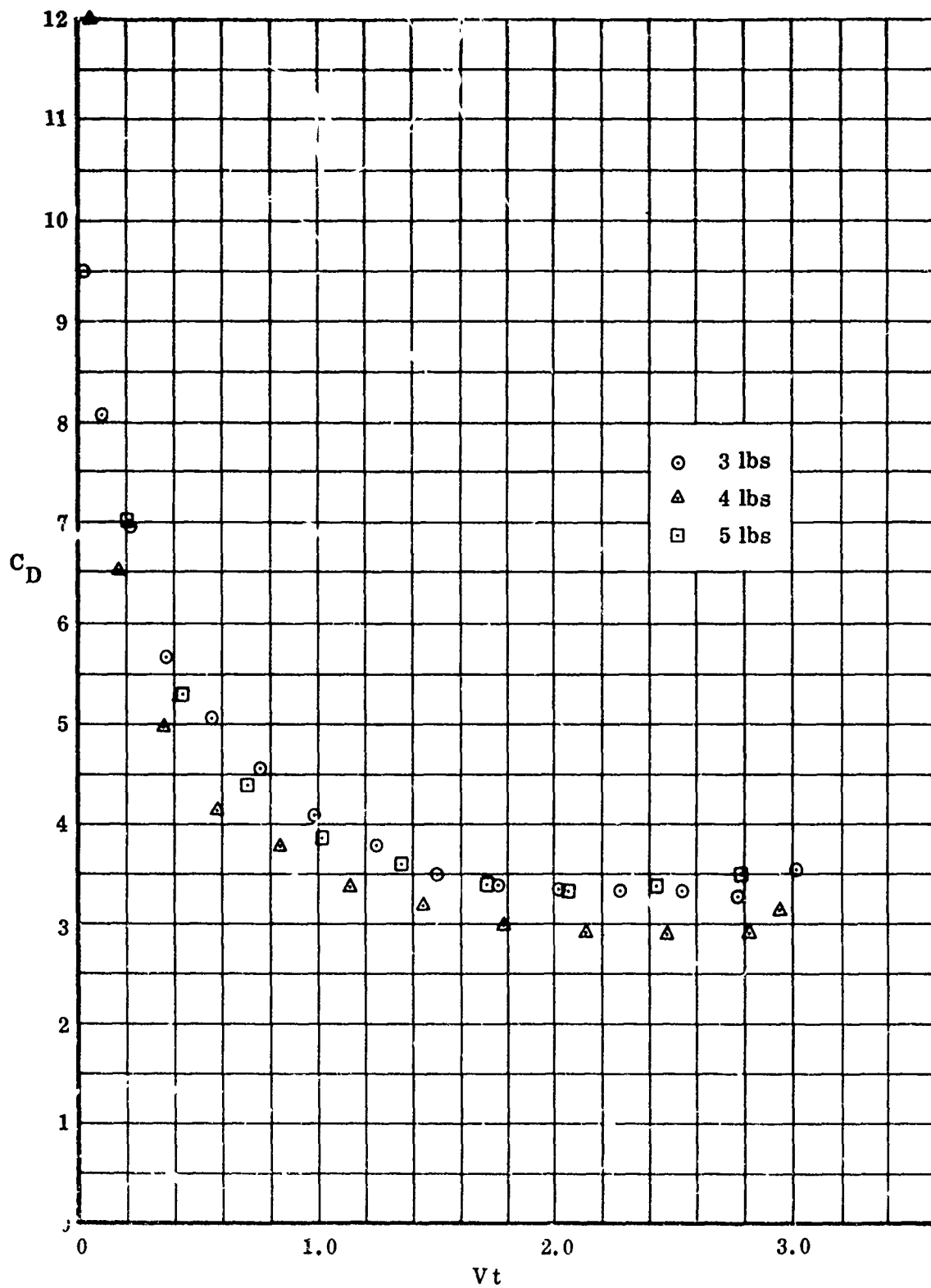


FIGURE 86. VISCOUS DRAG COEFFICIENT FOR TRAPEZOID PLATE

tube (see Figure 84), and trapezoidal flat plate — the latter offered the most clearly defined data, especially for calculation of apparent mass.

The recorded data were surprising in two more ways: First, the drag coefficients obtained near the end of the plots were about three (based on the frontal area), which seemed to be too high. Second, the drag coefficients in the beginning stages of the run were high, with indications that the drag was more nearly proportional to  $V$  than to  $V^2$ .

The data were analyzed according to the concept of indicial functions. Northrop assumed that the curve for the particular derivative or coefficient under consideration could be built up from a series of step functions. For example, from the tests made so far it can be assumed that the derivative of the drag with respect to  $V$  (or perhaps  $V^2$ ) is a function of time alone. Using velocity as an example, this can be written as.

$$D(t) = \frac{d}{dt} \int_0^t D_v(\tau) V(t-\tau) d\tau \quad (149)$$

where  $D_v(\tau)$  represents the value of the drag for a unit step function of velocity. This equation can be evaluated by taking the Laplace transform of both sides to give

$$D(s) = s D_v(s) V(s) \quad (150)$$

and hence,

$$D_v(s) = \frac{D(s)}{s V(s)} \quad (151)$$

Equation (151) was derived under the hypothesis that a  $D_v(t)$  could be defined which was independent of the driving force and, hence, of the velocity history. It was not necessarily expected that this would be true, but that by examining the test data and seeing if the resultant curves would collapse, a proper functional relationship could be obtained which would permit a step function to be defined which could be used to reproduce the test time histories. As an example of this, two other definitions which were considered to define the step function were

$$D(t) = \frac{d}{dt} \int_0^t D_{v^2}(\tau) V^2(t-\tau) d\tau \quad (152)$$

and

$$D(vt) = \frac{d}{dvt} \int_0^{vt} D_{vt}(\tau) V^+(vt-\tau) d\tau \quad (153)$$

Equations (149), (152), and (153) together with alternative formulations were examined to determine which would best collapse the test data for the different weight increments. Equation (153) showed the most promising results of all those tested. However, the preliminary test data indicated a discrepancy for the various weight differences. While the shapes of the resulting curves were similar, the magnitude differed. In order to better correlate the data, a step function was added to the solution to account for data beyond the test period. The magnitude of the step was set equal to the last data point, so that

$$\int_0^{\infty} D_f e^{-svt} dvt = D_f \int_{(vt)_f}^{\infty} e^{-svt} dvt = D_f \left[ -\frac{1}{s} e^{-svt} \right]_{(vt)_f}^{\infty} \quad (154)$$

and, assuming  $s > 0$

$$\mathcal{L}\{D_f(vt)\} = D_f \frac{e^{-(vt)_f s}}{s} \quad (155)$$

Through the use of this modified expression, the parameter  $D_v(s)$  was evaluated for  $0 < s \leq 5.0$  for incremental weights of 3, 4, 5, 6, and 7 pounds, Figure 87. Excellent agreement is shown for the 3-, 4-, and 7-pound test runs, while the 5- and 6-pound runs did not conform. A detailed examination of the testing techniques and the instrumentation arrangement revealed that the instrumentation was simply not sensitive enough for runs with incremental weights greater than 7 pounds.

In spite of the inadequacy of the test data accuracy, an attempt was made to determine the time-dependent response to a step input. For this purpose the results obtained by the definition of Equation (153) were used and the inverse Laplace transform was obtained to see if any additional problem areas would be encountered.

A study of the properties of the Laplace transforms indicated that the values of the quantity  $D(s)/V^2(s)$ , Figure 88, would have to approach a constant for large values of  $s$ . This was required to retain a finite force at the start of acceleration. For this

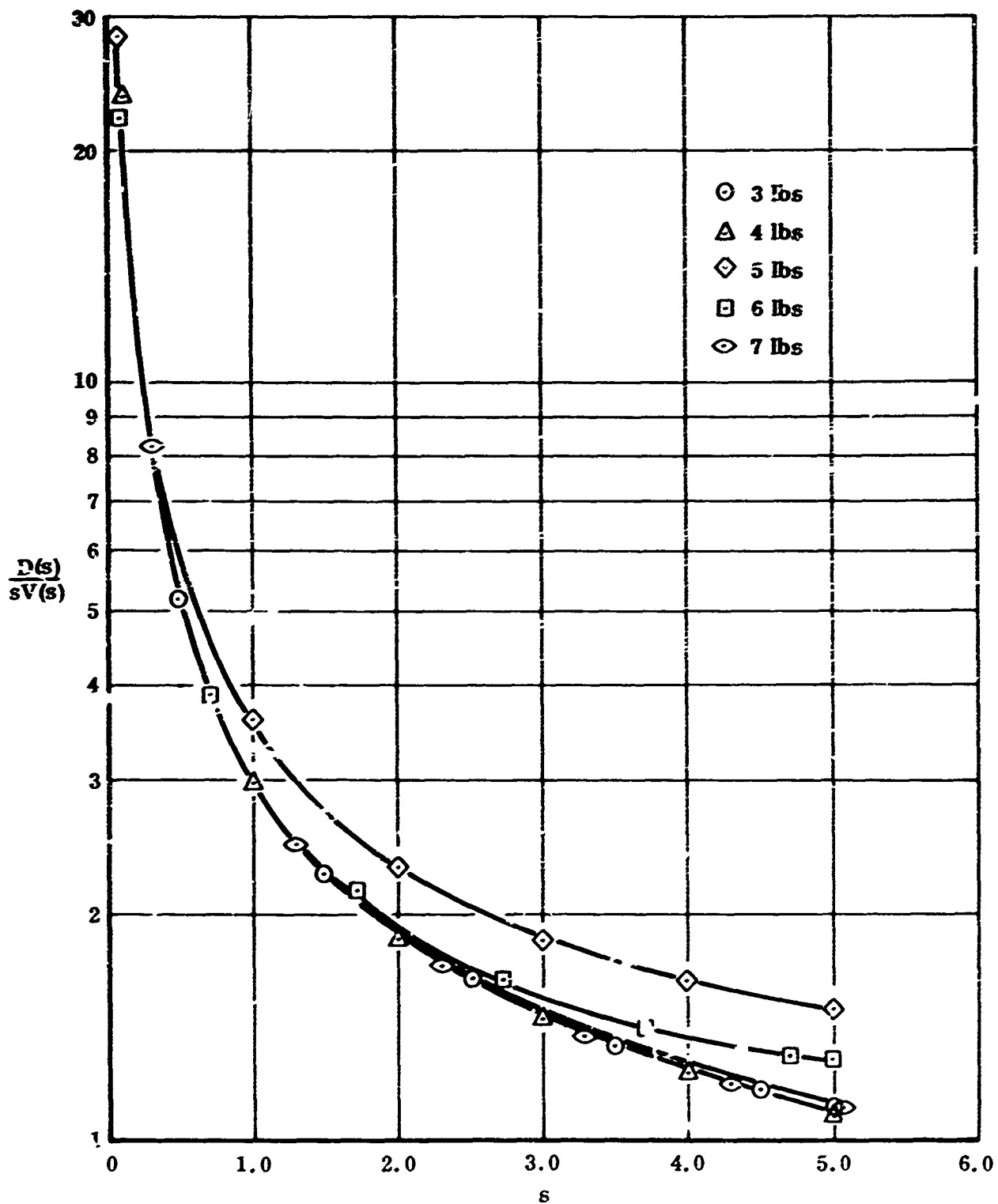


FIGURE 87. TRANSFORMED EXPRESSION FOR DRAG FORCE DUE TO IMPULSIVE VELOCITY SQUARED



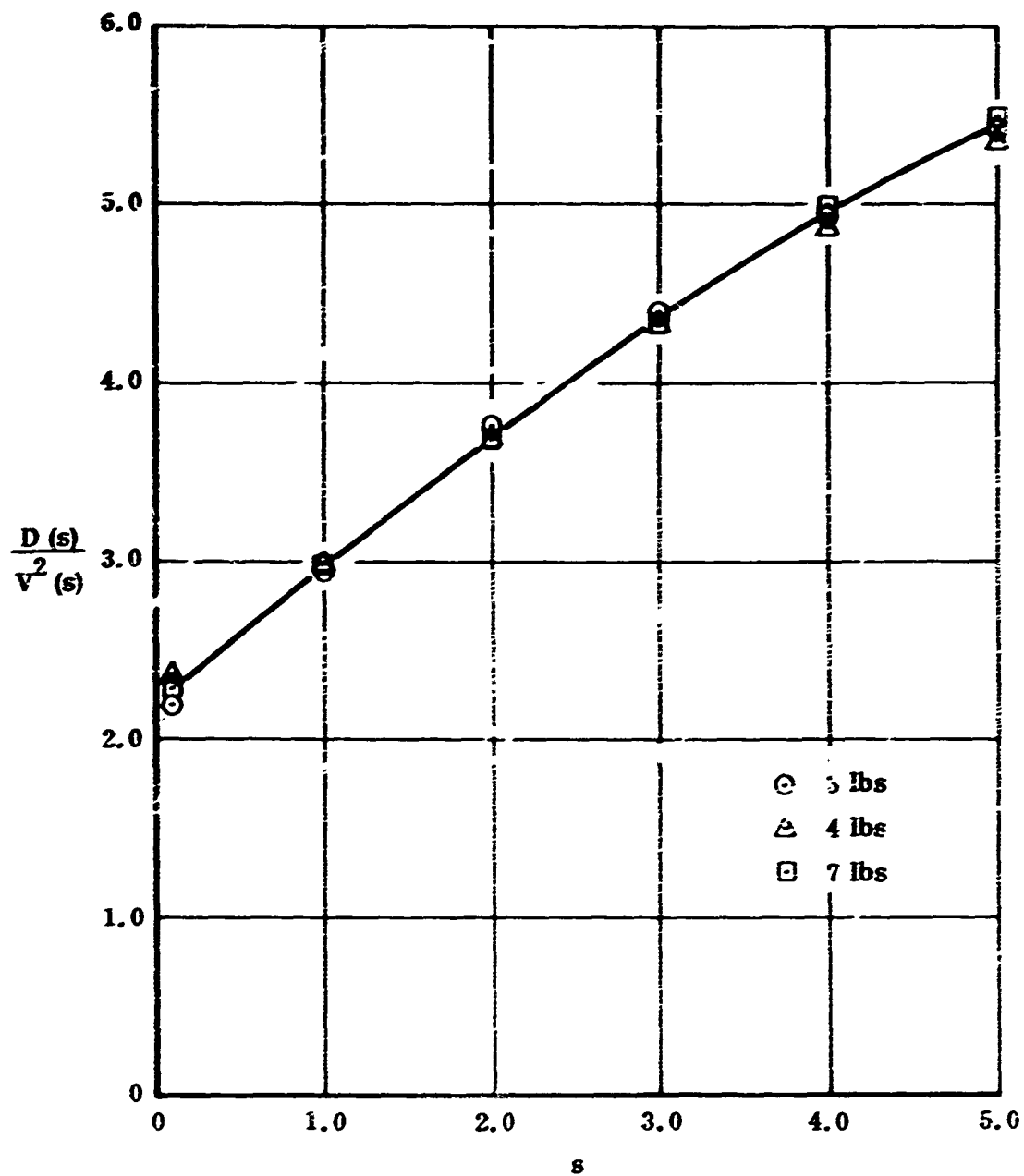


FIGURE 88. TRANSFORMED DATA FOR DRAG DUE TO IMPULSIVE VELOCITY SQUARED

reason, the values of the ratio were evaluated at large values of  $s$  as shown in Figure 89. Over this larger range of  $s$  the previously obtained correlation between the test loads was lost. This is not surprising since the increase of the parameters corresponds to a decrease in the  $vt$  parameter so that the scatter obtained at large  $s$  values can be attributed to errors in measuring the very low forces at the very early part of the model acceleration.

A typical curve

$$\frac{D(z)}{V^2(z)} = \frac{20.6}{z+20} + 2.2 \quad (156)$$

was selected within the range of the test data scatter and the drag variation with time due to a step input of  $V^2$  was obtained as shown in Figure 90.

This study has shown that a possibility exists of obtaining the time-dependent calculation of forces and moments of a shape accelerating from rest using a combination of testing in a relatively simple water tank and analysis of these results by using the indicial function concepts of Reference 45. Although the present study was restricted to the drag of relatively simple models, no special difficulties should be encountered in treating any force or moment history for much more complicated shapes.

Although no practical and usable results have been obtained to enable the prediction of aerodynamics of V/STOL aircraft, the procedure described appears very promising for future refinement and ultimate use in obtaining prediction techniques.

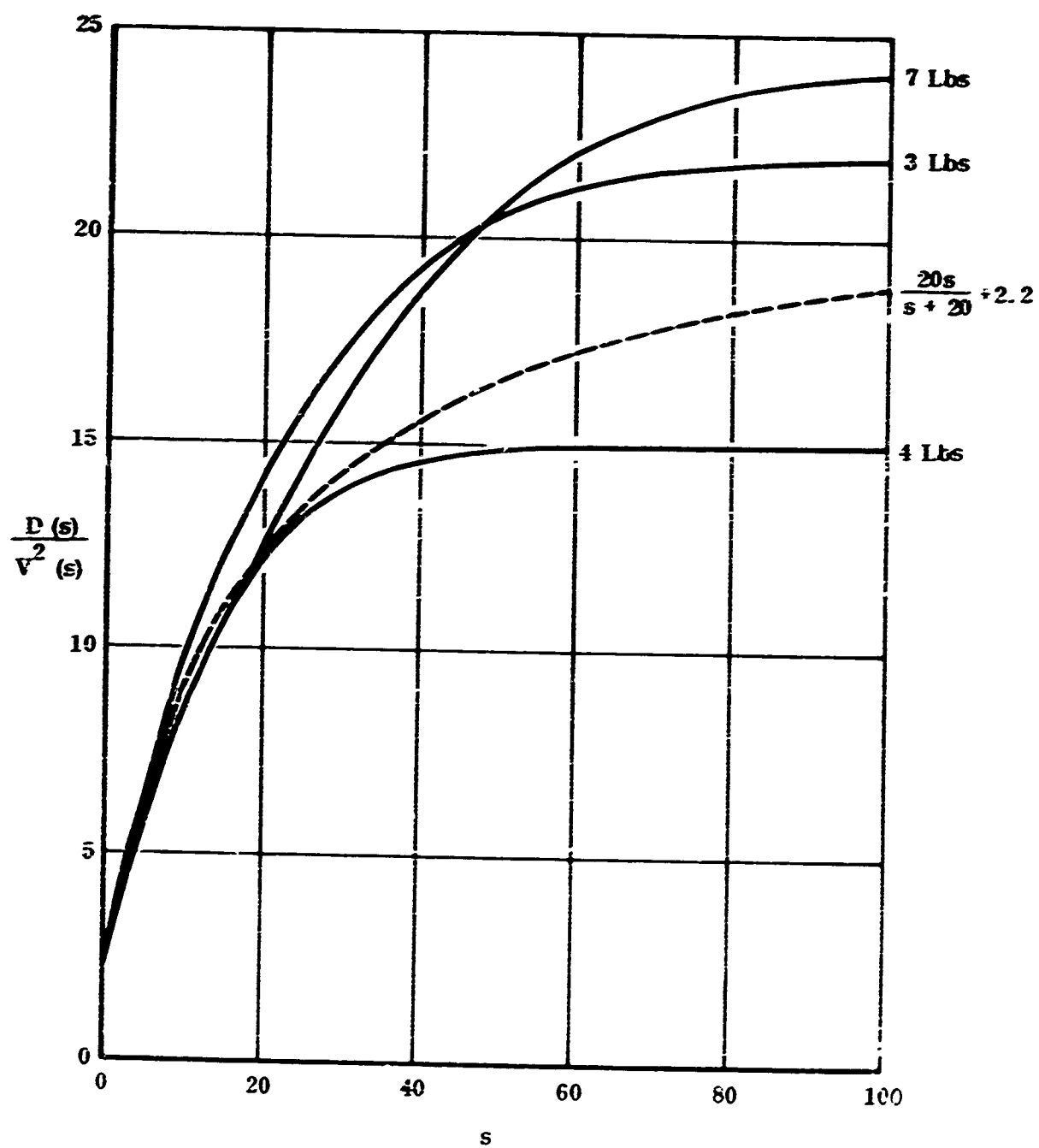


FIGURE 89. TRANSFORMED DATA OVER LARGER RANGE OF  $s$

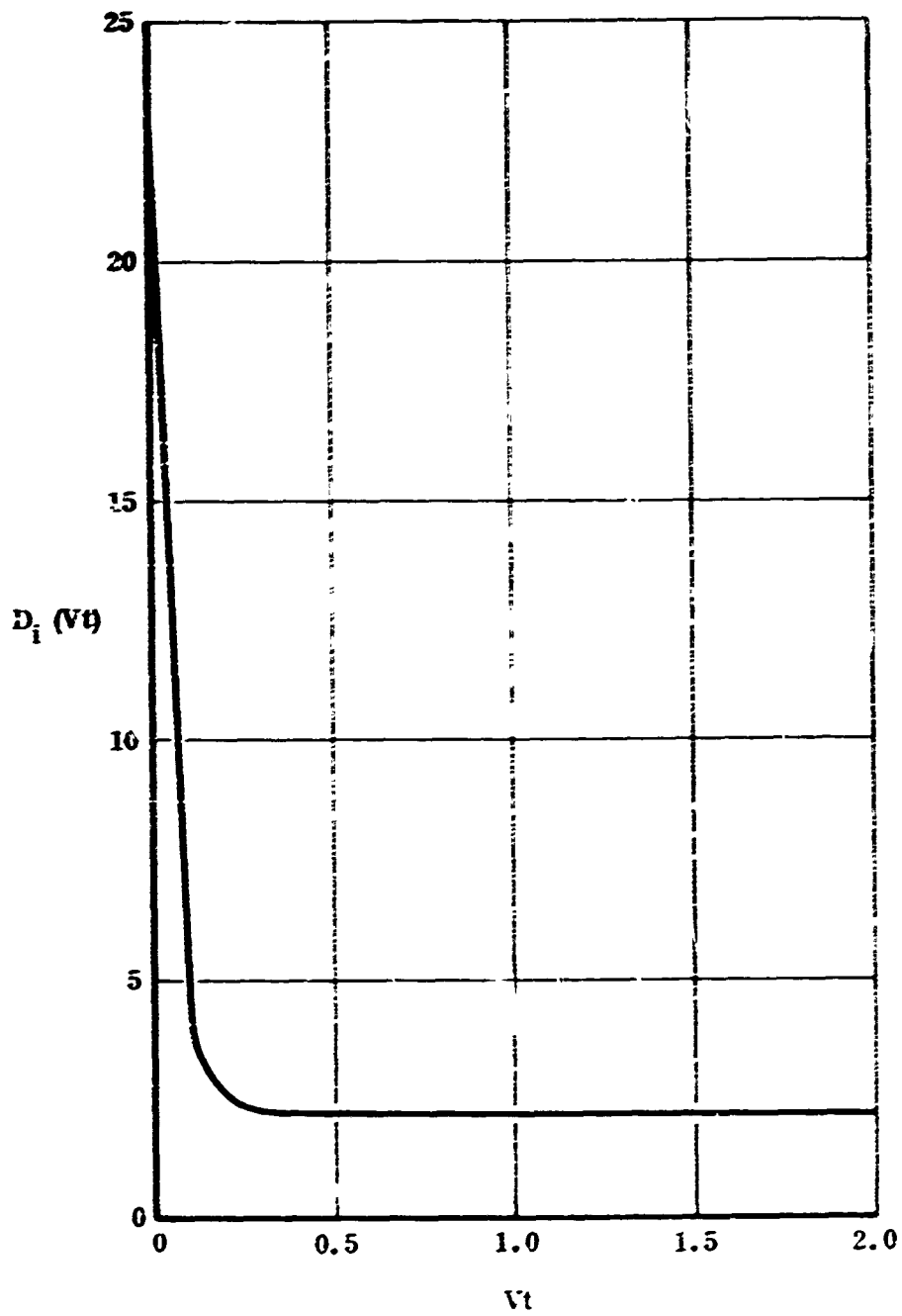


FIGURE 90. DRAG DUE TO IMPULSIVE CHANGE IN VELOCITY

## APPENDIX I

### EFFECT OF ROTARY VARIABLES

In Figure 1  $p$ ,  $q$  and  $r$  represent the magnitudes of the rotary variables defined in the coordinate system shown. The effect of the rotary variables  $p$ ,  $q$  and  $r$  on the development of the jet may be represented by a change in the mainstream velocity vector. The perturbed mainstream velocity vector at a given point along the jet centerline is expressed as

$$\bar{U}_p = \bar{U}_\infty - (p\hat{i} + q\hat{j} + r\hat{k}) \times \bar{R}$$

where  $\hat{i}$ ,  $\hat{j}$ ,  $\hat{k}$  are unit vectors in the fixed coordinate system and  $\bar{R}$  is the position vector of the given point along the jet centerline.

In evaluating the jet-induced flow field, the computations are carried out for a number of segments as shown in Figure 2. Each segment is treated as a separate jet, with proper initial conditions and the appropriate mainstream velocity. The number of integration steps per segment may be arbitrarily specified. The perturbed mainstream velocity vector is assumed constant over the extent of each segment.

In the following discussion, subscripts 1 and 2 refer to jet properties of the segments I and II of Figure 2.

The jet of diameter  $d_{o1}$  is located at  $X_{o1}$ ,  $Y_{o1}$ ,  $Z_{o1}$ . Initial conditions for segment I are

$$d^* = 1, \quad U_j^* = \frac{U_{j1}}{U_\infty} = 1, \quad m_1 = \frac{U_{j1}}{U_\infty}$$

The initial jet exhaust vector is utilized as an approximation to locate the midpoint A of segment I. At this point  $\frac{|\bar{U}_{p1}|}{U_\infty}$  is determined by vector addition as shown, where

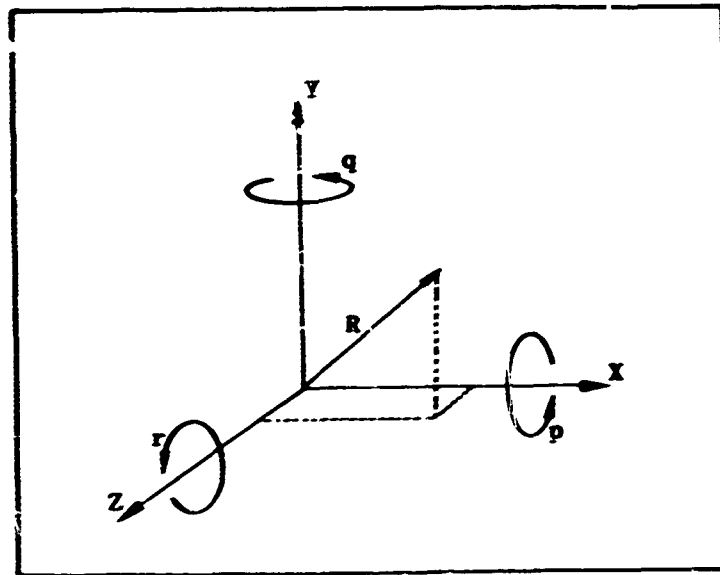


FIGURE I-1. DEFINITION OF ROTARY VARIABLES

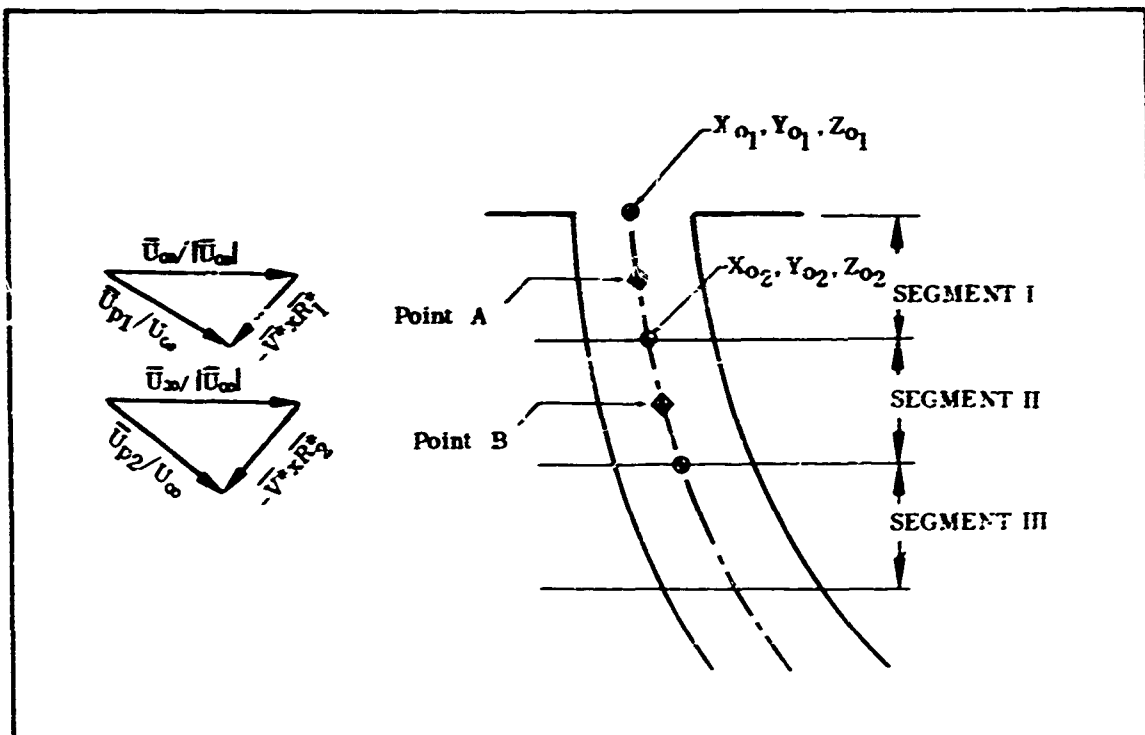


FIGURE I-2. COMPUTATIONAL SCHEME FOR ROTARY VARIABLES

$$\bar{V}^* = \frac{d_0}{U_\infty} (p\hat{i} + q\hat{j} + r\hat{k})$$

$$R^* = \frac{\bar{R}}{d_0}$$

The direction cosines of the perturbed mainstream velocity vector  $\bar{U}_{p1}$  are determined and a local coordinate system is established, centered at  $X_{o1}$ ,  $Y_{o1}$ ,  $Z_{o1}$ , and aligned with the perturbed mainstream velocity vector and the jet exhaust vector (see discussion of arbitrarily directed jet).

The effective inverse velocity ratio for segment I is

$$m_{1,eff} = \frac{U_{p1}}{U_\infty} \frac{U_\infty}{|\bar{U}_{p1}|} = m_1 / \frac{|\bar{U}_{p1}|}{U_\infty}$$

The equations for  $\dot{U}_j$ ,  $\dot{d}$ , and  $\dot{X}$  are then integrated numerically over the extent of segment I.

Point  $X_{o2}$ ,  $Y_{o2}$ ,  $Z_{o2}$  then becomes the origin of the next jet, with a diameter of  $d_{o2} = d^* d_{o1}$ , where  $d^*$  is the last computed value of the nondimensionalized jet diameter of segment I.

Other initial conditions for segment II are

$$d^* = 1., \quad U_{j2}^* = \frac{U_{j2}}{U_{p2}} = 1., \quad m_2 = \frac{U_{j02}}{U_\infty} = U_j^* m_1$$

where  $U_j^*$  is the last computed value of the nondimensionalized jet velocity in segment I.

The jet velocity direction after the integration over the extent of segment I is used to approximately locate midpoint B. At this point  $\frac{|\bar{U}_{p2}|}{U_\infty}$  is evaluated and the direction cosines of the perturbed mainstream velocity vector  $\bar{U}_{p2}$  are determined.

A new local, jet-oriented coordinate system is established, centered at  $X_{o_2}$ ,  $Y_{o_2}$ ,  $Z_{o_2}$ . The effective inverse velocity ratio for this segment is

$$m_{z\text{ eff}} = \frac{U_{wz}}{U_\infty} \frac{U_\infty}{|U_p|} = U_j^* m_i / \frac{|U_{pz}|}{U_\infty}$$

The equations for  $U_j^*$ ,  $d^*$ ,  $X^*$  are then integrated over the extent of segment II.

The computations described above continue until integration over the extent of the entire jet has been accomplished. Although each segment is treated as a separate jet, the segments are linked to each other in determining the degree to which the jet has deformed from its initial circular cross section. This is done by setting

$$D_{o_2} = D_1, \quad D_{o_3} = D_2$$

i.e., specifying the initial ratio of minor to major axis for a given segment to be equal to the last computed value for the previous segment.

The induced velocity components at a given control point are determined by summing the velocity components due to each segment of the jet. Again each segment is treated as a separate jet for these computations.

Figure 3 shows the effect of the rotary variable  $r$  on the centerline of a jet exhausting normally into a crossflow at a velocity ratio  $U_\infty/U_{j_0} = .125$ . One curve ( $r^* = \frac{rd_0}{U_\infty} = 0.0$ ) shows the centerline of the undisturbed jet exhausting into a crossflow at this velocity ratio. It was computed by considering the jet to consist of a number of segments, as described in detail in the preceding discussion, with  $\bar{V}^* = 0.0$  for each segment. The centerline computed in this manner deviates less than 1 percent from previously computed results.

The sign convention for the rotary variable  $r$  was established in Figure 1. For  $r^* < 0.0$  the perturbed mainstream velocity  $|U_p| < U_\infty$  and the jet centerline shows less deflection. For  $r^* > 0.0$  the perturbed mainstream velocity  $|U_p| > U_\infty$ , which results in a greater deflection of the jet centerline.

Induced velocity components in the plane of the jet exit were evaluated for two values of  $r^*$ . Table 1 shows the incremental change in velocity components at three control points as a function of the rotary variable  $r^*$ . It can be observed that  $\Delta(u/U)/\Delta r^*$ ,  $\Delta(v/U)/\Delta r^*$  and  $\Delta(w/U)/\Delta r^*$  are not constant at each control point. Since the incremental changes in induced velocities are directly related to the induced forces and moments due to the rotary variable, it is desirable to establish the range over which they could be considered linear with  $r^*$ .



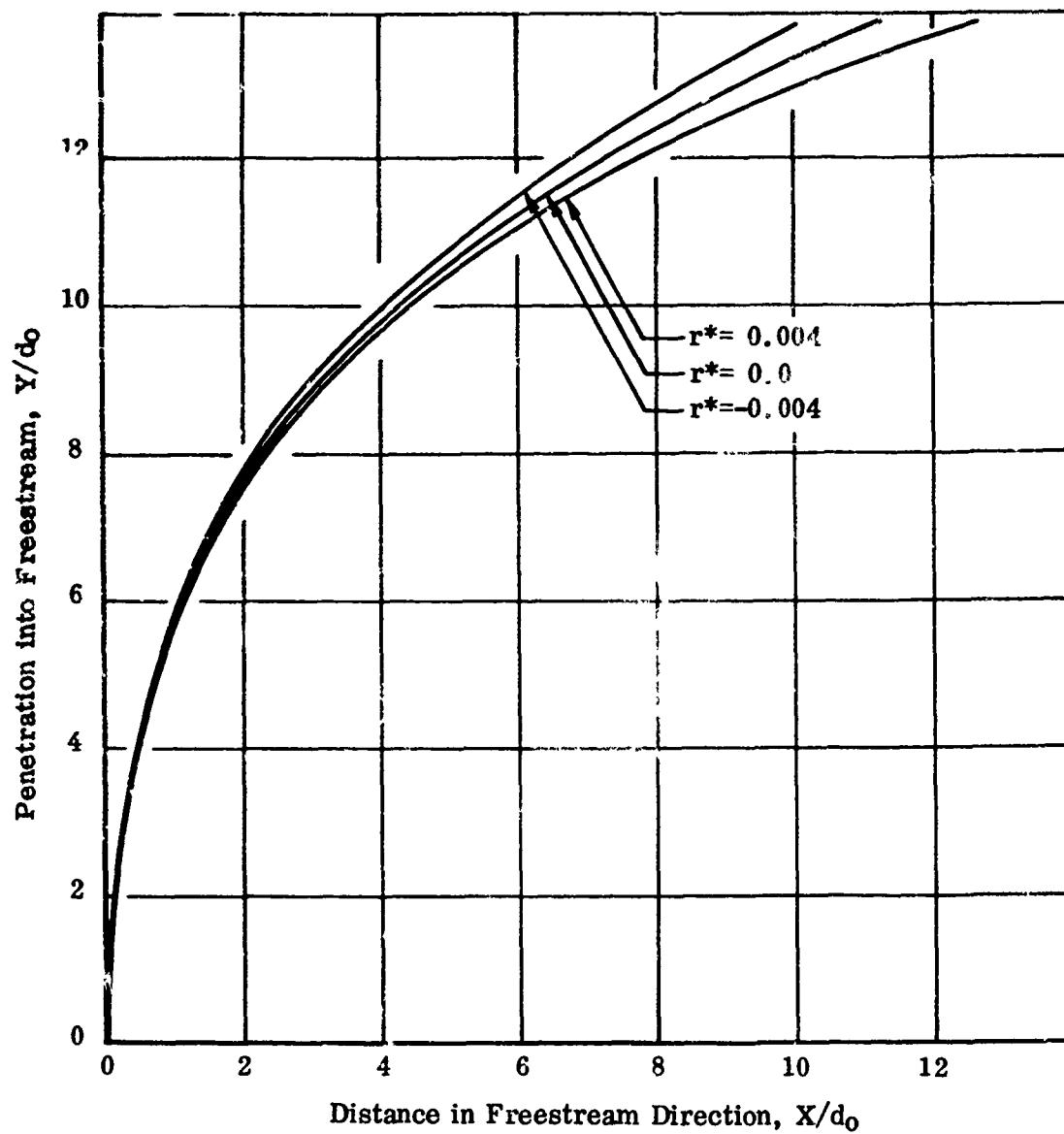
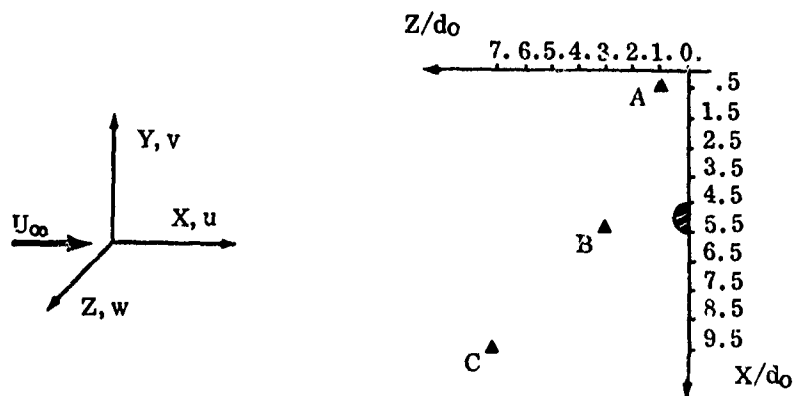


FIGURE I-3. EFFECT OF ROTARY VARIABLE ON A JET CENTERLINE



$r^*$	Point A			Point B			Point C		
	$\Delta u/U$	$\Delta v/U$	$\Delta w/U$	$\Delta u/U$	$\Delta v/U$	$\Delta w/U$	$\Delta u/U$	$\Delta v/U$	$\Delta w/U$
.002	-.000866	.000391	-.000602	-.000998	.000296	-.000337	-.000409	-.000486	.000017
.004	-.001898	.001153	-.001068	-.001954	.000974	-.000580	-.000926	-.001121	.000043
-.002	.001036	-.000494	.000500	.000941	-.000410	.000256	.000518	.000349	-.000034
-.004	.002148	-.000779	.001115	.002114	-.000584	.000588	.001144	.000646	-.000058

TABLE I-I. EFFECT OF ROTARY VARIABLE ON INDUCED VELOCITY COMPONENTS

	X = .95, Z = .7			X = .55, Z = .7			X = .15, Z = .7		
	u/U	v/U	w/U	u/U	v/U	w/U	u/U	v/U	w/U
q = 0.	.0180	-.0307	-.0411	.0337	-.0162	-.0296	.0273	-.0016	-.0095
q = .1	.0179	-.0303	-.0407	.0334	-.0159	-.0292	.0269	-.0015	-.0093
C/C	.0177	-.0299	-.0410	.0332	-.0156	-.0294	.0267	-.0013	-.0094
	X = .95, Z = .1			X = .55, Z = .1			X = .15, Z = .1		
	u/U	v/U	w/U	u/U	v/U	w/U	u/U	v/U	w/U
q = 0.	-.0131	-.1073	-.0239	.1482	-.1985	-.1790	.0342	.0159	.0048
q = .1	-.0130	-.1070	-.0236	.1474	-.1974	-.1784	.0339	.0158	.0050
C/C	-.0135	-.1075	-.0242	.1498	-.1985	-.1793	.0334	.0163	.0049

TABLE I-II. EFFECT OF ROTARY VARIABLE IN A REACTION CONTROL CONFIGURATION

The velocity components of Table 1 were obtained by considering an equal number of integration steps along the  $\hat{Z}'$ -axis in solving for the geometry of the jet. This means that for every value of  $r^*$  a different length  $s$  of the jet was considered in evaluating the induced velocity components. In an effort to separate the effects due to a change in the rotary variable from the effects due to integrating over a variable length of the jet, two different approaches to establishing an equivalent length  $s$  were utilized.

One approach was to sum contributions to each induced velocity component due to the singularity distribution along the jet centerline until the contribution from a given segment represented less than .1 percent of the total up to this point. Further contributions were neglected. The other method utilized a straight line approximation for the jet centerline to determine an equal length  $s$  of the jet for each value of  $r^*$ .

For both of the methods described above, the axis of rotation was taken through the jet exit and the behavior of the incremental changes in velocity components at the various control points was examined. For the range of  $r^*$  considered, which encompasses a variation of  $r$  from .1 to .4 radians/sec, it appears that the incremental changes in velocity components are small enough, relative to the overall accuracy of the method, to preclude a meaningful determination of the quantities  $\Delta(u/U)\Delta r^*$ ,  $\Delta(v/U)\Delta r^*$ ,  $\Delta(w/U)\Delta r^*$ .

Computations to determine the effect of rotation about an axis other than the jet exit were carried out. Rotation about the center of gravity in a reaction control configuration for the XV-6 was chosen as an example. Computations with the moment arm  $l = 11.2$  ft,  $d_0 = .2$  ft,  $U_{j0} = 400$  ft/sec,  $U_\infty = 50$  ft/sec and  $q = .1$  rad/sec again showed small changes in the induced velocities evaluated in the plane of the jet exit. A check case in which the freestream velocity was assumed to be uniformly perturbed over the extent of the jet,  $\bar{U}_p = \bar{U}_\infty + \Delta\bar{U}$ , where  $\Delta\bar{U} = l \times q = 1.12$  ft/sec, was also computed. Table 3 shows induced velocity components at various control points for  $q = 0.$ ,  $q = .1$  and the check case. Again, indications are that the effects due to the rotary variables in a reaction control configuration are negligible.

## APPENDIX II

### DETERMINATION OF TRAILING VORTEX INTEGRAL

The integral  $\int_{-\infty}^{\infty} \frac{dx_1}{r^3}$  in Equation (121) may be written in the form

$$\int_{-\infty}^{\infty} \frac{dx_1}{X\sqrt{X}} \quad \text{where} \quad X = a + b x_1 + c x_1^2$$

using the same notation as Equation (123)

$$\text{Now} \quad \int_{-\infty}^{\infty} \frac{dx_1}{X\sqrt{X}} = \frac{2[2c\xi + b]}{(4ac - b^2)\sqrt{a + b\xi + c\xi^2}} - \frac{4\sqrt{c}}{(4ac - b^2)}$$

$$\text{Let} \quad a_1 = \frac{\tan \beta_c}{\cos \alpha_c}$$

$$b_1 = \tan \alpha_c$$

$$\xi = 0$$

$$\text{then} \quad a = x^2 + (y - \eta - a_1 \xi)^2 + (z + b_1 \xi)^2$$

$$b = -2[x - a_1(y - \eta - a_1 \xi) + (z + b_1 \xi)b_1]$$

$$c = 1 + a_1^2 + b_1^2$$

$$\begin{aligned} \text{Thus } ac - \frac{b^2}{4} &= [1+b_1^2] \eta^2 + [a_1^2+b_1^2] \xi^2 + 2a_1 \xi \eta - 2[\eta + \eta b_1^2 + a_1 x + a_1 b_1 z] \eta \\ &\quad + 2[\xi b_1 - \eta a_1 - a_1^2 x - b_1^2 x] \xi \\ &\quad + \eta^2 + \xi^2 + a_1^2 x^2 + b_1^2 x^2 + b_1^2 y^2 + a_1^2 z^2 + 2a_1 xy - 2b_1 xz + 2a_1 b_1 z \end{aligned}$$

$$\text{Now } \xi = \xi_i + (\eta - \eta_i) \frac{|\eta|}{\eta} \tan \phi_i$$

So that with

$$A_1 = 1+b_1^2$$

$$A_2 = a_1^2+b_1^2$$

$$A_3 = 2a_1$$

$$A_4 = -2[\eta + \eta b_1^2 + a_1 x + a_1 b_1 z]$$

$$A_5 = -2[a_1 \eta - b_1 z + a_1^2 x + b_1^2 x]$$

$$A_6 = \eta^2 + \xi^2 + a_1^2 x^2 + b_1^2 x^2 + b_1^2 y^2 + a_1^2 z^2 + 2a_1 xy - 2b_1 xz + 2a_1 b_1 z$$

$$\text{We obtain } ac - \frac{b^2}{4} = A_1 \eta^2 + A_2 \xi^2 + A_3 \xi \eta + A_4 \eta + A_5 \xi + A_6$$

$$\text{and then } ac - \frac{b^2}{4} = A \eta^2 + B \eta + C$$

$$\text{where } A = A_1 + A_2 \tan^2 \phi_i + A_3 \frac{|\eta|}{\eta} \tan \phi_i$$

$$B = 2A_2 \left[ \xi_i - \eta_i \frac{|\eta|}{\eta} \tan \phi_i \right] \frac{|\eta|}{\eta} \tan \phi_i + A_3 \left[ \xi_i - \eta_i \frac{|\eta|}{\eta} \tan \phi_i \right] + A_4 + A_5 \frac{|\eta|}{\eta} \tan \phi_i$$

$$C = A_2 \left[ \xi_i - \eta_i \frac{|\eta|}{\eta} \tan \phi_i \right]^2 + A_5 \left[ \xi_i - \eta_i \frac{|\eta|}{\eta} \tan \phi_i \right] + A_6$$

$$\text{Now } 2c\xi + b = 2(F\eta + G)$$

$$\text{where } F = \frac{|\eta|}{\eta} \tan \phi_i - a_1$$

$$G = \xi_i - \eta_i \frac{|\eta|}{\eta} \tan \phi_i - x + a_1 y - b_1 z$$

$$\text{Thus } \int \frac{dx}{r^3} = \frac{F\gamma + G}{(A\gamma^2 + B\gamma + C)\sqrt{(x-\xi)^2 + (y-\eta)^2 + z^2}} - \frac{\sqrt{1+a_1^2+b_1^2}}{A\gamma^2 + B\gamma + C}$$

$$\text{Now } (x-\xi)^2 + (y-\eta)^2 + z^2 = \gamma^2 + D\gamma + E$$

$$\text{where } D = -2 \left[ \eta + x \frac{1}{\gamma} \tan \phi_c - \left( \xi - \gamma \frac{1}{\gamma} \tan \phi_c \right) \frac{1}{\gamma} \tan \phi_c \right] / (1 + \tan^2 \phi_c)$$

$$\text{and } E = \frac{x^2 + y^2 + z^2 - 2x \left[ \xi - \gamma \frac{1}{\gamma} \tan \phi_c \right] + \left[ \xi - \gamma \frac{1}{\gamma} \tan \phi_c \right]^2}{1 + \tan^2 \phi_c}$$

Thus Equation (121) becomes

$$dw_c = \frac{\frac{1}{4\pi} \left[ y - \gamma + \frac{\tan \beta_c}{\cos \alpha_c} (x - \xi) \right] d\gamma \left[ \frac{F\gamma + G}{\sqrt{1 + \tan^2 \phi_c} (\gamma^2 + D\gamma + E)^{3/2}} - \frac{\sqrt{1 + a_1^2 + b_1^2}}{A\gamma^2 + B\gamma + C} \right]}{A\gamma^2 + B\gamma + C}$$

$$\text{Now } y - \gamma + \frac{\tan \beta_c}{\cos \alpha_c} (x - \xi) = H\gamma + I$$

$$\text{with } H = - \left[ 1 + a_1 \frac{1}{\gamma} \tan \phi_c \right]$$

$$\text{and } I = y + a_1 x - a_1 \left[ \xi - \gamma \frac{1}{\gamma} \tan \phi_c \right]$$

so that finally we obtain

$$w_c = \frac{1}{4\pi} \int_{\gamma_1}^{\gamma_2} \left\{ \frac{(H\gamma + I)(F\gamma + G)}{\sqrt{1 + \tan^2 \phi_c} (A\gamma^2 + B\gamma + C) \sqrt{\gamma^2 + D\gamma + E}} - \frac{\sqrt{1 + a_1^2 + b_1^2} (H\gamma + I)}{A\gamma^2 + B\gamma + C} \right\} \frac{d\gamma}{d\gamma}$$

# APPENDIX III

## Auxiliary Curves Used in Empirical Prediction Methods for the Wing

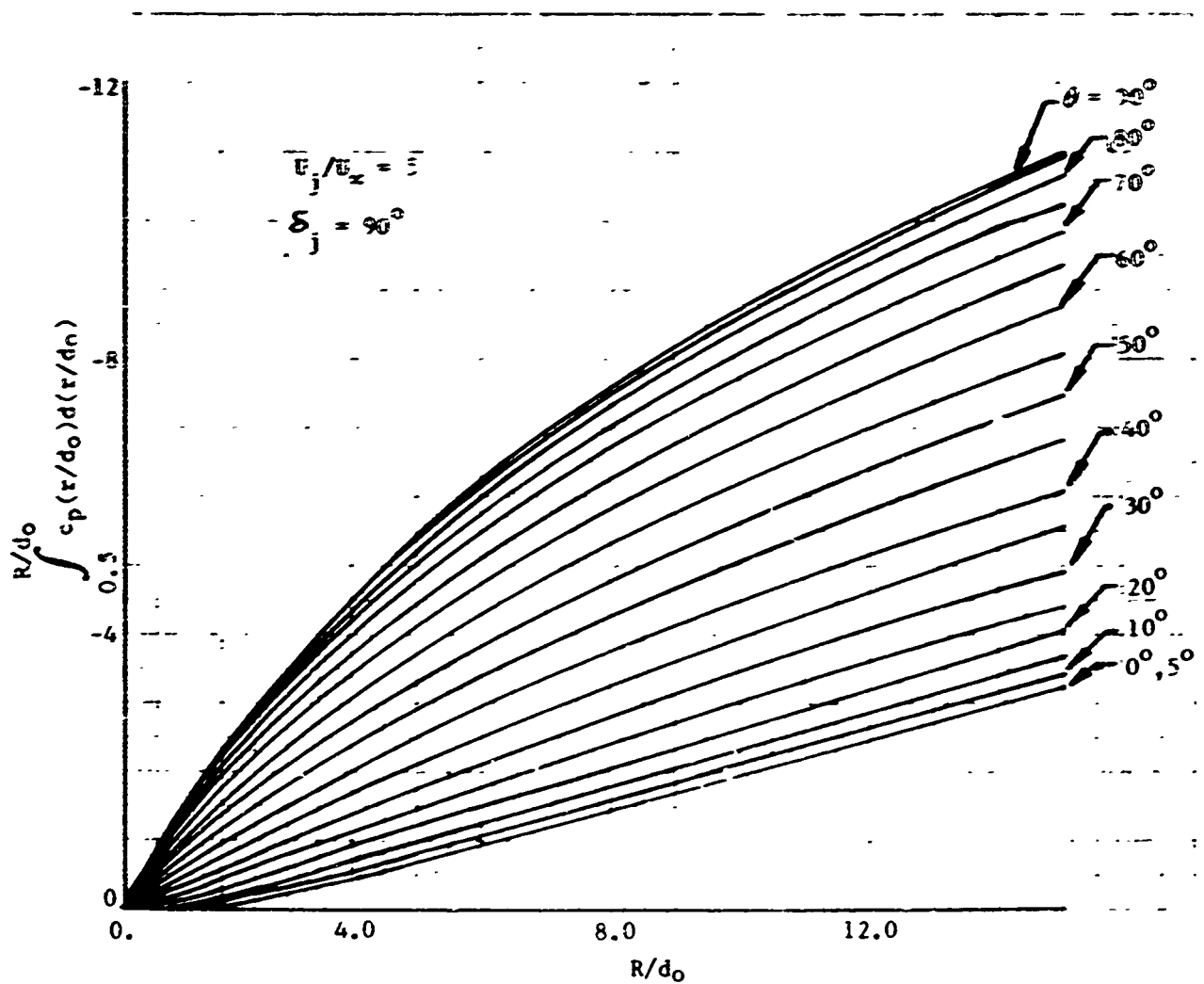


FIGURE III-1. SURFACE FORCE DISTRIBUTION AROUND A JET

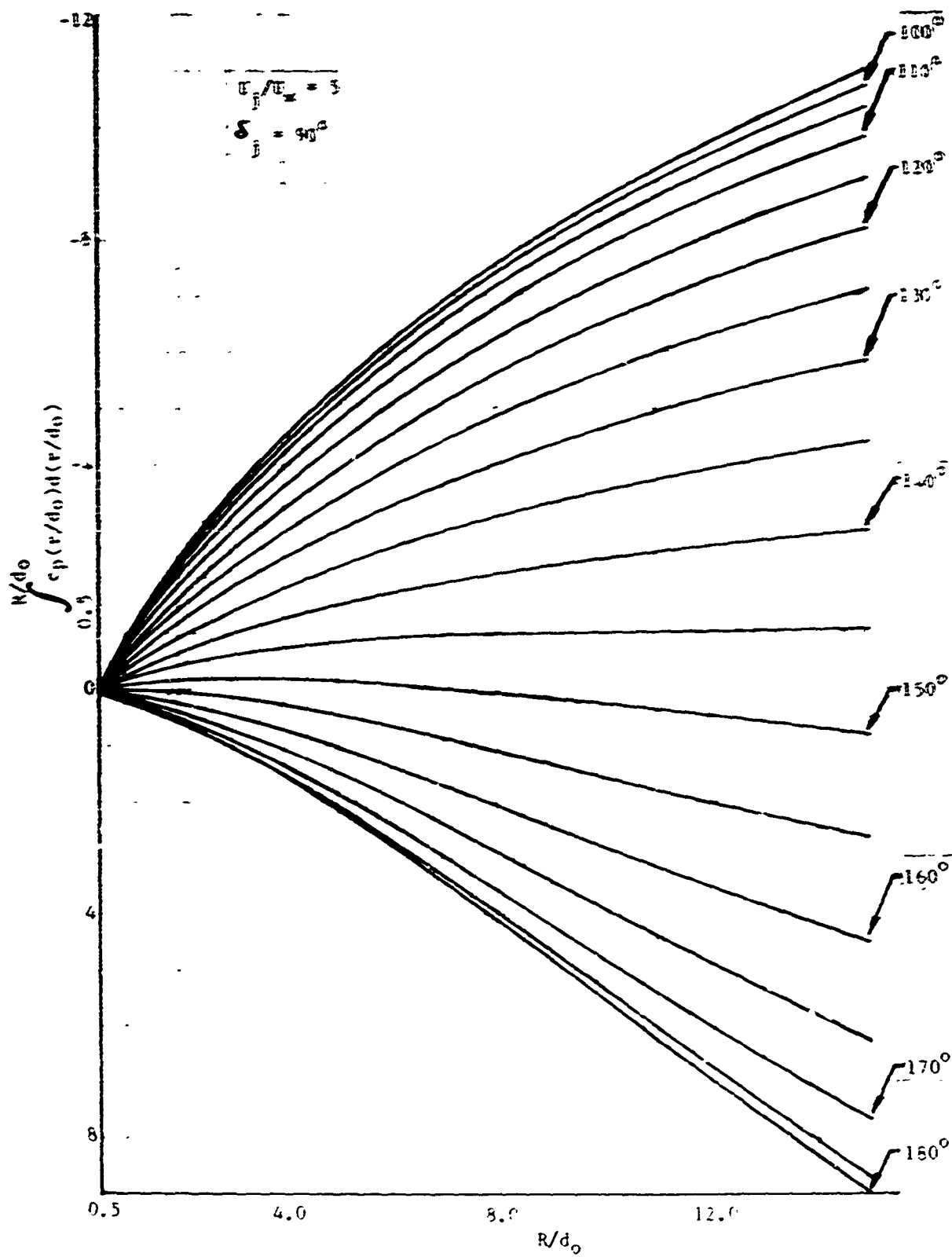


FIGURE III-1. (concluded)



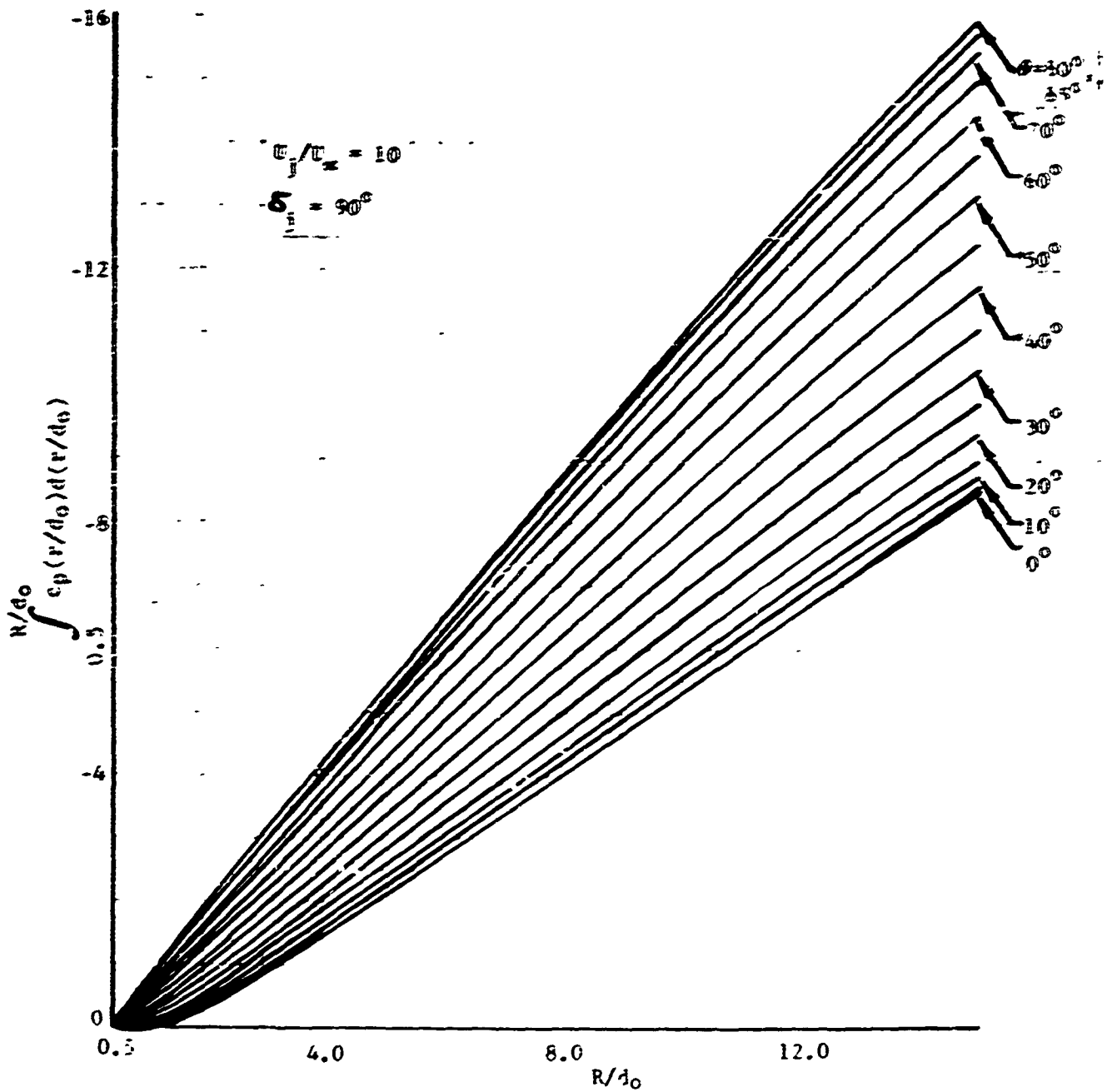


FIGURE III-2. SURFACE FORCE DISTRIBUTION AROUND A JET

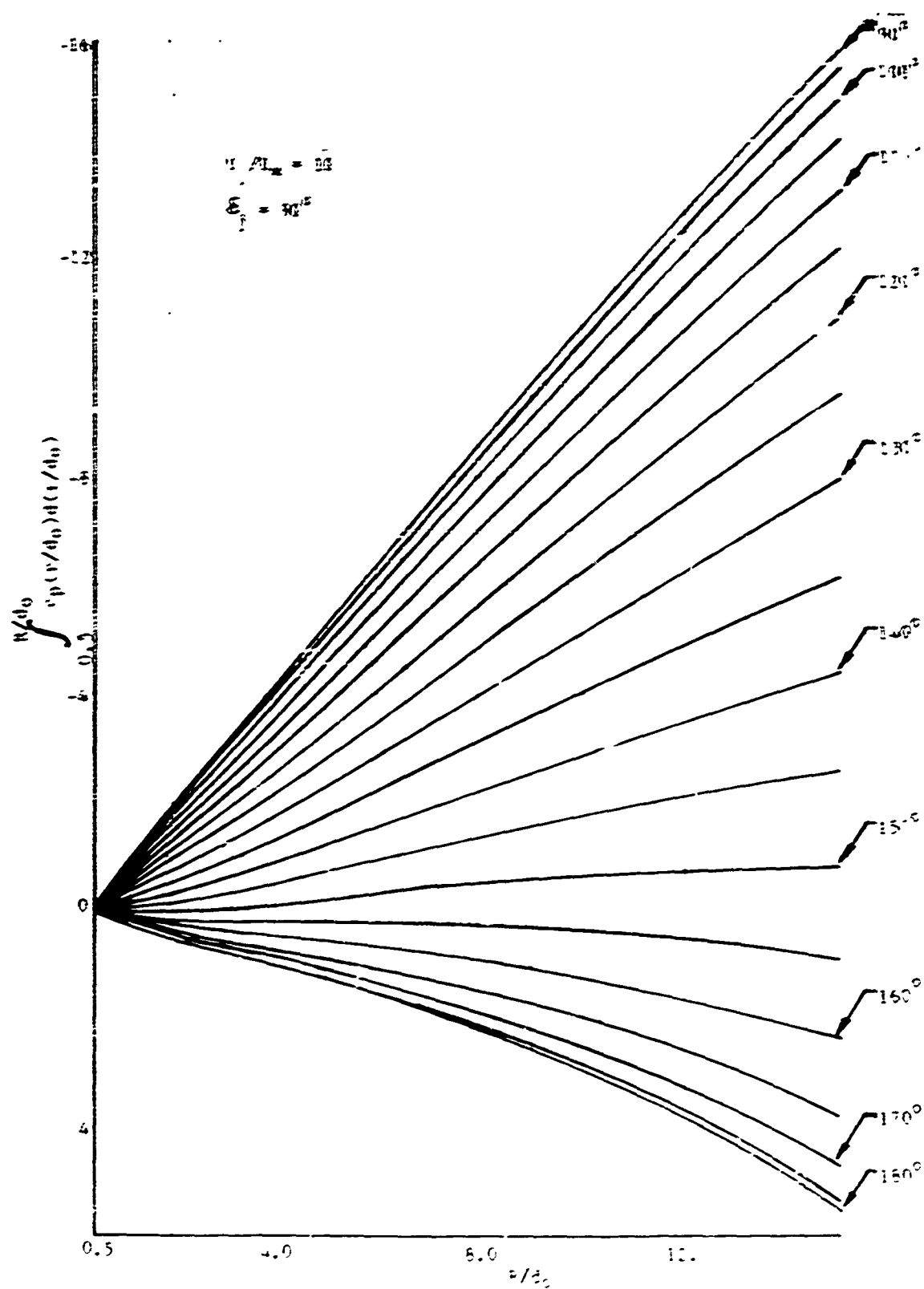


FIGURE III-2. (concluded)

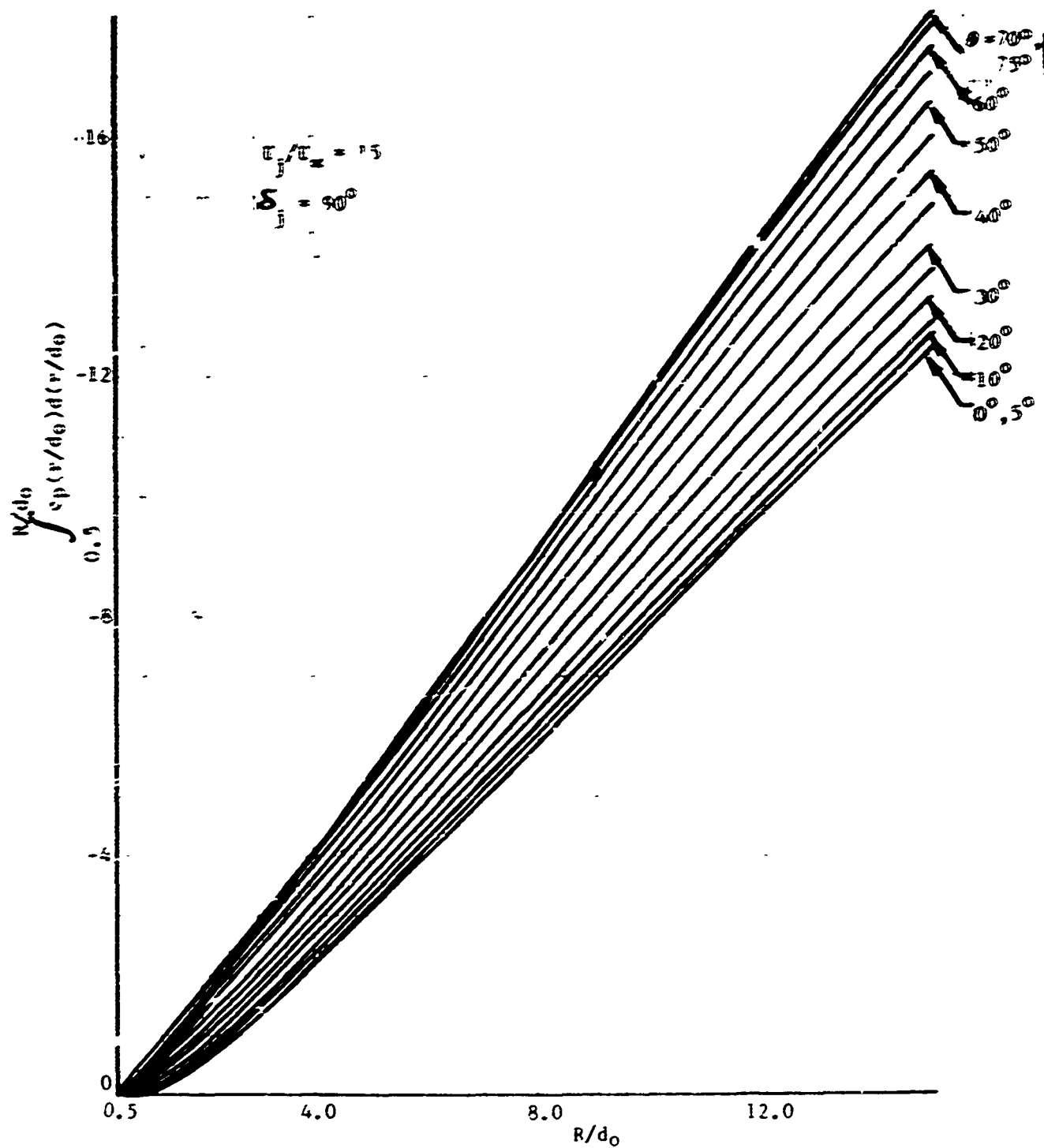


FIGURE III-3. SURFACE FORCE DISTRIBUTION AROUND A JET

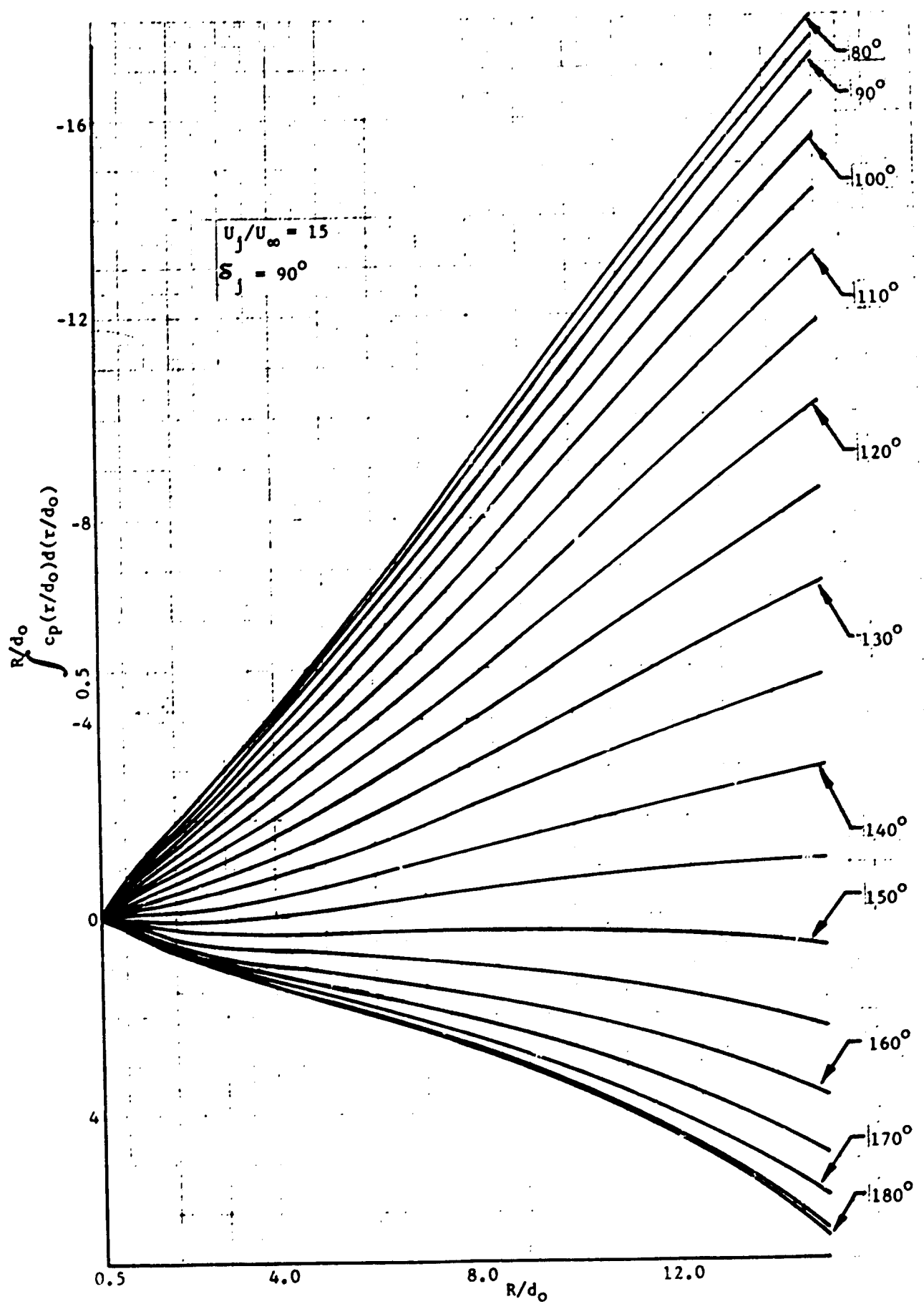


FIGURE III-3. (concluded)

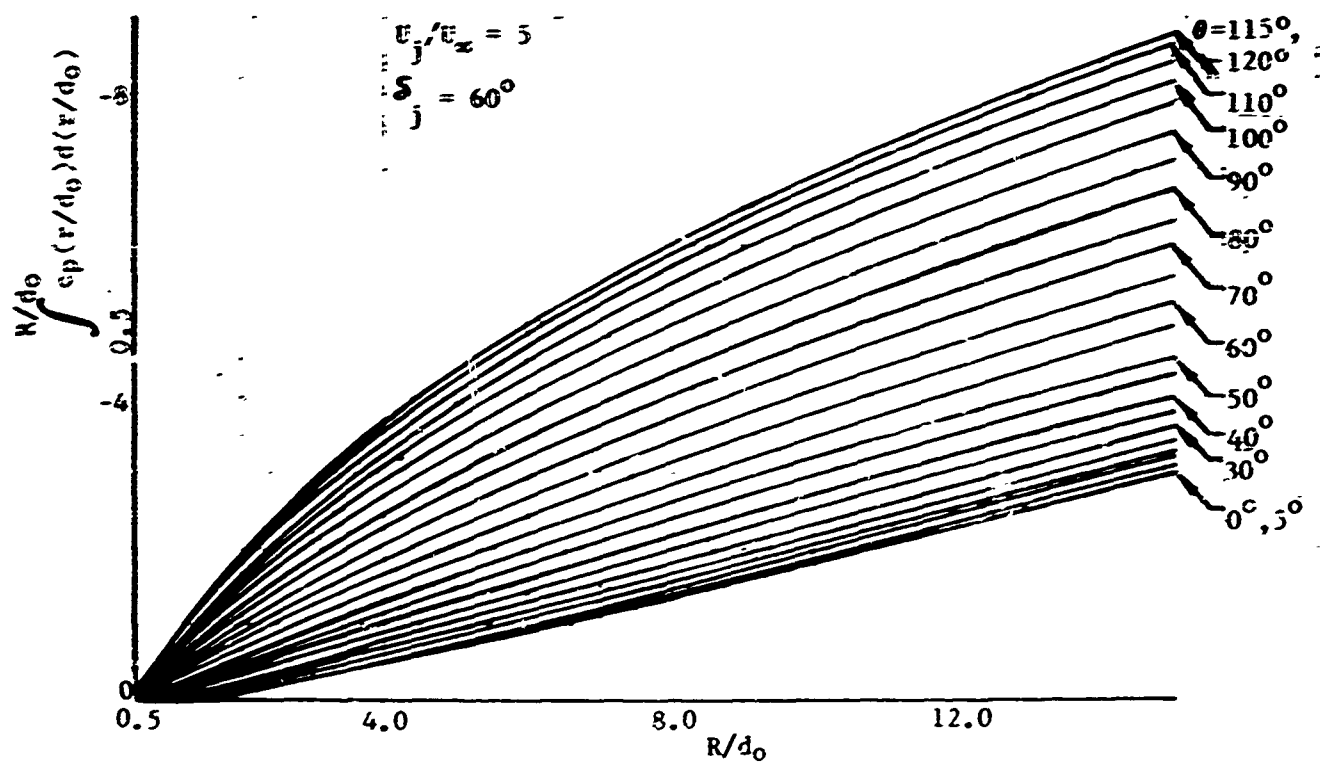


FIGURE III-4. SURFACE FORCE DISTRIBUTION AROUND A JET

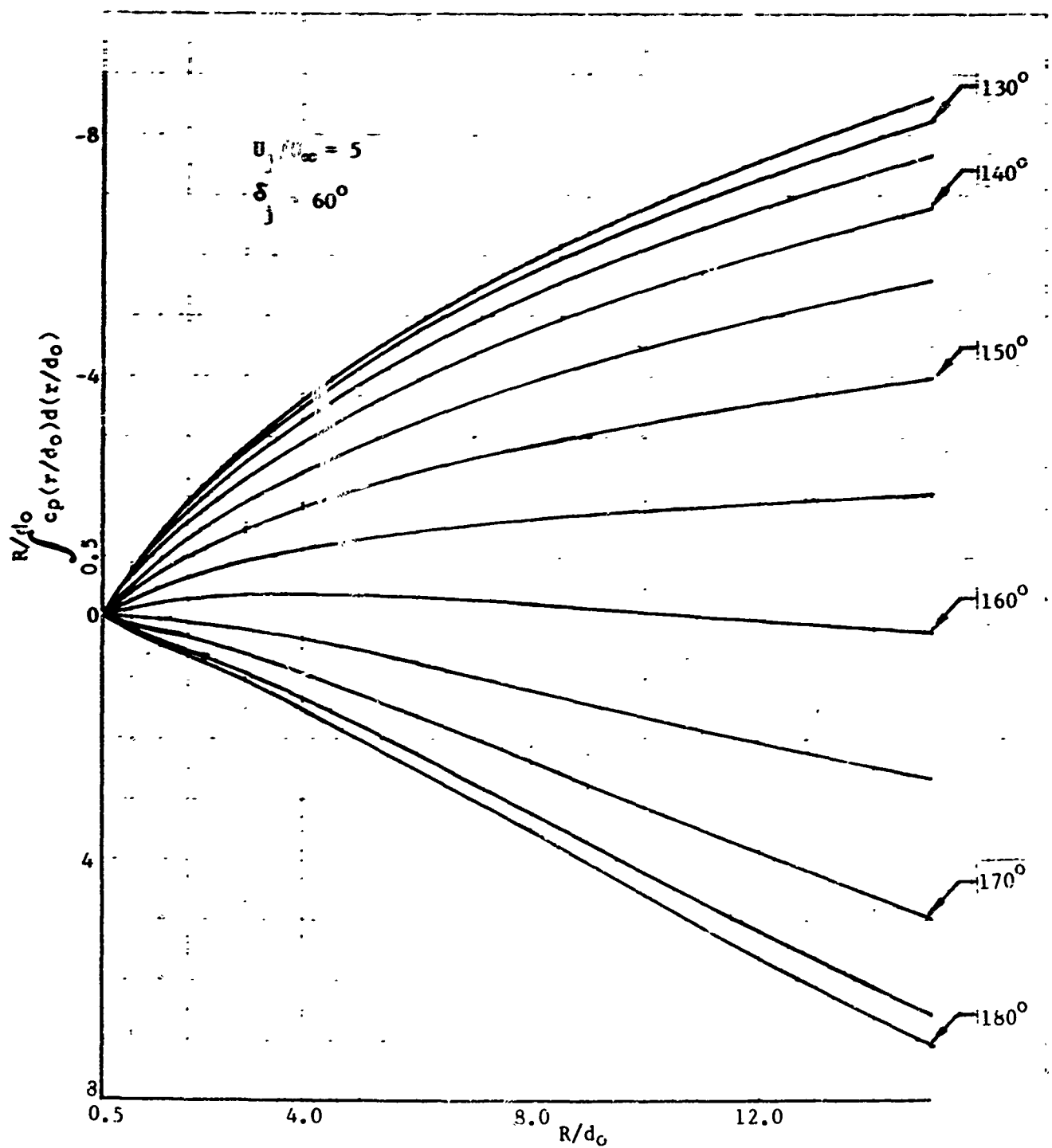


FIGURE III-4. (concluded)

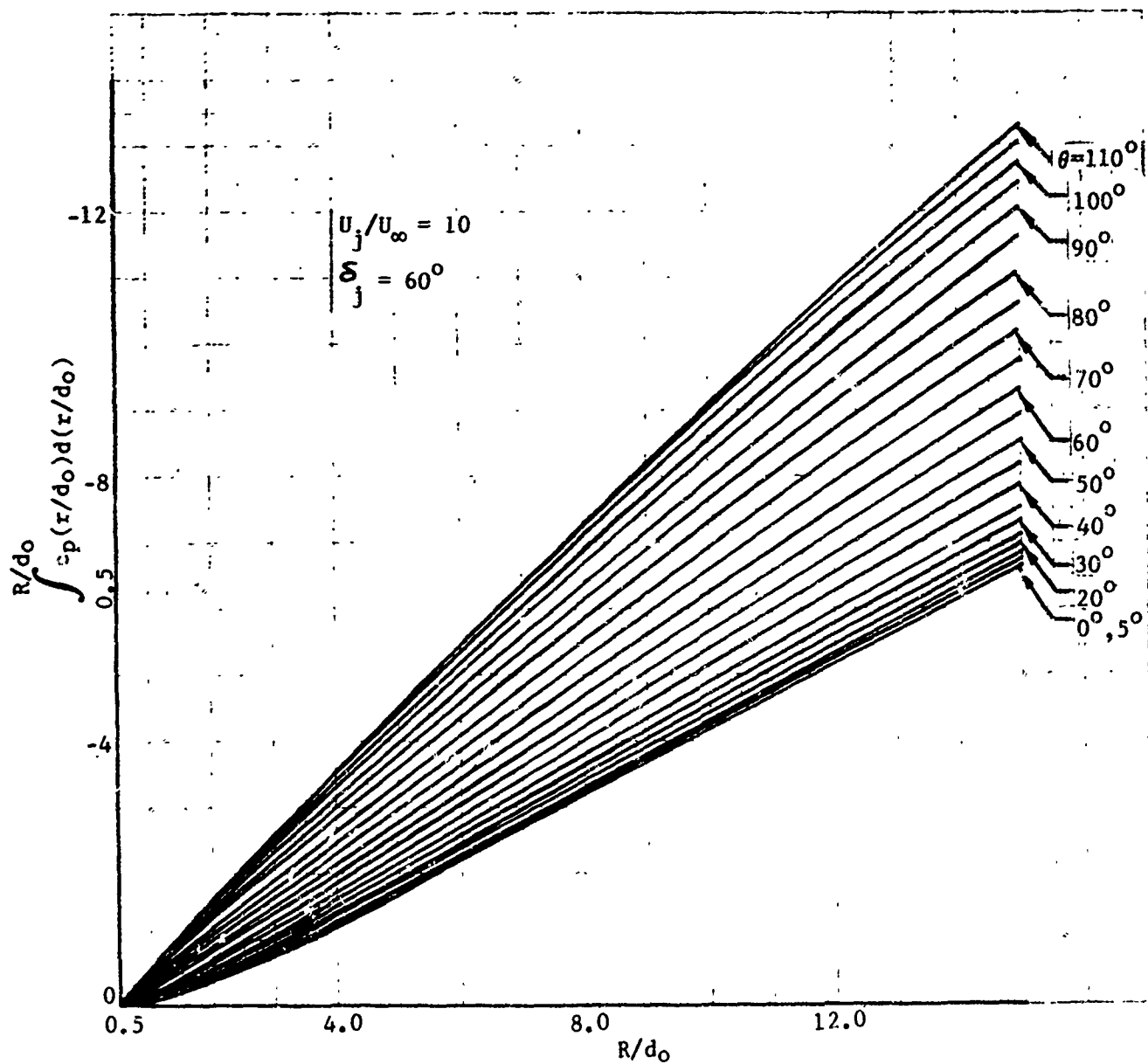


FIGURE III-5. SURFACE FORCE DISTRIBUTION AROUND A JET

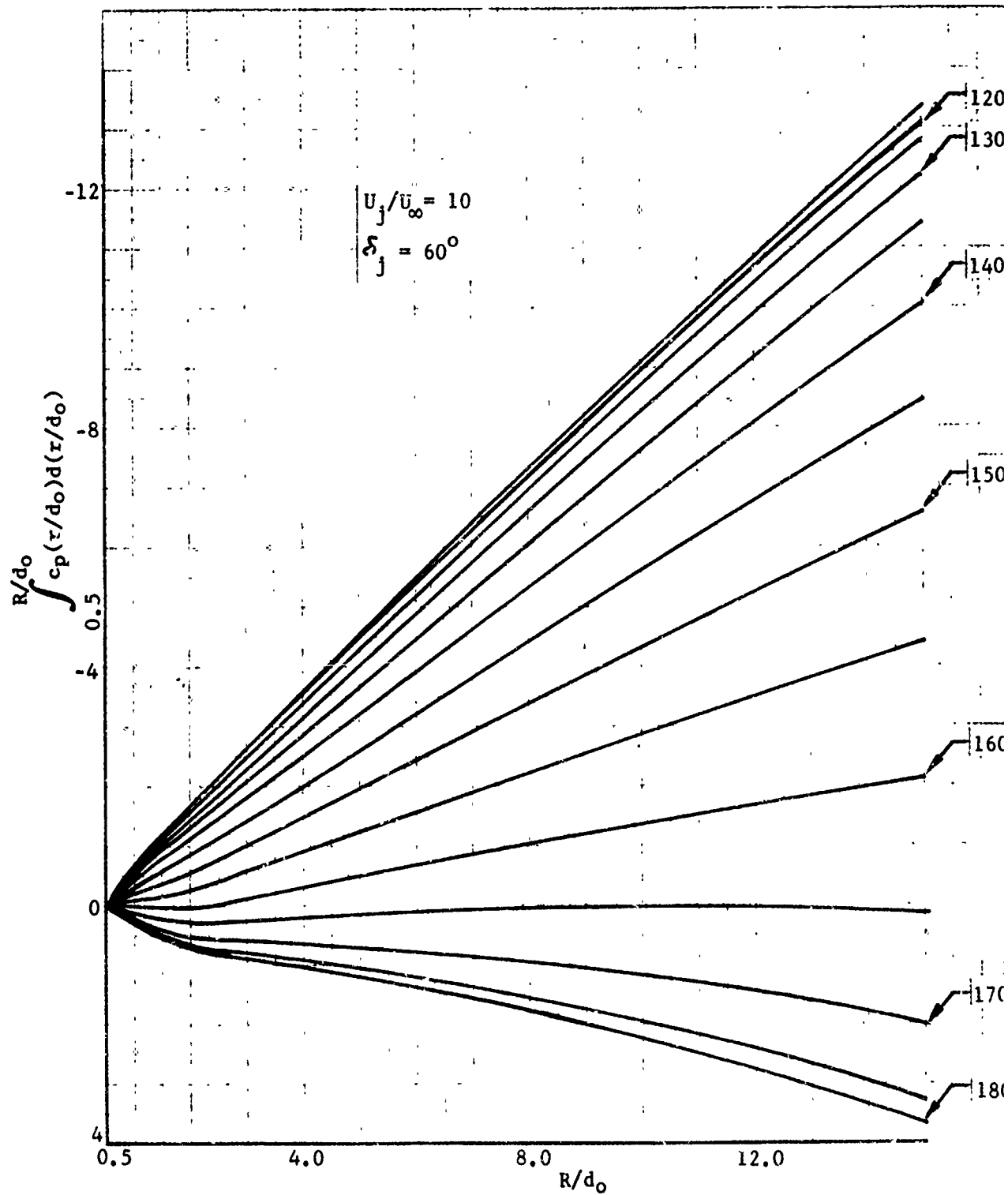


FIGURE III-5. (concluded)



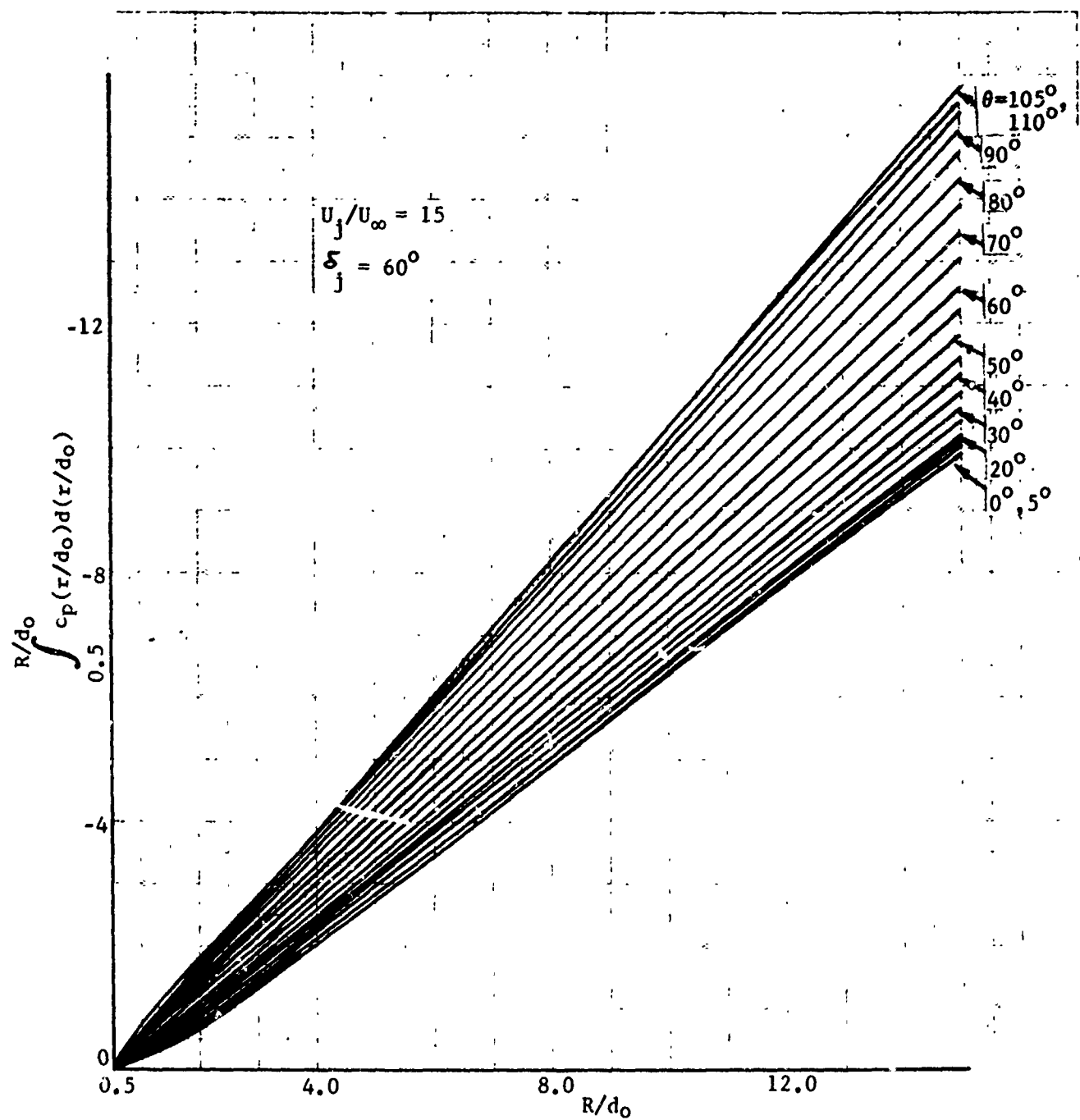


FIGURE III-6. SURFACE FORCE DISTRIBUTION AROUND A JET

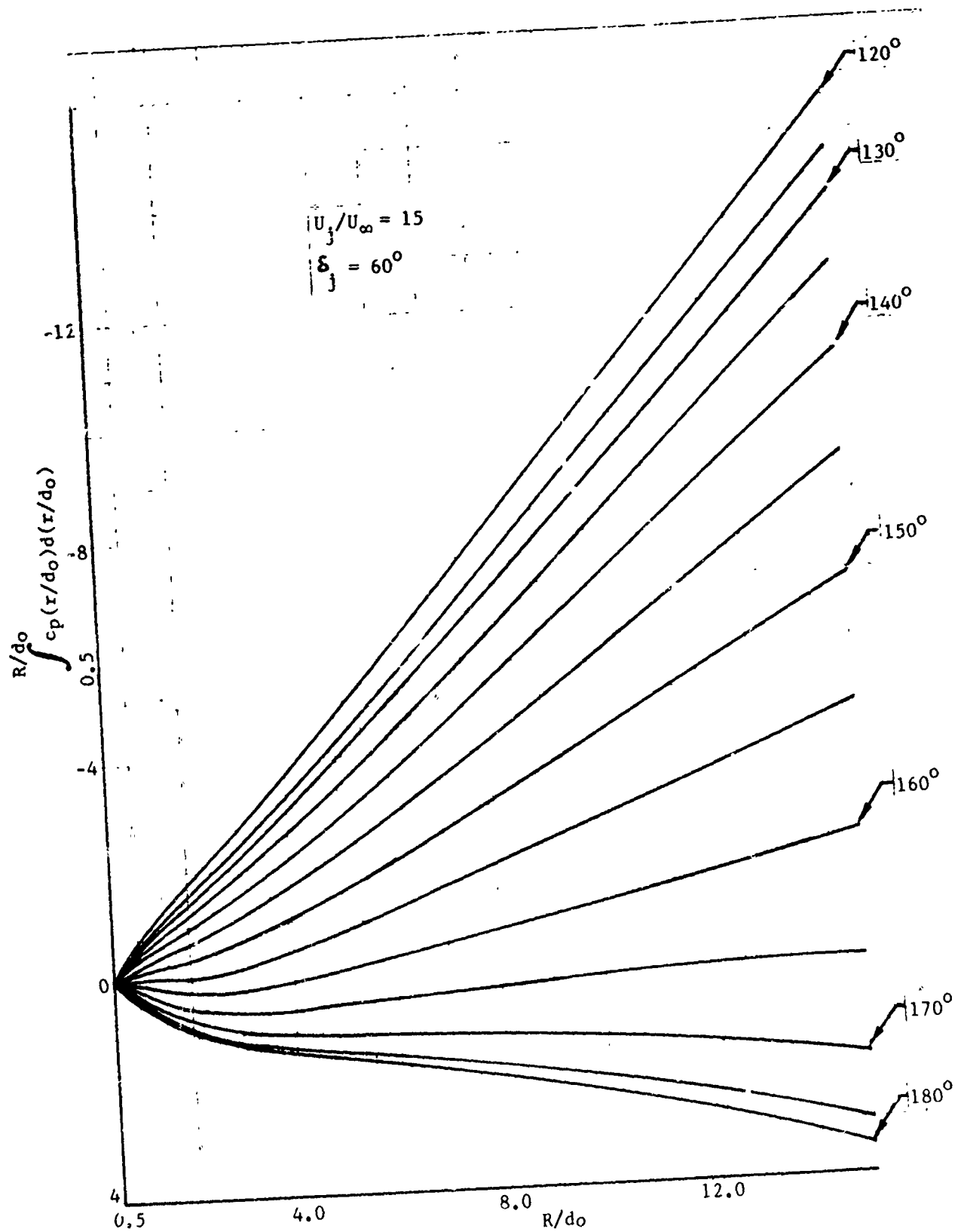


FIGURE III-6. (concluded)

## REFERENCES

1. Ellison, D. E., et al, "USAF Stability and Control Datcom," Air Force Flight Dynamics Laboratory, Wright-Patterson Air Force Base, Ohio, October 1960.
2. "Analysis of a Jet in a Subsonic Crosswind," (Symposium Proceedings) NASA SP-218, September 1969.
3. Fricke, L. B., Wooler, P. T., and Ziegler, H., "A Wind Tunnel Investigation of Jets Exhausting into a Crossflow," Air Force Flight Dynamics Laboratory Technical Report AFFDL-TR-70-154, Volumes I-IV, December 1970.
4. Wooler, P. T., Burghart, G. H., and Gallagher, J. T., "Pressure Distribution on a Rectangular Wing with a Jet Exhausting Normally into an Airstream," Journal of Aircraft, Vol. 4, No. 6, November-December 1967, pp. 537-543.
5. Abramovich, G. N., "The Theory of Turbulent Jets," The MIT Press, Cambridge, Massachusetts, 1963.
6. Ricou, F. P., and Spalding, D. B., "Measurements of Entrainment by Axisymmetrical Turbulent Jets," Journal of Fluid Mechanics, Volume 11, 1961, pp. 25-32.
7. Keffer, J. F., and Baines, W. D., "The Round Turbulent Jet in a Cross Wind," Journal of Fluid Mechanics, Volume 15, 1963, pp. 481-486.
8. Jordinson, R., "Flow in a Jet Directed Normal to the Wind," British Aeronautical Research Council R&M 3704, 1958.
9. Margason, R. J., "The Path of a Jet Directed at Large Angles to a Subsonic Free Stream," NASA TN D-4919, 1968.
10. Platten, J. L. and Keffer, J. F., "Entrainment in Deflected Axisymmetric Jets at Various Angles to the Stream," University of Toronto, Mech. Eng. TP6808, June 1968.
11. Shadunov, G. S., "Calculation of the Axis of a Jet in a Cross Flow," Soviet Aeronautics, Volume 9, No. 2, 1969.

## REFERENCES (Continued)

12. Wu, J.C., McMahon, H.M., Mosher, D.K., and Wright, M.A., "Experimental and Analytical Investigations of Jets Exhausting into a Deflecting Stream," *Journal of Aircraft*, Volume 7, No. 1, January-February 1970, pp. 44-51.
13. Bradbury, L.J.S. and Wood, M.N., "The Static Pressure Distribution Around a Circular Jet Exhausting Normally from a Plane Wall into an Airstream," RAE Technical Note AERO 2978, August 1964.
14. Gelb, G.H. and Martin, W.A., "An Experimental Investigation of the Flow Field About a Subsonic Jet Exhausting into a Quiescent and a Low Velocity Airstream," *CASJ*, Volume 12, No. 8, October 1966.
15. Wooler, P.T., "Flow of a Circular Jet into a Cross Flow," *Journal of Aircraft*, Volume 6, No. 3, May-June 1969, pp. 283-284.
16. Hall, G.R., "Scaling of VTOL Aerodynamic Suckdown Forces," *Journal of Aircraft*, Volume 4, No. 4, July-August 1967, pp. 393-394.
17. Hess, J.L. and Smith, A.M.O., "Calculation of Potential Flow about Arbitrary Bodies," *Progress in Aeronautical Sciences*, Volume 8, ed. by D. Kücheman, Pergamon Press, New York, 1967.
18. Thwaites, Bryan, *Incompressible Aerodynamics*, Clarendon Press, Oxford, 1960.
19. Milne-Thomson, L.M., *Theoretical Hydrodynamics*, The MacMillan Company, New York, 1968, Fifth Edition.
20. Theodorsen, T.H., "Theoretical Investigation of the Ducted Propeller Aerodynamics," Volume I, Republic Aviation Report, August 1960.
21. Grahame, W.E., "Aerodynamic Effects of Lift-Jet and Lift-Fan Inlets in Transition Flight," *Journal of Aircraft*, Volume 6, No. 2, March-April 1969, pp. 150-155.
22. Sacks, Alvin H., "Aerodynamic Forces, Moments and Stability Derivatives for Slender Bodies of General Cross Section," NACA TN 3283, November 1954.
23. Wassor, Howard R., "Studies of a Method for Predicting Nonlinear Aerodynamics of Arbitrary Bodies," NOR 69-44, March 1969.

## REFERENCES (Continued)

24. Bryson, A.E., "Symmetrical Vortex Separation on Circular Cylinders and Cones," *Journal of Applied Mechanics*, Volume 26, No. 4, pp. 643-648, December 1959.
25. Hoerner, S.F., "Fluid-Dynamics Drag," 1958.
26. Weissinger, J., "The Lift Distribution of Swept Back Wings," NACA TM 1120, March 1947.
27. Critzos, C.C., Heyson, H.H., Boswinkle, R.W., "Aerodynamic Characteristics of NACA 0012 Airfoil Section at Angles of Attack from 0° to 180°," NACA TN 3361, January 1955.
28. Thwaites, B., *Incompressible Aerodynamics*, page 349, Oxford University Press, 1960.
29. Williams, J. and Wood, M.N., "Aerodynamic Interference Effects with Jet-Lift V/STOL Aircraft Under Static and Forward Speed Conditions," *Zeitschrift fur Flugwissenschaften*, Volume 15, No. 7, July 1967, pp. 237-256.
30. Milne-Thomson, L.M., *Theoretical Hydrodynamics*, The MacMillan Co., New York, 1968, 5th Edition, Chapters VIII and XVI.
31. Streeter, V.L., *Handbook of Fluid Dynamics*, McGraw-Hill Book Co., New York, 1961, Chapters IV and XIII.
32. Skifstad, J.G., "Aerodynamics of Jets Pertinent to VTOL Aircraft," AFAPL-TR-69-28, March 1969.
33. Gentry, G.L. and Margason, R.J., "Jet-Induced Lift Losses on VTOL Configurations Hovering In and Out of Ground Effect," NASA TN D-3166, 1966.
34. Shumpert, P.K. and Tibbetts, J.G., "Model Tests of Jet Induced Lift Effects on a VTOL Aircraft in Hover," NASA CR-1297, March 1969.
35. Wyatt, L.A., "Static Tests of Ground Effect on Planforms Fitted with a Centrally-Located Round Lifting Jet," Ministry of Aviation, C.P. 749, 1962.
36. Spreeman, K.P. and Sherman, I.R., "Effects of Ground Proximity on the Thrust of a Simple Downward-Directed Jet Beneath a Flat Surface," NACA TN 4407, 1958.
37. Anon, Conference on V/STOL and STOL Aircraft, NASA-SP-116, April 1966.

## REFERENCES (Continued)

38. Hall, G.R., "Scaling of VTOL Aerodynamic Suckdown Forces," *Journal of Aircraft*, Volume 4, No. 4, July-August 1967.
39. McLemore, H.C., "Jet-Induced Lift Loss of Jet VTOL Configurations in Hovering Condition," NASA TN D-3435, 1966.
40. Davenport, E.E. and Spreeman, K.P., "Thrust Characteristics of Multiple Lifting Jets in Ground Proximity," NASA TN D-513, 1960.
41. Hall, G.R., "Sealing of VTOL Recirculating Phenomena," Paper Presented at the AFFDL V/STOL Technology and Planning Conference, September 1969.
42. Hall, G.R. and Rogers, K.H., "Recirculation Effects Produced by a Pair of Heated Jets Impinging on a Ground Plane," NASA CR-1307, 1969.
43. Lavi, R., Hall, G.R., and Stark, W.W., "Fullscale Ground Proximity Investigation of a VTOL Fighter Model Aircraft," NASA CR-1098, June 1968.
44. Vogler, R.D., "Ground Effects on Single and Multiple Jet VTOL Models at Transition Speeds over Stationary and Moving Ground Planes," NASA TN D-3213, 1966.
45. Tobak, Murray, "On the Use of the Indicical Function Concept in the Analysis of Unsteady Motions of Wings and Wing-Tail Combinations," NACA TR 1188, 1954.
46. Skulsky, R.S., "A Conformal Mapping Method to Predict Low Speed Aerodynamic Characteristics of Arbitrary Slender Re-entry Shapes," *Journal of Spacecraft, and Rockets*, Vol. 3, No. 2, February 1966, pp. 247-253.
47. Thwaites, Bryan, *Incompressible Aerodynamics*, Clarendon Press, Oxford, 1960, Chapter VIII.
48. Multhopp, H., "Die Berechnung der Auftriebsverteilung von Tragflügeln," *Luftfahrtforsch*, Volume 15, pp. 153-169. Translated as R.T.P. Translation Number 2392 or Rep. aer. Res. Coun., London 8516, 1938.
49. Schrenk, D., "A Simple Approximation Method for Obtaining the Spanwise Lift Distribution," NACA TM 948, 1940.
50. Werner, J.E. and Chang, H.S., "Analytical Determination of the Induced Flow due to a Jet in a Subsonic Crossflow," New York University, NYU-AA-70-21, September 1970.